UNIVERSIDAD COMPLUTENSE DE MADRID
FACULTAD DE ÓPTICA Y OPTOMETRIA

TESIS DOCTORAL

Simulación y caracterización de correcciones ópticas: impacto de diseños, aberraciones monocromáticas y policromáticas

Simulation and characterization of optical corrections : impact of design, monochromatic and polychromatic aberrations

MEMORIA PARA OPTAR AL GRADO DE DOCTOR

PRESENTADA POR

Sara El Aissati Aissati

Directoras

Susana Marcos Celestino
María Viñas Peña

Madrid

© Sara El Aissati Aissati, 2022

UNIVERSIDAD COMPLUTENSE DE MADRID

FACULTAD DE ÓPTICA Y OPTOMETRÍA

TESIS DOCTORAL

SIMULACIÓN Y CARACTERIZACIÓN DE CORRECCIONES ÓPTICAS: IMPACTO DE DISEÑOS, ABERRACIONES MONOCROMÁTICAS Y POLICROMÁTICAS

SIMULATION AND CHARACTERIZATION OF OPTICAL CORRECTIONS: IMPACT OF DESIGN, MONOCHROMATIC AND POLYCHROMATIC ABERRATIONS

MEMORIA PARA OPTAR AL GRADO DE DOCTORA

PRESENTADA POR

SARA EL AISSATI AISSATI

DIRECTORAS

SUSANA MARCOS CELESTINO

MARIA VIÑAS PEÑA

UNIVERSIDAD COMPLUTENSE DE MADRID

FACULTAD DE ÓPTICA Y OPTOMETRÍA

TESIS DOCTORAL

SIMULACIÓN Y CARACTERIZACIÓN DE CORRECCIONES ÓPTICAS: IMPACTO DE DISEÑOS, ABERRACIONES MONOCROMÁTICAS Y POLICROMÁTICAS

SIMULATION AND CHARACTERIZATION OF OPTICAL CORRECTIONS: IMPACT OF DESIGN, MONOCHROMATIC AND POLYCHROMATIC ABERRATIONS

MEMORIA PARA OPTAR AL GRADO DE DOCTORA

PRESENTADA POR

SARA EL AISSATI AISSATI

DIRECTORAS

SUSANA MARCOS CELESTINO

MARIA VIÑAS PEÑA

UNIVERSIDAD
COMPLUTENSE
MADRID

Laboratorio de Óptica Visual y Biofotónica
Instituto de 'Daza de Valdés'
Consejo Superior de Investigaciones Científicas

Facultad de Óptica y Optometría
Universidad Complutense de Madrid
Programa de doctorado Óptica,
Optometria y Visión

۞ سارة العيساتي ۞

بِسْمِ اللَّهِ الرَّحْمَٰنِ الرَّحِيمِ

ACKNOWLEDGEMENTS

Querido/as amigos/as, compañero/as, familiares y lectores,

Si habéis llegado a esta parte deciros que habéis aterrizado en la mejor parte de la tesis, ya que sin el apoyo y la sabiduría de las maravillosas personas que nombraré a continuación esta experiencia que he intentado trasladar a estas páginas no hubiera sido posible.

En primer lugar, y sin duda alguna me gustaría agradecer de corazón a mis dos supervisoras. ***Susana*** muchas gracias por acogerme primero como estudiante de máster y luego como candidata a doctora. Siempre te estaré agradecida por confiar en mis capacidades sin hacerlo yo misma, y por animarme siempre a dar lo mejor de mi. Por darme la oportunidad de conocer y tener relación con personas de renombre en el ámbito de la visión. Por esto y mucho más MUCHAS GRACIAS Susana. ***Maria*** que empezó siendo también mi directora de máster y a guiarme ya en ese entonces en un sistema óptico, al que aún le tengo miedo. Gracias por compartir tu conocimiento conmigo y por hacerme partícipe de cada pequeño y grande proyecto que te traías entre manos. Muchísimas gracias Maria. Gracias a las dos por ser mi ejemplo a seguir en este mundo llamado....CIENCIA.

Como no hay manera de agradecer de forma colectiva y al mismo tiempo a todas las magníficas personas que me rodean lo haré por orden cronológico (intentaré tener la barra de error más pequeña posible):

Como en las películas empiezan los créditos…3…..2…..1....

Ana gracias por acompañarme primero en la locura de empezar hacer el TFM en un laboratorio de gran calibre y luego en hacer la tesis. Me ha encantado tenerte de compañera de laboratorio, como aprendices beginners en un sistema enorme de Óptica Adaptativa, alinear un filtro espacial por primera vez, ir a un congreso internacional juntas y millones de cosas más. Mucho ánimo con tu tesis, y sabes que si tienes cualquier duda me puedes preguntar.

Carlos Dorronsoro, gracias por todas las veces que decías 'Sara, ahora tengo 10min para ti' esas mini reuniones que luego se alargaban mucho más, y por ser una parte importante de mis primeras etapas de esta experiencia, llamada tesis.

Clara esa persona que admiro por las millones de virtudes que tiene. La primera persona que conocí en VioBio tras mis supervisoras en el laboratorio de al lado. Con la frase estoy en el laboratorio contiguo haciendo medidas dime si necesitas algo, poco a poco entre una cosa y otras aprendí a alinear contigo, a modificar 'script de Matlab' con mucho miedo al principio a estropear cualquier cosa. Hora y horas a oscuras alineando se hicieron más amenas con tus playlist 'curiosas' y descansos mandados (around 11:00h). Gracias por tus consejos y por cuidarme, y estar pendiente de mis funciones vitales. Prometo cambiar poco a poco. Eres mi ídolo.

Dani Pascual, eres un máquina con un corazón latiendo. Decir que el número que más he marcado en el laboratorio después del de Maria es el tuyo, lo dice TODO. Agradezco todas las veces que te he llamado y has bajado más rápido que un relámpago. Solo con tu presencia se arreglaban las cosas 'no siempre', a veces había que subirlas a la mesa de operaciones - me fascina cada vez que veo esas enormes manos arreglando algo tan pequeño y con tanta delicadeza. Espero tener un Dani como tú a todos los laboratorios a los que vaya.

Edu nos conocimos por tener de peregrinación un sitio en común, el despacho 304. Yo iba a visitar a Clara, Rocío o Miriam, y tú no lo sé…. mejor no preguntar. Entre charlas random y preguntas inesperadas, llegaste a ser un Edu especial con abrazos únicos e 'inocentes'. Gracias por ser

como eres y por la energía que desprendes. Voy a dejar el tema de viajes para una segunda parte porque sino no acabaría nunca -lo bien que me lo paso contigo.
Xoana esa personita encantadora y trabajadora que sin darme cuenta me supero en esta carrera. Super orgullosa de ti, SIEMPRE. Gracias por tenerme en cuenta en todos tus planes y locuras. Por la frase 'avisa cuando llegues a casa' que sale tan dulce de tu boca 'de hermana mayor'.
Rocio, mi única química favorita, una parte esencial en mis últimos años de tesis, mi psicóloga privada sin cobro. Me encanta charlar de ciencia y de todos los temas posibles contigo. Las horas se me pasan volando, y lo que eran 5min de chequeo normal se alargan sin darnos cuenta, y a mí me encanta. Mucha suerte en tu tesis y no olvides que puedes contar conmigo siempre.
James y Andres, mis compañeros de cumple mes. Tenemos pocas oportunidades para sacar conversación, pero cuando lo hacemos se siente súper cómodo, lo disfruto mogollón, y aprendo un montón de vosotros. Tener la impresora en el despacho ha sido un 'bonus'.
Carlos, el intruso del grupo VioBio. Nos conocimos por compartir pasillo, luego coincidimos varias veces en el ascensor (de las pocas personas que dicen ¡Hola!) y por las galletas del café. Y sin darnos cuenta compartimos grupo del IOSA y la RED de Doctorandos del CSIC. Agradezco cada uno de estos sucesos por unirnos. Eres un hombre increíble.
Lekha, that wonderful person who landed one day in my office. I could write sentences and sentences about your impact on me and on this thesis, but I keep them to myself (all positive, and I hope you already know). Thank you for the wonderful conversations we have on super varied topics, and thanks to that I realize how much we have in common. Thank you for teaching and sharing with me a piece of your beautiful India, you know that I am a number ONE fan. Good luck, in this final stage of the thesis, and like the initial one I have you and you have me with full support.
Victor, hacía mucho que no conocía una persona tan competitiva 'en el buen sentido, siempre' en el ámbito intelectual. Te admiro por ello. Magic te anima en esta última etapa, y te recuerda que hay que comer y dormir.
Elena, la persona más correcta de VioBio. Gracias por ayudarme siempre en las tareas burocráticas aunque las pida unos microsegundos antes del deadline. Es algo que tengo que arreglar de mi, calcular mejor los tiempos. Y que sepas que me encanta siempre tu versión de la realidad. Y gracias a ***Nohelia*** también por tu ayuda siempre.

Antes de empezar mi doctorado, hice una estancia de investigación en Murcia, y allí conocí al conjunto perfecto de pareja y gallega (además de personas maravillosas en el Loum, un saludo enorme). Y el inesperado destino hizo que nos volviéramos a encontrar en Madrid. Gracias destino.

Alberto y Lucie gracias por ser tan entrañables. ***Alberto*** mi superhéroe con barba y con capa invisible, que apareció en mis últimos años de tesis. Con tu sincera frase 'Dime si necesitas algo' lo arreglas TODO. Gracias por animarme y ayudarme a resolver esos problemas de simulación en 'Matlab'. Hay personas que están hechas para explicar y arreglar TODO si les das un lápiz y un papel, y tú eres uno de ellos. Me encantan tus esquemas simplificados de problemas súper complicados, y me encantas tú.
Carmen, yo sí que de mayor quiero ser como tú. Una científica luchadora con estilo. Disfruto todas nuestras charlas de puerta de despacho o sentada enfrente con tus 'petos característicos', dando consejos de la vida misma. Me encanta que vengas a despedirte de mí cada vez que te vas a casa, y siempre tengas para mí frases súper reconfortantes y preciosas, que alegran a cualquiera. Eres la mejor, y debes saberlo.
Judith, la postdoc más enrollada cuando la conoces. Gracias por compartir conmigo todas tus experiencias de las que se puede aprender mogollón. Tus charlas son todo monólogos de aprendizaje.

Qué pena que haya venido el COVID y no hayamos tenido más tiempo para pasarlo bien pero que sepáis que de alguna forma os estoy agradecida por ser parte de esta experiencia.

Pilar, esa persona con corazón de oro y con abrazos súper reconfortantes, que apareció un día en la comida, luego en una quedada….y poco a poco un 'MUST' en esta experiencia. Mucha suerte en la tesis, e intentaré no perderme nada de tu increíble progreso. Eres un sol.

Edu junior, tus bromas las voy cogiendo poco a poco. Y espero que tú las mías también, aunque soy muy mala. Mucha suerte en tu tesis, y con lo apañado que eres seguro que sin problema.
Lupe y Alejandra, parece que competimos con quien de las tres se queda más tarde en el despacho. Pero no es que nos guste la silla del despacho o el 'screen' del ordenador, sino que no sabemos cómo lo hacemos que terminamos siempre a las tantas. Hay que aprender a dejar atrás este hábito, pero poco a poco. Ánimo con esas tesis.
Amal, creía que no había personas que mezclasen 'darija' y español indiferentemente, además de mis hermanas y yo, hasta que te conocí. Es súper gracioso escucharnos. Si decides empezar el camino de hacer la tesis, tengo millones de consejos para ti que espero que te ayuden.
Fernando, la última persona en unirse a la lista, pero que se siente tan cercano. Gracias por aparecer en VioBio, y gracias por tus consejos Rochester life-style.

Sole, Marisa y Maria Luisa, esas mujeres tan cariñosas y serviciales. Gracias por estar pendiente siempre de mí y ayudarme en cada cosa que pedía. Teniéndoos soy la niña mimada, con privilegios en el Instituto de Óptica.

In addition to having wonderful people at VioBio, I have had the opportunity to meet wonderful people on the other side of the world, in **SEATTLE**. A city that now I love for many reasons. Many thanks to Susana for giving me this opportunity and to ***Ram*** for welcoming me into his lab as one of the members for a few wonderful months. Thanks to ***Palash, Vimal, Ben, Tang, Sierra, Ayoub, Mery, and Emily*** for making my stay in Seattle an unforgettable experience. ***Ram***, my stay supervisor, I have all your late-stage advice written in capital letters. Thank you very much.

I don't forget ***Hana***, my sweet-crazy friend in Seattle for being the way you are and for opening your house to me and trusting me as if we had known each other all our lives. I hope we see each other soon, Insha Allah.

Muchas gracias por apoyarme y por entender mi tiempo limitado ***Nora, Albena y Yas*** esas maravillosas personas que conocí en la Facultad y luego se convirtieron en una Hermosa Amistad.
José Manuel mi tutor de la facultad por estar siempre pendiente de mis deadlines administrativos de la Uni y a **Beatriz** por solucionar todas mis dudas del programa de doctorada. Muchas gracias a los dos y lo siento por ser tan pesada.

Enrique, Merche, Andrea Curatolo, Pablo, miembros del IOSA, junta directiva de la RED de Doctorand@s…y un etc ….gracias por aparecer en mi camino.

Y por ser los últimos no significa que no hayan sido importantes, sino lo contrario mis padres, mi familia. ***Mamá y papá***, esas personas increíbles y cariñosas que me apoyan incondicionalmente y dan más de lo que tienen de lo inmaterial y material***. Papá*** cuando te pregunten la próxima vez qué hace tu hija mediana ya tengo la solución, ya les puedes decir que es DOCTORA, seguro que no preguntan más (la respuesta de trabaja ennn ……algo…de …como, queda sospechosa). ***Mamá***, esta etapa de la tesis ha tenido muchos altibajos que hemos compartido y superado juntas, gracias por estar siempre para mí. ***Somaya, Mariam y Omar*** esas criaturas tan pesadas que quiero un montón..que siempre están preguntando que cuándo acabó…la respuesta correcta es: creo que pronto. A mis abuelos y tios/as gracias por estar orgullosos de mí, y que sepáis que yo lo estoy más de vosotro/as.

Soy afortunada de teneros a todos/as y por ser cada uno una parte muy importante de mi vida.
Siempre se queda alguien por el camino de no estar agradecido, y me mil disculpo por ello.
Muchas gracias de nuevo a los nombrados y a los no nombrados.

Sara El Aissati Aissati firmante como Sara Aissati.

thank you

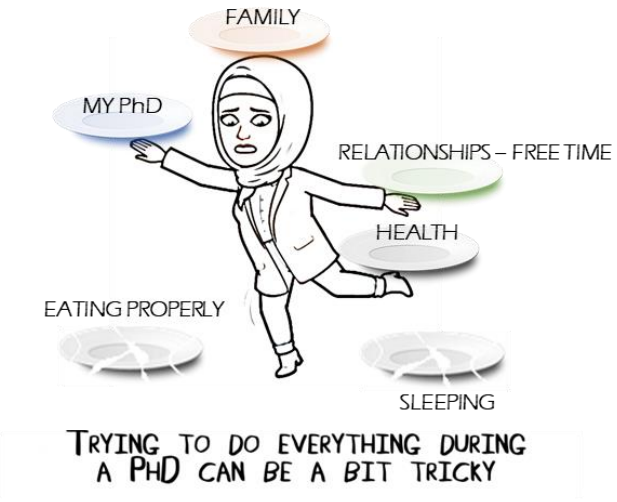
FAMILY
MY PhD
RELATIONSHIPS – FREE TIME
HEALTH
EATING PROPERLY
SLEEPING
TRYING TO DO EVERYTHING DURING A PHD CAN BE A BIT TRICKY

FUNDING

The research developed during this thesis would have not been possible without the funding received from the following public and private institutions:

- FPU-PhD fellowship of the Spanish Government (FPU16/01944 -MECD) to Sara El Aissati.
- Youth Entrepreneurship and Employment Strategy fellowship of the Spanish Government (MTMSS) to Sara El Aissati.
- European Research Council "Bio-inspired optical corrections of presbyopia". Ref. 294099 PI: Susana Marcos.
- Spanish Government Grant "Optical imaging technologies and opto-biomechanical models for diagnosis and personalized treatment in ophthalmology".FIS2014-56643-R. PI: Susana Marcos
- Master Clinical Research Agreement "Duplication and Calibration of the SimVis Simulator" (WP1), Johnson & Johnson Vision Care, Inc. USA. PI: Susana Marcos.
- Master Clinical Research Agreement "Evaluation of the SimVis System with 1-Day ACUVUE® Moist Multifocal Optics" (WP2), Johnson & Johnson Vision Care, Inc. USA. PI: Susana Marcos.
- "Photobonding strategy for a reversible multifocal IOL". Sponsor: PhysIOL, Belgium. PI: Susana Marcos.
- Spanish Government Grant FIS2017-84753-R. PI: Susana Marcos.
- European Research Council under the ERC-H2020-MSCA-IF-GF-2019-MYOMICRO-893557 to Maria Vinas.

KEYWORDS

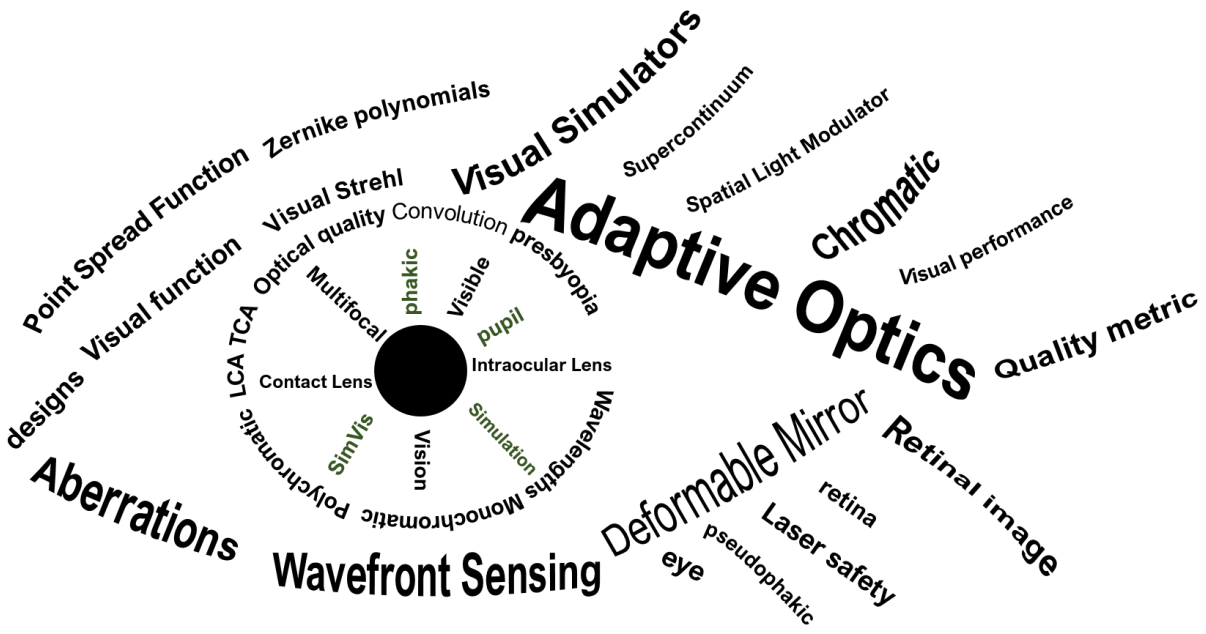
Point Spread Function
Zernike polynomials
Visual Simulators
Supercontinuum
Spatial Light Modulator
Visual Strehl
Optical quality
Convolution
presbyopia
Chromatic
Visual performance
Visual function
designs
LCA TCA
Multifocal
phakic
Visible
pupil
Adaptive Optics
Quality metric
Contact Lens
Intraocular Lens
Wavelengths
Monochromatic
Polychromatic
SimVis
Vision
Simulation
Deformable Mirror
Retinal image
retina
Laser safety
Aberrations
Wavefront Sensing
eye
pseudophakic

Table of contents

ACKNOWLEDGEMENTS III

FUNDING IX

KEYWORDS XI

SUMMARY OF THE THESIS XIX

RESUMEN DE LA TESIS EN CASTELLANO XXI

LIST OF COMMONLY USED ABBREVIATIONS XXIII

CHAPTER 1. INTRODUCTION 1

1.1. MOTIVATION 2

1.2. THE VISUAL PROCESS 2
1.2.1. Ocular optics 2
1.2.2. Basic aspects of neural processing in the retina 4
1.2.3. Basic concepts of the integration of visual information in the visual cortex 5

1.3. THE OPTICAL QUALITY OF THE EYE 6
1.3.1. Monochromatic aberrations 7
1.3.2. Chromatic aberration 10
1.3.3. Optical quality metrics 13
1.3.4. Double-pass retinal image quality 17
1.3.5. Representing retinal image using convolution 18
1.3.6. Interaction between monochromatic and chromatic aberrations 19

1.4. THE STILES-CRAWFORD EFFECT 21
1.4.1. The Optical Stiles-Crawford Effect (OSCE) and the Stiles-Crawford Effect of the First Kind (SCE-I) 21
1.4.2. Measurement of human cone-photoreceptor alignment (OSCE) 21

1.5. AGING PROCESS IN THE EYE 24
1.5.1. Accommodation, Presbyopia, and Cataract 24
1.5.2. Presbyopia solutions 25
1.5.3. The effect of chromatic dispersion on pseudophakic eyes 30

1.6. ADAPTIVE OPTICS VISUAL SIMULATORS 32
1.6.1. Adaptive Optics: The technique 32
1.6.2. Principal components of an AO system 33
1.6.3. Visual simulators from the research laboratory to the clinic. 37

1.6.4. Applications of Adaptive Optics 37

1.7. OPEN QUESTIONS 41

1.8. GOALS OF THE THESIS 42

1.9. HYPOTHESES 43

1.10. STRUCTURE OF THE THESIS 43

CHAPTER 2. METHODS 47

2.1. OPTICS SYSTEMS IN VIOBIO LAB 49
2.1.1. General description of the monochromatic AO system 49
2.1.2. General description of the polychromatic multichannel AO visual simulator 50
2.1.3. General description of the Laser Ray Tracing 54
2.1.4. Clinical visual simulator SimVis Gekko SimVis2eyes 55

2.2. EXPERIMENTAL IMPLEMENTATIONS DURING THIS THESIS 57
2.2.1. Double-pass aerial retinal imaging 57
2.2.2. Acousto-optic module: wavelength selection automatization 58
2.2.3. Psychophysical channel: white light illumination 59
2.2.4. Transverse Chromatic Aberration channel 60

2.3. EXPERIMENTAL PROCEDURES FOR IN VIVO MEASUREMENTS 61
2.3.1. General protocols with human subjects 61
2.3.2. Measurements, correction, and inductions of aberrations in the AO systems 62
2.3.3. Measurements of retinal images of the human eye 63
2.3.4. Measurements of chromatic aberrations of the human eye 64
2.3.5. Measurements of the optical/objective Stiles-Crawford effect in the human eye 64

2.4. PSYCHOPHYSICAL EXPERIMENTS 66
2.4.1. Visual stimuli 66
2.4.2. Manipulation of retinal blur 66
2.4.3. Psychophysical techniques used under Adaptive Optic controlled aberrations 67

2.5. OPTICAL QUALITY ANALYSIS 69
2.5.1. Optical quality metrics 69
2.5.2. Double-pass optical quality metric 69
2.5.3. Correlation metric 70

CHAPTER 3. PRE-OPERATIVE SIMULATION OF POST-OPERATIVE MULTIFOCAL VISION 69

3.1. INTRODUCTION 71

3.2. METHODS **72**
3.2.1. Multifocal IOL 72
3.2.2. Patients and surgery 72
3.2.3. Visual simulation platforms 73
3.2.4. Visual test & experimental protocol 76
3.2.5. Data analysis 77

3.3. RESULTS **77**
3.3.1. Predicted through-focus visual performance with simulated M-IOLs: a comparison across visual simulators 77
3.3.2. TF VA with simulated M-IOLs pre-operatively and implanted M-IOLs post-operatively 77
3.3.3. Post-operative monochromatic-monocular TF VA vs. Polychromatic-binocular TF VA 81

3.4. DISCUSSION **82**

3.5. CONCLUSIONS **83**

CHAPTER 4. OPTICAL AND VISUAL QUALITY WITH PHYSICAL AND VISUALLY SIMULATED PRESBYOPIC MULTIFOCAL CONTACT LENSES **85**

4.1. INTRODUCTION **87**

4.2. METHODS **88**
4.2.1. Subjects 88
4.2.2. Multifocal Contact Lenses 89
4.2.3. AO Visual Simulator 89
4.2.4. On bench through-focus optical quality 91
4.2.5. In vivo measurements on presbyopic subjects 91
4.2.6. Data analysis 92

4.3. RESULTS **92**
4.3.1. Calculated Through-focus optical performance of the lens alone 93
4.3.2. Through-focus optical performance of the SimVis-simulated M-CLs 93
4.3.3. Experimental through-focus optical performance on-bench 94
4.3.4. Experimental through-focus optical and visual quality *in vivo* 95

4.4. DISCUSSION **99**

4.5. CONCLUSIONS **101**

CHAPTER 5. MATCHING CONVOLVED IMAGES TO OPTICALLY BLURRED IMAGES ON THE RETINA **103**

5.1. INTRODUCTION **105**

5.2. METHODS **106**

5.2.1. Convolved images 106
5.2.2. On bench testing 107
5.2.3. Subjects 107
5.2.4. Experimental protocol 108
5.2.5. Simulation of the effects of chromatic aberration 109
5.2.6. Data analysis 109

5.3. RESULTS 110
5.3.1. Wavefront aberrations (HOAs) and Visual Strehl (VS) 110
5.3.2. Experimental convolved images vs optical blur 111
5.3.3. Visual Acuity with real aberrations and convolved images 112
5.3.4. Simulations of mono- and polychromatic effects on retinal images 113

5.4. DISCUSSION 114

5.5. CONCLUSIONS 116

CHAPTER 6. GENDER IDENTIFICATION OF FACES UNDER MANIPULATED OCULAR OPTICS 117

6.1. INTRODUCTION 119

6.2. METHODS 120
6.2.1. Subjects 120
6.2.2. Optical quality 120
6.2.3. Stimuli 120
6.2.4. Experimental procedure and Psychophysical measurements. 121
6.2.5. Data analysis 122

6.3. RESULTS 122
6.3.1. Subject Optical quality 122
6.3.2. Gender Identification vs Visual Acuity 124
6.3.3. Optical quality and visual performance 125

6.4. DISCUSSION 127

6.5. CONCLUSIONS 128

CHAPTER 7. TESTING THE EFFECT OF OCULAR ABERRATIONS IN THE PERCEIVED TRANSVERSE CHROMATIC ABERRATION 127

7.1. INTRODUCTION 129

7.2. METHODS 130
7.2.1. Subjects 130
7.2.2. Transverse Chromatic Aberration measurement channel 130

7.2.3. Experiments 131
7.2.4. Computational Analysis of Perceived Transverse Chromatic Aberration 132
7.2.5. Data analysis 134

7.3. RESULTS 134
7.3.1. Wave aberration at different wavelengths and AO-correction 134
7.3.2. Psychophysical LCA 134
7.3.3. Experimental Optical and Perceived TCA: Impact of AO-correction of HOAs 135
7.3.4. Reflectometric OSCE 136
7.3.5. Computational perceived TCA 137

7.4. DISCUSSION 139

7.5. CONCLUSIONS 142

CHAPTER 8. LONGITUDINAL CHROMATIC ABERRATION IN PATIENTS IMPLANTED WITH TRIFOCAL DIFFRACTIVE HYDROPHOBIC IOLS 143

8.1. INTRODUCTION 145

8.2. METHODS 146
8.2.1. Patients 146
8.2.2. Psychophysical best focus at different wavelengths and distances 146
8.2.3. Data analysis 147

8.3. RESULTS 147
8.3.1. Chromatic difference of focus from psychophysical measurements 147
8.3.2. Refractive and visual outcomes for the IOL implanted 150

8.4. DISCUSSION 151

8.5. CONCLUSIONS 152

CHAPTER 9. CONCLUSIONS 153

SCIENTIFIC ACTIVITIES DURING THIS THESIS 159

REFERENCES 167

SUMMARY OF THE THESIS

Background

The eye is an optical element that projects images of the world onto the retina. This optical system is not perfect, as it suffers from aberrations as well as diffraction and scattering that degrade retinal image quality. In recent years, a large number of techniques based on Adaptive Optics (AO) have been developed for the measurement and correction of ocular aberrations. Measurements of the eye with AO systems have allowed a better understanding of the contribution of the different components of the eye to the degradation of image quality. Furthermore, the manipulation of optical aberrations allows understanding of the connections between optical degradation and perceived visual quality. The optics of the eye change with age, eye diseases, and treatments. Therefore, understanding the sources of variations in natural aberrations, the interactions between monochromatic aberrations and chromatic aberrations (Longitudinal Chromatic Aberration 'LCA' and Transverse Chromatic Aberration 'TCA'), and the impact of optical blurring on vision is key. This knowledge allows to shed light on some basic mechanisms of the eye and, among others, to guide the design and optimization of new alternatives for the correction of presbyopia (multifocal intraocular lenses and multifocal contact lenses), as well as other more complex personalized refractive and presbyopic corrections. Visual simulators based on AO are excellent tools to investigate vision under natural and modified optics in monochromatic and polychromatic conditions. A wavefront sensor in combination with an active optical element (deformable mirror, spatial light modulator, or simultaneous vision simulators based on SimVis technology) and a psychophysical channel allows investigating the optics of the eye, the neural adaptation processes behind, and the response to modified or simulated optics. In addition to modifying the optics using active elements, it can also be done using Fourier optics, convolving the PSF (Point Spread Function) characteristic of an aberration pattern with our object. This allows us to study the impact of convolved images by different patterns of aberrations on visual performance (in both monochromatic and polychromatic conditions).

Methods

A custom-developed polychromatic multichannel AO system (Visual Optics and Biophotonics Lab, IO-CSIC, Madrid, Spain) has been used to carry out the projects described in this thesis. The system is currently made up of 8 different channels: the illumination channel, with light from a supercontinuous laser source (SCLS); the AO channel, whose main components are the Hartmann-Shack wavefront sensor and the deformable mirror; the SLM channel, which incorporates the Spatial Light Modulator to simulate complex patterns (refractive and diffractive); the retinal camera channel, which allows capturing aerial images of the retina; the testing channel that allows evaluating the simultaneous vision simulator (SimVis technology), as well as real intraocular lenses in a cuvette or phase plates; a psychophysical channel consisting of a Digital Micro-mirror Device that allows displaying high-resolution visual stimuli, illuminated with monochromatic light or white light; Badal's system to correct and induce defocus; and the pupil monitoring channel, which allows you to monitor the size of the pupil and the position of the subject during measurements.

Another monochromatic AO system has also been used, with the essential components (deformable mirror and wavefront sensor) and a psychophysics channel. And also the Ray Tracing system (LRT).

Results and Conclusions

Using a polychromatic multichannel AO visual simulator has allowed the characterization of ocular optics in polychromatic conditions, and to study the interaction between monochromatic and chromatic aberrations. LCA measurements have been performed, and the data is consistent with previous studies in the literature. TCA was measured for the first time in this system, controlling for aberrations, pupil size, to study its impact together with the Stiles-Crawford effect. It was found that by correcting for aberrations, the perceived TCA value increased, suggesting that we can extend the observation that the presence of monochromatic optical aberrations protects vision against LCA to protection against TCA as well. Visual simulators have enabled the simulation of complex multifocal designs for presbyopia, providing subjects with the experience of multifocal vision. Through-focus measurements of optical quality (double-pass retinal images) and visual measurements (visual acuity) were performed, both on bench and real subjects. And measurements were made on both simulated lenses and real lenses. Both measures captured the extent of contact lens focus consistent with their addition. There weren't any differences between the real lenses and the simulations, both reproduce the multifocal pattern. Visual performance with multifocal intraocular lenses was also predicted, both in an AO environment and in a clinical simulator, prior to implantation in real subjects. The difference between the through-focus visual acuity curves with preoperative visual simulations and the postoperative data was in good agreement. In the case of simulation using convolved images, a systematic decrease in visual performance was found with visual acuity and retinal image quality in polychromatic light that seems to be mainly associated with a lack of favorable interaction between chromatic and monochromatic aberrations in the eye.

RESUMEN DE LA TESIS EN CASTELLANO

Introducción

El ojo es un elemento óptico que proyecta imágenes del mundo en la retina. Este sistema óptico no es perfecto, ya que sufre de aberraciones, así como difracción y dispersión que degradan la calidad de la imagen retiniana. En los últimos años, se han desarrollado un gran número de técnicas basadas en Óptica Adaptativa (AO) para la medida y corrección de las aberraciones oculares. Las mediciones del ojo con sistemas de AO han permitido comprender mejor la contribución de los diferentes componentes del ojo a la degradación de la calidad de las imágenes. Además, la manipulación de las aberraciones ópticas permite comprender las conexiones entre la degradación óptica y la calidad visual percibida. La óptica del ojo cambia con la edad, las enfermedades oculares y los tratamientos. Por lo tanto, comprender las fuentes de variaciones de las aberraciones naturales, las interacciones entre las aberraciones monocromáticas (HOA) y cromáticas (Aberración cromática longitudinal 'LCA' y Aberración cromática transversal 'TCA') y el impacto de la borrosidad óptica en la visión es decisivo. Este conocimiento permite arrojar luz sobre algunos mecanismos básicos del ojo y, entre otros, orientar el diseño y optimización de nuevas alternativas para la corrección de la presbicia (lentes intraoculares y lentes de contacto multifocales) , así como otras correcciones refractivas más complejas y personalizadas. Los simuladores visuales basados en la AO son excelentes herramientas para investigar la visión bajo ópticas naturales y modificadas en condiciones monocromáticas y policromáticas. Un sensor de frente de onda en combinación con un elemento óptico activo (espejo deformable, modulador espacial de luz o simuladores de visión simultánea basados en la tecnología SimVis) y un canal psicofísico permite investigar la óptica del ojo, los procesos de adaptación neural detrás de él y la respuesta a la óptica modificada o simulada. Además de modificar la óptica mediante elementos activos se puede realizar mediante óptica de Fourier, convolucionando la PSF (Función de dispersión de un punto) característico de un patrón de aberraciones con nuestro objeto. Esto nos permite estudiar el impacto de imágenes convolucionadas por diferentes patrones de aberraciones en el rendimiento visual (tanto en condiciones monocromáticas como policromáticas).

Metodología

Un simulador visual policromático multicanal de AO (Visual Optics and Biophotonics Lab, IO-CSIC, Madrid, España) se ha utilizado para llevar a cabo los proyectos descritos en esta tesis. El sistema actualmente está formado por 8 canales diferentes: el canal de iluminación, con luz procedente de una fuente láser de supercontinuo ; el canal de AO, cuyos componentes principales son el sensor de frente de onda Hartmann-Shack y el espejo deformable; el canal SLM, que incorpora el modulador de luz espacial para simular patrones complejos (refractivos y difractivos); el canal de cámara de retina, que permite capturar imágenes aéreas de la retina; el canal de testeo que permite evaluar el simulador de visión simultánea (tecnología SimVis), así como, lentes intraoculares reales en una cubeta o placas de fase; un canal psicofísico que consiste en un dispositivo de micro-espejo digital que permite mostrar estímulos visuales de alta resolución, iluminados con luz monocromática o luz blanca; el sistema de Badal para corregir e inducir el desenfoque; y el canal de monitoreo de la pupila, que permite monitorear el tamaño de la pupila y la posición del sujeto durante las mediciones.

También se ha utilizado otro sistema AO monocromático , con los componentes esenciales (espejo deformable y sensor de frente de ondas) y un canal de psicofísica. Y un sistema de trazado de rayos.

Resultados y Conclusiones

Utilizando un simulador visual multicanal policromático de AO, ha permitido la caracterización de la óptica ocular en condiciones policromáticas, y estudiar la interacción entre aberraciones monocromáticas y cromáticas. Se han realizado medidas de LCA, y los datos coinciden con estudios previos de la literatura. Se midió por primera vez la TCA en este sistema, teniendo control de las aberraciones, diferentes tamaños de pupila, para estudiar su impacto junto con el efecto Stiles-Crawford. Se encontró que al corregir las aberraciones, el valor de la TCA percibido aumentó, lo que sugiere que podemos extender la observación de que la presencia de aberraciones ópticas monocromáticas protege la visión contra la LCA a una protección contra la TCA también. Los simuladores visuales han permitido la simulación de diseños multifocales complejos para la presbicia, proporcionando a los sujetos la experiencia de la visión multifocal. A través de medidas a través de foco de la calidad óptica (medida de retina de doble paso) y medidas visuales (agudez visual), tanto en banco óptico como en sujetos reales. Y tanto en lentes simuladas como lentes reales. Ambas medidas capturaron la extensión de foco de las lentes de contacto en corcondancia con su adición. Apenas se observaron diferencias entre las lentes reales y las simulaciones, ambas reproducen el patrón multifocal. También se predijo el rendimiento visual con lentes intraoculares multifocales, tanto en un entorno AO como en un simulador clínico, antes de la implantación en sujetos reales. La diferencia entre las curvas de agudeza visual a través de foco con simulaciones visuales preoperatorias y los datos postoperatorios estuvieron en buena concordancia. En caso de la simulación mediantes imágenes convolucionadas se encontró una disminución sistemática en el rendimiento visual con la agudeza visual y la calidad de la imagen retiniana en luz policromática que parece estar asociada principalmente con una falta de interacción favorable entre las aberraciones cromáticas y monocromáticas en el ojo.

LIST OF COMMONLY USED ABBREVIATIONS

A
Add = Addition
AO = Adaptive Optics
AOTF=Acousto-optic Tunable Filter
AOSLO=Adaptive Optics Scanning Laser Ophthalmoscope
AOVS=Adaptive Optics visual simulators
ATR=Against –the-rule-astigmatism
B
BF=Best Focus
BCVA=Best Corrected Visual Acuity
C
Cyl = Cylinder
CL = Contact Lens
CSF=Contrast Sensitivity Function
CM=Command matrix
CCD=Charge-coupled device
CMOS=Complementary metal oxide semiconductor
Conv=Convolution
C_n^m=Zernike coefficient (order n; frequency,m)
CRT=Capsular Tension Ring
CDVA=Corrected Distance Visual Acuity
CDF=Chromatic difference of focus
D
D = Diopters
DM = Deformable Mirror
DMD=Digital Micro Mirror
DoF = Depth of Focus
DCIVA=Distance Corrected Intermediate Visual Acuity
DCNVA=Distance Corrected Near Visual Acuity
DL=Diffraction limit
E
EDOF = Extended Depth of Focus
ETDRS=Early Treatment Diabetic Retinopathy Study
Eq=Equation
F
FT=Fourier Transform
FFT=Fast Fourier Transform
FoV = Field of View
G
GI=Gender Identification
H
HOAs=High Order Aberrations

HASO=Hartmann-Shack
HiSFs=High Spatial Frequency
HD=Holographic Diffuser

I

IM=Interaction Matrix
IR=Infrared
IOL = Intraocular Lens

J

K

L

LCA=Longitudinal Chromatic Aberration
LOAs=Low Order Aberrations
LCoS=Liquid crystal on Silicon
LRT=Laser Ray Tracing
LoSFs=Low Spatial Frequency
LSF=Line Spread Function

M

M-CL = Multifocal Contact Lens
M-IOL=Multifocal Intraocular Lens
MTF = Modulation Transfer Function

N

NCSF= Neural Contrast Sensitivity Function

O

OTF=Optical Transfer Function
OSCE=Optical/Objective Stiles-Crawford effect

P

PSF=Point Spread Function
PTF=Phase Transfer Function
PP=Pupil plane
Poly=Polychromatic

Q

QUEST=Quick Estimate by Sequential Testing

R

RMS = Root Mean Square wavefront error
RS = Refractive Surgery
RF= Radio Frequency
RP=Retinal plane

S

SA=Spherical Aberration
SCLS=Supercontinuum Laser Source
SLD=Superluminiscest Diode
Sph = Spherical error
SimVis = Simultaneous Vision Simulator
SLM = Spatial Light Modulator
SFs=Spatial Frequencies
SR=Strehl Ratio
SCE=Stiles-Crawford effect

T

TCA=Transverse Chromatic Aberration
TL = Tunable Lens
TF = Through-focus
U
UV=Ultraviolet
UCVA=Uncorrected Visual Acuity
V
VA = Visual Acuity
VS = Visual Strehl
VSOTF=Visual Strehl Ratio
VIS=Visible
W
WTR=With-the-rule-Astigmatism
W(x,y) Wave aberration in Cartesian coordinate
W(ρ,θ) Wave aberration in the normalized radial coordinate
WL=White Light
X
Y
Z
Z= Zernike

1

CHAPTER 1. INTRODUCTION

The human eye is an example of a relatively simple optical instrument that provides exceptional functionality. But even with the simplicity of ocular optics, it was a long process to reach the almost complete understanding that we have today. The optics of the eye resemble an aplanatic design with partial correction for spherical aberration and coma. This is due to a natural balance between cornea and lens aberrations in the young eye, which is progressively lost during normal aging. Although interest in the eye is intrinsic to human nature, it was around the time of Galileo, in the XVII century, that scientific exploration of the eye started. From then on, continuous progress was made, in part due to the evolution of optical instruments. Telescopes and microscopes have been closely tied to the eye, as the ultimate observer was a human. Paradoxically, Adaptive Optics, originally conceived to couple with ground-based telescopes, has been used to avoid the resolution limitations of the eye in both imaging the retina and projecting images onto the retina. Measurement of the optical quality of the eye, and the capability of modifying the eye's optics (allowed by adaptive optics), opens the possibility of exploring the spatial limits of vision and understanding and proposing new alternatives for vision correction

The current chapter presents a brief review of current knowledge on the measurement and impact of monochromatic and chromatic aberrations on visual function, as well as a brief review of the state-of-the-art of Adaptive Optics and solutions for Presbyopia.

1.1. MOTIVATION

Due to scattering, diffraction, and both monochromatic and polychromatic aberrations, the optical quality of the human eye has long been known as being far from diffraction-limited. Adaptive Optics (AO) visual simulators have been used successfully for a multitude of applications. In brief, AO has helped us better understand how ocular aberrations and combinations of aberrations affect vision. Measurement of the aberrations allows us to simulate the subject's point spread function (PSF), which can be convolved with images of the outside world, and to illustrate the impact of those aberrations on retinal image quality. Furthermore, having the opportunity to work with a custom multichannel polychromatic AO visual simulator system with psychophysical channels has allowed us to investigate the effects of monochromatic and chromatic aberrations on vision, in normal subjects as well as in pseudophakic eyes.
Furthermore, adaptive optics allows the simulation of different optical designs on real eyes before surgery or lens fitting, even before lenses are manufactured. Patients can see through the optics (contact lenses or intraocular lenses) mapped as a phase map onto the active components of the adaptive optics visual simulator (a deformable mirror or a spatial light modulator), and experience the world through that correction. This application is particularly well-suited to test visual perception and visual performance of treatments for presbyopia, the age-related loss of crystalline lens accommodation affecting 100% of the population over 45 years of age.

1.2. THE VISUAL PROCESS

The vision process can be divided into three stages: the first corresponds to *ocular optics*, corresponding to the formation of images on the retina by the optical system of the eye; *photoreceptor processing*, where photoreceptors sample the retinal image and convert the light energy into nerve impulses that travel to further steps in the visual process, and, finally, the *neural processing* of the image that allows the perception of the final image (**FIGURE 1.1**).
The steps involved in the visual process are the following:

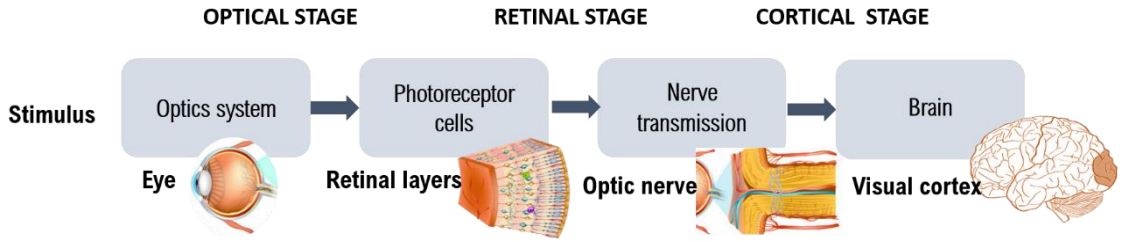

FIGURE 1.1. Schematic representation of the 3 stages of the visual process. The human eye (optical stage), layers of the retina (retinal stage), and the visual pathway from the retina via the optic nerve to the primary visual cortex (cortical stage).

1.2.1. Ocular optics

Anatomically the eye has an approximately spherical shape of about 24 mm in diameter in an adult person. The optical system of the eye is made up of two lenses, the cornea, and the crystalline lens, and by the transparent media, the aqueous humor and the vitreous humor (**FIGURE 1.2**).

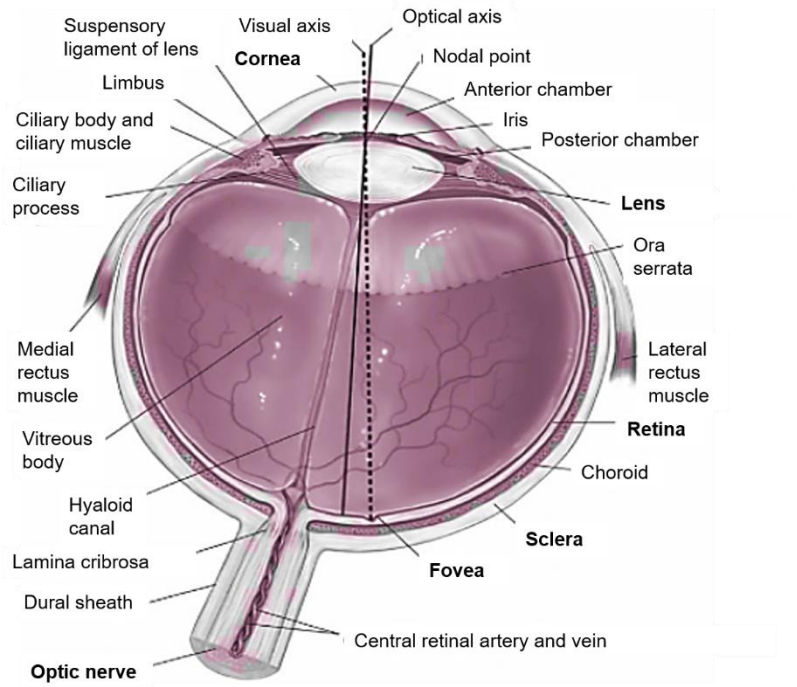

FIGURE 1.2. Horizontal cross-section of the human eye indicating the structures of the eye, the visual axis (the central point of the image focusing in the retina), and the optical axis [1].

Below, we describe the optical elements that light encounters as it passes through the eye, in the normal image formation process.

First, the light passes through the *cornea*, a transparent avascular tissue but with a large number of nerve endings. It is about 12 mm in diameter, about 0.6 mm thick, and has a refractive index of 1.366. Due to the abrupt change in the refractive index that light undergoes in the air-corneal transition, most of the power of the eye will be generated in this step (73%). The space immediately behind the cornea is the anterior chamber that contains the *aqueous humor*, responsible for nourishing the cornea. Next is the iris, a colored muscle that acts as a diaphragm controlling the amount of light that enters the eye. The opening of the diaphragm and where the light penetrates is what is known as the *pupil*, with a diameter that can vary from 2 mm to 8 mm in a young adult. This variation, depending on the level of illumination, controls the amount of light that reaches the retina and plays a fundamental role in the quality of the retinal image. A large diameter removes the system from the condition of paraxiality and favors optical aberrations; in turn, a small diameter improves the depth of focus and limits aberrations, since it allows only those rays closest to the axis of the system to pass. However, the smaller this diameter, the greater the diffraction effects.

After passing through the pupil, the light encounters the *crystalline lens*, a transparent structure controlled by the ciliary muscle, which (in the young eye) is capable of modifying its own shape to achieve a clear image on the retina. Its refractive index varies from one zone to another from 1.42 in the center to 1.39 in the periphery.

Then, the light passes through the posterior chamber filled with *vitreous humor*, a substance with a gelatinous texture that has a mainly structural function, giving consistency to the ocular structure. The light eventually reaches the back of the eye where the retina is located.

1.2.2. Basic aspects of neural processing in the retina

The *retina* is part of the central nervous system at the back of the eye that contains *photoreceptors*, called *rods* and *cones*. Those are cells that when they receive a suitable light stimulus are excited and transduce electromagnetic energy into electrochemical signals, which are transmitted through successive neurons in the retina itself and then to the brain.

The central area of the retina, called the macula, has an area of approximately 5.5 mm in diameter, is rich in cones, and is surrounded by a non-photosensitive pre-retinal pigment, which acts as a filter (cornea and lens also play a role)[2]. The macula is specially trained for sharp and detailed vision and prevents short-wavelength radiation from reaching that area of the retina. The center of the macula has a depression that occupies approximately 1.5 mm in diameter and subtends an angle of 5º, it is called the *fovea*. In the central portion of the fovea, the foveola, the image of the fixation object is formed. The foveola or central fovea is composed entirely of cones (200 µm of the retina), which have a long and thin structure of roughly 2.5 µm in the fovea and rapidly increase outside the fovea to 10 µm in the periphery. The total number of cones in the retina is 6.4 million. Rod diameter is roughly 3 µm at a field angle of 18° and increases in size to 5.5 µm in the periphery. There are roughly 125 million rods in the retina [3, 4]. A photoreceptor is distinguished by the presence of a single photopigment. Because rhodopsin is found in all rods, there is only one type of rod photoreceptor. There are three varieties of cone photoreceptors known as red, green, or blue cones (designation is long-, medium-, and short-wavelength-sensitive cones, or L, M, and S-cones, depending on which portion of the spectrum their photopigment absorbs the most) [5]. Normal trichromatic color vision utilizes all three cone photopigments (**FIGURE 1.3**). Cones respond to high levels of brightness and are responsible for daytime vision, while rods are characterized by high sensitivity to light, detecting objects at extremely low lighting levels, thus allowing night vision. The rod vision is known as scotopic vision, cone vision as the photopic, and intermediate vision where the two types of photoreceptors intervene as mesopic vision [6]. In addition, the sensibility of photoreceptors to light varies with the pupil entry position, being generally optimal for rays coming near the center of the pupil (known as the Stiles-Crawford effect)[7-10]. This phenomenon is detailed in section 1.4.

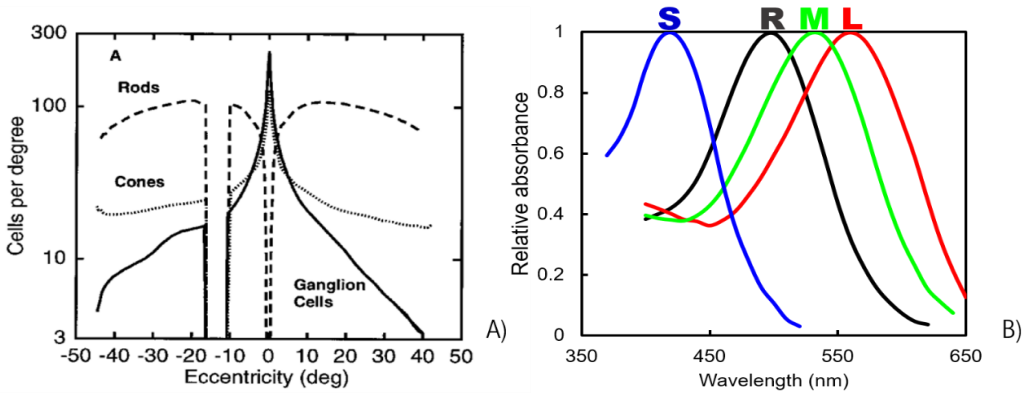

FIGURE 1.3. A) Linear density of cones, rods, and ganglion cells as a function of eccentricity in the human retina. (Modified from Curcio et al. [3, 4]). B) Normalized absorbance spectra for human visual pigments. There is one kind of rod photoreceptor (R) and three kinds of cone photoreceptor (Red (L-cone), Green (M-cone), and Blue (S-cone) (Replotted from Dartnall et al. [5]).

Intensive information processing takes place in the retina before sending visual signals to the brain. **FIGURE 1.4** shows a section of the retina with the cells that form it and how they are connected,

in layers from the outside to the inside of the eye. It can be observed that between ganglion cells and photoreceptors there are three other types of cells: horizontal, amacrine, and bipolar so that the transmission of information can follow different paths within the connection of the different retinal cells and that it will depend on their location on the retina. Thus, in the fovea, each photoreceptor cone connects with a bipolar cell, and this in turn with a ganglion following the most direct path [11, 12].

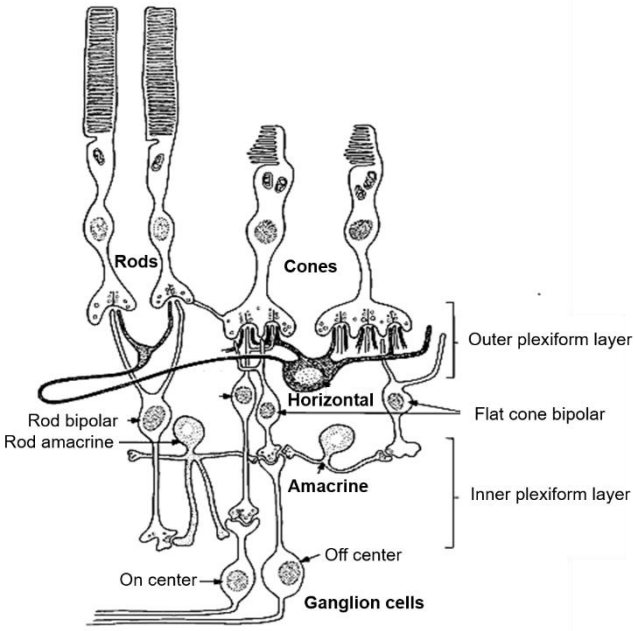

FIGURE 1.4. Schematic diagram of the retina and their major synaptic connections. Rods, Cones, Horizontal, Amacrine, Bipolar, and Ganglion cells (From Kandel et al. [11]).

1.2.3. Basic concepts of the integration of visual information in the visual cortex

The information at the exit of the eye continues its way through the visual pathway until it reaches the primary visual cortex (**FIGURE 1.5)**.

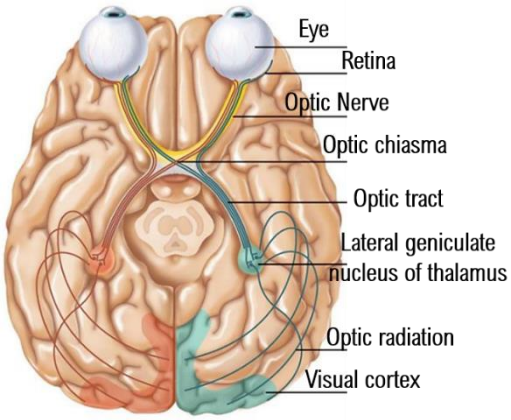

FIGURE 1.5. The primary pathway by which the eye sends signals to the visual cortex. Consisting of the optic nerve/optic tract, the lateral geniculate nucleus, and the optic radiation.

The fibers that leave the eye forming the optic nerve reach the optic chiasm without interruption and from there they go to different areas of the brain. Most of them (approximately 80%) send information through the optic tract to the lateral geniculate nucleus, the rest is information for the

control of functions of the eye movement, the pupillary reflex to light, and also, for processes of synchronization of biological rhythms (hypothalamus).

In the optic chiasm, there is a decussation of visual information from the optic nerves, such that information from the left visual field reaches the right lateral geniculate nucleus and vice versa for the left lateral geniculate nucleus.

Visual information leaves the lateral geniculate bodies through optical radiation that routes it to the *primary visual cortex (V1).* The primary visual cortex is a layer of cells about 2 mm thick located in the occipital part of the brain. Contains approximately 200 million cells compared to 1.5 of the lateral geniculate body. These cells were classified into simple and complex cells [13].

Finally, and for the first time in the entire perception process, cells appear in the primary visual cortex that receives input from both eyes, that is, there is a binocular convergence that will allow the construction of a single image of the visual scene.

The cells that form the primary visual cortex (stratified in 6 layers) are arranged in vertical columns related to the orientation of the stimulus. It should be noted that there are also other layers of the cortex (from V2 to V5) that participate in the visual process by performing various tasks. Thus, for example, zone V4 would be related to color vision.

In conclusion, the human visual system that has been described is modular and parallel. Basically, three stages could be differentiated: optics (focusing on the image), retinal (signal transduction light in electrical impulses), and brain processing.

1.3. THE OPTICAL QUALITY OF THE EYE

The image formed by the eye's optical system is not perfect because the eye suffers from aberrations, centering errors, diffraction, and scattering. All these phenomena contribute to the degradation of the retinal image. Scattering occurs mainly in the crystalline lens. It is practically negligible in the young eye but increases with age, causing a notable loss of transparency of the lens in patients with cataracts [14]. Diffraction is essentially produced by the edges and size of the pupil and affects the maximum resolving power of the eye, acting as a low pass filter for spatial frequencies of the image [15].

Although the eye is by no means a perfect optical instrument,-it suffers from optical aberrations-, its potential for accommodation, the field of view, adaptation, movements, and resolution that make it unique.

Aberrations can be divided into two main groups: monochromatic and chromatic aberrations (**FIGURE 1.6**). The following sections will describe them in more detail.

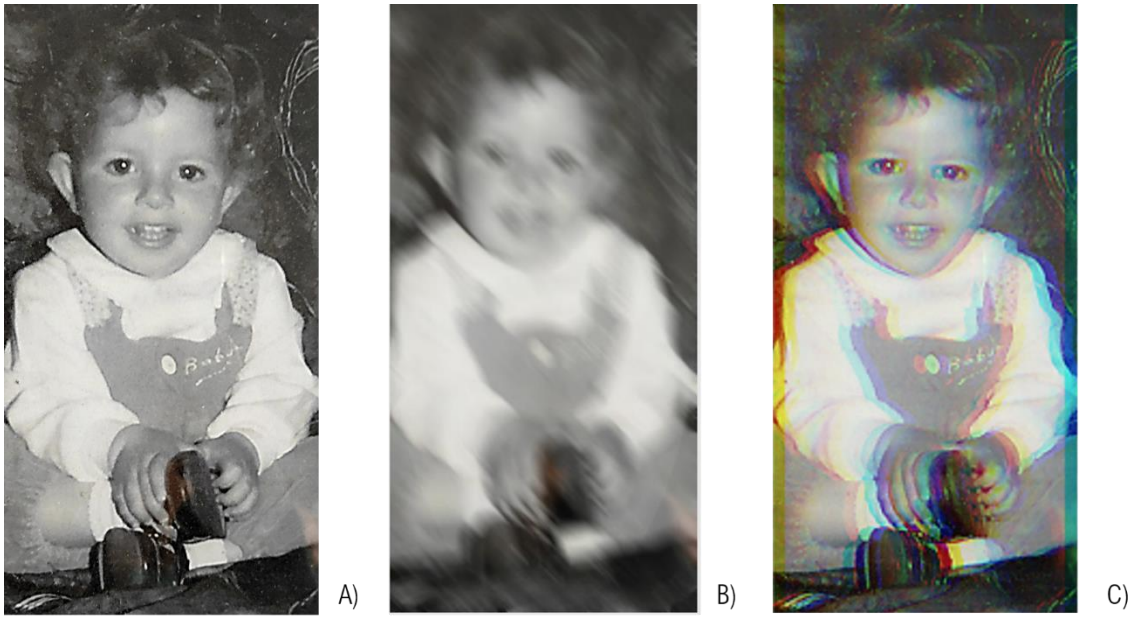

FIGURE 1.6. Simulated image A) Diffraction limit; B) monochromatic aberration defocus + astigmatism; C) Chromatic aberration. Image modified from the original (gray scale), using Matlab (convolution with defocus and vertical astigmatism) and chromatic aberration with Adobe Photoshop®, (Model thesis author).

1.3.1. Monochromatic aberrations

Monochromatic aberrations are those present when only one wavelength is considered, and arise from the geometry, irregularities, tilts, and decentration of the components of the system. The magnitude of the geometrical aberrations increases with the diameter of the exit pupil [6, 16-18].

The monochromatic wavefront aberration is usually described in terms of the wave aberration, *W (x,y),* the distortions of the wavefront as it goes through an optical system. Where the wavefront is the surface containing the point of a wave on the same phase and is orthogonal to the corresponding ray.

FIGURE 1.7 A) shows an aberration-free optical system, where all the parallel rays entering the pupil will intersect the retina (image plane) at the same point, or equivalently, the wavefronts will be spherical, centered on the image point. However, when the optical system is aberrated **FIGURE 1.7** B) there is no longer a point focus: the different rays will intersect the retina (image plane) at different points, and the wavefronts will no longer be spherical.

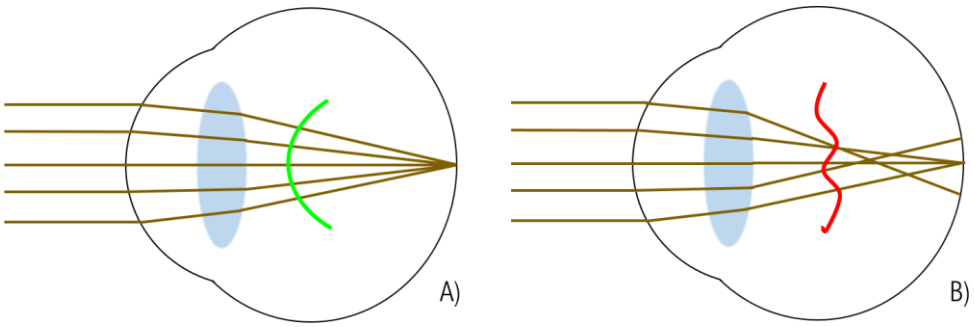

FIGURE 1.7. A) Schematic representation of a non-aberrated eye; B) Aberrated eye

Thus, the optical aberration can be described in terms of wave aberration maps: the distance that each point of the wavefront departs from the ideal sphere at the exit pupil [19]. An example of a

wave aberration map is shown in **FIGURE 1.8**, where the color indicates the distance between the wavefront and the reference sphere.

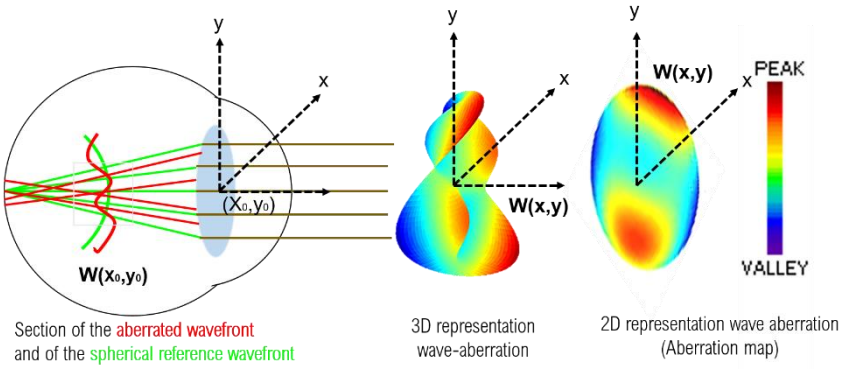

FIGURE 1.8. Schematic representation of the wave aberration. Wave-aberration values (distances between the aberrated wavefront and the spherical reference) can be represented as a z-coordinate referred to the pupil plane (three-dimensional representation) or two-dimensional color map (Aberration map).

The wave aberration of a general optical system can be described mathematically by a polynomial series. Zernike polynomial expansion has become the standard for representing ocular wave aberration data because they are orthogonal over the unit circle, and ocular aberrations usually refer to circular pupils [20]. Therefore, a wave aberration can be described as a summation of Zernike polynomial functions weighted by the so-called Zernike coefficients, which indicate the magnitude of each particular aberration present:

$$W(x,y) = \sum_{n,m} c_n^m \, Z_n^m \, (x,y) \quad \text{Eq.}(1.1)$$

where W(x,y) is the wave aberration phase in microns as a function of polar coordinates, c_n^m are the corresponding Zernike coefficient and Z_n^m (x,y) is the Zernike polynomial of order 'n' and frequency 'm'. The Optical Society of America (OSA, currently OPTICA) established a set of recommendations regarding the sign, normalization, and order that will be followed throughout this thesis [21].

The predominant ocular aberrations are called low-order aberrations (refractive errors): defocus, which characterizes myopia, hyperopia, and astigmatism. Optometric refraction, i.e. defocus and astigmatism in diopters can be calculated from Zernike polynomials using the following formulas [22, 23]:

$$M = \frac{-c_2^0 \, 4\sqrt{3}}{r^2} \; ; \; J_0 = \frac{-c_2^2 \, 2\sqrt{6}}{r^2} \; ; \; J_{45} = \frac{-c_2^{-2} \, 2\sqrt{6}}{r^2} \quad \text{Eq. (1.2)}$$

where coefficients (C_n^m , 'M' defocus, and 'J' astigmatism at 0º or 45º) are in micrometers, and 'r' is the pupil radius in mm. Such refractive errors are usually corrected with spectacles or contact lenses.

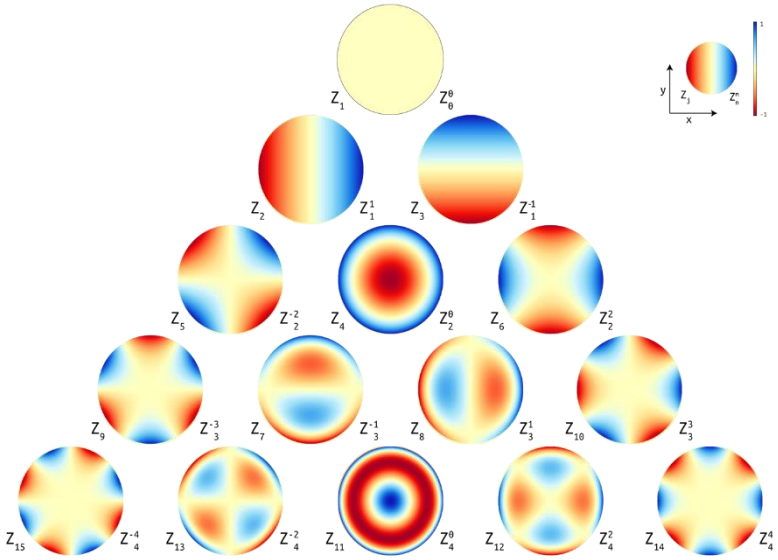

FIGURE 1.9. Representation of the Zernike base functions up to 4th order.

But the eye also suffers from other optical aberrations, called high-order aberrations (HOAs), which are not usually measured in clinical practice; sophisticated optical systems are needed for its measurement.

The first references to measurements of the optical aberrations go back two centuries ago [24, 25]. In the first half of the 20th century, we can find measurements of some high-order aberrations. The ocular spherical aberration was measured for the first time by Ames and Proctor in 1921 [26] followed by Ivanoff in 1947 [27]. In 1961 the ocular wave aberration was measured by Smirnov [28] by subjective methods using the Vernier alignment technique. The crossed-cylinder aberroscope [29] was another subjective measurement technique proposed several decades ago, based on the Tscherning aberroscope from the beginning of the last century [30] and later became objective [31, 32].

Other more recent techniques are the spatially resolved refractometer [33], the ray-tracing [34, 35], and the Hartmann- Shack wavefront sensor [36].

The widespread adoption of aberrometry, both in research laboratories and commercial systems in the clinic have shown that aberrations vary from individual to individual [37, 38], with age [39-41], with the pupillary diameter [42, 43], with refraction [44-46], with eccentricity [47-49], with accommodation [50, 51], etc.

The Root Mean Square (RMS) wavefront error is typically used as a global metric for optical quality from the Zernike coefficients (wave aberration) and represents the amount of deviation between a perfect wavefront and the real one. Lower RMS is indicative of good optical quality. A theoretical "zero" value implies a perfect concordance between the wavefront and the reference sphere. RMS is generally used as an objective quantitative metric of optical quality at pupil plane level, either including all aberration, high order aberrations, or individual terms or orders. In Eq. (1.3), the piston (c_0^0) and tilts ($c_0^{+/-1}$) have been removed, since they only represent a displacement of the image, not a degradation.

$$\mathrm{RMS}=\sqrt{\sum_{n,m}(c_n^m)^2} \qquad \mathrm{Eq.(1.3)}$$

where c_n^m is the Zernike coefficient corresponding to the order 'n' and the frequency 'm'. RMS is measured in microns (μm).

Monochromatic high-order aberrations (HOAs) are measured using monochromatic light, most often in near-infrared (NIR). The reduced sensitivity of the human eye to NIR light, which makes the measurements more pleasant for the subjects, is one advantage of using NIR instead of visible light. This also allows measurements to be taken without the need for any medicines to paralyze or dilate the pupil (depending on the experimental condition). Furthermore, the human fundus has a higher NIR reflectance than the visible. As a result, the quantity of light needed to image the retina and measure the aberrations is lowered, which is critical for staying under the recommended maximum exposure limits [52]. Since aberrations are often used to evaluate the optical contribution to visual performance, it is important to extrapolate their magnitudes in the visible spectrum. Several studies show that HOAs are similar in NIR and green light [53-56]. The only significant difference occurs for defocus, due to the longitudinal chromatic aberration of the eye, discussed in the next section, which can be calculated from the chromatic difference in focus between the red and blue ends of the spectrum [55].

1.3.2. Chromatic aberration

Due to the wavelength dependence of the refractive index of the intraocular media, the human eye does not focus all wavelengths onto one single spot on the retina. This phenomenon is referred to as chromatic aberration and adopts two forms: Longitudinal Chromatic Aberration (LCA) and Transverse Chromatic Aberration (TCA).

Longitudinal Chromatic Aberration (LCA)

Longitudinal chromatic aberration (LCA) is estimated from the chromatic difference of refraction [57] corresponding to extreme wavelengths. The refractive index of the human eye is higher for shorter wavelengths than for the longer wavelengths, and so the eye is more myopic for shorter wavelengths and hyperopic for long wavelengths.

LCA has been investigated since the 1940s, and many studies have measured LCA in the human eye experimentally and estimated it theoretically. Wald and Griffin [58] employed a specially designed spectral stigmatoscope to measure the LCA of the eye using a subjective method. In 1998, Rynders et al. [59] employed a double-pass apparatus to measure the off-axis LCA using both subjective and objective methods in the visible-light range. In 1999, Marcos et al. [53] employed a spatially resolved refractometer to measure the LCA objectively in the visible range. Some studies have measured LCA using reflectometric techniques, and in particular, wavefront sensing such as the Hartmann-Shack at different wavelengths [60, 61]. In 2015, Vinas et al.[62] studied the discrepancies between the human eye's LCA using both objective (Hartmann-Shack wavefront sensor, double pass retinal image) and psychophysics measurement methods. In the range of 488–700 nm, the average LCAs were 1.00 D (objective method) and 1.51 D (subjective method). The observed differences between the psychophysical and reflectometric LCA may arise, from the fact that the reflection of the retinal layer varies across the spectrum (deeper layers reflecting a larger proportion of the longer wavelengths and the nerve fiber layer reflecting a larger proportion of the shorter wavelengths) [52, 62, 63]. In **TABLE 1.1** the LCA (D) value is summarized for the different studies previously reported.

TABLE 1.1. LCA was reported in previous studies.

Study (O: Objective, S: Subjective)	Range Wavelength (nm)	Average value (D)
Wald and Griffin., (S)	365–750	3.2
Rynders et al., (O)	458–633	1.0
Marcos et al., (O)	450–650	1.26
Fernández et al., (O)	700–900	0.4
Manzanera et al., (O)	440–694	1.75
Vinas et al., (O)	488–700	1.00
Vinas et al., (O)	700–950	0.45
Vinas et al., (S)	488–700	1.51

FIGURE 1.10 shows the results of a collection of publications and the prediction of the Thibos et al. [64] chromatic-eye model. The eye model is emmetropic to 589nm.

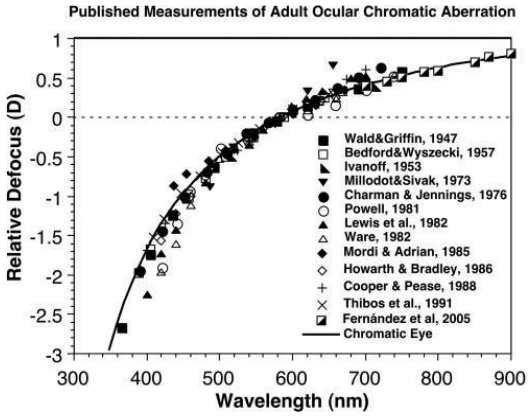

FIGURE 1.10. Published measurements of adult ocular chromatic aberration, compared with the Indiana chromatic-eye model Thibos et al. [64]. Adapted from Wang et al [65].

From results in the literature, the magnitude of the LCA of the eye is around 2 D across the visible spectrum (from 400 to 700 nm) [66, 67]. LCA appears to be rather constant across the population and with age [68, 69], and the presence of monochromatic aberration plays a negligible role in the LCA [62].

The replacement of the crystalline lens of the eye by an intraocular lens (IOL) likely modifies the LCA, depending on the chromatic dispersion of the lens material as well as other design features of the implant [70]. The increased number of IOL designs and materials have brought attention to LCA [56, 71-75]. In general terms, the more dispersive the IOL material (lower Abbe number), the greater the LCA. There have been proposals of IOL (refractive-diffractive) designs aiming at correcting the ocular LCA [76]. Also, diffractive designs must largely affect the LCA at different distances. In this thesis, the longitudinal chromatic aberration is studied in pseudophakic patients in **Chapter 8**, which presents in vivo LCA measurements in pseudophakic patients bilaterally implanted with diffractive hydrophobic IOL.

Transverse Chromatic Aberration (TCA)

Transverse chromatic aberration in the eye is defined as the variation of retinal magnification with wavelength, with objects in blue light being less magnified than red light. It is more common to

define the TCA in the eye in terms of the angle between the two principal rays with different wavelengths [77, 78] **FIGURE 1.11** B). Transverse chromatic aberration is larger for off-axis objects but for axial objects, there is still transverse chromatic aberration since the fovea is located almost 5° from the optical axis. While there is almost no intersubject variability in the LCA, the TCA findings from different research studies varied greatly in both magnitude and direction. Individual variances in the location of the fovea with respect to the optical axis [79], deviations in pupil centration [80], and different degrees of misalignment of the optical components of the eye might account for some of the variability. Variances in measuring conditions might also cause differences (pupil size, luminance, etc.). While some studies utilize a centered pinhole pupil or Maxwellian view to evaluate optical TCA [77, 81], others use a normal view [82, 83]. Because of aberrations and the Stiles-Crawford effect, the later measurement of TCA is referred to as perceived TCA [64, 84, 85]. Marcos et al. [53] estimated the differences between optical and perceived TCA, and directly evaluated the effect of both the Stiles–Crawford effect and aberrations, which had been frequently hypothesized in the literature to explain differences between TCA measurements and the effect of chromostereopsis [77, 84-86].

Reports of TCA come primarily from subjective methods that use different forms of a two-wavelength Vernier alignment task [64, 77, 81, 83] and recently from image-based methods in an AO scanning laser ophthalmoscopy [87-90]. In **Chapter 7** of this thesis, measurements and discussion on the impact of the Stiles-Crawford effect and monochromatic aberrations in the TCA are interpreted. In **TABLE 1.2** the TCA (arcmin) values are summarized for the different studies previously reported.

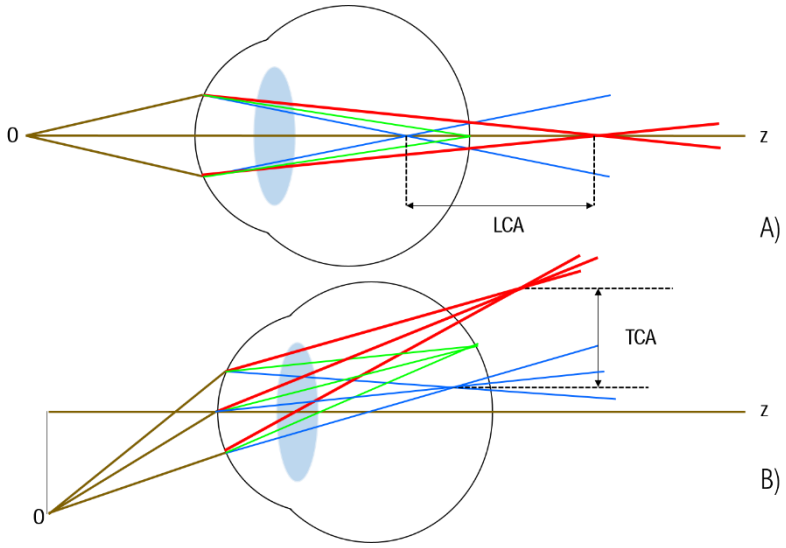

FIGURE 1.11. A) Longitudinal Chromatic Aberration in the eye. Rays of longer wavelength (red) are focused behind the retina and shorter wavelength rays (blue) are focused in front of the retina while medium wavelengths (green) are focused on the retina; B) Transverse Chromatic Aberration for centered pupil and off-axis object point.

TABLE 1.2. TCA data was reported in previous studies. A positive sign indicates that is nasal to the optical axis while a negative sign indicates that is temporal to the optical axis in object space (Horizontal TCA arc min).

Study (O: Objective, S: Subjective)	Range Wavelength (nm)	Average value (arcmin)
Hartridge et al., (S)	486-656	+0.6
Kishto et al., (S)	unspecified wavelength	+0.3
Ogboso et al., (O)	435-572	+0.9, +0.6 to +1.2
Thibos et al., (S)	433-622	+0.60, -0.36 to +1.67
Simonet et al., (S)	486-656	+0.43, -0.20 to +1.28
Rynders et al., (S)	497-605	0.8 up to 2.70
Marcos et al., (O)	473-601	0.52-1.84
Winter et al., (O)	543-843	~2.00
Yangchun Deng et al., (O)	639-786	2.00 to 2.80

1.3.3. Optical quality metrics

Several optical quality metrics have been defined, generally calculated from the measured wave aberrations. There have also been numerous attempts to correlate optical and visual quality, as optics impose the first limitation to vision. Optical quality metrics can be defined in the pupil plane, although, unlike retinal image quality, those have been poorer predictors of visual quality. For the purposes of this thesis, we will use retinal image quality metrics.

Retinal image quality

Retinal image quality is calculated from the wave aberration, which is the phase of the so-called pupil function:

$$P(\rho,\theta) = A(\rho,\theta) \cdot e^{\frac{-i2\pi}{\lambda} W(\rho,\theta)} \quad \text{Eq.}(1.4)$$

where $A(\rho,\theta)$ denotes the amplitude over a certain pupil diameter, which can be a unit amplitude or an apodization if the Stiles-Crawford effect is taken into account (section 1.4), $W(\rho,\theta)$ is the wave-aberration and λ is the wavelength. In this equation (Eq), ρ is the normalized radial coordinate and θ is the azimuthal angle (these coordinates are derived from Cartesian coordinates x and y).

Point spread function

The Point Spread Function (PSF) is the distribution of luminance in the image of a point source of light. It is dependent on diffraction, blur, aberrations, pupil size, and scattering of light in the ocular media. The point spread function for a perfect optical system (only limited by diffraction) is the Airy disk. Mathematically, the PSF is the squared modulus of the Fourier transform (FT) of the pupil function described previously [91] .

$$PSF(x,y) = |FT(P(\rho,\theta))|^2 \quad \text{Eq.}(1.5)$$

Line spread function

The Line Spread Function (LSF, the image of an infinitely narrow line) is an integration over one variable of the point spread function:

$$\mathrm{LSF}\ (x) = \int_{-\infty}^{\infty} \mathrm{PSF}(x,y)\,dy \quad \text{Eq. (1.6)}$$

Optical transfer function

The Optical Transfer function (OTF) is the Fourier transform of the PSF. The OTF is a complex function that defines the translation and contrast reduction of a periodic pattern:

$$\mathrm{OTF}\ (x,y) = \mathrm{FT}\left(\mathrm{PSF}(x,y)\right) \quad \text{Eq.(1.7)}$$

where (x,y) are the spatial frequencies of the pattern along the perpendicular direction. Also, OTF can be calculated directly from the wavefront aberration by performing the autocorrelation of the pupil function:

$$\mathrm{OTF}\ (x,y) = \mathrm{MTF}\ (x,y) \cdot e^{i\mathrm{PTF}_{(x,y)}} \quad \text{Eq.(1.8)}$$

The resulting OTF includes two-component; the modulation (MTF) and the phase (PTF) transfer function. A high-quality OTF is indicated by high MTF values and low PTF values.

Modulation transfer function

The Modulation Transfer function (MTF) is the ratio of the image contrast to the object contrast as a spatial frequency. Mathematically, it is the modulus of the FT of the PSF.

$$\mathrm{MTF}\ (x,y) = |\mathrm{FT}(\mathrm{PSF}(x,y))| \quad \text{Eq.(1.9)}$$

This function describes the modification of sinusoidal waves through the optical system; it also indicates to what extent the optical system transmits the frequency content of the object to the image. If the system has aberrations, the MTF will fall faster, worsening the transmission of frequencies from object to image. The contrast reduction is greater for high spatial frequencies, that is, for fine details in the image.
The modulation or contrast (C) is defined as the difference between the extreme intensity values (I) and the average intensity, known as the Michelson contrast.

$$C = \frac{I_{max} - I_{min}}{I_{max} + I_{min}} \quad \text{Eq.(1.10)}$$

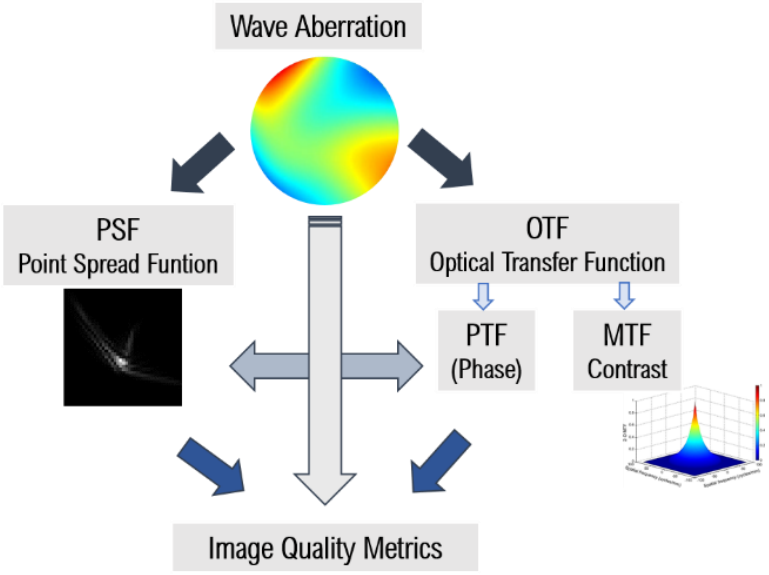

FIGURE 1.12. Summary diagram of image quality metrics.

Polychromatic image quality

Given that the world is polychromatic, it is necessary to estimate not only monochromatic but polychromatic retinal image quality. Because multiple wavelengths of light are mutually incoherent, the wave aberration (W(x,y)) for each wavelength is addressed independently. The most common strategy to estimate polychromatic image quality including monochromatic, longitudinal, and transverse chromatic aberrations [53, 92-94] involves the polychromatic point spread function (PSF_{poly}). The PSF_{poly} is calculated as the superposition of the monochromatic PSFs for each wavelength defocused by longitudinal chromatic aberration (defocus) and displaced by transverse chromatic aberration:

$$\mathrm{PSF}_{\mathrm{poly}}(x,y) = \sum_{\lambda} \mathrm{PSF}_{\lambda}(x,y) \quad \text{Eq.}(1.11)$$

Van Meeteren [93] computed OTFs for the average human eye for equal-energy white light using representative average values of both chromatic and monochromatic aberrations (assumed to be independent of wavelength) acquired from the literature.

Marcos et al. [53] measured the monochromatic aberration using a spatially resolved refractometer, as well as LCA and TCA, at six different visible wavelengths (between 450 and 650 nm). They interpolated monochromatic aberration data from individual participants at 10 nm intervals, then generated monochromatic point spread functions (PSFs), weighted by the photopic spectral sensitivity curve for the CIE standard observer $V(\lambda)$, shifted by the TCA, and integrated to produce the polychromatic PSF of an individual eye.

Thibos et al. [23] considered computing the value of a particular metric for each wavelength in a polychromatic source and then averaging the results,

$$\mathrm{Metric}_{\mathrm{poly}} = \int V(\lambda) \cdot \mathrm{Metric}(\lambda)\, d\lambda \quad \text{Eq. (1.12)}$$

where weighting the luminous efficiency function *V*(λ) shows how visual sensitivity to monochromatic light changes with wavelength. They also suggested that polychromatic image quality measurements for point objects be computed similarly to monochromatic image quality metrics.

Ravikumar et al. [92] used an ocular chromatic aberration model based on population average levels of LCA to investigate the impact of various levels of monochromatic aberrations and TCA. As well as to compute the polychromatic image quality of the human eye from a single measure of monochromatic aberration, weighted by the luminance of the polychromatic source at the corresponding wavelength:

$$\mathrm{PSF}_{\mathrm{poly}} = \int_{\lambda}^{\lambda} \mathrm{PSF}\,(\lambda)\cdot \mathrm{L}\,(\lambda)\,\mathrm{d}\lambda \quad \text{Eq.(1.13)}$$

where L(λ) is the luminance of the polychromatic source at the corresponding wavelength.

In this thesis, we have calculated the polychromatic PSF using the approach used in Marcos et al.[53], the PSF(λ) for different wavelengths, calculated from the corresponding wavefront aberrations. The PSFs were weighted by the photopic spectral sensitivity curve V(λ) and by the source luminance spectrum for each wavelength L(λ). The LCA was incorporated taking into account the defocus at each wavelength and summed with lateral shifts, linearly interpolated from the TCA value.

$$\mathrm{PSF}_{\mathrm{poly}} = \int_{\lambda \mathrm{l}}^{\lambda s} \mathrm{PSF}\,(\lambda_{\mathrm{s,l}})\cdot \mathrm{V}\,(\lambda_{\mathrm{s,l}}) \cdot \mathrm{L}\,(\lambda_{\mathrm{s,l}})\,\mathrm{d}\lambda_{\mathrm{s,l}} \quad \text{Eq.(1.14)}$$

where λ corresponds to the wavelengths of the spectrum (s-short wavelengths and l-long wavelengths).

This way of computing $\mathrm{PSF}_{\mathrm{poly}}$ has been used and characterized in **Chapter 5**.

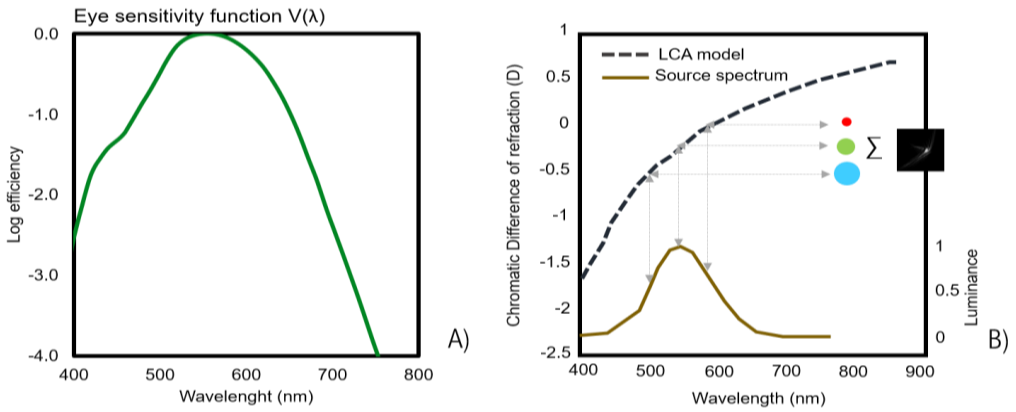

FIGURE 1.13. A) Eye sensitivity function V (λ) is greater at 555nm CIE 1978 (photopic); B) The polychromatic PSF is computed as the sum of luminance-weighted monochromatic PSFs Eq. (1.14). A monochromatic PSF is derived using monochromatic aberrations plus the focus shift associated with LCA and the lateral displacement associated with TCA for each wavelength in the source spectrum; the diagram displays three such PSFs schematically as blur disks of various diameters. The height of the source spectrum curve shown below the LCA curve determines the brightness weighting of each blur disk. Modified from Ravikumar et al. [92].

1.3.4. Double-pass retinal image quality

The basic problem that arises when analyzing the quality of the image formed by the eye on the retina is the impossibility of accessing the image space. The first proposed solution to this problem was provided by Flamant more than half a century ago [95]. It was an ophthalmoscopic system that formed the image of a slit in the retina, capturing the light reflected using a photographic plate. The orientation of the slit at different angles provided a direct measure of the ocular optical quality. Later studies confirmed the validity of this work, although the duration of the experiment made it very uncomfortable for the subject studied and impossible to implement at a clinical level. The introduction of new technologies in image recording (first using photomultipliers and then CCD cameras) improved the technique [96, 97], which evolved with the use of a point source to the current called double-pass system (DP) [98]. **FIGURE 1.14** represents the general scheme of a typical DP system. The first pass starts with the collimated point light source passing through the entry pupil (P1) and then through the Badal system. The point source is focused onto the retina of the eye to complete the first pass. In the second pass, the light reflected by the retina passes through the entire system again (the Badal system and the exit pupil (P2)), forming the image in the plane of the CCD camera through the objective.

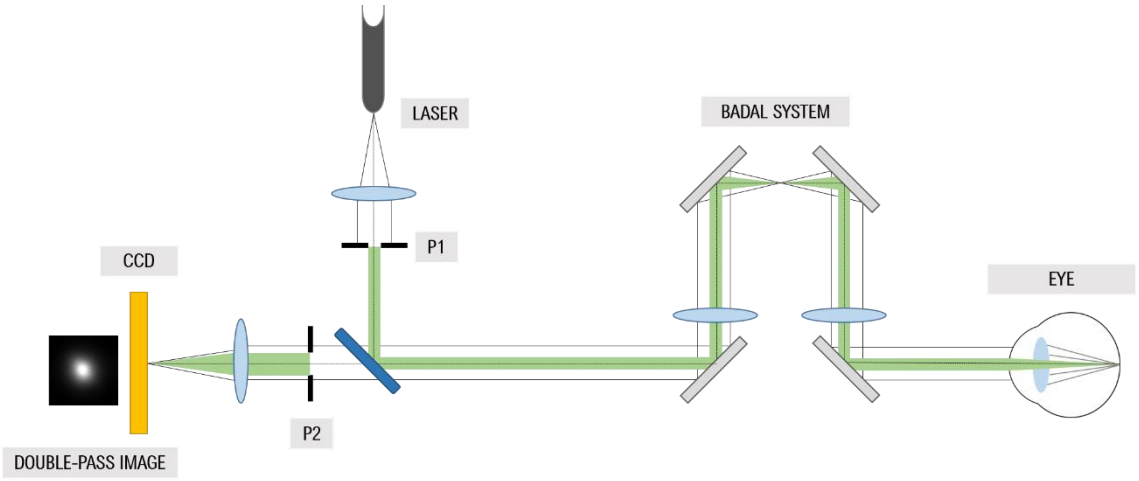

FIGURE 1.14. Basic schematic of a double pass (DP) system, where P1 (typically 2mm) is the entrance pupil and P2 (normally between 3-6mm) the exit pupil.

Therefore, from the image that is formed on the retina, the shape of the PSF of the eye is obtained. The intensity distribution obtained with the DP system may be represented as the convolution ("⊗" represents convolution operator) of the PSF of the first pass (PSF_1) with the second one (PSF_2) [99]:

$$I(x,y) = PSF_1(-x'_1,-y'_1) \otimes PSF_2(x'_2,y'_2) \quad \text{Eq.}(1.15)$$

There are two possible configurations for the double-pass system: symmetric and asymmetric.

Symmetric DP corresponds to the case where the entrance and exit pupils of the system are of the same size. In this case, the OTF of the first and second steps will be identical, thus it has the drawback that, since the two steps are equivalent, the information on asymmetric aberrations is lost [100].

In the asymmetric DP, which is the one usually used, the pupil of the first step has a very small diameter, so in that step, the system can be considered limited by diffraction, that is, the eye does not have any degradation effect on the formation of the image. Thus, the ocular MTF is obtained for a pupillary diameter equal to that of the largest pupil (or the subject's natural pupil). This shows the effect not only of symmetric aberrations but also of odd and irregular aberrations, such as coma [101].

1.3.5. Representing retinal image using convolution

Convolution is a general method for computing the quality of the retinal images degraded by a given point-spread function PSF (x,y).

$$\text{Retinal image} = (x,y) = \text{PSF}\ (x,y) \otimes O\ (x,y) \quad \text{Eq.}(1.16)$$

where O(x,y) is the object and "⊗" represents the two-dimensional convolution operator.

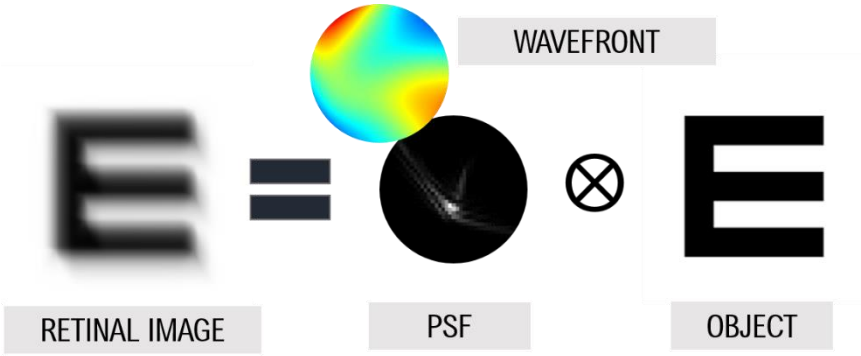

FIGURE 1.15. Convolution of a letter E with the point spread function calculated from the wave aberration data of one real subject. 6mm pupil size.

The point-spread function changes with wavelength and retinal location. Given that the eye is an isoplanatic system i.e. the human point-spread function is rather constant in the central 20 degrees, and therefore Eq.(1.16) is an appropriate approximation for representing the images projected onto the retina in the experiments of this thesis (typically subtending around 2 deg) [49].

Flamant (1955) pioneered the application of the Fourier theory of optics, presenting the convolution of a slit target with the eye's Line Spread Function [95]. Since this pioneering work, numerous studies have used convolved images to represent the images of the outside world onto the retina. For example, Artal [102] published the first computations of two-dimensional (2-D) extended foveal images using experimental double-pass PSFs in a significant study. More recently, the PSF utilized in convolution has been derived as the Fourier transform of the pupil function, where the phase is the wavefront aberration and the modulus is the optical system's transmittance.

Convolution calculations are frequently used to show differences in retinal image quality across patients with different aberration profiles [103], treatments (e.g., intraocular lenses on different eyes [104]), or across the peripheral retina in the same subject [105].

Peli and Lang [106] used filtered images using the OTF of the multifocal intraocular lenses (IOLs) (divided by the OTF of the monofocal IOL) to simulate the appearance of images through eyes with

a multifocal IOL implanted monolaterally and presented them to the monofocal IOL-wearing eye for inter-eye comparison.
Applegate et al. [107] used an image convolution-based approach to evaluate the effects of individual aberration terms on visual acuity. Legras et al. [108] utilized convolved images to model the deterioration caused by defocus, astigmatism, and spherical aberration in order to determine the smallest levels of these aberrations that created just visible variations and compared them to real defocused images obtained with trial lenses for varied pupil sizes and monochromatic and polychromatic light. Sawides et al. [109, 110] used convolved images in experiments investigating the adaptation to blur produced by High-Order Aberrations or to astigmatic blur [111, 112].

Previous research has used a variety of strategies to reduce further degradation of the convolved stimulus viewed through the subject's optics, including deconvolution with the observing optics, inverse filters, and shrinking the observing pupil, as well as adaptive optics to correct the eye's aberrations. Despite the widespread usage of convolved images to describe retinal image quality, the assumptions that underpin this method have rarely been studied. Some authors have observed differences between the degradation imposed by real blur or by convolution.

de Gracia et al. [113] has found substantial variations in visual acuity (VA) when simulated stimuli are used instead of optical manipulation of the aberration pattern in natural viewing, and Ohlendorf et al. [114] discovered that VA was worse with simulated spherical error and significantly worse with simulated astigmatic defocus than with real optical defocus of similar magnitudes. The source of the inconsistencies could not be determined.

In **Chapter 5** we used convolved images and Adaptive Optics to evaluate potential differences between real and convolved blur, in monochromatic and polychromatic light.

1.3.6. Interaction between monochromatic and chromatic aberrations

The human eye is affected by both spatial and chromatic (LCA and TCA) imperfections, which degrade the quality of the retina image and, as a result, limit vision. To analyze the relative contributions of the eye's monochromatic aberrations and LCA, several studies have estimated the retinal image quality of the eye assuming the best focus in green (highest sensitivity of the M-cone class) and that corresponding to the other wavelengths, relatively defocused by the LCA. These allow on the one hand to calculate the MTF for the different cone classes, i.e. for the peak sensitivity and bandwidth of the S-, L- and M- cone classes. On the other hand, by adding the PSFs corresponding to various wavelengths, weighted by the retinal spectral sensitivity, the optical quality in white light can be calculated (and therefore, the relative contribution of monochromatic and polychromatic light to retinal image quality. See Section 1.3.3 in this chapter for details on the estimations of MTFs and PSFs for monochromatic and white light.

The impact of chromatic aberration on vision appears to be lower than that expected from its relatively large amounts. Traditional views (based on the assumption that the eye is diffraction-limited) expect the MTF of the S-cone (blue) to have a lower frequency cut-off (by a factor of 3–5) than the M/L cone (red-green) because of the LCA [115]. Besides, the lower density of S photoreceptors in the retinal mosaic could be an additional reason limiting the resolution in blue. While, with this view, poorer optics could match a sparser S-cone density, the relatively broad spectral sensitivity of the cones would not prevent sharper or more blurred regions of the spectrum be sampled by different cone classes. Another classical hypothesis is that short-wavelength

absorbed by macular pigments play a role in minimizing chromatic aberration in the blue part of the spectrum. However, it has been estimated that the spectral filtering by the ocular media has a very minor impact on the MTF [116].

If the eye acted as a camera, with a lens with such large chromatic aberration, the resulting image should have colored borders ("fringes"), similar to what you'd see on a cheap lens camera. Artificial lens designs are typically achromatized to improve quality. However, results of providing the eye with an “achromatizing lens” have not resulted in an improvement of visual quality [26, 117-119]. Zhang et al. [120] found that a 0.4 mm misalignment of an achromatizing lens relative to the eye cancels any spatial vision benefit the lens provides.

A potential explanation is that, similarly to the visual system adaptation to high order aberrations, the eye may be adapted to chromatic aberration. A recent study by our group concluded that the perceived quality of images blurred by an equivalent amount of blur chromatic defocus was significantly lower in monochromatic blurred green images than monochromatic blurred blue images, suggesting a contingent adaptation to blue and blur [121].
In addition, it has been reported that monochromatic aberration plays a protective role against chromatic aberrations. Optical simulations [116, 122] revealed that the combination of natural monochromatic aberrations and polychromatic aberrations,reduces the MTF for M- and L-cones as compared to the perfect optical eye, however, the MTF S-cones is not significantly reduced (relative to M- and L-MTF). This fact indicates that monochromatic and chromatic aberrations should not be considered separately and there a certain degree and a protective balance against chromatic blur.

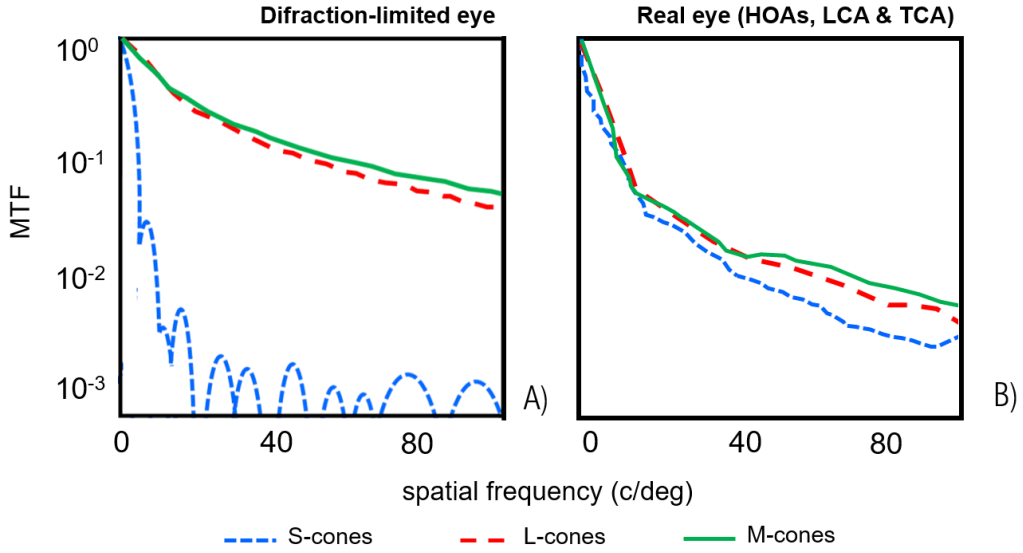

FIGURE 1.16. Polychromatic MTs computed with a 6-mm pupil for L cones (dashed line), M cones (solid line), and S cones (dotted line) for A) diffraction limit with LCA only and B) with measured LCA, TCA, and wave aberration (HOAs). Modified from M-CLellan et al.[116] (2002).

1.4. THE STILES-CRAWFORD EFFECT

In 1933, Walter Stanley Stiless and Brian Hewson Crawford initially reported the Stiles-Crawford effect (SCE), while working on a device to measure the area of the eye's pupil [8]. They assumed that all portions of the pupil contributed equally to visual perception, but due to errors in this premise, their equipment to measure the pupil did not perform as expected. They discovered that light entering the pupil from the center contributed more to vision than light entering from the off-axis pupil point. As a result, the SCE is used to characterize a reduction in the visibility of obliquely incoming light on the retina, which is linked to light interaction with cone photoreceptors [10]. When the stimulus penetrates closer to the pupil edge, this effect becomes more pronounced, reducing visual sensitivity to about a fifth of its maximum value when the pupil is large. This impact becomes more significant as the stimulus gets closer to the pupil edge, reducing visual sensitivity to about a quarter of its maximum value when the pupil is large.

The SCE characterization can take three different variations: The Stiles-Crawford effect of the first kind (SCE-I), is related to a psychophysical decrease in brightness with oblique incidence; the Stiles-Crawford effect of the second kind (SCE-II), is related to a subjective hue shift with obliquely incident light, and will not be covered in this thesis; and the Optical Stiles-Crawford effect (OSCE) where the brightness reduction with the oblique incidence of light is measured objectively by light backscattered from the retina [123].

1.4.1. The Optical Stiles-Crawford Effect (OSCE) and the Stiles-Crawford Effect of the First Kind (SCE-I)

The cone photoreceptors in the human retina exhibit a directional sensitivity. Light arriving via the center of the pupil (or, equivalently, entering the cones along their axis) is viewed as brighter than light entering at the edge of the pupil if the cones are directed toward the center of the pupil (i.e., at a larger angle). This effect is known as the Stiles–Crawford effect of the first kind (SCE-I), and is commonly measured using psychophysical techniques. A subjective comparison is made between a reference field entering at the pupil center, where the sensitivity is maximum, and a test field scanning the pupil horizontally, vertically, or at an angle. Two common processes have been used to measure this effect: 'bipartite filed process' in which the reference and test fields are seen side by side compared in brightness using a dual-path setup and the test (or reference) is modified until the two seem to be equally bright [124, 125]. A 'flicker field process' alternates one field with the other at a set frequency so only the test or the reference is visible at any given moment. Their brightness (or time of appearance) is matched until the flicker is no longer visible [126-128]. Unfortunately, the availability of these measurements has been limited due to the lengthy experimental periods and high level of cooperation necessary for psychophysical studies.

1.4.2. Measurement of human cone-photoreceptor alignment (OSCE)

Reflectometric techniques have also been shown to reliably estimate the peak of the optical/ objective Stiles-Crawford effect (OSCE) [123, 127, 129]. In this technique, a region of the fovea is illuminated typically in Maxwellian view, and images are collected at the pupil plane. When the photopigment is bleached, a portion of the light entering the cone's inner segments is guided along the outer segment and then scattered back into the pupil region corresponding to the cones' axis.

A Gaussian function is generally used to fit the relative luminous efficiency (in psychophysical measures) or the distribution of directed or guided reflectance (in reflectometric studies) at the plane of the pupil:

$$I = I_{max}\ 10^{-\rho\ (x-x_0)^2+\ (y-y_0)^2}\ \text{Eq.}(1.17)$$

where x_0 and y_0 are the coordinates of the peak point with the best luminous efficiency or guided reflectance (i.e., the location where the cones are closest to the pupil plane) and where rho (ρ) is a directionality metric (the greater the rho, the more precisely tuned the function is). Although directionality is higher (higher rho values) in reflectometric measures than in psychophysical measurements, it has been shown that reflectometric produces the same estimate for the location at the pupil plane to which the photoreceptors are orientated [127, 130].

The first reports for a reflectometry technique applied to photoreceptor alignment were presented by Kraupskopf [131]. The study showed some change in reflectance after bleaching, attributable to the directional features of the photoreceptors. The first systematic measurements of retina's directional reflectance were carried out by Van Blokland and Norren [130] developed this optical approach, as did Gorrand and Delori [132]. Burns et al.[129] implemented new instrumentation that was capable of imaging the whole output distribution of light in the pupil for every particular pupil entrance location. For a single entering position, it can acquire a full two-dimensional intensity distribution of the light exit distribution.

The Photoreceptor Alignment Reflectometry (PAR) technique is based on the optical reversibility principle, which asserts that a waveguide that takes light impinging on one end at a certain angle distribution will emit light going through the waveguide in the opposite direction from the same angular distribution[129]. For photoreceptors, this means that if the light arrives at the cones from the pupil at a preferential angle, then light reflected or scattered back into the photoreceptor outer segments from deeper retinal layers will be emitted at the same angle when it emerges from the cones, and thus directed back toward the pupil (**FIGURE 1.17**). Although there are various sources of reflections, scattering, and absorption in the fundus, when the retina is illuminated, there are three main components of light that return out of the eye. The first component is emerging of light that enters the cones, travels through the outer segment, is backscattered or reflected at the base of the outer segment, and then returns to the pupil via the photoreceptors (the guided component). The light that has been scattered both in the retina and choroid is the second component. The third component is caused by a specular reflection from the inner limiting membrane, which generates an image of the source near to the retina in the foveal region due to the curvature of the foveal depression. For these last two components, a fraction of the returning light will intersect the pupil, giving the impression that the pupil is uniformly illuminated from the outside. Because the guided portion of the light fills only a portion of the pupil, whereas the other two components fill the entire pupil, it is theoretically possible to measure the directional properties of the human photoreceptors by measuring the spatial distribution of the light emerging from the pupil when the retina is illuminated. Prior work has shown that the directional component is maximized by the use of green light, while IR produces a larger background component [133-135]. Also, while the maximum intensity of the distribution is higher for a given entry pupil (that matches the position of the peak), the normalized intensity distribution is similar regardless of the entry location [123, 127].

Work by Marcos and Burns [136] showed that ocular Laser Ray Tracing (LRT) images collected in green light contain similar information to that obtained with the PAR technique. In LRT the entry beam is moved across the pupil, and a series of retinal images are collected. Pupillary intensity distribution maps were obtained by integrating the light intensity in the retinal images and fitted to Eq.(1.17) (plus a background). The cone directionality peak obtained from PAR and LRT in the same patients matched within average both eyes +0.54 ± 0.06 / -0.88 ± 0.30 mm (horizontal/vertical coordinates).

The studies presented in **Chapter 7** use cone directionality measures obtained from LRT to investigate the impact of OSCE on the perceived TCA.

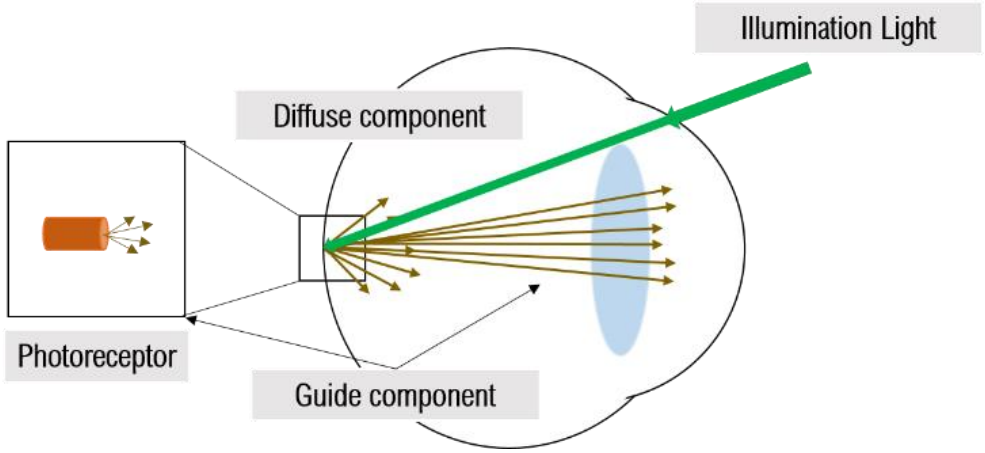

FIGURE 1.17. Illustration of the process described above for determining the directionality of cone photoreceptors using light. Modified from Burns et al. [129].

1.5. AGING PROCESS IN THE EYE

1.5.1. Accommodation, Presbyopia, and Cataract

With advanced age, both the optical system and the neuronal levels experience remarkable anatomical and physiological changes that affect different aspects of the visual process [137], such as spatial and temporal vision, color vision, and accommodation [138]. These alterations are considered normal phenomena associated with aging, although in their most advanced stage cause serious vision loss (cataracts, glaucoma, macular degeneration, etc.).

In this thesis, we evaluate optical and visual quality in presbyopic and cataract patients (pre- and post crystalline lens replacement by intraocular lenses)

The crystalline lens is one of the components of the eye responsible for the formation of images on the retina, and the one that by modifying its shape, generates the necessary power changes to accommodate and focus on objects at different distances [139]. Our understanding of the mechanism of accommodation is based on the theory of Helmholtz [140], with their respective modifications. Hess, Gullstrand, and Fincham expanded the Helmholtz theory. Recently the theories have been modified by Weale and by the contributions of Fisher's experimental and theoretical studies [141-143].

The crystalline lens is an elastic and transparent tissue that lies behind the pupil, attached to a group of muscles that surround it in ring-shaped 'ciliary muscles' through the elastic fibers of the zonule. During the accommodation process, the ciliary muscles contract and reduce the space left in their center, thus relaxing the tension to which the fibers of the zonule are subjected. This means that the equatorial diameter of the lens decreases and its thickness increases, making its anterior surface more curved **FIGURE 1.18**. This increases its optical power allowing to focus of near objects. Relaxation of the ciliary muscles causes the reverse process (unaccommodated form) and makes it possible to form an image of distant objects.

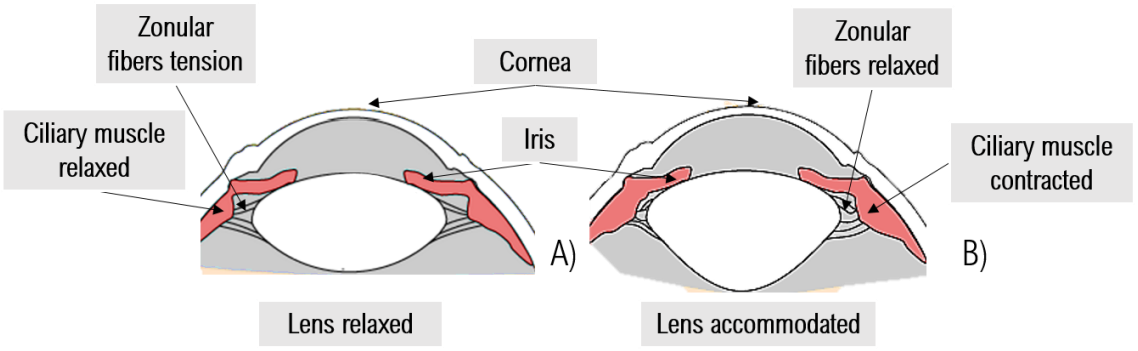

FIGURE 1.18. Diagram of the Helmholtz theory of accommodation. A) A cross-section of the anterior segment during relaxation of accommodation. B) Accommodation leads to contraction of the ciliary body muscle leading to relaxation of the zonules and rounding of the lens. The increased anteroposterior thickness of the lens increases the converging power of the eye.

Presbyopia is the loss of accommodation due to aging [144]. With age, the crystalline lens increases its rigidity and becomes more sclerotic, resisting deformation when the ciliary muscle contracts [145, 146]. As a result, it cannot bulge enough on its front face to increase curvature and diopter power to focus on near objects. It is a gradual process that begins from childhood, producing a loss of the amplitude of accommodation (minimum distance at which an object can be seen),

which begins to result evident between the ages of 40 and 50, and affects 100% of the population [147]. In 2020, it was estimated that 1.4 billion people globally had presbyopia and the prevalence is expected to peak at approximately 2.1 billion in 2030 [148, 149]. Although the measured prevalence of presbyopia is greater in regions with longer life expectancies, it is estimated that 94% of those with significant near vision disability due to uncorrected presbyopia live in developing countries [150]. Currently, there are various optical solutions for the treatment of presbyopia that will be discussed in the next section 1.5.2.

As the lens ages, it not only loses its accommodative capacity, but also increases its weight and thickness, the index gradient flattens, the surfaces increase their curvature, and the spherical aberration changes to more positive values [151]. These changes are due to the continuous growth of the lens, accumulating fibers in the lens nucleus. Chemical modifications also occur, inducing a decrease in the transparency and increased scattering of the lens, resulting in a cataract. Depending on the distribution of the opacities, the cataract is classified as *nuclear*, when the opacity is central; *cortical*, when the opacity is in the area of the lens cortex; and *posterior subcapsular*, if a plaque-like opacity is observed in the posterior subcapsular cortex. There are other factors, in addition to age, that can lead to the formation of cataracts such as trauma, certain radiation, or prolonged intake of drugs.

1.5.2. Presbyopia solutions

There are numerous strategies to treat presbyopia, either non-surgical (spectacles or contact lenses) or surgical (modifications in the cornea or IOL implant) treatments, which aim at restoring visual functionality at near [152, 153], **FIGURE 1.19**. None of these solutions restore the full dynamic ability of the young eye's 'accommodation', but increased understanding of the coupling of the lens design with the eye's options, and lens designs will lead to optimization of the treatments and patient selection.

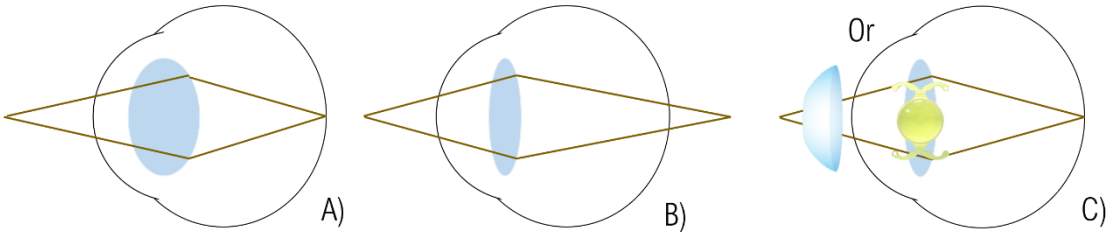

FIGURE 1.19. Near vision process A) in a young eye (accommodation); B) in a presbyopic eye without correction; C) in a presbyopic eye with correction using contact lenses (CL) or intraocular lenses (IOL).

Current most frequent presbyopic solutions are based on different principles: alternating vision, monovision, and simultaneous vision **FIGURE 1.20**.

The solutions for alternating vision are bifocal or progressive spectacles lenses, where changes in gaze and/or head position allow the selection of the viewing zone for the desired distance [152, 154]. In monovision solutions, one eye is corrected for distance and the other for near vision (usually the dominant eye for far and the non-dominant for near). It is common to use contact lenses to apply monovision, although intraocular lenses are also an option [155, 156].

An increasingly popular treatment to compensate for the effects of presbyopia is based on simultaneous vision solutions, usually in the form of contact lenses or intraocular lenses, where the eye is simultaneously corrected for both near and far vision [157, 158]. Simultaneous vision represents a new visual experience in which a focused image for near vision is projected onto the patient's retina overlaid with a degraded image for distance vision, or a focused image for distance vision superimposed on the defocused image of the near scene [159].

This form of correction implies a visual compromise by which depth of focus is gained for high-contrast objects, but glare and loss of contrast are generated in the retinal image, which becomes more apparent the lower the contrast of the object is [160]. The superposition image produces a reduction in contrast sensitivity that improves significantly over time [161]. The problem is more acute in low light conditions and mainly affects near vision [162].

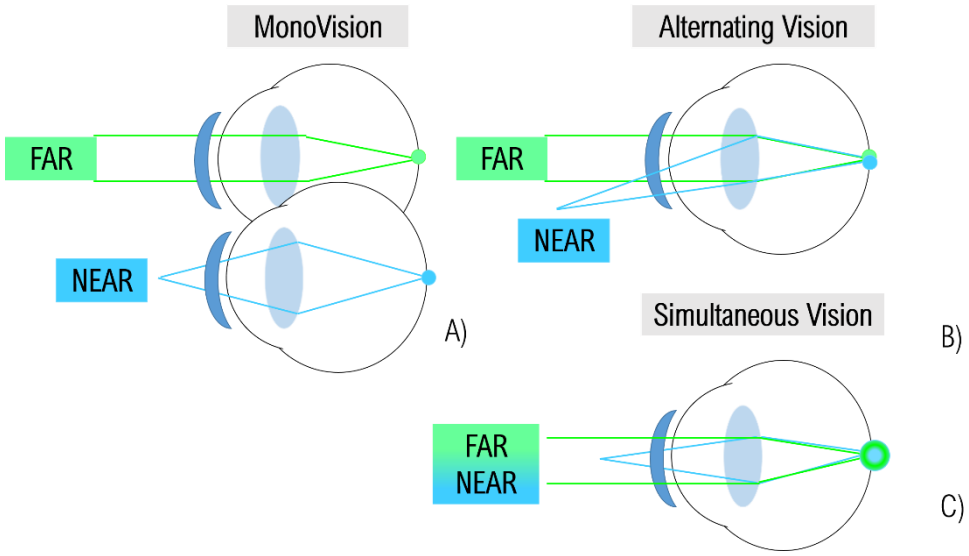

FIGURE 1.20. Schematic diagram of different presbyopic corrections; A) MonoVision: usually, the dominant eye, is corrected for far viewing (green), and the other eye is corrected for near viewing (blue); B) Alternating Vision: the lens is split into two sections. The larger, primary section corrected for far vision (green), while the smaller,secondary section allows seeing near (blue); C) Simultaneous Vision: superposing far and near images on the retina (green and blue).

1.5.2.1. Contact Lens designs for presbyopia

Contact lenses (CL), compared to spectacles, provide a wider field of vision because they are closer to the eye, which produces less distortion and they are suitable when a surgical procedure is not indicated, although their application for the correction of presbyopia is still limited, as there is a tendency of reduction of the use of contact lenses as age increases. Often this decrease is due to the imbalance between near and far vision as, patients are not able to handle the contact lens, because they do not see it clearly [163, 164].

Simultaneous Vision contact lenses are normally refractive lenses (segmented or smooth profiles) and can come on various designs: two focal points for far and near (bifocal), a smooth transition of power between the focal lengths for far and near, multifocal contact lenses (M-CLs) (**FIGURE 1.21 B)**. The distribution of the near and distance regions can also vary, as the central region can be either devoted to distance or near. Also, the CLs can have low, intermediate, and near additions

(add). Any point on the retina receives overlapped focused and unfocused images, in such a way that there is a reduction of contrast in the image [165-167].

In the study presented in **Chapter 4,** we investigated a center-near smooth profile contact lens design

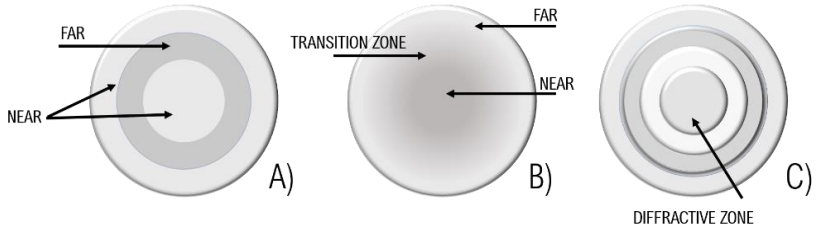

FIGURE 1.21. Different designs of M-CLs; A) Concentric; B) Aspherics; C) Diffractive.

Aspheric design

Currently, the most widely used manufacturing designs in the field of CLs are progressive designs with aspherical geometry, with a wide variety of designs available on the market. Aspherical CLs designs are rated for a certain viewing distance in the central area and an aspherical curve that produces a progressive variation in power as you approach the periphery. There are two types of CLs designs within spherical geometry: Center-Near Designs (C-N) and Center-Distance (C-D). C-N designs have the maximum positive power at their geometric center and decrease towards the periphery [168]. The opposite is C-D designs **FIGURE 1.21** B**)).**

CLs with C-N designs are made up of a central spherical zone with a refractive power intended for near vision and an aspheric curve that progressively decreases graduation power towards the periphery, modifying the radius of the anterior, posterior, or both surfaces. The radius of curvature is flattened from the center to the periphery on its external face, thus achieving a lens with greater converging power in the center than in the periphery. Most multifocal aspheric lenses have a C-N design. To this category belongs the contact lens 1-DAY ACUVUE® MOIST MULTIFOCAL (Aspheric center-near design, Johnson & Johnson Vision Care, Inc) studied in **Chapter 4**.

CLs with C-D designs have a central spherical zone with a refractive power intended for distance vision and an aspheric curve that progressively increases the prescription towards the periphery on the anterior surface of the CL to compensate for near vision. In this type of design, the radius of curvature is reduced from the center to the periphery on its external face to achieve a CL with more convergent power (ADD) in the peripheral region. These lenses are usually used in both eyes, or in the dominant eye, while the non-dominant eye would fit a C-N lens. In both C-N and C-D lenses, vision at different distances depends on the pupil size being large enough to allow light to pass through the pupil after refracting in different areas of the CL.

This asphericity induces a spherical aberration (SA) that causes multifocality through the depth of focus within the eye (DOF). The SA is negative in the C-N designs and positive in the C-D designs. Even though the best image suffers a certain degradation due to the induced SA, this is counteracted with increases in depth of focus[169-173].

1.5.2.2. Intraocular lenses designs for presbyopia

The first intraocular lens (IOL) implant was performed in 1950 by Harold Ridley [174]. The implanted lens was made of PMMA (polymethylmethacrylate). Since then, materials, designs, and techniques

have continually evolved. The classic model of intraocular lens, which is still the most frequently implanted today, is the monofocal design. Monofocal intraocular lenses designed with a fixed focal length, provide patients with optimal visual quality in far vision, but the quality degrades rapidly at near so that patients require the use of near spectacles. Accommodative or pseudo-accommodative, multifocal, hybrid or EDOF lenses have emerged as options to treat presbyopia [175].

Accommodative IOLs

Accommodative lenses are monofocal lenses with flexible haptics capable of mobilizing their optical zone, thus varying their focus. When the ciliary muscle contracts, the zonular fibers relax and the energy released allows the lens to move forward, thus increasing its dioptric power to focus at close or intermediate distances. In practice, the true accommodative effect achieved with these designs is small and highly variable [176].

Multifocal IOLs

Multifocal IOLs (M-IOLs) aim at producing multiple foci or expanding the depth of focus in the eye. We can divide multifocal IOLs according to the optical principle used to create multifocality in refractive or diffractive lenses:

Refractive lenses: based on the phenomenon of refraction of light, which is the change in direction experienced by a ray of light obliquely passing from one medium to another with a different refractive index (IOL material). This type of lens uses a multizonal refractive method using do with alternating concentric rings of different diopter power, which focus some for far vision and others for near vision. When the light rays pass through the lens, two simultaneous foci are produced, and it is the brain that 'chooses' the right one at each moment for each distance while 'discarding' the other. The addition for near vision varies throughout the different models between + 2.50D and + 3.00D. The initial designs included 2 or three different refractive zones, whereas the more current ones show a greater progression through the use of 4-5 concentric rings and include an aspherical profile of the optic zone (center) [177-180].

Diffractive lenses: based on the scattering phenomenon that light experiences when it passes through the edge or step of a transparent surface. Diffractive lenses use the optical principles of diffraction and refraction to form two independent focal points, far and near. The design of these lenses incorporates a refractive surface with a specific refractive index, in which diffractive steps are carved. The bifocal effect is achieved by causing the simultaneous formation of a far focus (refractive effect) and a near focus due to the effect of the steps carved into the lens. The higher the height of the steps, the greater the addition for near vision [181-183]. Trifocal IOLs improve the quality of intermediate vision, which is penalized in bifocal lenses [184, 185].

One of the intraocular lenses studied in this thesis was the diffractive aspherical trifocal lens (FineVision Pod F, PhysIOL, Belgium). These trifocal IOLs have a biconvex design with a diffractive structure on its anterior surface that spreads light to obtain pseudo-accommodative vision (patented FineVision Technology) [186].
The FineVision lens combines two diffractive structures that adjust to provide +3.50 diopters for near vision and +1.75 diopters for intermediate vision. This makes it easier for patients to see up

close without additional assistance and increases their independence between intermediate and near vision glasses. The anterior surface design of the diffractive trifocal IOL is apodized, convoluted, and diffractive. Due to the variation in the height of the steps of the diffractive structure of the IOL across the pupil, the distribution of energy for different distances can be controlled. The amount of energy directed to the far vision focus is greater than that directed to the intermediate and near vision foci with increasing apertures, caused by a gradual decrease in the height of the diffractive steps from the center to the periphery.

Therefore, these lenses become more refractive for eyes with large pupils to the benefit of the far distance [182]. They are designed with 4 open double C haptics for better stability and made of a medical-grade hydrophilic acrylic copolymer, which contains an ultraviolet filter (BlueTech technology ensures protection against blue light).

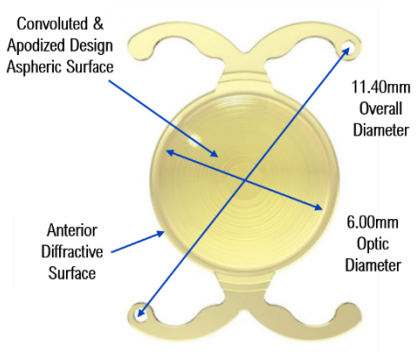

Model	POD F
Material	Material 26% Hydrophilic Acrylic
Overall diameter	11.40mm
Optic diameter	6.00mm
Optic	Biconvex Aspheric Trifocal
Haptic design	Double C-loop & Posterior Angulated Haptic F
Filtration	UV & Blue Light
Refractive index	1.46
Abbe number	58
Additional power (IOL plane)	+1.75D & +3.50D

FIGURE 1.22. Diffractive multifocal lens (FineVision Pod F, PhysIOL, Belgium), next to the table with technical characteristics of the intraocular lens. Modified from PhysIOL page [186].

This intraocular lens has also been characterized in a previous study by our group performing optical quality measurements (double-pass aerial retinal point images and E-letter stimulus images, on bench) and visual acuity measurements, simulated with different visual simulators and the real lens itself [187]. In **Chapter 3**, the simulation of this lens will be studied with different simulation platforms, before and after the implantation of this IOL in patients.

Extended Depth of Focus (EDOF) IOLs

The latest evolution of multifocal lens designs is the concept of extended depth of focus. They are considered a new category of IOL and aim to improve intermediate vision trying not to compromise vision in the far and near areas [188-190]. Extended depth-of-focus IOLs have an extended far focus area that goes into the intermediate distance [185]. Intermediate vision, with extended-depth-of-focus IOLs, offers good intermediate vision quality and decreased near visual acuity. Patients obtain better contrast sensitivity values and fewer ocular aberrations, however, this type of lens can produce photic phenomena, glare, and halos.

1.5.3. The effect of chromatic dispersion on pseudophakic eyes

The chromatic dispersion of IOLs, not the cornea or other ocular media, causes the majority of pseudophakic longitudinal chromatic aberration. In pseudophakic eyes, implanted IOLs with larger chromatic dispersion cause more longitudinal chromatic aberration [71, 191].

The dispersion properties of the IOL material are defined by the Abbe number:

$$\text{Abbe number} = \frac{n_D - 1}{n_F - n_C} \quad \text{Eq.}(1.18)$$

where n_D, n_F, and n_C are the refractive indices of the material at the wavelengths of the Fraunhofer spectral lines D (587.6 nm), F (486.1 nm), and C (656.3 nm) respectively [192]. Materials with lower chromatic dispersion generally have larger Abbe numbers, which range from 35 to 60 for current IOL materials and can be measured using refractometers and goniometers.

In pseudophakic eyes, IOLs with higher chromatic dispersion create increased longitudinal chromatic aberration, according to both experimental (or computational predictions) and in vivo measurements of chromatic difference of focus. Zhao and Mainster [193] have also demonstrated that without changing other eye model parameters, pseudophakic performance increases with increasing Abbe number. Perez-Merino et al. [56] measured monochromatic aberrations at two wavelengths (532 nm and 785 nm) in two groups of pseudophakic eyes with IOLs of different materials (Tecnis, Abbott Medical Optics, Inc., and Acrysof IQ, Alcon Laboratories, Inc.), and found statistical differences in the chromatic difference of focus (0.46 D and 0.75 D, respectively), consistent with the Abbe number of the two IOL materials. According to Vinas et al. [194] the eyes with the monofocal hydrophobic IOL showed a slight but constant greater longitudinal chromatic aberration than the eyes with the monofocal hydrophilic IOL (a difference of 0.16 D and 0.15 D from psychophysical and wavefront-sensing methods, respectively, in the visible 480 to 700 nm range). The discrepancy is explained by the hydrophobic material's lower Abbe number.

Furthermore, when the number of multifocal IOLs increases, the LCA pattern with this novel diffractive optic should be considered: Millan et al. [70] found that bifocal diffractive IOLs increase the positive LCA of preceding ocular media in far vision after testing two bifocal diffractive lenses. The greater the LCA, the more dispersive the IOL material is (lower Abbe value). Bifocal diffractive IOLs, on the other hand, tend to reduce the amount of LCA in near vision. This achromatizing effect changes linearly with addition power and may partially compensate for the eye's LCA in near vision, depending on the IOL material and the amount of refractive LCA produced.

The objective of IOL design is to have as minimal residual aberration as possible, replicate the LCA of the phakic eye, and get the combination of material/design that works best to extend the range of vision. Lenses with a higher Abbe number have less light dispersion and hence less chromatic aberration, resulting in possibly improved vision quality. To fully comprehend the clinical importance of chromatic refractive variations regarding new IOL materials and design more research is required. In **Chapter 8**, the longitudinal chromatic aberration of a trifocal lens with hydrophobic material will be studied.

With the increasing number of CLs and IOLs designed to correct presbyopia, it becomes increasingly necessary to provide patients with the experience of vision with presbyopia corrections.

Visual simulators are particularly attractive for evaluating the patient's visual quality with new optical designs before a CL fitting or their surgical implantation [156, 157] and sometimes even before the lens has been manufactured. This extraordinary ability to simulate new ophthalmic corrections makes it possible to investigate the interactions between the ocular optics and given optical corrections.

Section 1.6.3 provides an overview of different visual simulators either in a laboratory or clinical use.

1.6. ADAPTIVE OPTICS VISUAL SIMULATORS

Adaptive Optics (AO) for Visual Science is an example of an interdisciplinary and dynamic field of research. The complex study of vision and the eye takes advantage of this technology, originally imported from Astronomical Optics. The measurement and subsequent correction of the ocular aberrations permit images of morphology and distribution of the photoreceptors of the retina with unprecedented resolution [195, 196]. Beyond those imaging applications and possibilities, adaptive optics can be used not only for the correction of aberrations but for its manipulation. We can perform visual testing through a manipulated wavefront and compare the results across different optical conditions [110, 187, 197, 198]. We have the perfect tool to study the actual impact of optics in vision and understand how we see the world. This thesis will mostly focuses on such applications.

1.6.1. Adaptive Optics: The technique

Turbulence in the Earth's atmosphere limits the spatial resolution of ground-based telescopes. In 1953, Horace W. Babcock [199] proposed a solution to this problem of imaging objects in space through atmospheric turbulence and introduced the idea of an adaptive optical element capable of correcting the time-varying aberrations caused by this turbulence. Due to the technical complexity of measuring atmospheric aberrations and manufacturing and controlling a deformable mirror to correct them, the first successful demonstration of adaptive optics in astronomy was only performed until 1977 by Hardy and his colleagues [200]. Many of the main ground-based telescopes are now equipped with adaptive optics, which can sometimes produce images with a higher resolution than those obtained from the Hubble Space Telescope [201].

In the 1990s, an Adaptive Optics system was first applied to the eye, based on the new ocular aberrometer Hartmann-Shack wavefront sensing, by Liang et al.[36]. The first AO device used to correct the aberrations of the eye was a segmented mirror, which proved capable of correcting astigmatism and of increasing the quality of retinal images [36, 202]. Liang et al. (1997) presented the first closed-loop AO system that could correct higher-order aberrations in the eye in a high-resolution retinal imaging AO system and provide "Supernormal Vision and High-Resolution image" [203]. This first system required 4 or 5 loops and 15 min for each loop of measuring and correcting the wave aberration to complete the correction. Wavefront sensing was not yet automated for the eye and each frame of Hartmann-Shack spots required tedious adjustment of the centroid. Liang et al.[203] were able to improve contrast sensitivity beyond what was possible with a conventional spectacle correction and obtained higher contrast images of the cone mosaic that Miller et al. [204] had previously obtained without adaptive optics.

Real-time correction of the wave aberration [205, 206] was not possible until the development of automated wavefront sensing, which allowed the first real-time measurement of the eye's wave aberration [207]. Fortunately for vision science, an adaptive optics system operating with a closed-loop bandwidth of only a few hertz is adequate to capture the most important temporal changes [208]. The use of the AO system to measure, correct or induce aberrations, opens a wider range of experiments to understand how optics and vision are entangled, both in the high-resolution retinal image and psychophysical testing.

1.6.2. Principal components of an AO system

A conceptual schematic of AO as employed for retinal imaging and vision testing is shown in **FIGURE 1.23**.

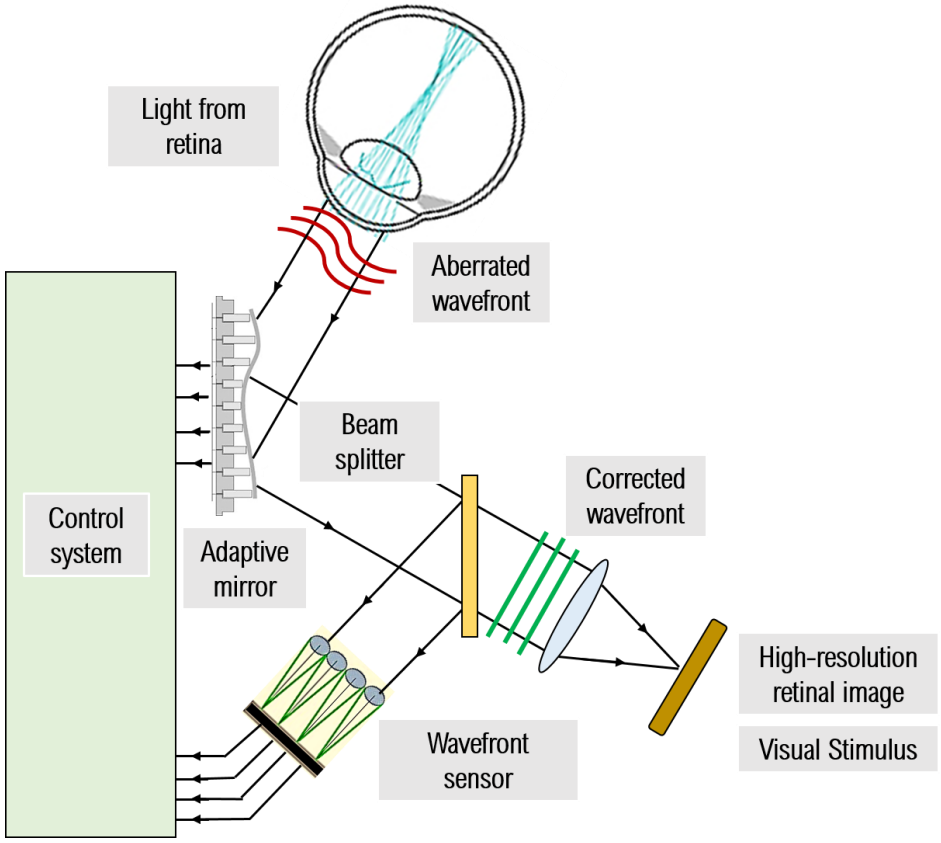

FIGURE 1.23. Basic scheme of an Adaptive Optics (AO) system in vision.

As illustrated, AO systems consist of three main components [209]:

Wavefront sensor: measures the optical aberrations in the pupil plane of the eye. Although there are many types of wave sensors, the Hartmann-Shack wavefront sensor is almost used for the eye [36, 202].
Control system: converts the raw output from the wavefront sensor into voltage commands which are sent to the wavefront corrector. In an AO system for vision science, the control algorithm is the crucial link between the wavefront sensor and the wavefront corrector.
Wavefront corrector: compensates for the aberrations measured by generating a shape which is ideally combined with the aberration profile. The wavefront corrector is placed in a plane conjugate to both the pupil of the eye and the wavefront sensor. The most common wavefront corrector consists of a continuous reflective surface and an array of adjacent computer-controlled actuators or electrodes that physically or electrically push and pull on the surface, transforming it into the desired shape. Wavefront correctors have been available for many years, although their construction is an active area of research [210].

1.6.2.1.Wavefront sensing techniques

Wavefront sensing is a key technology required to better understand the optical quality of the eye and to develop advanced vision correction methods, such as adaptive optics, customized contact lenses, and/or laser refractive surgery. The most commonly used wavefront sensors are the spatially resolved refractometer [33, 211], the laser ray-tracing technique [212, 213], and the Hartmann-Shack wavefront sensor [36, 202]; the last two mentioned have been used in this thesis. Wavefront sensors measure the aberrations of the entire eye generated by both corneal surfaces and the crystalline lens. Wavefront sensors can be categorized by whether the measurement is based on a subjective or objective method and whether the wavefront sensor measures the light going into the eye or coming out of the eye.

Hartmann-Shack Wavefront Sensor

The Hartmann-Shack wavefront sensor contains a two-dimensional array of a few hundred lenslets, all with the same diameter and the same focal length. The light reflected from a laser beam projected on the retina is distorted by the wave aberration of the eye. The reflected light is then spatially sampled into many individual beams by the lenslet array and forms multiple spots in the focal plane of the lenslets. A CCD camera placed in the focal plane of the lenslet array records the spot array pattern for wavefront calculation. For a perfect eye (i.e., an aberration-free or diffraction-limited eye), light reflected from the retina emerges from the pupil as a collimated beam, and the Hartmann-Shackspots are formed along the optical axis of each lenslet, resulting in a regularly spaced grid of spots in the focal plane of the lenslet array (as shown in **FIGURE 1.24** A)). In contrast, individual spots formed by an aberrated eye, are displaced with respect to the optical axis of each lenslet. (as shown in **FIGURE 1.24** B)). The displacement of each spot is proportional to the wavefront slope at the location of that lenslet in the pupil and is used to reconstruct the wave aberration of the eye.

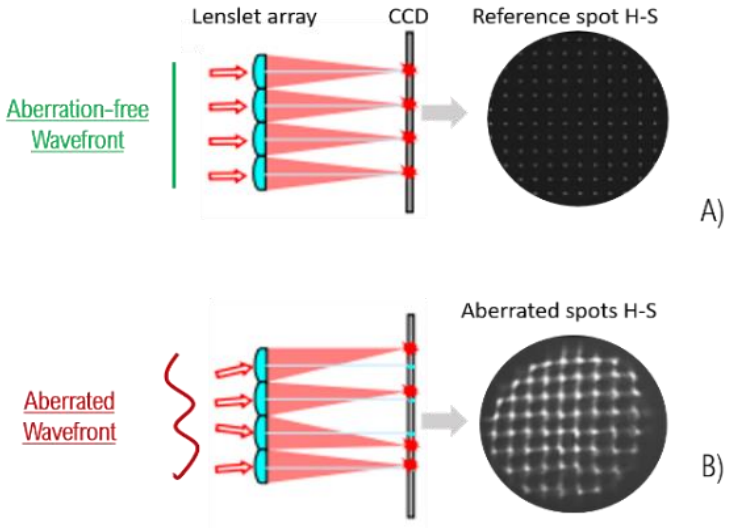

FIGURE 1.24. Illustration of an A) aberration-free wavefront (green); B) An aberrated wavefront (red) reaching the Hartmann-Shack (H-S) wavefront sensor.

1.6.2.2. Wavefront correctors: Active optical elements for visual simulation

There are several strategies to alter the phase profile of the incident wavefront by changing the physical length over which the wavefront propagates, like in the case of deformable mirror technology (while keeping the index of refraction constant). Other devices, such as those based on liquid crystal technologies, rely on localized changes in the refractive index (while keeping the physical length constant). Or the new generation based on Opto-adjustable lenses that change their shape very quickly, changing their optical power, keeping the index of refraction constant, in response to electrical signals. All these strategies are used in the AO system during this thesis.

Deformable Mirror

The deformable mirror (DM) used in this study consists of a continuous flexible reflective membrane that is controlled by a series of actuators located at its rear, deforming the mirror in the desired way. The actuators of the magnetic deformable mirror are composed of a magnet and located behind the reflective membrane and a coil. The surface of the mirror, depending on the voltage applied, is deformed by the active movement of the actuators to introduce gains/delays in the optical path of the different parts of the wavefront after reflecting the beam on the mirrored surface. The emerging wave presents a phase that is as flat as possible, if what we want is to correct the incident wavefront.

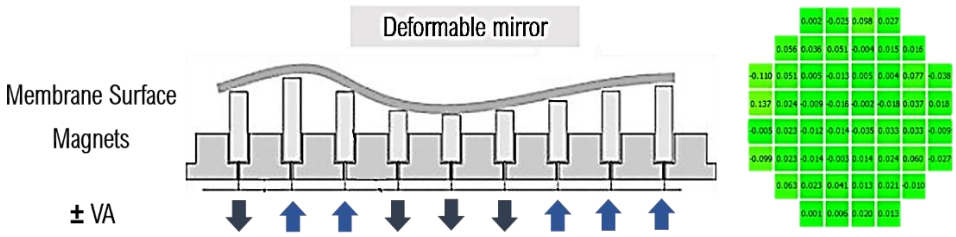

FIGURE 1.25. Schematic representation of the continuous flexible surface magnetic deformable mirror and the corresponding 52 actuators in the MIRAO52 (Imagine eyes, France).

The main disadvantage of this type of device (DM) is its inability to simulate complex patterns with abrupt phase changes. To simulate abrupt phase changes its use other types of devices, such as Spatial Light phase modulators. The deformable mirror in this thesis has been used to correct the aberrations of the system and the eye, in addition to inducing patterns of aberrations of subjects.

Phase modulators Spatial Light Modulator

In general, Spatial Light Modulator (SLM) devices are capable of modulating amplitude, phase, and polarization of incident light, depending on the device. They are usually based on Liquid Crystals on Silicon (LCoS), which due to their optical properties and their anisotropy, the molecules are capable of changing their orientation in the presence of an electric field [214]. These devices allow modifying the phase of a wavefront by applying different voltages to the different pixels of the device, modifying the refractive index and subsequently the optical path. As a consequence, the phase difference is created between the different pixels where each level of phase is linked to a different level of gray corresponding to a certain phase difference in the interval 0-2π [215].

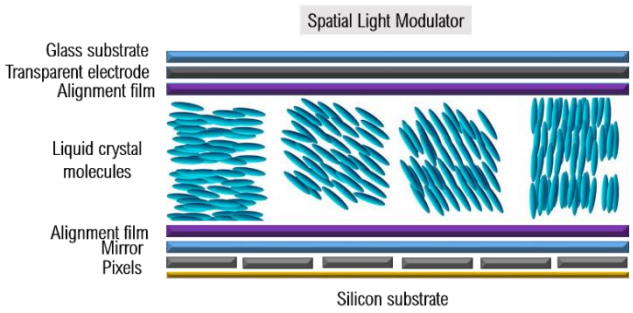

FIGURE 1.26. Schematic of the Liquid Crystal on Silicon (LCoS) SLMs. Adapted from Rosales-Guzmán et al. [216].

SLM [217] presents greater versatility than deformable mirrors continuous-membrane since as they are not subject to a continuous surface, they can introduce abrupt phase changes, allowing the simulation of more complex multifocal patterns [218]. The main disadvantage of this type of device is the residual chromatic aberration that it generates, therefore both the calibration of the device and the generation of phase patterns must be done with monochromatic light to avoid unwanted chromatic effects [219]. This simulation technology has been used in this thesis to simulate diffractive IOLs lenses in **Chapter 3**.

Tunable lens SimVis technology

The fundamental basis of simultaneous vision is the fact of being able to focus several images located in different foci at the same time. To carry it out, an optical system or device that can generate this simultaneity. One example of this is the Tunable lens (TL) which allows us to control both the power and the operating time, enabling temporal multiplexing (Sim+Vis Technology™) [220].There are a wide variety of TLs on the market operating on different principles [221]. In this thesis we will focus on the liquid-membrane principle since the lens installed in our system is of this type. The lens consists of an optical fluid (refractive index =1.30) within a container. One of the optical surfaces of the container is a transparent rigid material, while the other one is a polymer membrane. The lens has an integrated electromagnetic actuator that controls a circular ring located above the membrane. Due to the pressure exerted by the ring on the membrane, the optical liquid is pumped causing the flexing surface to change its shape. Therefore, depending on the electrical current applied to the coil of the electrode, the optical power is changed [222].

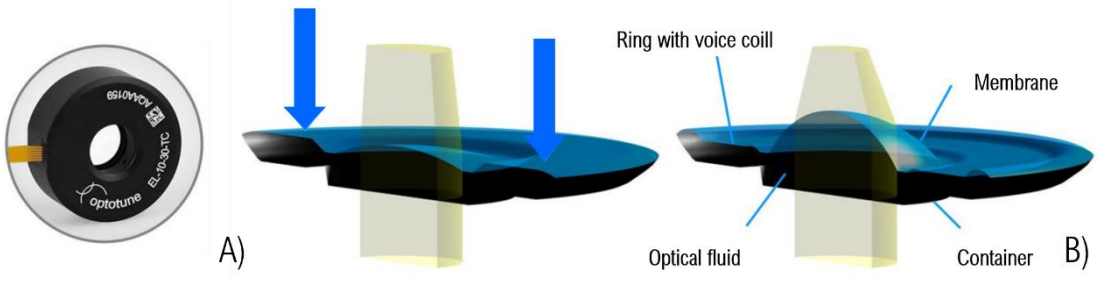

FIGURE 1.27. A) TL model EL-10-30-TC; B) Working principle of the EL-10-30 series. Adapted from Optotune website [222].

The temporal multiplexing principle is detailed in Methods section 2.1.4 of this thesis, together with the SimVis application developed by the 2eyesVision company. This simulation technology has been used in **Chapters 3 and 4**, to represent diffractive IOL or contact lenses respectively.

1.6.3. Visual simulators from the research laboratory to the clinic.

In recent years, the main optical technologies such as those previously described in section 1.6.2 (DM, SLM, and TL), have migrated from large laboratory tables to more compact visual simulation systems, and in some cases, they have become commercially available.

Some of the first visual simulators are the monocular CRX1 [223, 224] from Imagine Eyes (Orsay, France) based on the deformable mirror or the binocular VAO [225, 226] from Voptica (Murcia, Spain) based on the SLM. These two simulators are bench-top and monocular.
In contrast, the SimVis Gekko™ [227] recently, developed by spin-off 2EyesVision (Madrid, Spain), is a binocular, head-mounted, see-through device that provides a natural view of the environment around the patient. SimVis is based on the use of temporal multiplexing with TL, a novel technology explained in section 2.4.1

1.6.4. Applications of Adaptive Optics

Adaptive Optics has been used in the last years to image the retina with unprecedented resolutions and to perform psychophysics under manipulated optics.

1.6.4.1. Adaptive Optics in retinal imaging

The use of AO has also helped retinal imaging methods. AO now permits routine analysis of single cells in the eye, such as photoreceptors. The capacity to visualize these structures in real-time allows researchers to monitor normal retinal function, the course of retinal disease, and the efficacy of disease treatments on a microscopic spatial scale, as well as enhance surgical procedures.

Roorda et al. [196] built the first closed-loop Adaptive Optics Scanning Laser Ophthalmoscopy (AOSLO) to correct high-order aberrations and deliver real-time, microscopic images of the living human retina with unprecedented optical quality. AOSLO is a powerful retinal imaging tool with a high spatial and temporal resolution [228]. It enables imaging of retinal structures at a cellular level, such as cone photoreceptors, at specific locations inside retinal tissue. A confocal scanning laser microscope with adaptive optics that uses the eye's optics as the microscope objective is known as an AOSLO [229]. A concentrated point is scanned over the sample (the human retina), similar to confocal microscopy, and the backscattered light is captured at every scan location by a single element integrating detector. To reject out-of-focus light, a pinhole is put in front of the detector in a plane conjugate to the focused region on the sample. The diameter of this pinhole is one of the most important factors in determining the microscope's resolution.
Moreover, using AO in conjunction with OCT [230] has improved lateral resolution, reduced speckle, and increased sensitivity in both traditional flood illumination and scanning laser ophthalmoscopes.

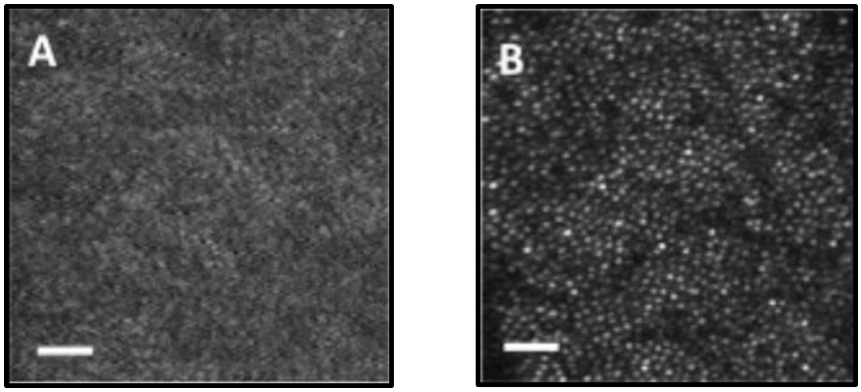

FIGURE 1. 28. AOSLO images of the retina as an example. A) An AOSLO image of a small region of the parafoveal retina without adaptive optics correction. B) The same region of the retina with the AO control loop turned on, showing all cones in this area. Adapted from Burns et al. [231].

1.6.4.2. Adaptive Optics for vision testing

The use of AO in combination with a psychophysical channel to correct aberrations in the human eye has become a useful tool for simulating visual experience, for example with new lens designs, before the lens is implanted or even manufactured [232, 233]. Several authors [234, 235] look at the influence of AO on visual function and the extent to which visual performance improves when correcting higher-order aberrations.

In this part, we will go through a few studies that looked at visual performance while using AO manipulated optics. Few studies have looked at how correction of high-order aberrations affects visual performance under varied luminance situations. Yoon and Williams [236] found a visual benefit by a factor of 1.2 -1.6 times in logMAR Visual Acuity (VA) when correcting monochromatic aberrations and when correcting both monochromatic and chromatic aberration (interference filter). Marcos et al. [237] measured visual acuity under AO correction for two different contrast polarities and different luminance conditions. With aberration correction, there was an improvement in visual acuity across all luminances, as shown in **FIGURE 1. 29** (green symbols).

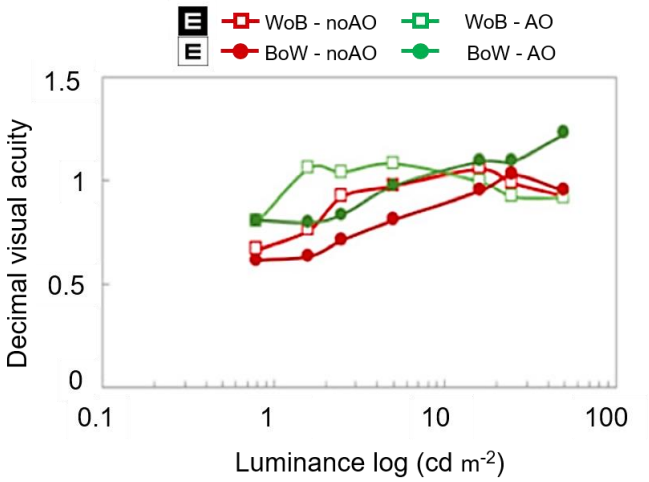

FIGURE 1. 29. Decimal visual acuity with (green) or without (red) AO correction of ocular aberrations, as a function of background luminance (in a log-linear scale) for Black on White (BoW) targets and as a function of foreground luminance (in a log-linear scale) for White on Black (WoB) targets. Adapted from Marcos et al. [237].

In myopes and emmetropes, Legras and Rouger [238] measured the visual benefit of correcting only defocus and astigmatism and when correcting high order aberrations (with AO, up to 5th order) in terms of contrast sensitivity (CS) and visual acuity, and examined the accuracy of wave aberrations based metrics to predict the impact of monochromatic aberrations on visual performance. When higher-order aberrations were corrected, both visual acuity and contrast sensitivity improved (1.25 to 1.64 VA, at 16c/deg CS). By measuring the contrast sensitivity function (CSF) in monochromatic and polychromatic conditions under natural aberrations and after AO correction for a wide range of angles and frequencies, de Gracia et al. [239] investigated the limits of the visual and optical improvement in retinal image quality. They discovered that when exposed to monochromatic light, the CSF increased by 1.35 times (just for the mid and high spatial frequencies) and was lower (0.93 times) when exposed to polychromatic light. The consistent higher benefit of correcting aberrations in the MTF in the CSF implies that the neural transfer function plays a considerable role in the limit of contrast perception.

Instead of focusing on correcting all aberrations using AO, Applegate et al. [240] looked at how combinations of defocus and spherical aberrations, as well as astigmatism and secondary astigmatism, may improve visual performance. They discovered that, while these combinations reduced VA as compared to no-aberrated circumstances, some particular combinations performed much better than one of the aberrations alone. When all other aberrations were corrected, de Gracia et al. [241] observed that combining coma with astigmatism enhanced decimal VA by a factor of 1.28 and 1.47 in two participants, respectively, versus VA with astigmatism alone. The impact of the coma/astigmatism combination is significantly lessened in the presence of usual normal levels of HOA.

According to Artal et al [242], the stimuli viewed through an individual's natural aberrations always appear sharper than those seen through a rotated version of the identical aberrations. They hypothesized that these findings may be the result of neuronal adaptation to the specific degradation caused by a person's HOA.

To examine blur perception and adaptation, Sawides et al. [109-111, 243] employed adaptive optics to correct aberrations and presented different modified images using AO. For example, correcting aberrations enhanced the subjective perception of sharpness of natural images and improved familiar face identification, but not facial expression recognition in most individuals.

Gambra et al.[244] looked at accommodative responses when aberrations were corrected and found that accommodative lag increases when coma and spherical aberrations are induced, but reduces when the aberrations are corrected. Sabesan et al. [245] assessed binocular visual performance in terms of correcting higher-order aberrations. They found that correcting aberrations enhances binocular summation as well as visual acuity.

AO has developed into such an outstanding instrument for studying the features of neural adaptation by controlled manipulation of the retinal image, and it has a wide range of applications in multifocality, binocular vision, and polychromatic vision research.

1.7. OPEN QUESTIONS

Visual simulators based on Adaptive Optics allow probing vision while manipulating the optics of the eye. They are particularly attractive to test vision with new optical designs such as intraocular lenses or contact lenses before these are prescribed or even manufactured. Despite visual simulators having been used for over a decade, and some making their way to the clinic, many questions still remain, in particular regarding the interactions between the subject's optics and a given correction, the impact of optical aberrations on visual perception, interactions between chromatic and monochromatic aberrations, and the extent to which a simulated correction represents vision with the actual physical lens in the patient.

The use of a custom-developed polychromatic visual simulator in this thesis has allowed us to manipulate the optics in multiple ways and address the following questions:

1. Can we truly predict the post-operative visual quality with a multifocal IOL using visual simulators?

2. Are visual simulators capable of replicating the visual performance of a contact lens?

3. To what extent, the optical and visual acuity with convolved stimuli are comparable to those obtained with natural optical aberrations?

4. What is the impact of aberrations on visual function, in particular visual acuity and a natural task such as gender facial recognition?

5. Do monochromatic aberrations and the Stiles-Crawford effect have an impact on the magnitude and direction of Transverse Chromatic Aberration?

6. What is the magnitude of the Longitudinal Chromatic Aberration in patients with diffractive multifocal intraocular lenses?

1.8. GOALS OF THE THESIS

The main purpose is to use a custom-made polychromatic multichannel AO visual simulator system to test vision with new multifocal designs for presbyopia and to study the impact of chromatic aberration on the visual field.

The specific goals are:

- To compare visual performance pre-operative and post-operative with the same M-IOL pattern using different visual simulators (from on-bech AO to binocular head-mounted Simultaneous Vision Simulators, SimVis Gekko™).

- To evaluate through-focus (TF) visual and optical quality in patients with M-CLs and with the corresponding simulated multifocal patterns simulated with SimVis technology using a polychromatic multichannel AO visual simulator.

- To understand the perceptual differences between convolved and optically blurred images, and to identify the origin of the discrepancies in monochromatic and polychromatic light.

- To evaluate the impact of aberrations in tasks with different spatial frequencies involved, such as gender face recognition or visual acuity.

- To study the impact and the interactions between Longitudinal Chromatic Aberration and Transverse Chromatic Aberration with the monochromatic aberrations, in vivo, in the same AO system.

- To evaluate the contribution of the Stiles-Crawford effect in the Transverse Chromatic Aberrations and on the retinal image quality (convolved images).

1.9. HYPOTHESES

The hypotheses of this thesis are:

- Visual simulators allow subjects to experience vision with multifocal corrections lenses before testing them on-eye, given an accurate representation/experience.
- Convolved images can predict retinal images, but some indications must be taken into account.
- Correcting aberrations (low and high-order aberrations) improves the performance of daily visual tasks such as gender identification.
- Monochromatic and chromatic aberrations interact favorably so that the presence of monochromatic aberrations mitigates the impact of the longitudinal chromatic aberrations.

1.10. STRUCTURE OF THE THESIS

The body of this thesis is structured as follows:

CHAPTER 1 starts with a brief introduction to the major concepts used and the motivation of the thesis.

CHAPTER 2 provides a description of the different optical setups and an overview of the psychophysical methods used throughout this thesis. In particular, it includes descriptions of the two generations of Adaptive Optics systems to measure and correct subjects' aberrations and their specific characteristics, the Simultaneous Vision Simulator, and the Laser Ray tracing that we used to measure the optical/objective Stiles-Crawford effect (OSCE) objectively. It also describes the psychophysical experiments that have been carried out during the thesis, the methodology, and the protocols common to the different studies.

CHAPTER 3 presents a study that evaluates the quality of various visual simulating technologies by comparing vision with simulated M-IOLs pre-operatively and implanted M-IOLs post-operatively in the same patients. Two simulator platforms were used: (1) a custom-developed AO system, with two visual simulator devices: an SLM and TL (SimVis); and (2) a wearable, binocular large field of view SimVis Gekko™ clinical simulator. Through-focus decimal visual acuity (TF VA) was measured on eight presbyopic patients (1) monocular in monochromatic light using four-alternative-forced-choice; (2) binocular using a clinical optotype in white light.

CHAPTER 4 presents the ability of a simultaneous vision visual simulator (SimVis) to represent center-near M-CLs (low, medium, and high near addition). On-bench, though focus (TF) optical quality of SimVis-simulated M-CLs was obtained from double-pass (DP) images and images of an E-letter stimulus using an artificial eye. Visual acuity (VA) and DP retinal images were measured TF with the M-CL on the eye and through SimVis simulations of the same M-CLs on ten presbyopic subjects.

CHAPTER 5 investigates why convolved images are perceived more degraded than the same image blurred with optical defocus. We hypothesized that the positive interactions between the monochromatic and chromatic aberrations in the eye are lost in the convolution process. To test this hypothesis, we evaluated optical and visual quality with natural optics and with convolved images (on-bench, computer simulations, and VA in seven subjects), using a polychromatic multichannel AO system with monochromatic (555nm) and polychromatic light illumination.

CHAPTER 6 investigates how manipulated aberrations influence face gender identification (GI) performance. Five conditions were evaluated for GI and VA: natural aberrations, AO-correction, 90deg rotated aberrations, and 2 external patterns, one better and worse. For the GI experiment, we convolved images for each manipulated aberration condition (set of 200 male/ 200 female, randomly presented and alternating conditions in blocks of 100 images). For VA, the conditions were mapped in the DM, using eight-alternative-forced-choice. Images were presented through fully corrected optics. Nine subjects participated in the study, whose aberrations were measured to estimate their Visual Strehl (VS).

CHAPTER 7 presents measurements of the TCA in eleven subjects using 2D-two-color Vernier alignment, for two pupil diameters. For a small pupil (2-mm), referred to as 'optical TCA' (oTCA), and for a large pupil (6-mm), referred to 'perceived TCA' (pTCA). Also, the TCA was measured

through both natural aberrations and AO-corrected aberrations, using a polychromatic multichannel AO visual simulator system. We performed computer simulations of pTCA incorporated LCA, the subject's HOAs measured with Hartmann-Shack, and optical/objective Stiles-Crawford effect (OSCE), measured objectively by Laser Ray Tracing.

CHAPTER 8 presents measurements of the LCA in patients bilaterally implanted with a hydrophobic trifocal intraocular lens. Measurements were performed using psychophysical (480-700 nm), in a polychromatic AO system. Measurements were performed on ten patients (20 eyes) and LCA was computed from the chromatic difference of focus curves as the difference between 480 nm and 700 nm at near, intermediate, and far.

CHAPTER 9 presents a summary of the major finding of this thesis, their implications for the state-of-the-art.

2

CHAPTER 2. METHODS

The current chapter describes the experimental setups used in this thesis, especially two different Adaptive Optics (AO) systems developed previously at the Visual Optics and Biophotonics Lab (VioBio Lab) [198, 246]. In this chapter we describe also the objective and psychophysical experiments measurements that have been carried out during the realization of this thesis, and the methodology common to the different studies described in later chapters.

Both systems have the basic elements of an adaptive system, but with different capabilities that specify to the studies that were carried out. The monochromatic AO system was the first generation of AO and has been used to test the effects of manipulating the optical aberrations on visual perception and visual performance. In particular, to test the visual benefits produced by correcting high-order aberrations on visual acuity [237], contrast sensitivity [239], familiar face and facial expression recognition [243], accommodation dynamics [244], the ability of the visual system to adapt to the level and orientation of the aberrations [110], and the impact of astigmatism [112, 247, 248].

The polychromatic multichannel AO visual simulator system was the second generation of AO and has allowed for the first measurements of monochromatic and polychromatic aberrations in the phakic and pseudophakic eye with objective and subjective techniques in a broader spectral range (supercontinuous laser) and has represented a significant advance in visual simulation capabilities, combining for the first time different visual simulators technologies such as the deformable mirror, phase plate, spatial light modulator, and tunable lens working in temporal multiplex mode [187, 194, 218, 249].

The author of the thesis worked in both systems but at different levels of involvement. In the monochromatic AO system as a basic user of psychophysical measurements aiming at investigating the impact of aberrations on vision, and neural adaptation to aberration, **Chapter 6.** However, the author of this thesis in the polychromatic multichannel AO visual simulator system has been involved in the alignment of the system, calibration of specific channels, and in the implementation of new channels or optical elements into the system such as those indicated in section 2.2. This has allowed the author to have more knowledge of the system and develop the projects that are detailed in the following chapters. This was done with the guidance of Dr. Maria Vinas and the help of the other members that make up the AO Team, supervised by Prof. Susana Marcos.

2.1. OPTICS SYSTEMS IN VIOBIO LAB

Both AO systems are described below, highlighting the particularities of each one. Both systems have a wavefront sensor (HASO) that allows the aberrations of the system and the eye to be measured. Once the aberrations are measured, they are corrected using a deformable mirror (DM). Both elements, the DM, and the HASO are in conjugate planes of the pupil and work in a closed-loop to measure and correct aberrations. In combination with the AO elements, a psychophysics channel allows to perform psychophysical measurements under aberration correction and manipulation.

For both AO systems, the measurements and close-loop correction of wave aberrations are performed following 4 different steps: Local Slopes Acquisition, Interaction Matrix Acquisition, Command Matrix Construction, and finally Close-Loop Correction (and/or induction) of wave aberrations. To perform this process an artificial eye is placed in the pupil plane of the system, consisting of a 50.8mm focal length achromatic doublet lens and a rotating diffuser as an artificial retina.

2.1.1. General description of the monochromatic AO system

The first AO system (monochromatic AO) in the Visual Optics and Biophotonics Lab (VioBio Lab) was designed and developed in 2006 [237]. A detailed description of the system has been presented in previous studies [198, 250, 251]. The primary application was dynamic measurements and correction of ocular aberrations in real-time. The main components of the system are a ***(1)*** Hartmann–Shack wavefront sensor (HASO 32 OEM, Imagine Eyes, France) composed by a matrix of 32 x 32 microlenses with 3.6-mm effective diameter and an electromagnetic deformable mirror (MIRAO, Imagine Eyes, France) with 52 actuators in a 15-mm effective diameter. For measurement and correction, of wavefront aberrations, respectively, they are placed at conjugate pupil planes of the system. ***(2)*** Illumination comes from a SuperLuminescent Diode (SLD) coupled to an optical fiber (Superlum, Ireland) emitting at 827 nm. According to the maximum permissible exposure (ANSI reference) we set an irradiance of 8μW on the cornea, for which we set the current limit to 90mA when measuring human eyes. ***(3)*** A motorized Badal system is used to compensate for refractive error. ***(4)*** The stimuli were presented on a CRT monitor (Mitsubishi Diamond Pro 2070, Australia) and were controlled by the psychophysical platform ViSaGe (Cambridge Research System, UK). ***(5)*** A pupil monitoring channel, consisting of a CCD camera (TELI, Toshiba, Japan) conjugates to the pupil. The camera allowed continuous viewing of the pupil and was used to perform proper centration of the subject's eye aligned to the system (x-y-z stage) using the line of sight as a reference.

The system was controlled using custom routines written in Visual C++ (Microsoft, Redmond, WA, USA) and Matlab (MathWorks, Natick, MA, USA) from two different computers, one controlling the AO system (DM, Hartmann–Shack wavefront sensor) and the Badal system, the other controlling the ViSaGe psychophysical platform and the Mitsubishi Monitor.

FIGURE 2.1 shows a schematic of the VioBio Lab monochromatic AO system that has been used in the study presented in **Chapter 6** of this thesis.

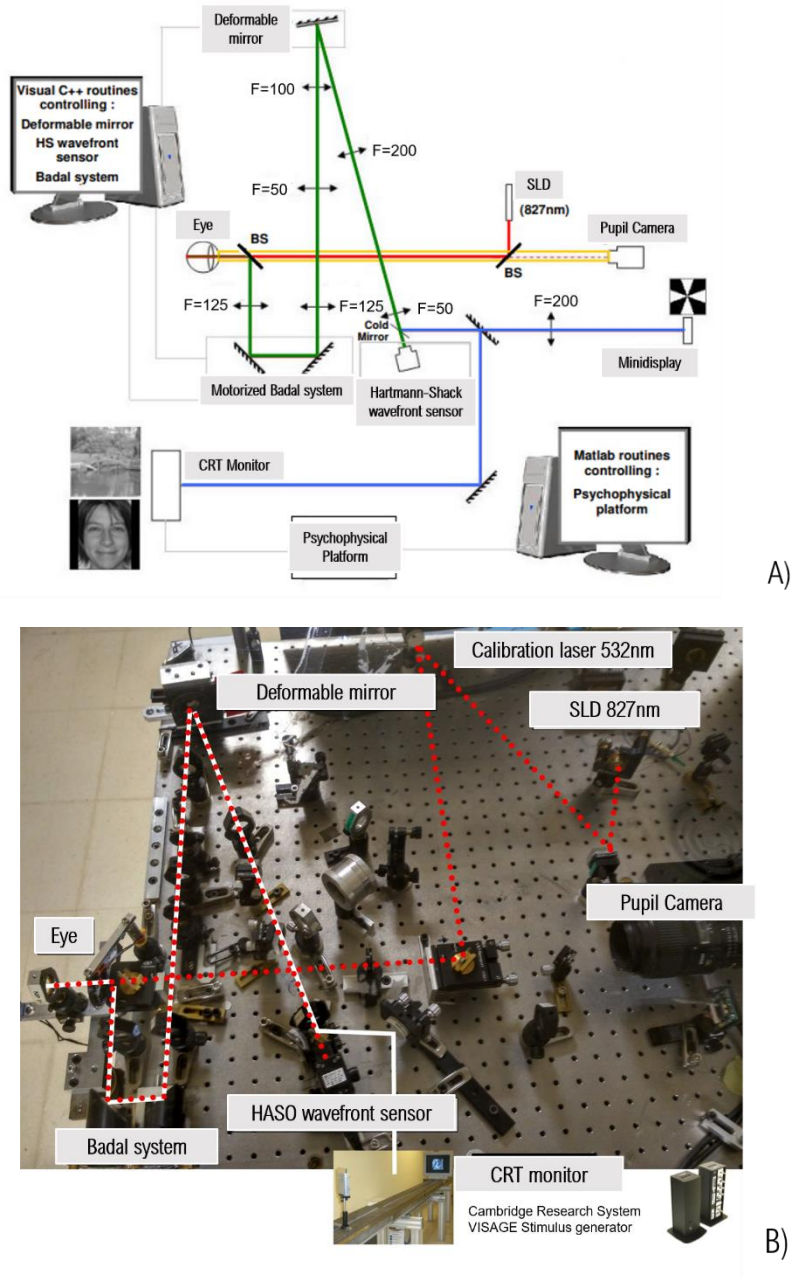

FIGURE 2.1. A) Schematic diagram of the system with its five channels: illumination channel with a 827 nm SLD source (red); AO-control channel with the Hartmann-Shack wavefront sensor and the deformable mirror (green); Psychophysical channels, one provided with a mini-display, the other with a CRT monitor (blue); Pupil monitoring channel (yellow). B) Image of the VioBio Lab monochromatic AO system and its main components. Modified from Sawides thesis [198] and Marcos et al. (2008) [237].

2.1.2. General description of the polychromatic multichannel AO visual simulator

The second AO system (polychromatic multichannel AO Visual Simulator) in the VioBio Lab was designed and developed in 2015 [246]. A detailed description of the system has been presented in previous studies [62, 187, 218, 246, 252] where it was used to evaluate visual benefits of AO correction, vision with simulated multifocal correction, optical aberrations in pseudophakic eyes, chromatic aberrations, and their visual impact, and neural adaptation to ocular aberrations.

FIGURE 2.2 and **FIGURE 2.3** show a schematic diagram and sky view of the polychromatic multichannel AO Visual Simulator set-up respectively.

The current configuration of the system is formed by 8 different channels. In the thesis process, improvements have been made to some of the channels that are detailed in section 2.2:

(1) **The Illumination-Channel**, contains a supercontinuum laser source (SCLS, SC400 femto-power 1060 supercontinuum laser, Fianium Ltd, United Kingdom), in combination with a dual acousto-optic tunable filter (AOTF) module (Gooch & Housego, United Kingdom), operated by radio frequency (RF) drivers, to automatically select the wavelengths in the different channels (visible 450–700 nm or near-infrared light 700–1100 nm, in our system configuration). Very recently, in 2020, the dual-module was substituted by a single VIS module (Fyla SL, Spain), which allowed higher control of the wavelength selection (more details in section 2.2.2).
The output is a collimated beam coupled to two independent multimode fibers. One for visible light (VIS) and the other for near-infrared (NIR) light, with a spectral bandwidth of approximately 12nm (10-12nm (VIS); 12-15nm (NIR)). The illumination coming from the two independent fiber channels of the SCLS enters the system collinearly through a hot mirror (HM), allowing wavefront sensing and retinal aerial imaging with VIS and NIR light. The 2-mm diameter beam entering the eye is slightly (1 mm) decentered with respect to the pupil center to avoid corneal reflections in the Hartmann-Shack images. A variable-size pupil (VS-P) allows modifying the beam size and position entering the eye. The illumination coming from the VIS multimode fiber is also used to monochromatically illuminate the visual stimuli. The laser power measured at the corneal plane ranged between 0.5 and 50 μW, which was one order of magnitude below the ANSI standards safety limits at all tested wavelengths [253].

(2) **The AO-Channel** consists of a Hartmann-Shack wavefront sensor (microlens array 40 × 32, 3.6 mm effective diameter, centered at 1062 nm; HASO 32 OEM, Imagine Eyes, France) and an electromagnetic deformable mirror (DM) (52 actuators, 15-mm effective diameter, 50-μm stroke; MIRAO, Imagine Eyes, France), to measure and correct subjects and system aberrations, respectively. Both devices are placed in conjugated pupil planes of the system through different relay lenses. Thus, an x2 magnification factor is achieved from the subject's pupil to the deformable mirror and an x0.5 magnification from the subject's pupil to the microlenses array plane.

(3) **The SLM-Channel** that consists of a reflective phase-only LCoS-SLM (PLUTO-VIS; VIS; resolution: 1920 × 1080; 0.7'' diagonal; Pixel pitch: 8.0 μm; image frame rate: 60Hz; max. resolution: 62.5 lines/m; 8bits, Holoeye Photonics AG, Germany) is used to generate the multifocal designs [218]. A linear polarizer is placed in the path of the SLM at the calibrated polarization angles, in this case, 232 degrees, to ensure maximum efficiency.

(4) **The Testing Channel**, placed in a conjugate pupil plane of the system, allows evaluating alternative simulating technologies. In the current configuration, it allows a) phase plates (i.e. representing angular or radial segmented zonal designs with different powers) [249], b) real IOLs (in a custom-developed cuvette). There are two possibilities to test real IOL, cuvette 0D IOL [187] and non-0D IOL (around 20D) using a Rassow system [254]. Or other simulating technologies, such as the tunable lens (Lens model: EL-10-30-TC; aperture: 10mm; tuning range: +8.3 to +20D; Offset lens: -5.00D, Optotune AG, Switzerland) called SimVis operating by temporal multiplexing [187].

(5) **The Retinal imaging-Channel** allows capturing retinal images, and consists of a CCD camera (Retiga 1300, CCD Digital Camera, 12-bit, Monochrome, 6.7 × 6.7 μm pixel size, 1024 × 1280

pixels; QImaging, Canada), and a camera lens (Sigma Mini-Tele 1:35, 135-mm focal length multi-Coated, Japan) in the 'double-pass retinal' imaging channel. The laser beam is filtered before entering the eye using a spatial filter. The implementation of the spatial filter as part of the implementations that were related to the thesis is detailed in section 2.1.5.

(6) **The Psychophysical-Channel**, placed in a conjugate retinal plane, consists of a Digital Micro-Mirror Device (DMD) (DLP® Discovery™ 4100 0.7 XGA, Texas Instruments, USA), and allows displaying visual stimuli with a 1.62 deg angular subtend. The DMD is monochromatically illuminated with light coming from the SCLS (555 nm) or with a fiber white light source (Halogen Fiber Light Sources LQ, Output Power 20–250 W, 3,000–3,400K, Linos; Qioptiq, Rhyl, UK). When light is perpendicularly incident on the flat surface of the DMD, light can be deflected towards two possible directions at ±12° (optical angle) by each micromirror, hence projecting high-resolution gray-scale stimuli. The brighter pixels are projected onto a common screen using the 'ON-position' while deflecting light away with the 'OFF-position' provides a darker appearance. The amount of time each pixel is ON or OFF is varied to create a gray scale image, with lighter gray pixels corresponding with mirrors being ON more than OFF. A D4100 DVI to DMD (D2D) Interface Board (Digital Light Innovations Incorporated, Texas Instruments Incorporated, USA) was added to the original DLP Discovery 4100 kit in this system's configuration to display a video on the DMD via a DVI interface and control the generations of gray scale images.

The DMD was calibrated to offer linear brightness levels and has an effective luminance of 100 cd/m^2 (calibrated with a Cambridge Research Systems ColorCal luminance-meter/colorimeter). The gamma correction was calibrated using the ViSaGe platform and the Cambridge Research System ColorCaL colorimeter, with 64 tones, linear fitting, and 64 readings per line. It was then applied to the DMD after being validated using a technique similar to that used in Psychtoolbox's Visual Gamma Demo [255]. A holographic diffuser (HD) placed in the beam path breaks the coherence of the laser, providing uniform illumination of the stimulus.

(7) **The Pupil Monitoring Channel**, which allows monitoring of pupil size and subject position during measurements. It consists of a camera (DCC1545M, High-Resolution USB2.0 CMOS Camera, Thorlabs GmbH, Germany) conjugated to the eye's pupil. Subjects are stabilized using a dental impression and the eye's pupil is aligned to the optical axis of the system (with an x-y-z stage moving a bite bar) using the line of sight as a reference, while the natural pupil is viewed on the monitor.

(8) **The Badal optometer Channel** (formed by two lenses of a 125-mm focal distance and two mirrors) allows correction or to induce defocus. Mounted on a motorized stage can be controlled by the researcher automatically or by the subject using a keyboard.

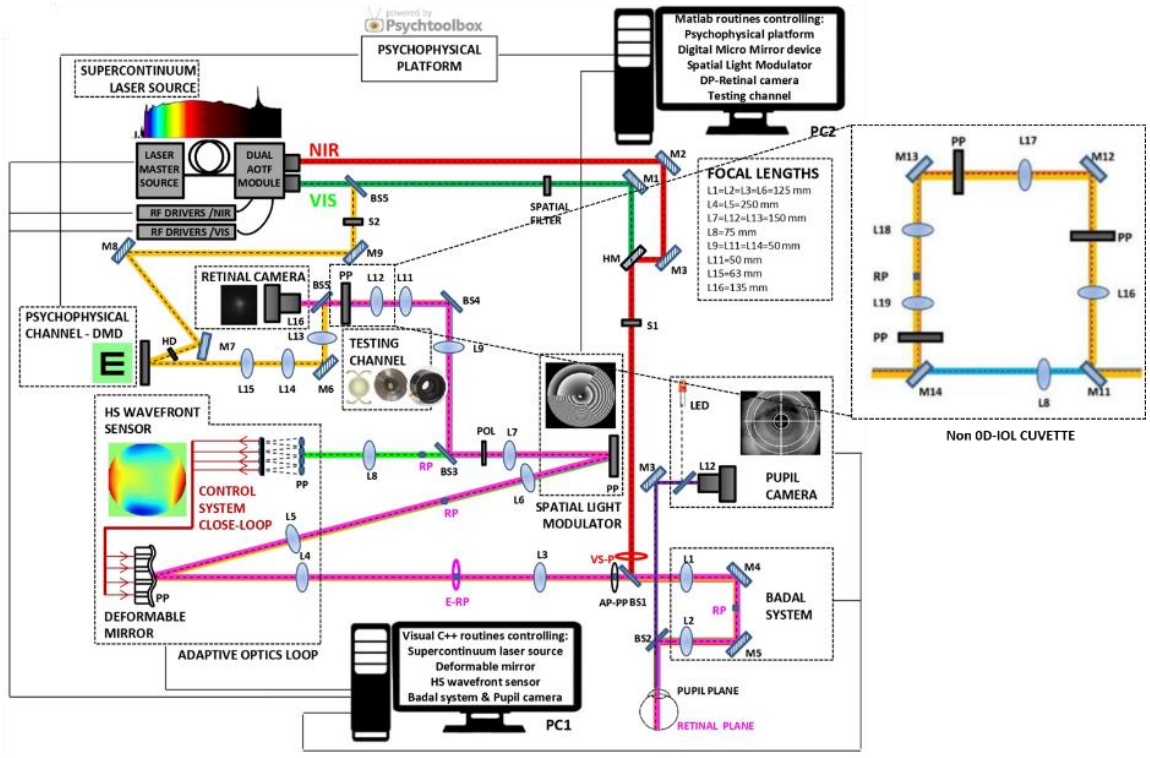

FIGURE 2.2. Schematic diagram of the VioBio Lab polychromatic multichannel AO visual simulator system with the different channels in its final configuration (2021): the illumination channel (red line), the AO channel (green line); the SLM channel (yellow line); the retinal imaging channel (pink line); the pupil monitoring channel (purple line), and the psychophysical channel (blue line). NIR: near-infrared light; VIS: visible light; RP: retinal plane; PP: pupil plane; BS: beam splitter; S: shutter; L: lens; M: mirror; HM: hot mirror; POL: polarizer; E-RP: retinal pinhole; AP-PP: artificial pupil; VS-P: variable size pupil. Modified from Vinas et al. and Benedi-Garcia et al. [246, 254].

Three automatized shutters allow simultaneous illumination of the eye and the stimulus for monochromatic light or white light. To ensure constant pupil diameter during measurements, an artificial pupil is placed in the first pupil plane of the system with x1 magnification from the subject's pupil.

All optoelectronic and mechanical elements of the AO set-up were automatically controlled and synchronized using ready-made or custom-built software programmed in Visual C++ and C# (Microsoft, Redmond, WA, USA) and Matlab (MathWorks, Natick, MA, USA).

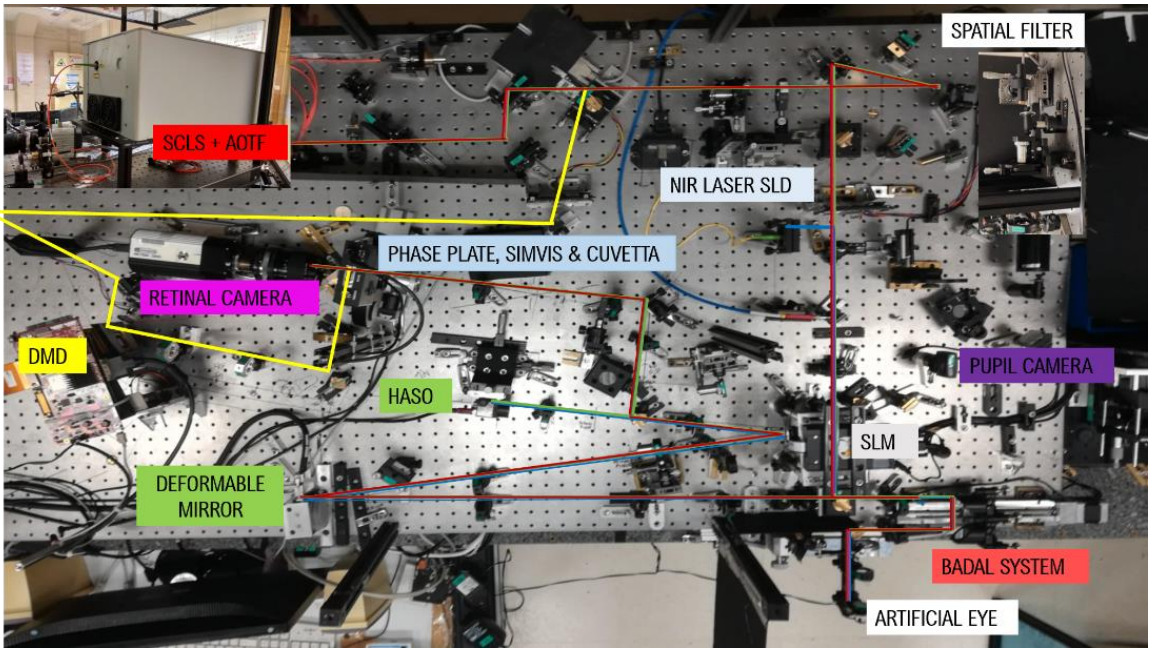

FIGURE 2.3. Sky photo of the VioBio Lab system in its 2019 configuration.

2.1.3. General description of the Laser Ray Tracing

The LRT in the VioBio Lab was designed and developed in 2003. A detailed description of the system has been presented in previous studies [46, 256]. The LRT is a double-pass technique since light is delivered into the eye and the reflection from the retina is captured on a CCD camera. The LRT used consisted of different channels: ***(1)*** illumination channel, the light source can be selected between two diode lasers emitting in green (532 nm; Brimrose, Baltimore, MA, USA) and infrared wavelengths (786 nm; Schäfter+Kirchhoff, Hamburg, Germany). Both lasers are attenuated below safety limits using neutral density filters. ***(2)*** The XY scanner (mod. 6210, Cambridge Technologies, Lexington, USA) consists of two rotating mirrors that deflect the incoming unexpanded laser pencil in such a way that in combination with collimating lenses compose the sequential sample pattern. Different sampling patterns can be configured in the scanner. In this thesis, we only use the hexagonal pattern (37 rays). ***(3)*** The light reflected off the retina is collected by a cooled highly sensitive CCD camera (12 bits, 30 frames per second with 2x2 binning, 1024x1024 pixels, pixel size: 14 µm x 14 µm, nominal maximum quantum efficiency: 20% (700 nm). Model 1M15, Dalsa, Waterloo, Canada), located conjugate to the eye's retinal plane. During the measurement, the retinal camera is synchronized with the scanner and the pupil camera. ***(4)*** The pupil channel, a CCD (8 bits, 60 Hz (video), 646 (horizontal) x 485 (vertical) pixels, pixel size: 7.4 µm x 7.4 µm. Model XC-55, Sony Corp., Tokyo, Japan) continuously monitors the pupil and records pupil images during the measurement. Pupil monitoring before the measurement helps to verify that everything is ready for the measurement**.** ***(5)*** To correct the refractive error, the system contains a Badal system capable of correcting the spherical error in a range of ±12D. ***(6)*** The visual fixation stimulus is presented on an external screen controlled by a pico-projector (854x480 pixels, Philips NV, Amsterdam, Netherlands; 55 lums). A neutral filter was placed after the pico-projector to produce an average luminance of ~30cd/m^2 in an otherwise dark environment.

The control and analysis software used in this thesis was developed previously in our group written in Visual Basic (Microsoft Corp., USA) combined with Matlab scripts.

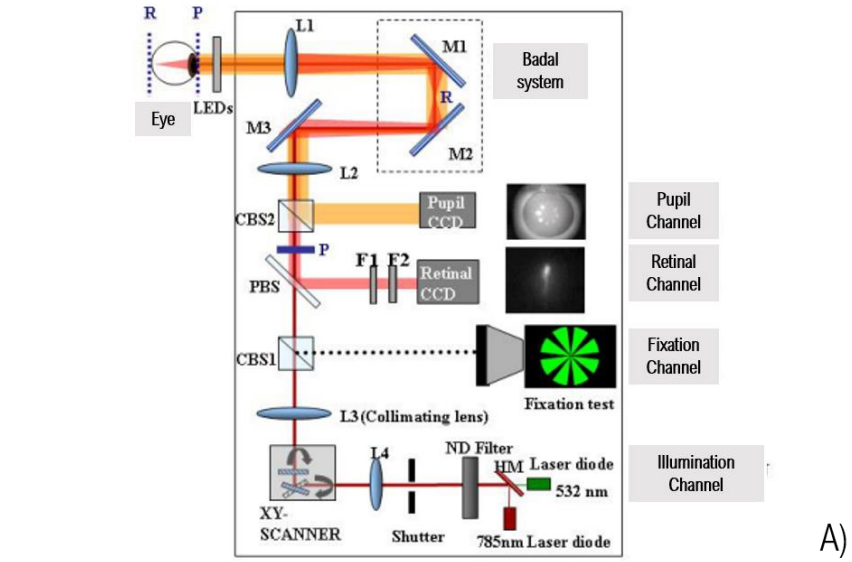

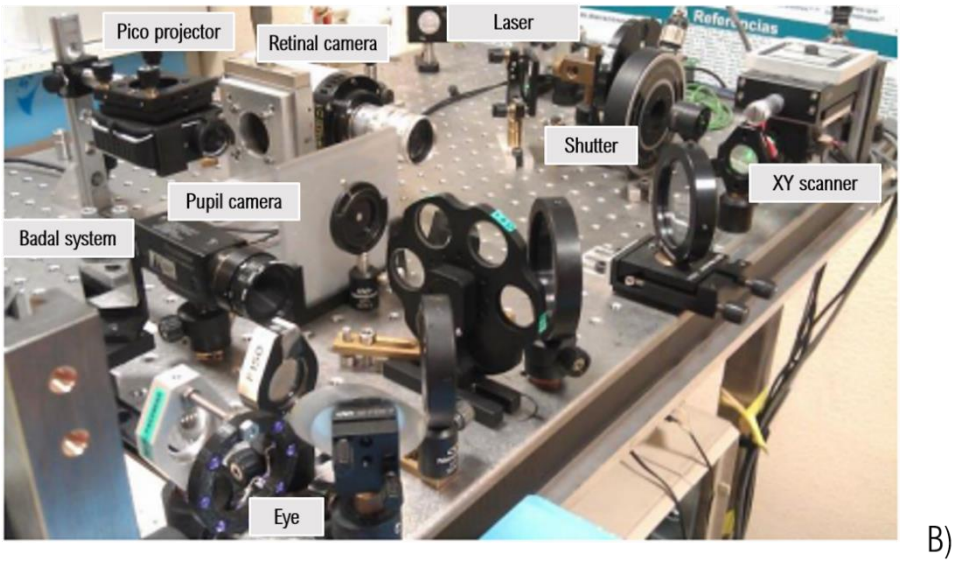

FIGURE 2.4. A) Schematic diagram of the LRT device: L1-L2 are 100mm focal length and L3-L4 are 50.8mm focal length achromatic doublets, M1-M2-M3 are plane mirrors, HM is a hot mirror, CBS1-CBS2 are cube beam splitters, PBS is a pellicle beam splitter, F1 and F2 are interferometric filters for 785 and 532nm, and P and R are planes conjugate to the pupil and retina, respectively. B) Custom image of LRT at VioBio lab and its main components. Modified from Perez-Merino thesis (2015) [257].

2.1.4. Clinical visual simulator SimVis Gekko SimVis2eyes

SimVis Gekko™ (2Eyes Vision S.L, Spain) [227, 258], is a recently developed programmable, portable see-through binocular device that can simulate any correction based on simultaneous vision. It allows patients to experience the real world through different commercial multifocal corrections prior to surgery. The SimVis Gekko™ uses the same Sim+Vis Technology™ describe briefly in the introduction part based on temporal multiplexing, to manipulate the optics of the eye thanks to accurate control of a TL that changes its power high speed, changing foci faster (up to 10kHz) than the flicker fusion of the human visual system and creating multifocal images in the patient's retina with static appearance. SimVis can replicate any through-focus power profile following the general pipeline with several steps that include: ***(1)*** estimating the lens performance typically using the Through-Focus Visual Strehl (TFVS) quality metric [259]. The TFVS of

intraocular or contact lenses can be calculated from phase maps, power maps, or refractive/diffractive real designs; ***(2)*** obtaining the time coefficients for temporal multiplexing matching the TFVS of the defining lens; ***(3)*** generating the corresponding SimVis temporal profile; ***(4)*** measuring and correcting the dynamic effects of the TL; ***(5)*** validating on-bench the SimVis simulations on a high-speed focimeter; ***(6)*** measuring the TF VA curves on patients with SimVis Gekko™ [220, 260, 261]. SimVis+ Technology™ is protected by patents that 2EyesVision has licensed [262-265].

FIGURE 2.5. SimVis Gekko™, binocular, programable, portable, wireless, and wide visual field device (2EyesVision S.L).

2.2. EXPERIMENTAL IMPLEMENTATIONS DURING THIS THESIS

2.2.1. Double-pass aerial retinal imaging

In this study, a spatial filter has been designed to convert the existing retinal channel into a double-pass system, to obtain the system and the subjects' PSFs measured with it, and thus be able to describe the quality of the eye objectively. The previous configurations act as a 'one-and-a-half pass', with the aerial image being the autocorrelation of the image of the laser spot with a 2-mm entry beam and 1-mm exit beam. Spatial filters are designed to 'clean-up' the laser beam, and achieve a beam with a smooth, 'Gaussian' intensity profile, since they allow eliminating unwanted multi-order energy peaks, passing only the central maximum of the diffraction pattern, and removing additional spatial noise from the system due to unwanted scattering rings **FIGURE 2.6.** The spatial filter (SF) assembly typically consists of a microscope objective, a pinhole, and a positioning mechanism. The positioning mechanism has x-y-z movements of micron precision, which centers the pinhole with the aperture of the microscope objective. The proper pinhole size depends on the focal length of the objective and the diameter of the original beam.

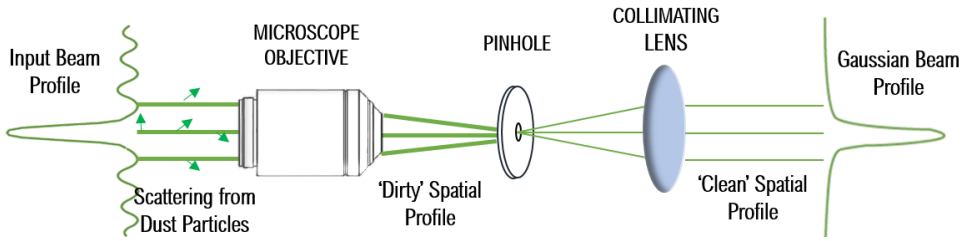

FIGURE 2.6. Illustration of the operation of an SF in removing intensity fluctuation from a laser beam profile.

The final configuration of the SF is composed of a 20x microscope objective, a 25 µm pinhole, and a 100 mm lens (achromatic doublet). The laser beam first passed through the first 20x microscope objective, until it reached the 25 µm pinhole. With the help of micrometers (x-y-z), the beam was made to pass through the pinhole centered and with maximum intensity. The 100 mm focal length lens was incorporated and, as before, with the help of micrometers, the beam was made to pass centered through the lens, without vignetting and with maximum intensity.

FIGURE 2.7 shows A) the current configuration of the SF implemented in the polychromatic multichannel AO system and B) the collimation of the beam was checked and a series of aerial images were taken through the focus already filtered AO-correction (range ± 1.00D step 0.50D).

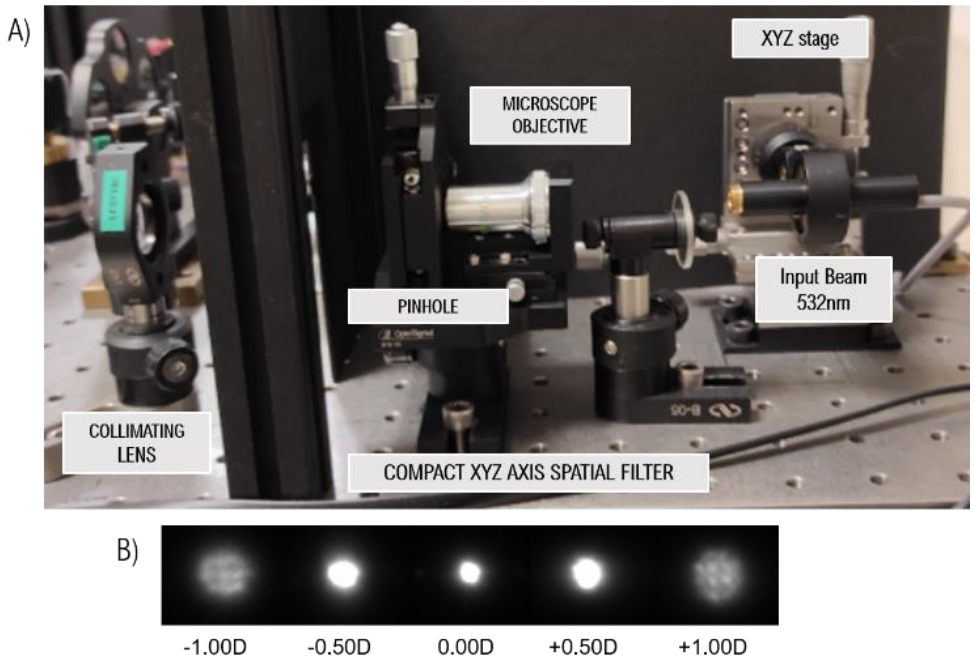

FIGURE 2.7. A) Current configuration of the SF (20x microscope objective, 25 µm pinhole, and an f'=100mm collimating lens; B) Image series of the retina 'PSF', obtained with the double-pass system once the beam was filtered with SF in the polychromatic multichannel AO visual simulator system.

In **Chapter 4** the filtered asymmetric double-pass system (laser spot with 2 mm entry beam and 4 mm exit beam) is used to take images on-bench and from real subjects through different conditions detailed in that chapter.

2.2.2. Acousto-optic module: wavelength selection automatization

The implementation of the AOTF (FYLA S.L, Spain) in the SCLS was carried out in the last stage of the thesis, so all the projects exposed in the thesis except one **Chapter 5,** were carried out with the old AOTFs configuration described in section 2.1.2. The new configuration of the AOTFs allows complete control and programming of the AOTFs, which gives the system the possibility of customizing important laser parameters for each project and the integration of the programming within the psychophysics paradigms. This new configuration of AOTFs allows modifying the intensity, illumination, and amplitude of each wavelength independently. The configuration of the AOTFs was made knowing the current spectrum of the supercontinuum laser (it was measured in the facilities of FYLA S.L), to optimize each wavelength at the maximum power and optimum spectrum. To obtain more power, it was necessary to go from the mono-channel configuration of the acoustic-optical modulator to a multi-channel configuration. The maximization of the power for each wavelength is carried out by maintaining a spectral shape as Gaussian as possible. **FIGURE 2.8** shows A) the AOTFs module box of FYLA S.L and B) the spectrum measured with a spectrometer (Ocean Optics, USB4000-Fiber Optic Spectrometer, 200-1100nm, USA).

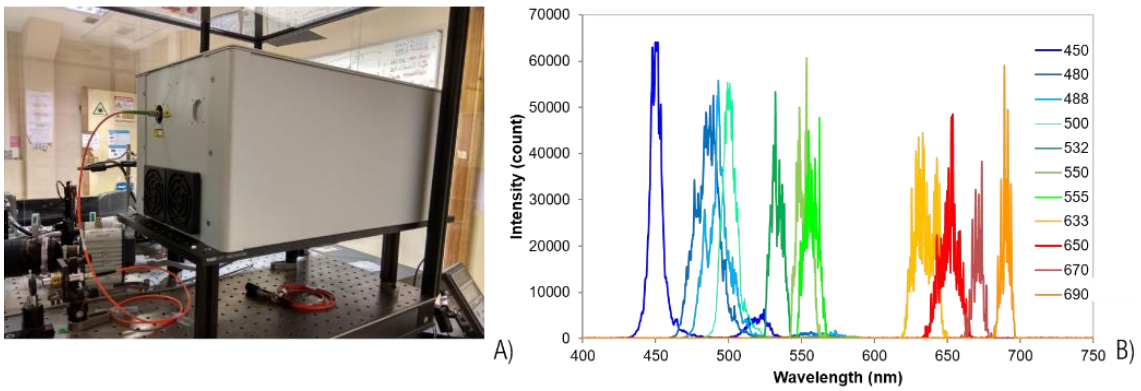

FIGURE 2.8. A) Hermetic box where the AOTFs FYLA S.L module is located, with the output of the optical fiber of the AOTFs and the laser output; B) Spectra measured with a spectrometer at the maximum power, with readjustment of the integration time for each wavelength, since there was a difference in saturation between the spectral extreme.

The AOTFs are controlled by a customized program in Matlab that allows changing from one wavelength to another in approximately less than 1s. It also allows customizing the wavelengths to be used by making all of them emit at the same initial power (maximum optimized), but changing the 'amplitude' and 'level' parameters and thus making them being perceived with the same luminance. (Equiluminance test, **Chapter 5**). Once the luminosity of each wavelength is equalized, they can be made to emit simultaneously. Being controlled, the AOTFs open a range of possibilities for illumination stimuli while performing different psychophysical tasks. Any wavelength from 400-700 can be set.

2.2.3. Psychophysical channel: white light illumination

To be able to capture polychromatic images and perform psychophysical tasks in polychromatic light as well as monochromatic light with the SCLS laser, a fiber-optic white light source was incorporated. The polychromatic illumination comes from a fiber optic White Light source (WL, Halogen Fiber Light Source LQ, Output Power 20W-250W, 3000-3400K, Linos, Qioptiq, UK). The power and the spectrum of the source were characterized with a spectrometer (Ocean Optics, USB4000-Fiber Optic Spectrometer, 200-1100nm, USA) before conducting the experiment. The implementation of the WL on the polychromatic multichannel AO visual simulator system follows the same path as the SCLS. In order not to obstruct the common path of the laser, the WL was introduced using a semi-periscope with a single mirror 45º that allows the incident beam to go through the HD to illuminate the DMD with homogeneous light. In **FIGURE 2.9** the implementation of the light source and the experimentally measured spectrum is shown.

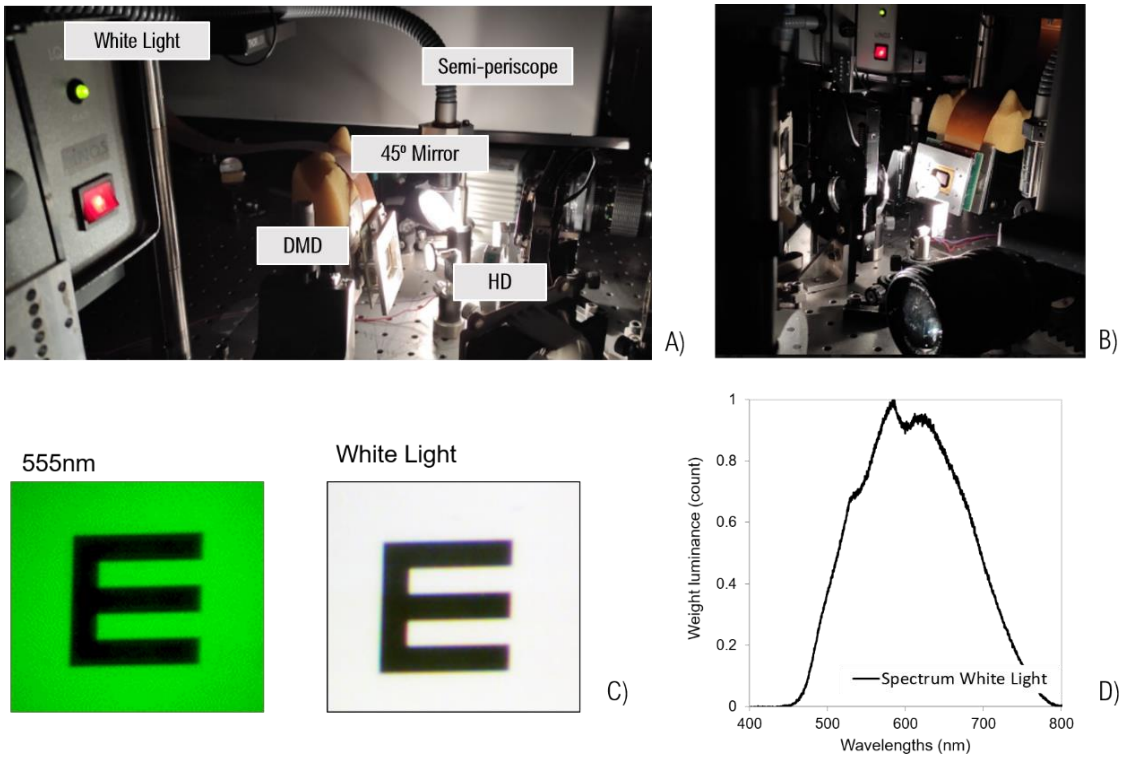

FIGURE 2.9. A) Essential components in the assembly of the WL for the illumination of the DMD (WL source mounted on a semi-periscope, the 45º mirror that sends the light to the HD to illuminate the DMD homogeneously; B) Illumination of the DMD with WL after passing through the HD source ON; C) Image of E-letter stimulus through the system, illuminated with monochromatic light (SCLS,555nm) and WL source and taken with a camera placed like a retina in an artificial eye; D) Normalized spectrum of WL measured with the spectrometer 400-800nm.

2.2.4. Transverse Chromatic Aberration channel

For a specific chapter in the thesis **Chapter 7**, a channel to measure TCA was implemented for the first time. This completes the ability of the polychromatic multichannel AO visual simulator system to measure both chromatic aberrations (LCA & TCA). The channel consists of a photographic slide with two concentric squares in two colors (blue in the background and red in the center) made with the magnification of the system (retinal plane) at Interphoto S.A (Madrid, Spain). The slide acted as a filter to divide both wavelengths into the two differentiated zones (red and blue). The material with which it is manufactured allows total extinction for the wavelength opposite to the color of the illuminated area (red area for 490nm and blue area for 680nm). The slide was mounted in a micrometer x-y-z stage that allows x-y movements to superimpose the slide on the stimulus projected onto the DMD, and z movement to focus it exactly on the conjugated retinal plane. **FIGURE 2.10** shows the x-y-z mount with the slide in a retinal plane, the photographic slide itself, and the illumination part.

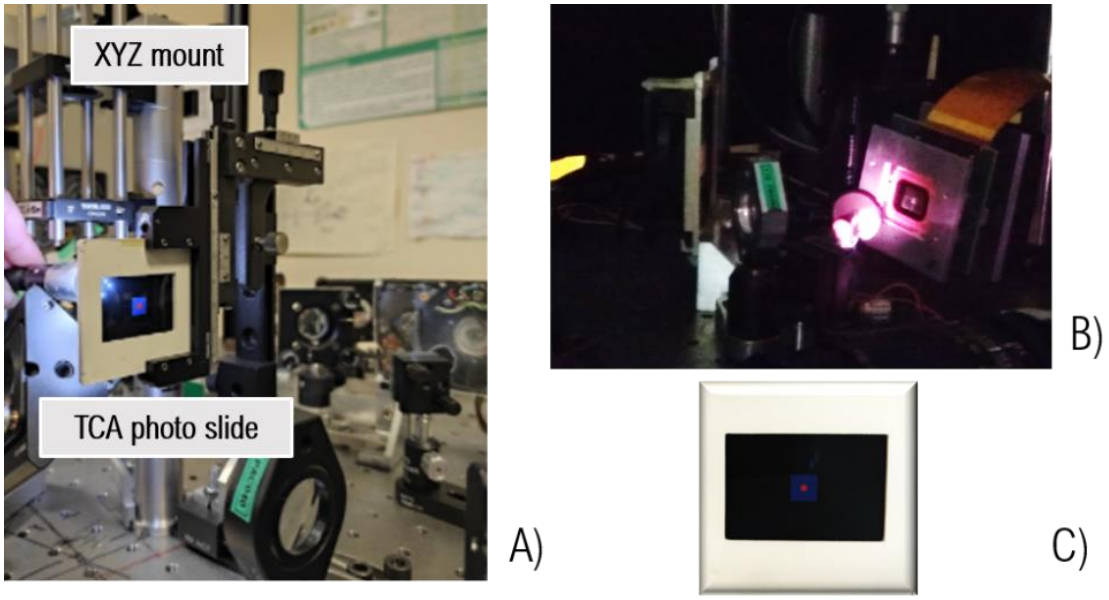

FIGURE 2.10. A) XYZ mount of the photographic slide implemented in the system on a retinal plane; B) Illumination of the DMD simultaneously with two wavelengths of the SCLS (490nm and 680nm); C) Photographics slide with two differentiated extinction zones (center red and peripheric blue).

2.3. EXPERIMENTAL PROCEDURES FOR IN VIVO MEASUREMENTS

This section describes the general protocols followed by the subjects who participated in the studies. A total of 56 subjects participated in the different experiments described in this thesis. The inclusion criteria for the studies were: good general health, no ocular pathology, no previous ocular surgery, required IOL power between 16 and 26D, and habitual soft contact lenses wearers (the last two criteria when the study requires it).

The studies were conducted in young or presbyopes subjects in an age range of 26 to 74 years old. The refractive error ranged from +0.75 D to -6.75 D with less than 1.25 D of astigmatism.

2.3.1. General protocols with human subjects

Ethics Statement

All participants were fully informed and understood the nature and possible consequences of the study and signed informed consent before enrollment in the study. All protocols met the tenets of the Declaration of Helsinki and had been previously approved by the Spanish National Research Council (CSIC) Bioethical Committee.

Refractive error measurements and ophthalmologic evaluation

Before the experiments, the subjects followed an exhaustive optometric evaluation at the School of Optometry Clinic of the University Complutense of Madrid (UCM) which includes sphero-

cylindrical refractive errors and tests for adverse effects to mydriasis. Subjects implanted with IOL received a complete ophthalmologic evaluation before enrollment in the study and surgery at Miranza IOA (Madrid, Spain). Also in the optometry cabinet corresponding to VioBio Lab (Institute of Optics), a measurement of the refractive error was carried out objectively using an autorefractor (AR 597, Humphrey Zeiss Inc., Germany) that allowed an initial adjustment for the measurement of the best subjective approach with the Badal system.

Pharmacological pupil dilation

All the experiments were performed under cycloplegia by instillation of Tropicamide 1%, 2 drops 10 minutes prior to the beginning of the study, and 1 drop every 1 hour. All the subjects had undergone a prior clinical assessment to test for adverse effects of mydriasis.

Alignment of the eye and pupil monitoring

For precise centration and alignment of the subject's eye to the optical system, a dental impression was obtained using nontoxic moldable paste on a mountable metal support. This impression was mounted on an x-y-z stage for the alignment. The eye's pupil was aligned to the optical axis of the system using the line of sight as a reference, while the natural pupil is viewed on the monitor. For fixation, the subjects may be looking at a red LED or at Maltase cross projected on the DMD.

Best subjective focus correction with the Badal System

The subject is asked to adjust the best subjective focus (starting from a myopic defocus automatically induced) by controlling the Badal system with a keyboard while looking at a blurred Maltase cross projected on the DMD, under their natural aberrations. The Badal system is used to correct the defocus of the subject instead of the DM, so as not to waste all the capacity of the DM that is used in correcting HOAs and inducing specific aberrations. The best subjective focus was obtained for the different states of aberrations (AO-correction or natural aberrations) under test. The process of searching for the best subjective focus is repeated several times until the standard deviation between the values is small and the mean of the values is chosen.

2.3.2. Measurements, correction, and inductions of aberrations in the AO systems

Before the measurement, correction, or induction of the aberrations in the subject's eye, the aberrations of the system are corrected by a 'flat mirror' loaded in the DM. After aligning the subject and placing the Badal at the best subjective focus, according to the protocol described above, the aberrations are measured to obtain the natural aberrations of the subject.

A closed-loop correction was then performed and the state of the DM was saved and applied accordingly to the psychophysical experiment. An AO-correction was assumed satisfactory if the residual aberration was below 0.23μm. In most cases, the residual was around 0.19μm. To check that the correction was efficient and stable, we measured the wave aberrations with the new state of the mirror and checked that the residual RMS is low. A stable closed-loop correction was obtained in 15 interactions (2-3 secs, at a rate of 13Hz).

AO-correction and pupil alignment were monitored through psychophysical experiments to ensure that each condition was performed under the desired state of aberration correction. Psychophysical measurements were performed under static corrections. A new close-loop AO-correction was performed if the RMS correction rises from the initial value. The part of inducing aberrations with the DM is done using part of the above protocol. Once the AO-correction close-loop is stable, and the amount of HOAs are very small, the amount of microns you want is added in each of the aberrations (astigmatism, coma, spherical, etc). Once induced, this state of the mirror is saved, which will then be loaded to see if the resulting wavefront reproduces the induced aberrations. The length of the experiment varied according to the specific psychophysical task, from 2 to 6 hours.

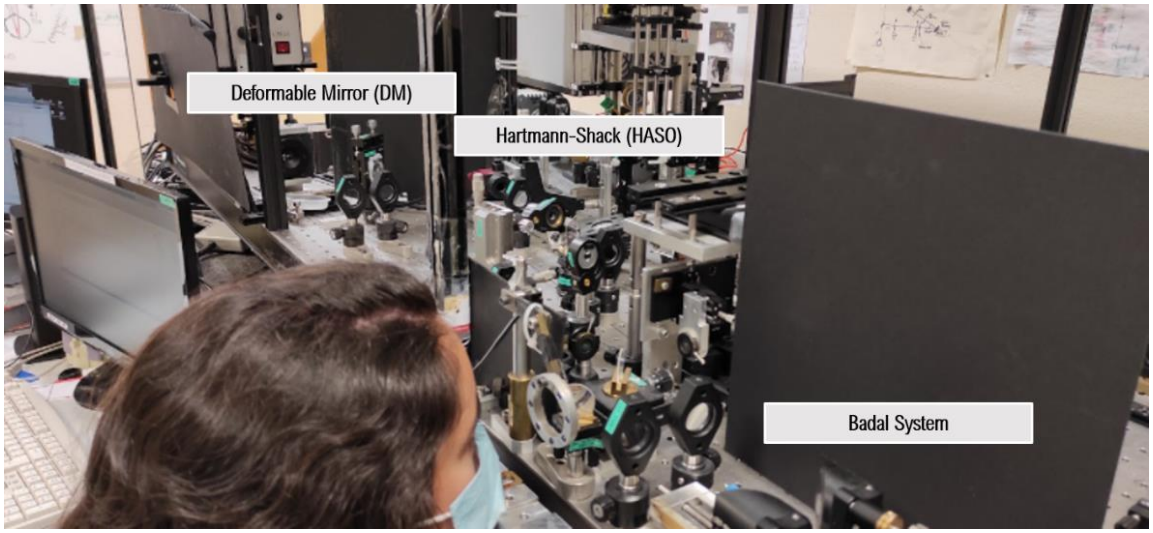

FIGURE 2.11. Polychromatic multichannel AO system and the main component when measuring and/or correcting the eye's aberrations or inducing extra aberrations.

2.3.3. Measurements of retinal images of the human eye

The double-pass retinal aerial image was obtained while the Badal system was moved to vary the vergence of the incident spatially filtered beam, and of the light reflected off the retina. In this way, the optical quality can be objectively obtained from aerial images. The Badal system is moved in a thorough-focus around the best subjective focus. A total of 19 aerial images were acquired for each condition (real or simulated lenses corrections) at steps of 0.25D. All measurements were foveal fixated on auxiliary spot, while the images were acquired. A dedicated interface was programmed in C# to simultaneously allow the control of the retinal camera and motorized Badal system every time that the camera captures an image through a defined range in the Badal. Measurements were obtained for 555nm. Exposure time was 4s. The irradiance at the pupil plane was in all cases lower than the safety limit prescribed by the ANSI [52, 253].

This process was used in **Chapter 4** to measure through-focus optical quality for the subject wearing the real M-CL or through the SimVis-simulated M-CL.

2.3.4. Measurements of chromatic aberrations of the human eye

Longitudinal Chromatic Aberrations

LCA was obtained from Hartmann-Shack and psychophysical measurements in this thesis. The process outlined below was followed for the LCA measures in two chapters of this thesis, **Chapter 7** and **Chapter 8**.

Once the subject is properly aligned, the best subjective focus for far-vision was initially searched with the Maltese cross illuminated at a reference wavelength of 555 nm and set as zero. Natural aberrations were measured with the Hartmann-Shack wavefront sensor and corrected in a closed loop at 880nm (NIR), and selected visible wavelengths. Experiments are performed first under natural aberrations and then under AO correction.

Objective Hartmann-Shack wave aberrations at different wavelengths

Wave aberrations were obtained for each wavelength (visible light and IR light). The defocus term (C_4) for the Zernike polynomial expansion was obtained for each wavelength, transformed to diopters, and reported as the average of at least three repetitions. The objective LCA is calculated as the objective chromatic difference of focus between 450 and 700 nm.

Psychophysical best focus at different wavelengths

Subjects adjusted their best subjective focus using the Badal system while viewing the stimulus illuminated with a series of different wavelengths in visible light (450-700nm). Subjects moved the Badal using the keyboard towards the position where the blurred stimulus appeared sharp for the first time. The best focus setting was repeated several times for each wavelength. The subjective LCA is calculated as the subjective chromatic difference of focus between 450 -700nm.

Transverse Chromatic Aberration

In this thesis, the two-color-two-dimensional Vernier alignment technique [266] was used to measure TCA in **Chapter 7**. The stimulus consisted of two concentric color squares (central red and external blue), with a static black cross in the periphery and an adjustable central cross in the center. The central cross is projected in DMD and illuminated simultaneously with two wavelengths coming from the SCLS. The subject's task is to align the horizontal and vertical black lines in both the blue and the red regions of the stimulus. From the displacement, it calculated the amount of TCA in arc min that the subject perceived.

2.3.5. Measurements of the optical/objective Stiles-Crawford effect in the human eye

The Optical Stiles-Crawford effect (OSCE) was an essential part of **Chapter 7**, to compute perceived TCA from experimental data, and was measured objectively using the LRT. The LRT system, described in section 2.1.3 was used to measure the intensity of the light reflected back from the retina as a function of the entry pupil. An earlier study demonstrated that the intensity of the retinal images (with green light illumination) across the pupil followed a Gaussian distribution,

with a peak that closely matched that obtained from dedicated photoreceptor alignment techniques [132] and the OSCE [267].

A laser beam (543 nm) was scanned across the pupil with the aid of dual galvanometric scanning mirrors. A total of 37 ray entry locations (at 1-mm steps) sampled a 6-mm pupillary region in a hexagonal sampling configuration, using the pupil center as a reference. Subjects fixated on a cross-target placed in a conjugate retinal plane, and the pupil was monitored on a CCD camera in the conjugate pupil plane to guarantee centration. A Badal optometer corrected for the eye's spherical refractive errors. Retinal aerial images of a spot were simultaneously captured using a cooled CCD retinal camera. The power incident on the cornea was 6.9 µW. An LRT measurement lasted approximately 1.5 s. Each measurement consisted of five consecutive runs, with a set of 37 aerial images of the retina for each run. A previous study, and additional control tests in the current study, demonstrated cone photobleaching after the first acquisition [123, 267].

Dedicated routines in Matlab were used to estimate the intensity of the aerial images (within a 20 pixels radius circle around the centroid) and to fit the resulting intensity estimates to Gaussian distributions as a function of pupil entry position, for average intensity data across four consecutive measurements **FIGURE 2.12.** The following function was used to fit the intensity as a function of entry pupil position:

$$I(x,y) = B + I_{max}\, 10^{-\rho[\![(x-x_0)^2+(y-y_0)^2]\!]} \quad \text{Eq.(2.1)}$$

where B is the background intensity, I_{max} is the intensity at the peak, ρ is a shape factor, and x_0 and y_0 are the pupillary coordinates of the peak.

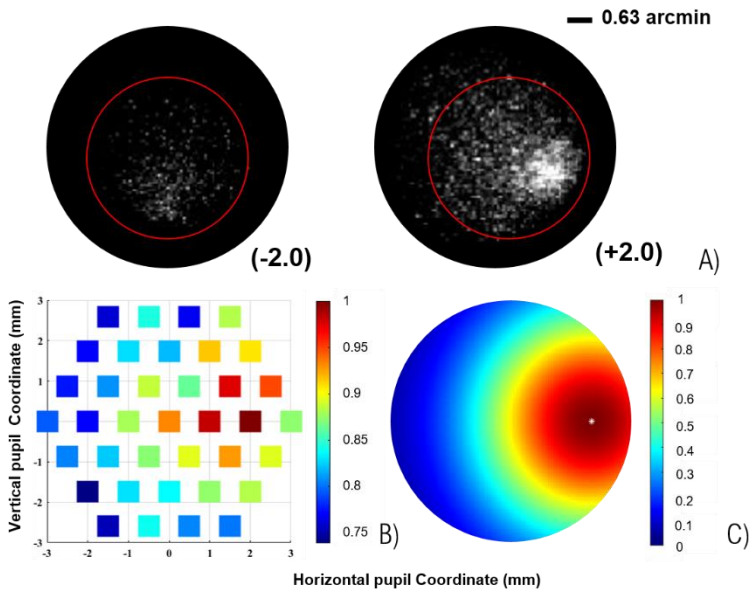

FIGURE 2.12. A) Laser Ray Tracing retinal aerial images at entry position locations (-2,0) and (+2,0) and calculations of the aerial image intensity (integrated within the area marked by the red circle, of 20-pixel radius, centered at the position of the image maximum intensity). B) Arial image intensity as a function of entry pupil position, for an LRT series of 37 images. Each square represents average intensity across four repeated measurements. C) Gaussian fitting of the LRT aerial image intensities (according to Eq.(2.1)). The asterisk marks the coordinates of the Stiless-Crawford peak. Positive horizontal coordinates stand for nasal displacements and vertical coordinates stand for superior displacements from the pupil center.

2.4. PSYCHOPHYSICAL EXPERIMENTS

Psychophysics studies physical stimuli and their interaction with sensory systems. Psychophysical tasks have been extensively used to conclude how information is processed by the visual and other sensory systems [268].

2.4.1. Visual stimuli

Depending on the psychophysical task, different images were used in the experiments, including high contrast Snellen E-letter (VA tests), Siemens star or Maltese cross (best focus), specific cross (TCA measure), and females-males faces (gender identification) (as shown in **FIGURE 2.13**). All the stimuli were presented on the DMD of the polychromatic multichannel AO system except for the faces and Maltese cross which were presented on the CRT monitor (monochromatic AO). In the polychromatic multichannel AO visual simulator, the stimuli subtended 1.62 degrees, while in the monochromatic AO the stimuli subtended 1.98 degrees.

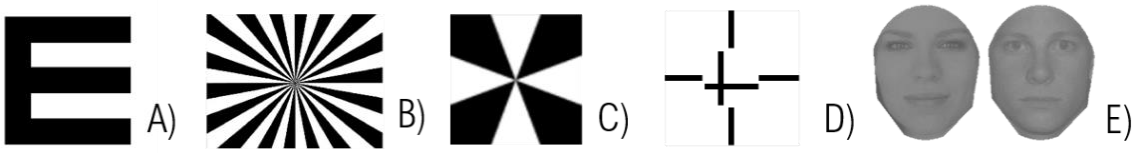

FIGURE 2.13. Example of stimuli used in the experiments of this thesis. A) Snellen E-letter (used in different sizes and orientations); B) Siemens star; C) Maltese Cross; D) TCA stimuli; E) Gender face female/male.

2.4.2. Manipulation of retinal blur

Retinal blur manipulation was performed differently, depending on the study. In the studies presented in **Chapters 3 and 4**, different visual simulators were used, a powerful tool to manipulate the aberration of the eye in the pupil plane non-invasively and in real-time. This allowed the simulation of different optical corrections for presbyopia. In the experiments presented in **Chapters 5 and 6**, we kept the patients' aberrations in a fully AO-corrected condition in the DM and manipulated retinal blur by projecting stimuli blurred by convolution with known aberrations (low and high-order aberrations). AO allows for the cancellation of all subjects' inherent aberrations, exposing observers to identical aberration patterns and assuring that any differences between subjects are due to their own neural processing and past neural adaptation.

Convolved images were generated using standard Fourier Optics [269] programmed in Matlab. The PSF was computed from natural aberrations, previously measured with Hartmann-Shack of each subject that participated in the studies. The scale of PSFs was calculated to match the pixel/angular scale of the original object, according to the viewing conditions, size of the stimulus, and magnification of each system (both AO systems in VioBio Lab). The Stiles-Crawford effect was not taken into account [127], but its effect (constant p of 0.1mm^{-2}) was simulated and found negligible for the purpose of our study. Double diffraction when viewing the convolved image through a diffraction-limited (convolution + artificial eye) was measured on-bench, and considered negligible. All computations were performed for constant pupil size and for optimal focus, estimated as the defocus term that optimized a Visual Strehl (VS) [259].

In **Chapter 5** and **Chapter 6**, the DM was also used to induce aberrations of the subjects, to compare optical blur and convolved blur.

In the experiment presented in **Chapter 7**, natural aberrations of the subjects were AO corrected with the DM, while the retinal blur was manipulated by projecting a chromatic stimulus (red/ blue TCA cross).

2.4.3. Psychophysical techniques used under Adaptive Optic controlled aberrations

For the quantification and evaluation of vision (visual performance or neural adaptation) different psychophysical experiments have been used throughout this thesis. The subject's responses were recorded (using a keyboard in all the cases) and analyzed in different ways according to the different psychophysical paradigms (specific details can be found in the corresponding chapter).

Visual Acuity

VA was measured using a four or eight Alternative Forced Choice procedure (4AFC- 4 orientations: up, down, left, right; 8AFC- 8 orientations the same as before plus the oblique positions) depending on the age of participants. The stimulus was a high contrast tumbling Snellen E-letter displayed on the DMD or CRT monitor. Subjects were asked to identify the orientation of the E-letter, whose size and orientation change with each trial. Each run consisted of 40 trials presented for 0.5 seconds. A QUEST (QUick Estimate by Sequential Testing) algorithm was programmed in Matlab with Psychtoolbox [255, 270, 271] to select the size of each stimulus and optimize the estimation of the spatial resolution threshold, following the subject's response. The threshold criterion was set to 75%. The threshold, VA measurement, was estimated as the average of the 10 last values. The measurements were discarded if convergence was not reached. VA was expressed in terms of decimal or LogMAR VA (logMAR = -log10|decimal acuity). More detail and specifications on **Chapters 3, 4, and 5.**

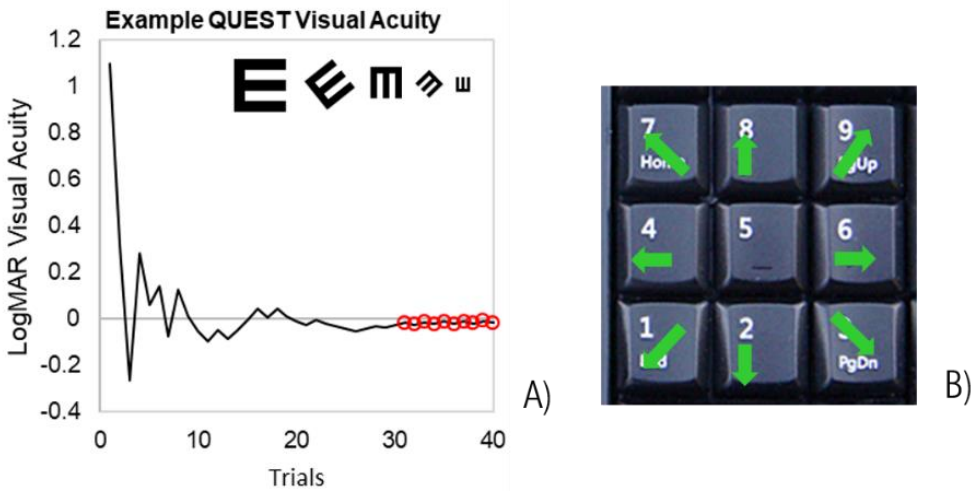

FIGURE 2.14. A) Example of VA QUEST, 40 trials convergence; B) Keyboard directions to indicate the different stimulus orientations (up-down (8,2), left-right (4-6), oblique (1,3,7 &9)).

Vernier alignment

The ability to detect the misalignment of two objects (for example two points, or two lines) is described by Vernier acuity [81]. Vernier acuity is used for the measurement of TCA. From the displacement of two black bars (two directions or one direction) on a red and blue background, the magnitude of perceived TCA in the fovea can be calculated. More detail and specifications on **Chapter 7**.

Gender identification

The gender face identification tasks consist of the presentation of faces (females and males faces without any distinctive gender data such as hair, beard, or mustache) presented randomly with convolved images for different manipulated aberrations under AO-correction of subject's aberrations. A rating scale experiment was used in which the subject provided a graded response from 1 to 3 (female) or 4 to 6 (male) according to their level of confidence in recognizing the gender face (1 and 4 for definitely sure, 2 and 5 for probably sure, 3 and 6 for a lower level of confidence on the face being female/males). Each image was presented during 0.5s, in blocks of 100 images (set of 200 females vs 200 males randomly). A fixation point stimulus was shown between faces. Percentage of correct and incorrect answers were computed to analyze the data for each block. More detail and specifications on **Chapter 6**.

Subjective Best Focus at different wavelengths

The best-perceived focus was obtained using the Badal system while looking at a specific blurred stimulus illuminated with a series of wavelengths in visible light. The subject moves the Badal until the stimulus looks sharp. The search for the sharpest image is repeated several times to have average measurements and a small standard deviation. More detail and specifications on **Chapter 8,**

2.5. OPTICAL QUALITY ANALYSIS

2.5.1. Optical quality metrics

From the wave aberration measurements using the Hartmann-Shack wavefront sensor, we can calculate the image of a point on the retina (PSF), MTF and OTF, are some of the metrics used to evaluate the optical quality of a retinal image, described in more detail in **Chapter 1** section 1.3. These measurements allow us to evaluate the optical quality of the subject's retinal image and compare it to the subject's perceptual perception.

The human eye is a low pass filter. This means that the reduction, in contrast, is greater for high spatial frequencies (fine details in the image). To describe the quality of an optical system, the Strehl ratio (SR) is usually used, a metric that represents the maximum of the image of a point on the retina of the aberrated optical system in relation to the maximum of the PSF of a system without aberrations.

If we weigh the SR with NCSF, as a result, we have Visual Strehl (VS), a metric that describes the optical quality of the subject eye, used in **Chapter 5** and **Chapter 6**. The NCSF is the neural contrast sensitivity function of the visual system ignoring optical factors and has been defined as the observer's contrast sensitivity function (CSF) divided by the MTF of their eye [259, 272, 273].

$$VS = \frac{\iint_{-\infty}^{\infty} NCSF_{(f_x,f_y)} \cdot OTF_{(f_x,f_y)}\ df_x\ df_y}{\iint_{-\infty}^{\infty} NCSF_{(f_x,f_y)} \cdot OTF_{DL_{(f_x,f_y)}}\ df_x\ df_y}$$

where *NCSF* is *N*eural *C*ontrast *S*ensitivity *F*unction, *OTF* the *O*ptical *T*ransfer *F*unction of an aberrated eye, OTF_{DL} the *OTF* of a diffraction limit (DL) eye, and (f_x,f_y) the spatial frequency coordinates.

In Marsack et al. [274] study, the VS metric has been shown to account for 81% of the variance in high-contrast logMAR VA, making this metric a strong predictor of visual performance in normal eyes.

2.5.2. Double-pass optical quality metric

As mentioned in previous sections on this thesis (section 1.3.4), the DP techniques offer an objective evaluation of the overall quality of the eye (ocular aberration and intraocular scattering). In **Chapter 4**, DP images were taken in real subjects and on-bench, in different conditions detailed in the corresponding chapter. The analysis of the images was performed using the maximum intensity of the DP aerial image normalized by the total intensity of the reference image (no lens, to avoid the effect of intensity fluctuations during measurements) at best focus. For that, a routine was created in Matlab that allowed the calculation of the average-maximum energy in a circle of 5 pixels around the maximum in a series of images taken with the same parameters (laser power, pupil diameter, exposure time). In this way, it was possible to obtain through focus curves of double-pass images **FIGURE 2.15.**

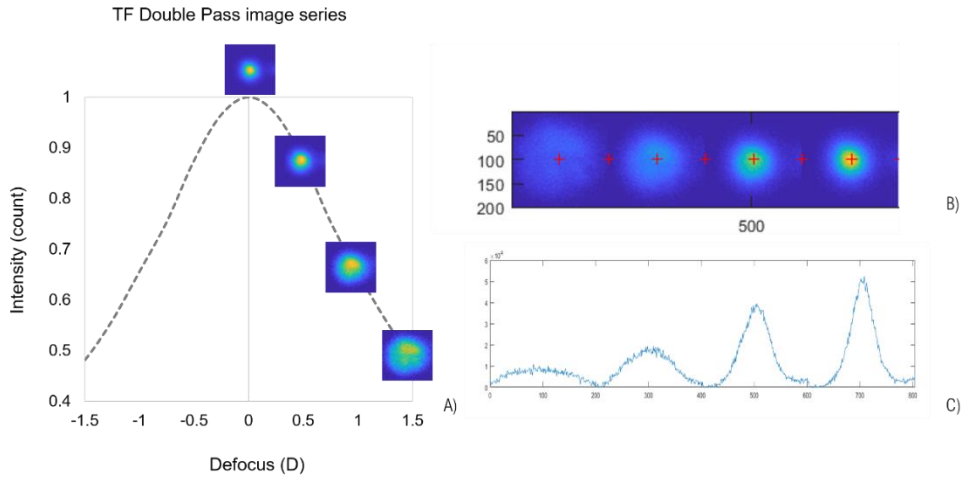

FIGURE 2.15. TF optical quality. A) TF DP of image maximum intensity, normalized to the intensity of the best focus no-lens image series (side images in each focus) of a 250μm point extended source; B) Series of pseudo-colored DP images where the point of maximum intensity (+) is indicated, and from there, an average of the adjacent pixels for the calculation of the intensity; C) Average intensity radial profile for each of the images in B).

2.5.3. Correlation metric

For the comparison of the quality of a series of images, in this thesis, the metric of 2D-correlation has been used [187]. After taking a series of images (1 pass-images, 1P), each one is correlated with a reference image. The stimulus used in all cases was a Snellen E-letter (**Chapter 4 and 5**). The image quality metric for the E-letter was obtained from the correlation coefficient (correlation of the E-letter with a reference monofocal correction and each collected image in the same conditions: laser power, pupil diameter, exposure time) of the image series after each image was centered.

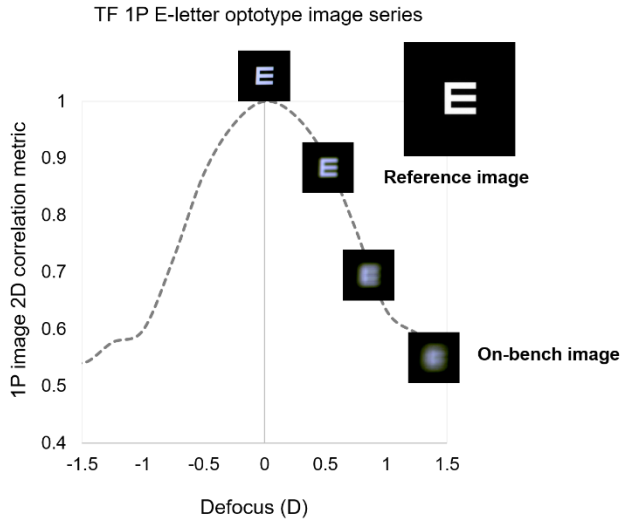

FIGURE 2.16. TF optical quality. TF image correlation metric (1P) of an E-optotype (side images in each focus), for a monofocal lens and the reference image.

3

CHAPTER 3. PRE-OPERATIVE SIMULATION OF POST-OPERATIVE MULTIFOCAL VISION

While multifocal intraocular lenses (M-IOLs) are increasingly implanted to correct for presbyopia, how one sees with a multifocal correction is hard to explain and imagine. This chapter presents a study to evaluate the quality of various visual simulating technologies by comparing vision with simulated M-IOLs pre-operatively and the implanted M-IOLs post-operatively in the same patients. This chapter is based on the paper by Vinas et al. [275], "Pre-operative simulation of post-operative multifocal vision' published in Biomed. Opt. Express (2019). The co-authors are **Sara Aissati**, Mercedes Romero, Clara Benedi-Garcia, Nuria Garzon, Francisco Poyales, Carlos Dorronsoro, and Susana Marcos.

This study was also described in the reviews papers by Marcos et al. [276], 'VioBio lab AO: technology and applications by women vision scientists' published in OPO (2019) and 'Simulating Outcomes of Cataract Surgery: Important Advances in Ophthalmology', published in Annu Rev Biomed Eng (2021) [277]. And also by Vinas [278] with the title 'From Astronomy to the clinic: Adaptive Optics based visual simulators' published in Europhysics News (2020).

Regarding contributions to conferences, this study was presented at XI Workshop on Adaptive Optics for Industry and Medicine with the title 'Visual simulation of multifocal lenses in patients before and after implantation of diffractive trifocal lenses' by **Aissati et al**.[279] presented as an oral contribution. This study was also presented as a poster contribution at the ARVO annual meeting in 2018 by Vinas et al.[280] under the title "Comparison of multifocal visual simulations in patients before and after implantation of diffractive trifocal lenses".

The author of this thesis implemented the experimental procedure in collaboration with Maria Vinas and Mercedes Romero, performed the experimental measurements on subjects, collected and analyzed the data in collaboration with Mercedes Romero and Maria Vinas, and revised the manuscript in collaboration with Maria Vinas and Susana Marcos with the rest of the co-authors.

3.1. INTRODUCTION

Multifocal corrections work under the principle of simultaneous vision, projecting simultaneously focused and defocused images on the retina, providing multifocality at the expense of reducing optical quality at all distances [153]. Visual simulators are proposed to provide patients the visual experience of a multifocal correction before this is applied to the eye (either in the form of intraocular lens, IOL, or contact lens, CL). However, to our knowledge, their capability to replicate real clinical corrections in real individual patients has not been fully demonstrated.

Visual simulators based on AO have allowed probing the visual system under manipulated optics [112, 218, 281, 282]. They are particularly attractive to test vision in patients with new optical designs [218, 249, 283] prior to delivering surgical corrections to the patient or even manufacturing the lenses. Simulations of new corrections with AO primarily serve to investigate interactions between the patient's optics and a given correction, to investigate differences across corrections, and eventually to select the correction that optimizes perceived visual quality and performance in patients [218, 249, 284].

In AO-based visual simulators, an active optical element (DM, SLM or TL) reproduces the equivalent phase map of a certain optical design in a plane conjugate to the subject's pupil plane, while the observer is looking at a visual stimulus. DM allows inducing aberrations [241, 247], or simulating smooth optical designs [285, 286] while controlling the aberrations of the subject [287]. On the other hand, SLMs [218, 283, 288, 289], generally LCoS-SLMs devices, are capable of reproducing abrupt phase maps due to their high spatial resolution, and to increase the effective phase range through the use of wrapped phase representations [214, 290]. Previous work has evaluated perceived visual quality at various distances with presbyopic corrections simulated in AO systems: multifocal angular and radially segmented corrections [218, 249], corneal inlays [291], or diffractive optics [237, 292]. A different approach is to place the real IOL in a cuvette in a conjugate pupil plane projected in the eye, although in this case, simulations are limited by the static nature of this approach [293]. To date most visual simulations have been limited to experimental environments [187, 294], given the relatively high complexity and large footprint of the simulators, although some have made their way into commercial products [283, 290, 295]. In these on-bench or desktop-based devices [235] the visual experience is limited to stimuli projected in a mini-display subtending a relatively small visual field, in many cases monocularly.

In order to increase the accessibility of visual simulations in the clinic, we use SimVis technology [220, 284] for simultaneous vision simulation, using TL working in a temporal multiplexing mode, i,e, scanning multiple foci to provide superimposed images on the retina, all of them with the same position and magnification, but corresponding to different planes in focus. The simulation of multifocal corrections relies on evaluating the TF energy distribution of the correction, from the knowledge of the spatially varying pupillary power distribution, and programming in the TL the corresponding time-varying focus changes. The simulated multifocal correction is tuned to match the TF optical quality (in terms of Visual Strehl) [274] of real existing multifocal lenses [220].

In a previous study [187], we compared TF optical and visual quality produced by real M-IOLs in a cuvette projected on the subject's eye with those same designs simulated with SimVis technology and with an SLM, incorporated in a polychromatic multichannel AO visual simulator 3- active-optical-elements, and we found good correspondence between performance of the real and simulated M-IOLs. The SimVis Gekko™ was developed for the pre-surgical simulation of presbyopic corrections based on the SimVis principle. This new device is binocular, see-through, allows a direct view of the real world, and has a larger visual field.

The current study evaluates visual simulation of M-IOLs using 2 different simulation technologies (SLM and SimVis technology) in patients before and after implantation of commercial diffractive trifocal lenses using two simulation platforms, an AO-based visual simulator and the clinical visual simulator, SimVis Gekko™ .

3.2. METHODS

TF VA was measured in eight subjects, five with clear crystalline lens and 3 with some degree of cataract, pre-operatively through simulated M-IOLs, using 2 different visual simulators, and post-operatively, after bilateral implantation of the same M-IOL.

3.2.1. Multifocal IOL

The simulated and later implanted lens was a trifocal diffractive IOL, the FineVision POD F (PhysIOL, Liège, Belgium), a hydrophilic (26% hydrophilic acrylic) aspheric multifocal diffractive IOL built with a combination of two bifocal diffractive patterns, one for far and near-vision and the other for far and intermediate-vision [182, 296]. The combination of the two diffractive structures provides 3 useful focal distances: 0.0 D for far-vision, +1.75 D addition for intermediate-vision and + 3.50 D addition for near-vision [187, 297].

3.2.2. Patients and surgery

The study was conducted on eight presbyopic patients (mean age: 60.4±7.7 years; range: 53 to 74 years): five of them with clear lens and three with different cataract grades. Measurements were performed pre-operatively (5 days before IOL implantation, on average) and post-operatively (30 days after IOL implantation, on average). All participants were acquainted with the nature and possible consequences of the study and provided written informed consent. All protocols met the tenets of the Declaration of Helsinki and had been previously approved by the Spanish National Research Council (CSIC) Bioethical Committee.

Patients received a complete ophthalmic evaluation prior to enrollment in the study and surgery at IOA Madrid Innova Ocular (Madrid, Spain). **TABLE 3.1** summarizes all pre- and post-operative data of the patients, indicating the instrumentation used for each measurement. The participating patients had already been scheduled for implantation of a trifocal diffractive IOL and their inclusion in the study did not affect any surgical parameter. The inclusion criteria for the study were: good general health, no ocular pathology, no previous ocular surgery, required IOL power between 16 and 26 D, and corneal astigmatism less than 1.25 D. Patients with diplopia (double vision) were excluded from the experiment. Patients were bilaterally implanted with the trifocal diffractive IOL, with a time difference of less than 7 days between surgeries in each eye. The required IOL power was computed with Barrett II Universal formula. The target refraction was emmetropia. Natural pupil of the subjects was in all cases higher than 4 mm.

All surgical procedures were performed by the same experienced surgeon (FP) under topical anesthesia and aided by a computer-assisted cataract surgery system (CALLISTO eye, Zeiss Cataract Suite Markerless; Carl Zeiss, Jena, Germany). IOLs were implanted through a 2.2-mm self-sealing clear corneal incision at 180 degrees (temporal) in right eyes and at 90 degrees (superior) in left eyes and about 1 mm anterior to the limbus. A femtosecond laser (CATALYS Precision Laser System, Abbott Medical Optics Inc., Santa Ana, CA, USA) was used to perform

the anterior capsulotomy (5-mm diameter) as well as lens fragmentation. The selected IOL was then implanted in the capsular bag with a single-use injection system (Accujet, Medicel, Thal, Switzerland). A capsular tension ring (CTR) was inserted in all eyes, followed by ophthalmic viscoelastic traces removal.

3.2.3. Visual simulation platforms

Two visual simulation platforms were used to perform the measurements before and after implantation of the M-IOLs: ***(1)*** a polychromatic multichannel AO-based visual simulator, which incorporates an SLM and a SimVis based on temporal multiplexing of a TL and ***(2)*** a SimVis Gekko™ visual simulator (described in section 2.1.4), **FIGURE 3.1**.

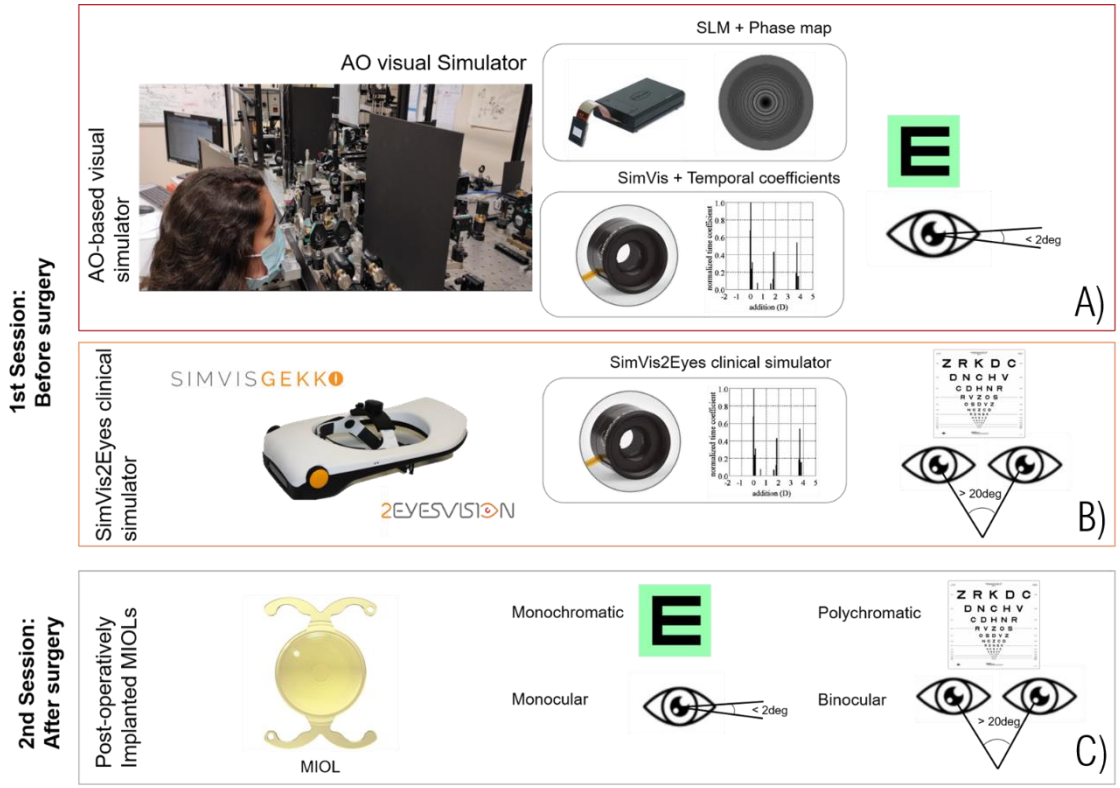

FIGURE 3.1. Visual simulation platforms. A) AO-based visual simulator incorporating the SLM and SimVis in the corresponding conjugate pupil planes of the AO system. M-IOL was simulated using a phase map and time coefficients for the SLM and SimVis, respectively. Measurements were performed monocularly at 555 nm; B) SimVis Gekko™, using time coefficients, working binocularly and with the stimulus in white light; C) M-IOL implanted in the eight patients. Post-operatively, measurements were performed monocularly (using a monochromatically illuminated green target projected in a DLP projector subtending a 1.62-deg field in an AO system) and binocularly in white light (ETDRS target at distance, subtending a 20 deg field).

Visual Simulation Platform 1: AO-based visual simulator

Visual tests were performed in the custom-developed polychromatic multichannel AO visual simulator system (**FIGURE 3.1** A), left) at the VioBio Lab, described in detail in section 2.1.2 of this thesis. In the current study, the visual stimulus in the AO system is seen through different active optical elements in 3 separate channels: ***(1)*** a reflective DM, used in this study to correct the system aberrations; ***(2)*** a reflective LCoS-SLM, and ***(3)*** a SimVis, both used to simulate the multifocal

designs. The M-IOL design was mapped in the SLM (as a spatial phase map) and on the SimVis (as a temporal profile) [187], as shown in **FIGURE 3.1** A).

SLM The diffractive multifocal component of the trifocal diffractive IOL was mapped onto a reflective phase-only LCoS-SLM, while the refractive component was adjusted with the Badal Optometer. The procedure to generate a multifocal phase map has been described in previous publications. In particular, the trifocal diffractive IOL was obtained, tested and validated in a prior work from our group [187].

In brief, the multifocal phase maps of the trifocal diffractive IOL was extracted in pseudophakic computer eye models from the knowledge of the surface height profiles of the lenses, provided by the manufacturer, as described in a previous publication [298]. The SLM addressable phase map was first evaluated from the multifocal phase map and later 2π-wrapped, so that the generated phase pattern was a grey-scale image, where each level of grey corresponds to a certain phase difference in the interval (0 2π). Phase-maps (**FIGURE 3.1** A)) were programmed for 4-mm pupil diameters and 555 nm wavelength.

SimVis The diffractive multifocal component of the trifocal diffractive IOL was also mapped onto the Simultaneous Vision Simulator (SimVis) [220, 284].

The simulated multifocal correction is tuned to match the TF optical quality (in terms of VS [259]) of real multifocal lenses. It is an iterative optimization of the electrical input signal driving the lens and, consequently, of the SimVis TF optical quality [220]. In particular, the temporal profile [298] that describes the trifocal diffractive IOL was obtained, tested, and validated in previous work [187]. The tunable lens of the SimVis was placed in an additional conjugate pupil plane. The time coefficients of the input signal were calculated for 4-mm pupil diameters and 555 nm wavelength (**FIGURE 3.2** A), bottom).

Visual Simulation Platform 2: SimVis Gekko clinical visual simulator

In this study, we also used the SimVis technology in a second simulation clinical platform (SimVis Gekko™ , **FIGURE 3.1** (B), left)), described in detail in section 2.1.4 of this thesis. The device has a wireless operation and allows observation of the real world with a multifocal correction. Both SimVis (Platform 1) and SimVis Gekko™ (Platform 2) use the same temporal multiplexing technology, and the same time coefficients to simulate the multifocal lens. However, the measurements in Platform 2 are binocular and are performed with white light with a clinical optotype (see section Visual tests & experimental protocol).

TABLE 3.1. Pre- and post-operative clinical data of the patients of the study. M/ F stand for male/female, respectively; age in years; R and L stand for measured right eye/left eye; [1]refractive error: Sph, spherical error; Cyl (Diopters), cylinder (Diopters); Axis(degrees); [2]BCVA, Best Corrected Visual Acuity and UCVA, Uncorrected Visual Acuity, measured under photopic lighting conditions with ETDRS (Early Treatment Diabetic Retinopathy Study, ETDRS; Precision Vision, Woodstock, IL, USA) chart; [3]Cataract grade (according to BCN 10 grading system, using frontal and cross-sectional slit-lamp lens images, ranging from N0 (clear lens) to N10 (dark lens); Prelex stands for Presbyopia Lens Exchange (clear lens). Shading indicates measured eye for each patient.

Pre-operative data

Subject/ Sex	Age	Eye	Sph[1]	Cyl[1]	Axis[1]	BCVA[1]	Cataract[3] grade	Days before surgery
S#1/F	70	RE	3.25	-	-	0.70	N3	4
		LE	3.75	-	-	0.90	N3	
S#2/M	60	**RE**	2.00	-	-	1.00	N1 + Subcaps post	3
		LE	2.25	-	-	0.80	N1 + Subcaps post	10
S#3/F	57	**RE**	0.75	-0.50	10	1.00	Prelex	3
		LE	1.00	-0.50	145	1.00	Prelex	
S#4/M	53	**RE**	2.50	-0.50	30	1.00	Prelex	6
		LE	2.50	-0.50	20	1.00	Prelex	
S#5/F	54	RE	1.00	-0.50	165	1.00	Prelex	3
		LE	0.75	-	-	1.00	Prelex	
S#6/M	74	**RE**	1.75	-	-	1.00	N4	1
		LE	1.75	-0.50	80	1.00	N3	
S#7/F	55	**RE**	1.50	-0.50	80	1.00	Prelex	5
		LE	2.75	-0.50	80	1.00	Prelex	4
S#8/F	60	RE	1.00	-0.50	140	1.00	Prelex	7
		LE	0.50	-	-	1.00	Prelex	2

Post-operative data

Subject/ Sex	Age	Eye	IOL power (D)	Sph[1]	Cyl[1]	Axis[1]	UCVA[1]	BCVA[1]	Days after surgery
S#1/F	70	RE	25.5	-0.25	-	-	0.95	1.00	24
		LE	26	-	-	-	0.76	0.76	
S#2/M	60	**RE**	22.5	-	-0.50	120	0.76	0.95	10
		LE	22.5	-	-0.50	65	0.72	1.00	3
S#3/F	57	**RE**	22	-	-	-	1.00	1.00	7
		LE	22.5	-	-	-	1.00	1.00	
S#4/M	53	**RE**	23.5	1.00	-0.75	170	0.72	1.00	7
		LE	23.5	0.50	-	-	0.80	1.00	
S#5/F	54	RE	24.5	-	-	-	0.95	0.95	13
		LE	24.5	-	-	-	0.95	0.95	
S#6/M	74	**RE**	21.5	-	-	-	1.00	1.00	8
		LE	21	-	-	-	1.00	1.00	
S#7/F	55	**RE**	23	-0.25	-0.50	105	0.80	1.00	6
		LE	25	-	-	-	1.00	1.00	8
S#8/F	60	RE	21	-	-	-	1.00	1.00	10
		LE	21.5	-	-	-	1.00	1.00	15

3.2.4. Visual test & experimental protocol

Through-focus Visual Acuity in the AO-based visual simulator

For the visual simulator Platform 1 (AO system), TF VA was measured using a 4AFC [299] procedure with Tumbling E-letters and a QUEST (Quick Estimation by Sequential Testing) algorithm programmed using Psychtoolbox [300]. The stimulus was projected in the Digital Micro-Mirror Device (DMD), illuminated monochromatically at 555 nm (>20 cd/m^2 with both, SLM and SimVis, measured at the retinal plane of the system). The QUEST routine for each VA measurement consisted of 40 trials, each one presented for 0.5 seconds, where the threshold criterion was set to 75%. The threshold (VA) was estimated from the average of the 10 last E-letter stimulus size values. VA was expressed in terms of decimal acuity (logMAR = -log$_{10}$|decimal acuity|) [301].

Measurements were performed monocularly, in a darkened room. Patients were stabilized using a dental impression and the eye's pupil was aligned to the optical axis of the instrument (using an x-y-z stage moving a bite bar) using the line of sight as a reference, while the natural pupil is monitored using a pupil camera. To ensure constant pupil diameter during the measurements, a 4-mm artificial pupil was placed in a conjugate pupil plane.

The patients were instructed on the nature of the experiment and performed some trial runs prior to the test. They were asked to adjust the Badal system position to achieve the best subjective focus. Through-focus measurements were obtained changing vergences with the Badal optometer ranging from -1.00 to + 4.00 D. TF VA was measured in the AO system pre-operatively monocularly, in one eye, (Session 1, with the M-IOL simulated either with the SLM or the SimVis -in a random order-) and post-operatively (without any simulator element) monocularly in the same eye.

Through-focus Visual Acuity in the SimVis Gekko clinical visual simulator

For the visual simulator Platform 2 (SimVis Gekko™ SimVis2Eyes, the binocular wearable device), VA was measured binocularly using a standard high contrast ETDRS clinical optotype in photopic lighting conditions (~85 cd/m^2), at best focus at different TF positions using trial lenses in dedicated slots in the simulator, from -1.00 to +4.00 D, in 0.25 D step. VA was obtained from the size of the smallest letter that the patient could discriminate in each condition. Measurements were performed with the optotype at a distance of 4 m, while the patient was wearing the head-mounted SimVis Gekko™ visual simulator. Proper alignment, as well as the correct interpupillary distance, was ensured by illumination with two lateral built-in LEDs sources in the device which are turned on wirelessly during adjustment. Patients were instructed to look at the stimuli with both eyes open, to move their head instead of moving their eyes, and to look through the central part of the optics of the system. Pre-operative measurements were performed with the trifocal diffractive IOL simulated for both eyes in the SimVis Gekko™ clinical device. Post-operative measurements were performed with the IOL implanted in the patient, and the SimVis Gekko™ correcting for the refractive error with a programmed monofocal correction.

3.2.5. Data analysis

TF VA curves were obtained pre-operatively with the simulated M-IOLs (in both tested platforms) and post-operatively with the implanted M-IOLs. The comparison between simulators and pre/post-operatively was expressed in terms of RMS difference of the linearly interpolated TF curves (in a 5.00 D range). RMS of the post-pre difference TF VA curves was taken as a metric for the quality of the prediction of the post-operative visual performance by the pre-operative visual simulators.

The similarity in the shape of the TF curves was done using a cross-correlation analysis, with lag k and rho values representing the largest spike of the series when the elements of both TFcurves match exactly and the correlation coefficient, respectively. Differences between results with the different simulators, and before and after surgery were statistically analyzed using paired-samples t-test. Statistical analysis was performed using (IBM SPSS Statistics 25 software, SPSS Inc., USA).

3.3. RESULTS

3.3.1. Predicted through-focus visual performance with simulated M-IOLs: a comparison across visual simulators

FIGURE 3.2 shows the TF VA for all 8 subjects pre-operatively, with the simulated trifocal diffractive IOL using the SLM (**FIGURE 3.2** A), pink), and the SimVis (**FIGURE 3.2** A), green), both in the AO system platform, as well as using the SimVis Gekko™ (**FIGURE 3.2** B), orange) and SimVis (**FIGURE 3.2** B), green). Black symbols represent VA (best focus for far) for a monofocal condition pre-operatively. In general, except for S#4, there is a high similarity between the TF VA curves measured with each simulator. Blue bars in each graph represent the VA difference (SLM – SimVis, **FIGURE 3.2** A); SimVis Gekko™ – SimVis, **FIGURE 3.2** B)) at each focus position.

On average, TF VA across subjects pre-operatively showed similar trends with the simulated trifocal diffractive IOL using the SLM (**FIGURE 3.3** A), pink), and the SimVis (**FIGURE 3.3** A), green), both in the AO system platform, as well as using the SimVis Gekko™ (**FIGURE 3.3** B), orange), as shown in **FIGURE 3.3**. The average RMS difference between the TF VA with the lenses simulated with SLM and the SimVis (measured monocularly and in monochromatic light) was 0.05±0.01, and the average RMS difference between TF VA with the lenses simulated in SimVis and SimVis Gekko™ (measured monocularly and in monochromatic light and binocularly and in white light) was 0.05±0.01. There is not a particular trend for the magnitude of the deviation as a function of the defocus position (near, intermediate or far) or for a particular simulator providing higher VAs than the other. The cross-correlations between the TF VA curves obtained using the SimVis and the SLM and between the TF VA curves using SimVis Gekko™ were statistically high (lag k = 0, rho = 0.889 and lag k = 0, rho = 0.955, respectively).

3.3.2. TF VA with simulated M-IOLs pre-operatively and implanted M-IOLs post-operatively

FIGURE 3.4 shows the comparison between the TF VA obtained through the visual simulations with the SimVis, with the AO-based platform (**FIGURE 3.4** A)) or the SimVis Gekko™ (**FIGURE 3.4** B)) pre-operatively (natural lens, solid lines), and post-operatively (M-IOLs, dashed lines). Blue bars in each graph represent the VA difference (pre- and post-operatively).

In general, there is a good correspondence between the TF VA curves measured pre-operatively (simulated M-IOL) and post-operatively (implanted M-IOL), in both platforms (AO and SimVis

Gekko™) for all subjects except for subject S#4. RMS difference is lower in patients with clear lens (0.06± 0.01 both for SimVis and for SimVis Gekko™), and higher in subjects with some degree of cataracts (S#1 catn3; S#6 catn4; S#2 catn + subcaps. posterior): 0.08±0.01 for SimVis and 0.09±0.01 for SimVis Gekko™). The patient with more severe degree of cataract, S#2, showed the higher RMS difference between pre- and post-surgery TF VA curves (0.39, and 0.44, with SimVis and SimVis Gekko™ , respectively).

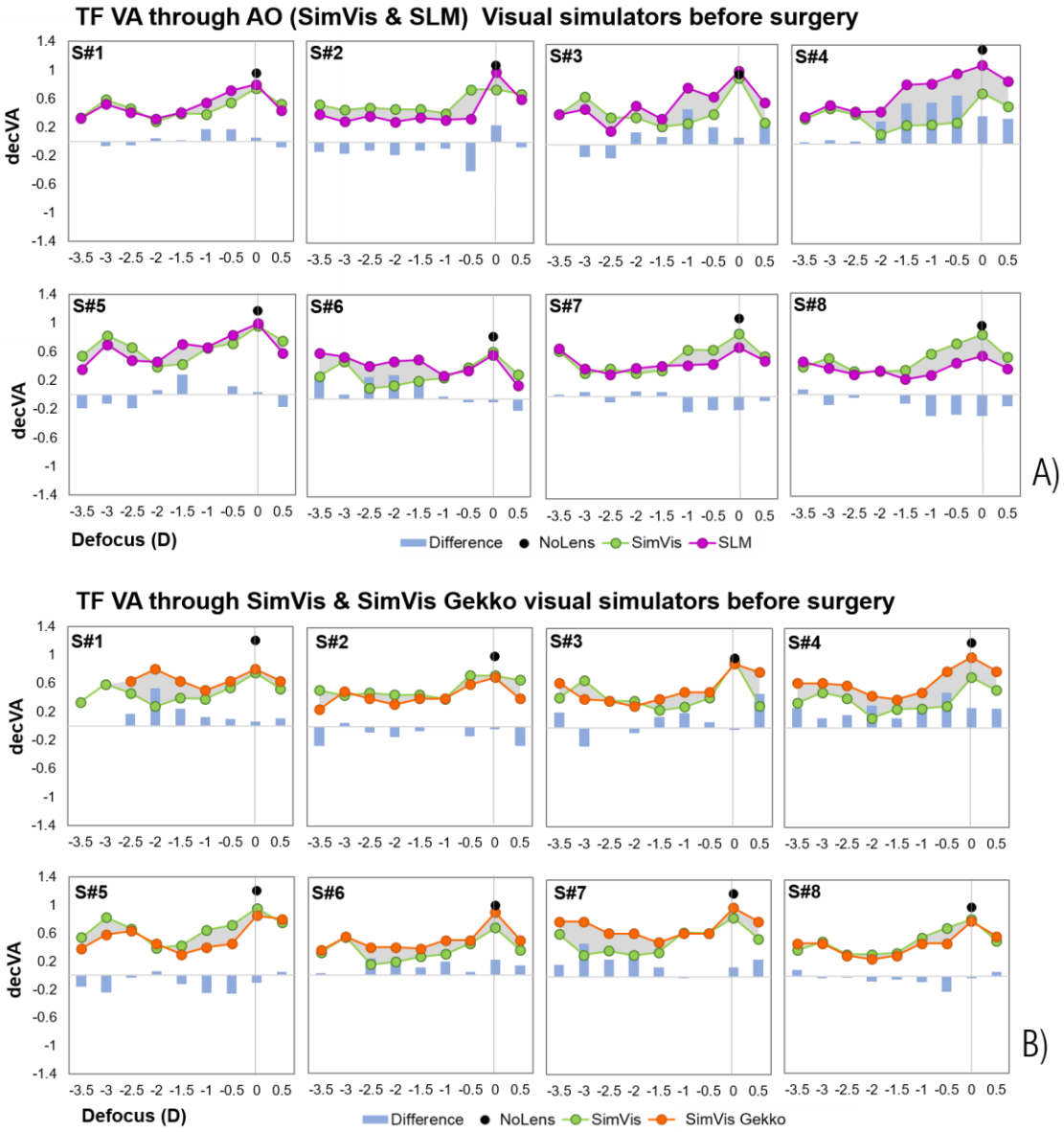

FIGURE 3.2. TF VA obtained through simulations before surgery. A) TF VA through AO_visual simulations (monocular, monochromatic) using the SLM (pink lines) and the SimVis (green lines), as well as VA for best subjective focus with no lens (black dots). Blue bars show the difference between SLM and SimVis. B) TF VA through SimVis Gekko™ (binocular, polychromatic) visual simulations (orange lines), and the SimVis (green lines) (monocular, monochromatic). Blue bars show the difference between SimVis and SimVis Gekko™ . Black dots show the VA for best subjective focus with no lens with the SimVis Gekko™ .

FIGURE 3.5 shows the intersubject average of the TF VA through visual simulations with SimVis (**FIGURE 3.5** A)) and SimVis Gekko™ (**FIGURE 3.5** B)) before surgery (natural lens, solid lines) and after surgery (M-IOLs, dashed lines). Blue bars in each graph represent the VA difference (pre- and post-operatively). The TF performance in both platforms is well captured before and after

surgery. Especially in the case of clear crystalline lens patients (upper row) (paired-samples t-test: $p > 0.05$). TF VA after surgery in patients with cataracts was higher than predicted by the simulations, while constant in the TF range (Ratio post/pre: 1.68±0.12 AO-platform; 1.65±0.11). In all cases, on average there is a significant cross-correlation between the shape of the TF VA curves in the 4D-range for clear lens and cataract patients using the AO-based platform(A, lag k = 0, rho = 0.853 and rho = 0.789) or the SimVis Gekko™ (B, lag k = 0, rho = 0.676 and rho = 0.870), respectively.

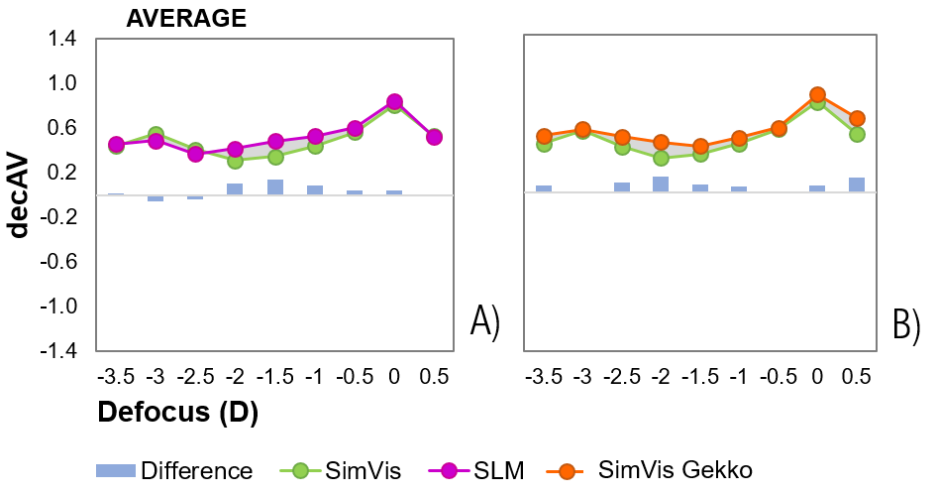

FIGURE 3.3. Averaged TF VA was obtained through simulations before surgery with all simulators. A) TF VA pre-operatively through AO_visual simulations (monocular, monochromatic) using the SLM (pink lines) and the SimVis (green lines). B) TF VA pre-operatively through SimVis (green lines) (monocular, monochromatic) & SimVis Gekko™ (orange lines) (binocular, polychromatic) visual simulations. Blue bars in each graph represent the VA difference (SLM – SimVis; SimVis Gekko™ – SimVis). The average error (standard deviation of repeated measurements, averaged across patients) was 0.058 ± 0.009 for SimVis, 0.086 ± 0.012 for SLM and 0.068 ± 0.009 for SimVis Gekko™ .

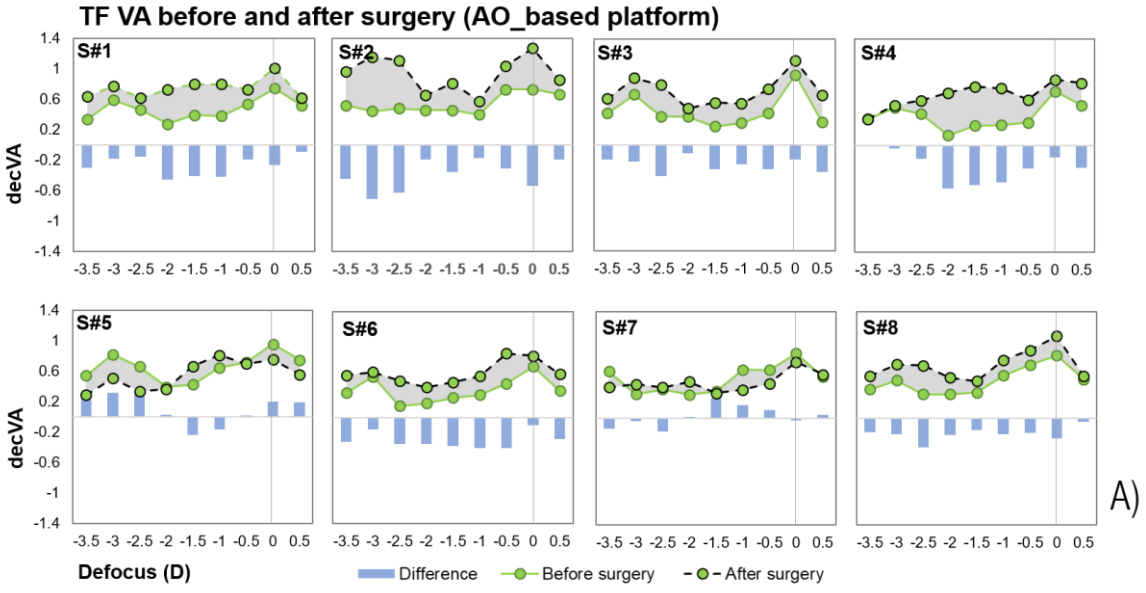

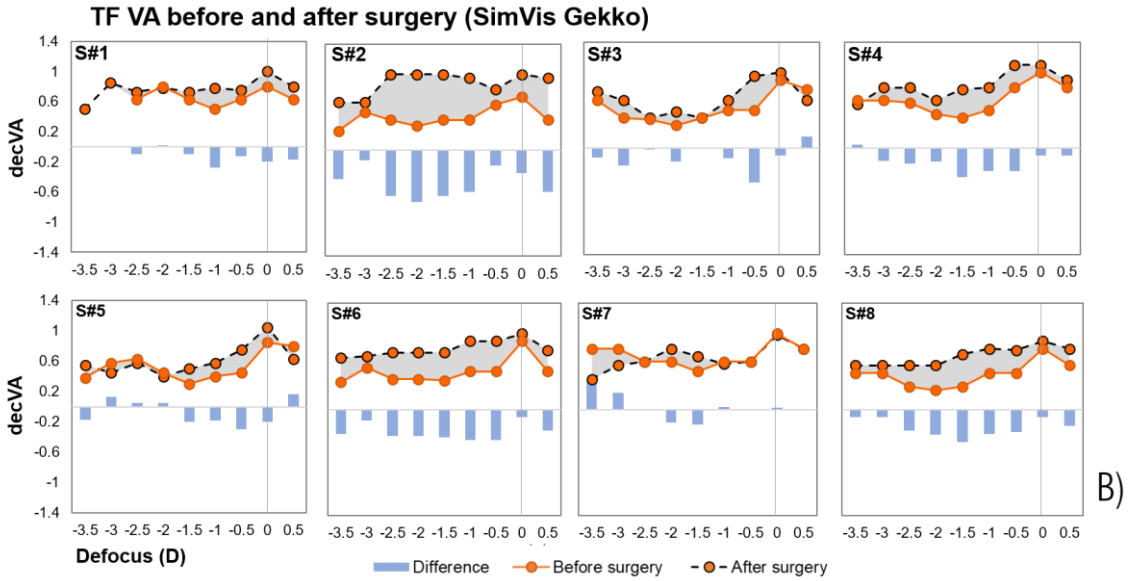

FIGURE 3.4. TF VA obtained before and after surgery. A) TF VA was measured with the AO-based platform (monocular, monochromatic) through visual simulations before (green solid lines) and after the surgery (green dashed lines). Blue bars show differences between pre-and post-surgery measurements. B) TF VA was measured with the SimVis Gekko™ platform (binocular, polychromatic) through visual simulations before (orange solid lines) and after the surgery (orange dashed lines). Blue bars show differences between pre-and post-surgery measurements. The average error (standard deviation of repeated measurements, averaged across all patients) for the simulations is indicated in **FIGURE 3.3**, and for the post-operative measurements with the M-IOL was 0.088 ± 0.010 in A and 0.073 ± 0.011 in B.

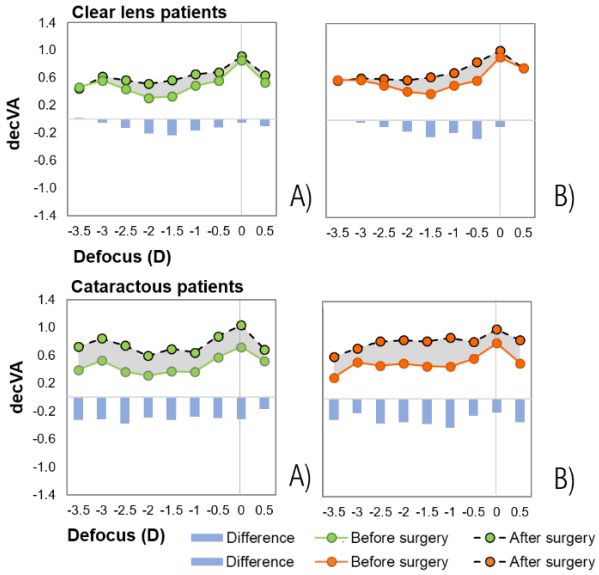

FIGURE 3.5. Averaged TF VA obtained before and after surgery for clear crystalline lens and cataract patients. A) TF VA was measured with the AO-based platform through visual simulations (green solid lines) and after the surgery (green dashed lines). Blue bars show differences between pre- and post-surgery measurements. B) TF VA was measured with the SimVis Gekko™ platform through visual simulations (orange solid lines) and after the surgery (orange dashed lines). Blue bars show differences between pre- and post-surgery measurements. The average error bar (standard deviation across patients) for the simulations is indicated in **FIGURE 3.3** , and for the post-operative measurements with the M-IOL in **FIGURE 3.4** . The average error bar (standard deviation across patients and platforms) for SimVis Gekko™ pre- operatively was 0.06 ± 0.01 and

0.05 ± 0.02, and for M-IOLs post-operatively was 0.07 ± 0.01 and 0.05 ± 0.01, for clear lens and cataract patients, respectively.

3.3.3. Post-operative monochromatic-monocular TF VA vs. Polychromatic-binocular TF VA

FIGURE 3.6 shows the TF VA after surgery: (1) monochromatic (555 nm) monocular TF VA measured with the AO-based simulator (green dots) and (2) polychromatic (white light)-binocular TF VA measured with the SimVis Gekko™ (orange dots) for all patients, as well as the average across patients (last panel). Measurements were performed in the two simulation platforms, although the real M-IOL was already implanted and no simulation was performed. In general, the TF VA curves measured in monochromatic-monocular conditions (green curves) and polychromatic- binocular conditions (orange curves) show similar trends. On average, there is a significant cross-correlation between the TF VA measured in polychromatic binocular conditions and monochromatic monocular conditions (lag k = 0, rho = 0.913). The blue bars (VA differences) are positive on average (0.07), indicating a slightly better binocular performance.

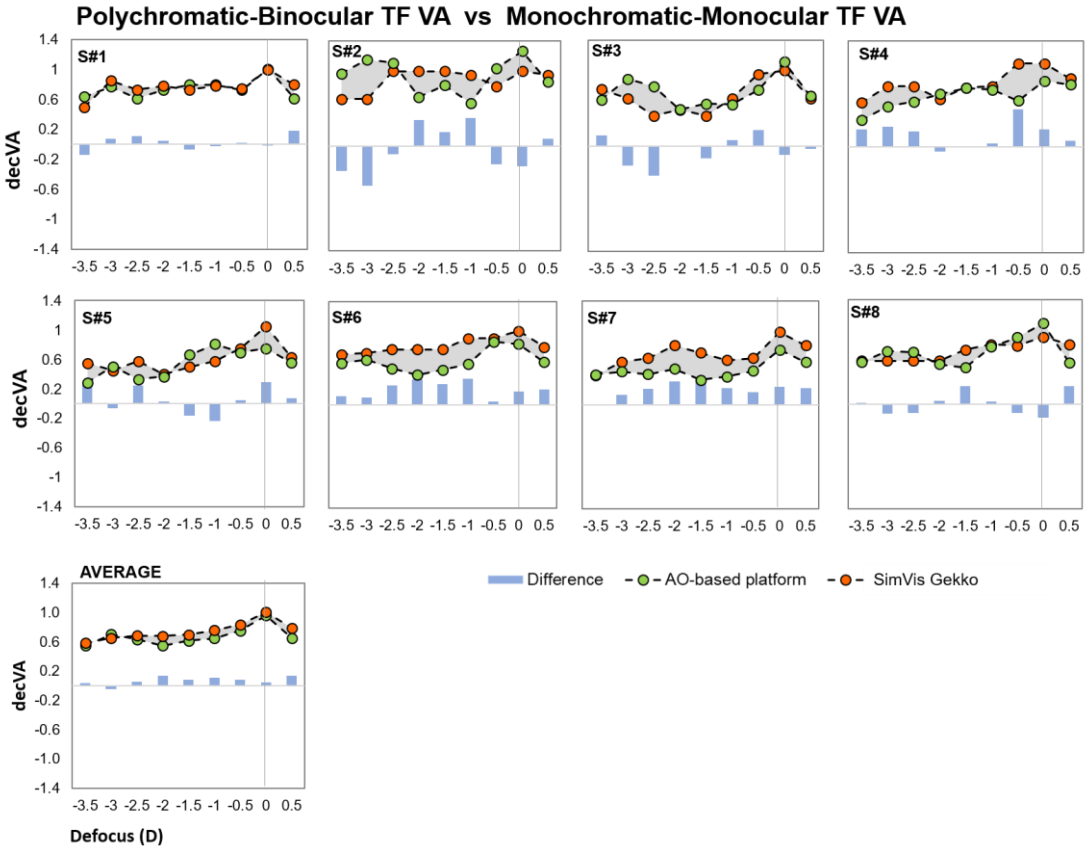

FIGURE 3.6. Post-operative monochromatic-monocular TF VA vs. Polychromatic-binocular TF VA. TF VA after surgery, with implanted trifocal diffractive IOL, measured monocularly and with a monochromatic stimulus (green dashed lines) and binocularly and with a white-light stimulus (orange dashed lines), for each patient, and averaged across patients. Blue bars show differences between both conditions. Average errors are indicated in **FIGURE 3.4**

3.4. DISCUSSION

This study presents pre-operative simulated TF visual performance in comparison with post-operative vision after implantation of a M-IOL. Our averaged TF VA curves with the implanted M-IOL show values of a similar order of magnitude to previous reports of patients implanted with the FineVisionTrifocal IOL: CDVA:1.00±0.03; DCIVA: 0.70±0.10; DCNVA: 0.68±0.06 in our binocular measurements with a clinical chart; CDVA: 1.00; DCIVA: 0.74; DCNVA: 0.76 in 21 eyes, measured monocularly by Poyales et al. (2016) [302]; CDVA: 1.12; DCIVA: 0.45; DCNVA: 0.89 in 30 patients, measured binocularly by Gundersen and Potvin (2017) [303]. While our average data are in good correspondence with TF visual performance reported in the literature in patients implanted with the FineVision trifocal IOL, the interesting finding in our study is the capability of the simulators to actually predict this performance pre-operatively and individually.

Visual simulators based on different active optical elements, such as DM [304], SLM [305] or IOLs in a cuvette [295], in monocular/binocular [187, 283, 306] configurations, are increasingly used to simulate vision through different multifocal lens designs [218, 232, 307]. To our knowledge, this is the first study where visual simulation of a given M-IOL pre-operative is directly compared to vision post-operatively with the implanted M-IOL, at the patient level. The comparison was made in patients that were implanted with diffractive trifocal lenses (the FineVision POD F, by PhysIOL), using two different simulating technologies (SLM and SimVis technology) and two different simulation platforms, an AO-based visual simulator and a binocular wearable clinical simulator, the SimVis Gekko™ .

In a previous study [187], we compared TF optical (on-bench) and visual quality (VA) (patients) through different simulation technologies (SLM, IOL in a cuvette, SimVis technology) in young phakic patients, and found that visual simulations in an AO system capture to a large extent the optical and visual performance obtained with projected real IOLs, as found in the current study **FIGURE 3.3**. In previous work [187], the crystalline lens was preserved, as the real IOLs (mounted in a cuvette) were projected onto a pupil plane. Recent work [287], suggests that the crystalline lens aberrations of a relatively young population (25-43) play a relative minor role in the performance of visual simulators replicating multifocal IOLs, at least in an SLM-based visual simulator.

The ultimate utility of visual simulators, no matter the technology behind them, relies on their capability to allow patients to experience vision before IOL implantation, since tested IOLs are designed to replace the natural crystalline lens. In this study, we compared directly pre-and post-operative TF visual quality with simulators and implanted real IOL, with clear crystalline lens and cataractous crystalline lens patients. TF visual quality pre-surgery (simulations) and after surgery (real IOL) are similar in clear crystalline lens patients (**FIGURE 3.5**, upper row). This is expected, since the cornea and the multifocal pattern is a much higher contributor than the crystalline lens to pre-operative TF visual quality in clear crystalline patients. In clear crystalline patients (**FIGURE 3.5** A) & B)), post-operative TF VA is slightly higher for intermediate distance than the simulated pre-operative data, probably due to scattering of the old crystalline lens, since in our previous study [187], with clear crystalline subjects shows no differences between simulators (SLM, SimVis and real IOL). Moreover, in the case of cataractous patients, where opacities decrease TF visual quality (**FIGURE 3.5**, lower row), visual simulators are still able to predict the relative TF performance post-operatively, at least up to the degree of cataract in the patients of the study, indicated by the high correspondence between the shape of the TF curves with the simulation pre-operatively and real IOLs post-operatively ($p = 0.006$ in the case of SimVis Gekko™). While a more comprehensive study of the role of the scattering produced by cataracts (and particularly in relation to the cataract

type and opacity distribution is needed) our results suggest that, at least in patients with mild cataracts, a simple conversion factor would be needed to project the expected TF performance after cataract removal from pre-operative simulation measurements.
SimVis simulation is robust, showing good correspondence between both binocular white light TF VA (measured with the clinical simulator) and monocular monochromatic TF VA (AO visual simulator). The slightly higher VA found binocularly over monocular measurements in the majority of subjects, occurring both with SimVis before surgery (**FIGURE 3.4**) and with the real M-IOL after surgery (**FIGURE 3.6**) can be explained by binocular summation, although this was not found to be statistically significant. It is likely that the binocular gain is counteracted by the presence of chromatic aberration in the white-illuminated target used in binocular measurements as opposed to the monochromatic stimulus of the monocular measurements. We did not attempt polychromatic measurements in the AO system, particularly as the SLM is known to be subject to chromatic artifacts [219]. Remarkably, the similarity of TF VA with SimVis and the real IOL with white targets indicate that chromatic effects are not a concern with the SimVis technology [220].

3.5. CONCLUSIONS

In general, we can conclude that visual simulators are able to predict the relative multifocal performance of a specific IOL design since TF VA pre-surgery (simulated IOL) and TF VA after-surgery (real IOL) show good correspondence. In particular, in the case of a trifocal diffractive design, the predicted range for multifocality is similar to the actual relative multifocal performance after surgery. Visual simulations are useful programmable tools to predict the relative visual performance with multifocal IOLs, both in an AO environment and in a large field of view SimVis binocular device.

In this chapter, we have demonstrated the ability of visual simulators to simulate an intraocular lens before being implanted in the subject, in the next chapter we will study the simulation ability of the SimVis simulator, in particular, to simulate contact lenses for presbyopia.

4

CHAPTER 4. OPTICAL AND VISUAL QUALITY WITH PHYSICAL AND VISUALLY SIMULATED PRESBYOPIC MULTIFOCAL CONTACT LENSES

As multifocal contact lenses (M-CLs) expand as a solution for presbyopic correction, a better understanding of their optical and visual performance becomes essential. Also, providing subjects with the experience of multifocal vision before contact lens fitting becomes critical, both to systematically test different multifocal designs and to optimize selection in the clinic. In this chapter, we evaluated the ability of a simultaneous vision visual simulator (SimVis) to represent M-CLs.

This chapter is based on the paper by Vinas et al. [308], 'Optical and visual quality with physical and visually simulated presbyopic multifocal contact lenses' published in TVST (2020). The co-authors are **Sara Aissati**, Ana Maria Gonzalez-Ramos, Mercedes Romero, Lucie Sawides, Vyas Akondi, Enrique Gambra, Carlos Dorronsoro, Thomas Karkkainen, Derek Nankivil, Susana Marcos

The work was presented as an oral contribution at ARVO annual meeting 2019 by Vinas et al.[309] under the same title.

The author of this thesis implemented the experimental procedure in collaboration with Maria Vinas and Ana Maria Gonzalez, performed the experimental measurements on subjects, collected the data in collaboration with Ana Maria Gonzalez, analyzed the data in collaboration with the rest of the authors, and prepared the manuscript in collaboration with Maria Vinas and Susana Marcos.

4.1. INTRODUCTION

M-CLs are increasingly used to correct presbyopia, the age-related loss of the accommodative amplitude in the eye [152, 169, 310, 311]. However, understanding of the optical and perceptual impact of M-CLs at the individual level is needed in order to identify the visual compromise of the various lens designs, and select the optimal lens for a patient.

M-CLs rely on the principle of simultaneous vision, where image quality of an image at far is slightly reduced in order to gain vision at near. There are multiple M-CL designs (mostly refractive, and rotationally symmetric)[152, 310, 311], with differences primarily in radial variation in refractive power (from abrupt changes between near and far zones to aspheric extended-depth-of-focus designs), on the region of the pupil devoted for near and far (center-near or center-distance vision), or the number of alternating zones for near and far (i.e. from 2 to 5 alternating zones) [311]. Some manufacturers offer M-CLs with slight variations of the design according to age, to account for age-dependent changes in pupil diameter, and refractive error [312].

Despite the increasing number of M-CLs [313, 314], prediction of their success prior to being prescribed in subjects is complicated. Several reports evaluate M-CLs on eye, in terms of TF VA and/or contrast sensitivity measurements, in some cases in comparison with monovision [315-318]. Generally, to understand intersubject variability of lens performance, researchers evaluate the impact of certain factors including pupil diameter or ocular aberrations [319-321]. However, this type of evaluation is time- and resource-consuming, and only allows a posteriori evaluation of visual performance. Besides, many clinical evaluations rely on patient satisfaction questionnaires. However, from those subjective evaluations it is sometimes difficult to disentangle dissatisfaction originating from the optical design and its perceptual tolerance from those associated to lens wear comfort [152].

AO visual simulators are particularly attractive to test vision in subjects with new optical designs prior to delivering or even manufacturing a lens[159, 307, 322-324]. AO-simulations of new corrections enable investigation of interactions between a subject's optics and a given correction, characterization of differences across corrections, and eventually selection of the correction that optimizes perceived visual quality and performance in subjects [325]. In previous studies [322, 323], we have simulated diverse novel refractive multifocal designs (concentric and asymmetric) as well as commercial refractive and diffractive IOLs using an SLM integrated in an AO system, and demonstrated equivalency between the patient's vision through the simulated lenses and physical lathe-manufactured phase-plates or physical IOLs in a cuvette.

Simultaneous vision simulators are specifically suited to simulate multifocal corrections, allowing systematic evaluation of multifocal designs. A two-channel visual simulator has been used to evaluate the effect of the magnitude of the near addition in visual degradation for far [326], the pupillary distribution of far and near zones in a bifocal design [327], or the orientation of asymmetric bifocal corrections [324]. In the SimVis [284, 328], the TF performance of a given multifocal pattern is mapped into a temporal pattern defining the time that TL spends at a given optical power, corrected by the dynamic effects of the TL [329]. Advantages of the SimVis over standard AO-based visual simulators include the fact that it is see-through, it provides a large field of view (20º), and it is very compact. These features have allowed for the concept to be translated into a binocular, wearable clinical device (SimVis Gekko™ ™). Previous studies have proven the capability of the SimVis technology to replicate vision with real refractive segmented IOLs and trifocal diffractive IOLs [325], and a high correspondence between pre-operative vision with SimVis Gekko™ and post-operative vision with the real implanted multifocal IOL **(Chapter 3).**

Is also useful for the patient and clinician to be able to compare across different multifocal options as a tool to guide decision. Likewise, SimVis can allow the prospective M-CLs wearers to test vision with different M-CL designs before putting them on their eyes. It is conceivable to use this technology to go through a M-CL fitting protocol using M-CLs programmed in the SimVis Gekko™ , largely reducing chair time, the number of physical lenses used, and patient's discomfort.

In this study, we programmed, for the first time, M-CL profiles in the SimVis, and tested real and simulated M-CLs (center-near aspheric CLs) in subjects. We compared visual quality through focus with the real and simulated M-CLs, and validated the accuracy of SimVis to replicate visual performance with those lenses.

4.2. METHODS

TF optical and visual quality with real M-CLs on-eye and SimVis simulations of the same M-CLs on the same subjects were evaluated using a multi-channel polychromatic AO visual simulator equipped with a double-pass channel, a SimVis channel, and a psychophysical channel to allow measurements on-bench and *in vivo.*

4.2.1. Subjects

The study was conducted on 10 presbyopic subjects (mean age: 52.3 ± 5.2 years; range: 47 to 64 years; SE: −3.44 ± 0.85 D), habitual CL wearers, who were fit with the corresponding add power M-CL, following the manufacturer fit assessment guide [330]. Measurements were performed monocularly, where the eye chosen for the lens fit was the sensorial dominant one. Three subjects were fitted with low (+1.25 D), three subjects with medium (+1.75 D), and four subjects with high (+2.50 D) add power M-CLs. All measurements were performed under natural viewing conditions with no dilated eyes. **TABLE 4.1** shows the refractive profile and the amount of aberrations (RMS) of the subjects, as well as the refractive base power and add power for each patient. For baseline information, the RMS for HOAs of the virgin eye (measured with the Hartmann-Shack wavefront sensor) is shown in the last column of **TABLE 4.1**.

All participants were acquainted with the nature and possible consequences of the study and provided written informed consent. All protocols met the tenets of the Declaration of Helsinki and had been previously approved by the Spanish National Research Council (CSIC) Bioethical Committee.

TABLE 4.1. Subjects' Refractive and Aberrations Profile

ID	Age (Years)	Pupil Diameter (mm)[a]	Rx (D)[b]	M-CL Power (D)[c]	Add (D)[d]	RMS (µm)[e]
S#1	51	4.97	-4.75	-5.25	Low	0.48
S#2	48	4.67	-0.50	-0.50	Low	0.31
S#3	47	5.12	-5.50	-5.50	Low	0.86
S#4	48	2.54	-3.25	-3.25	Medium	0.61
S#5	51	3.94	-2.25	-2.50	Medium	0.96
S#6	51	4.18	-1.75	-1.50	Medium	0.14
S#7	51	4.96	-5.00	-5.50	High	0.34
S#8	54	5.37	-3.25	-3.75	High	1.19
S#9	64	4.30	+2.50 -0.75 x180º	+2.50	High	0.59
S#10	58	4.71	-4.00	-3.75	High	0.97

[a]Natural pupil diameter (mm) obtained from aberrometry.
[b]Autorefractometer refraction.
[c]The base power of the selected M-CL.
[d]The add power of the M-CL (low: +1.25 D; medium: +1.75 D; high: +2.50 D).
[e]RMS for HOAs, for a 4-mm pupil diameter

4.2.2. Multifocal Contact Lenses

The M-CLs used in the study were the center-near aspheric 1-Day Acuvue Moist Multifocal (Johnson & Johnson Vision Care, Jacksonville, Fl, USA; Etafilcon A with LACREON technology, 58% water content). In this type of simultaneous vision solution [319], light rays passing through the pupil to form the retinal image encounter a smooth transition in power between distance and near corrections. Thus any region of the retina receives both in-focus and out-of-focus images.

In the 1-Day Acuvue Moist Multifocal, the design is a hybrid back curve design (BC 8.4; Diam 14.3 mm), with a gradual change in power between near and distance zones [331]. There is no distinct relative plus power to the distance prescription in the low add power lens. This lens shows no distinct transition point between the near and distance powers within the optical zone. The spherical periphery aims at helping the centration of the optics over the pupil. There are 61 distance powers (in 0.25 D steps from +6.00D to −9.00D) with three different add powers: low, +1.25 D; medium, +1.75 D; high, +2.50 D.

4.2.3. AO Visual Simulator

Measurements were performed in the polychromatic multichannel AO visual simulator system at VioBio Lab described in detail in previous publications [62, 332], and section 2.1.2 of this thesis. For the purposes of this study, the visual stimulus was seen through two different active optical elements: ***(1)*** a reflective DM, used in this study to correct the aberrations of the optical system; and ***(2)*** a SimVis based on temporal multiplexing of a TL, used to simulate the M-CL design.

SimVis Simulations

The SimVis temporal profiles for each M-CL (low, medium and high add powers) were estimated from calculations of the corresponding TF optical quality. All calculations were performed for a -5.00D refractive power and 4-mm pupil diameters. Computer simulation showed that in these

conditions, the differences in the TF optical quality produced by design differences across lens power were negligible (|RMS| difference < 0.004, between the curves corresponding to +2.50 and −5.50 D, the most extreme powers in our sample). **FIGURE 4.1** illustrates (for the high-add M-CL design and 4-mm pupil diameter) the five steps of validation of a SimVis programmed lens.

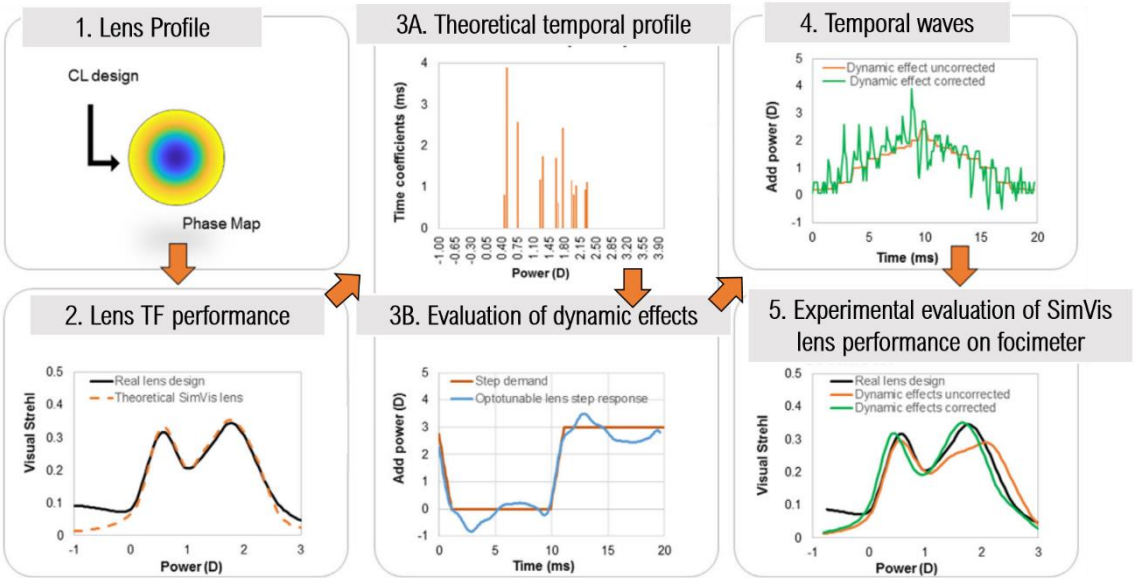

FIGURE 4.1. SimVis programmed lens characterization and validation of a lens design. (1) Calculation of the wave aberration (phase map) from the power map of the lens design. (2) Calculation of the TF performance (Visual Strehl optical metric). (3A) Theoretical temporal profile [328]. (3B) Estimation of the SimVis temporal coefficients obtained through an iterative optimization procedure [333]. (4) Experimentally evaluated the dynamic response of the tunable lens: its impulse response function is used to calculate the temporal corrected wave. (5) TF performance of the real lens (theoretical) and the SimVis programmed lens, with and without the correction of dynamic effects, measured using a high-speed dynamic focimeter [329] provided with a high-speed camera (3823 fps).

First, the wave aberration map (Phase Map) of each lens was calculated from the corresponding power maps provided by the manufacturer (**FIGURE 4.1**). Then, the MTF was estimated from the wave aberration and pupil function using Fourier Optics. The VS was used as an optical quality metric, estimated as the neural contrast sensitivity weighted Modulation Transfer Function (MTF) of the system [259, 334]. The through-focus lens performance was thus evaluated (**FIGURE 4.1** (2)). The calculation of the series of SimVis temporal coefficients describing a lens from the theoretical TF calculation has been described before [284, 328, 329] and is based on the equation described by Akondi et al. (2017) [328].

$$+q = k \sum_{i=1}^{n} (t_i)(Q_i) \quad \text{Eq.(4.1)}$$

where +q is the multifocal real lens pattern, t_i are the temporal coefficients (least squares with nonnegativity constraints), and Q_i is the monofocal term, in a certain through focus range (−1.00 to +3.00 D in steps of 0.05 D). These temporal coefficients stand for the weighting factors of a series of defocused monofocal PSFs, tuned to match the TF optical quality of the M-CL design in an iterative optimization procedure to obtain the theoretical temporal profile of the lens (**FIGURE 4.1** 3A).

In parallel, we evaluated the dynamic behavior of the TL that will be used to simulate the M-CL designs (**FIGURE 4.1** 3B). Its impulse response function [333] was used, along with the theoretical temporal profile of the lens, to calculate the temporal "corrected wave" in an iterative optimization of the electrical input signal driving the lens where some constraints are taken into account (20ms period, temporal coefficients of at least 0.1 ms and no more than 150 temporal coefficients to simulate the design) (**FIGURE 4.1** (4)) [325, 328, 329, 332]. Once we have the temporal waves, we used a high-speed dynamic focimeter [329], provided with a high-speed camera (3823 fps), to measure the TL response with and without the correction of dynamic effects (**FIGURE 4.1** (5)) and to evaluate the TF SimVis simulated lens performance.

The SimVis programmed lens is validated when it mimics the real lens design in terms of TF VS ratio, where the peaks of the design are not shifted more than 1/8 diopter from the real lens design and an error in the VS ratio (height) is less than 10%, 2.5 times the repeatability of the experimental simulations. The number of temporal coefficients will vary according to the real lens design and to the TL used to simulate the particular design. For the purposes of this study, we simulated three different lenses with the same refractive power (−5.00 D) and different add powers (low, +1.25 D; medium, +1.75 D; and high, +2.50 D add power M-CLs).

4.2.4. On bench through-focus optical quality

Temporal profiles for the different M-CL add powers were programmed in the SimVis of the AO visual simulator system. TF optical quality through the SimVis-simulated M-CLs was evaluated on bench in the AO visual simulator, using TF DP retinal images and TF retinal images of an E-letter optotype imaged on an artificial eye, following similar procedures as in Vinas et al. (2019) [325]. For the DP measurements, the artificial eye consisted of a 50.8-mm focal length achromatic doublet lens and a rotating diffuser as an artificial retina. For the 1P measurements, the artificial eye consisted of an objective lens (50.8 mm), and a CCD camera (DCC1240C - High-Sensitivity USB 2.0 CMOS Camera, 1280 x 1024, Global Shutter, Color Sensor, Thorlabs GmbH, Germany) acting as an artificial "retina". The stimuli were displayed in the DMD and subtended 1.62 degrees, illuminated with 555-nm light coming from the SCLS. In all measurements, focus shifts were achieved by moving a Badal optometer from +2.00 D to -3.00 D in 0.25-D steps, around the best foci for far distance.

4.2.5. In vivo measurements on presbyopic subjects

TF optical and visual quality were measured *in vivo* in 10 presbyopic subjects, through SimVis-simulated M-CLs and wearing the same real M-CLs, by TF DP image series and TF VA, respectively. The order of the measurements (M-CLs or SimVis) was randomly assigned using a random number generator.

In vivo through-focus optical and visual quality

TF optical quality (DP) and visual quality (VA) measurements were obtained for the subject wearing the real M-CL, or through the SimVis-simulated M-CL. The subjects looked for their best subjective focus while looking at a monochromatic (555 nm) stimulus. This position (average of 5 settings by the subject) was taken as the zero. All measurements were performed with a 4-mm artificial pupil.

TF DP retinal aerial images were obtained while the Badal system was moved from -3.00 D to +1.50 D in 0.25-D steps (around the best subjective focus at 555 nm). The subjects foveally fixated the auxiliary spot, while the images were acquired.

TF VA measurements were performed at different positions of the Badal optometer ranging from +1.00 to -4.00 D. VA was measured using an 8AFC [335] procedure with tumbling E-letters and a QUEST (Quick Estimation by Sequential Testing) algorithm programmed with the Psychtoolbox package [300, 336, 337] to calculate the sequence of the presented stimulus (letter size and orientation) in the test following the subject's response. The QUEST routine for each VA measurement consisted of 40 trials, each one presented for 0.5 seconds, where the threshold criterion was set to 75%. The VA measurement was estimated as the average of the 10 last stimulus values. The luminance of the stimulus was 20 cd/m^2. VA was expressed in terms of logMAR acuity (logMAR = -log$_{10}$|decimal acuity|)[301]. Variability of each VA measurement was obtained from the standard deviation of the 10 last stimulus values used to estimate the threshold in each measurement.

4.2.6. Data analysis

The DP image quality metric is defined as the maximum intensity of the images [338], with the intensity values normalized to the no-lens image at best focus. The same analysis was applied to TF DP measurements in subjects. In the case of the E-stimulus, the image quality metric was obtained as the image correlation coefficient (correlation of the image of the E-letter obtained for a given condition with the image of the E-letter with no lens). The conditions (laser power, pupil diameter, exposure time) were kept constant throughout the entire image series. TF visual quality curves (in subjects) were obtained from TF DP and TF LogMAR VA measurements with the real M-CLs and the SimVis-simulated M-CLs, as well as the no-lens condition as a reference.

In the case of the TF logMAR VA, depth of focus (DOF) was defined as the range of defocus over which the VA is within the 0.2 logMAR of the subject's best possible acuity, following the procedure by Collins et al. (2002) [339], which corresponds to a VS of approximately 0.12 [259, 340].

The comparison between the real and the SimVis-simulated TF performance was expressed in terms of RMS difference of the linearly interpolated TF curves (in a 4.00 D range), taking the real M-CLs as the reference. The RMS difference served as a metric for the goodness of the replication of the lens design by the SimVis simulator.

Statistical analysis was performed with SPSS software (IBM SPSS Statistics 26; SPSS, Inc., USA) to test differences across results with the SimVis-simulated and real M-CLs (paired-sample t-test) in both cases: on-bench and on subjects (n=10). To evaluate the shape similarity of the TF curves, cross-correlation of the SimVis-simulated and real M-CLs was calculated, and the correlation coefficient (rho, similarity, maximum of 1) and lag (k, offset between the series, minimum of 0) were reported.

4.3. RESULTS

We present TF optical and visual quality of M-CLs (low, medium and high add powers), for the following conditions: ***(1)*** TF optical quality (VS) of the M-CLs alone, calculated from the lens power profiles, which serves as input to the estimation of the SimVis temporal patterns; ***(2)*** TF optical quality measurements (DP and 1P stimulus images) with the SimVis-simulated M-CLs, on bench; ***(3)*** TF optical quality (DP) in subjects with the real M-CL on eye and with the SimVis-simulated M-

CL; ***(4)*** TF visual quality (VA) in subjects with the real M-CL on eye and with the SimVis-simulated M-CL.

4.3.1. Calculated Through-focus optical performance of the lens alone

FIGURE 4.2 shows the TF VS of the M-CL alone calculated from their power profile, for the M-CL of low (+1.25 D, blue), medium (+1.75 D, orange) and high (+2.50 D, grey) adds, respectively. The threshold for functional vision (VS=0.12) [259, 340, 341] is marked with a horizontal gray dashed line. An increase in the near add results in a decrease of maximum VS, a shift of best focus to intermediate vision, and an increase in DOF.

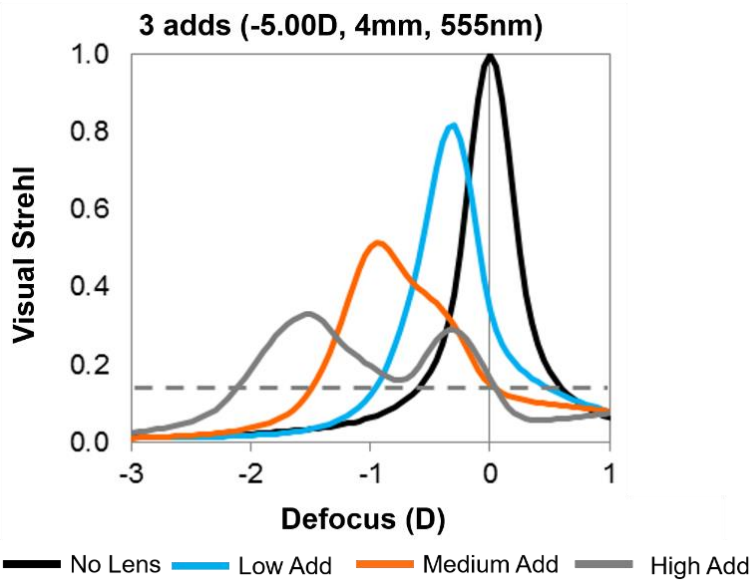

FIGURE 4.2. TF optical predictions of the lens alone. TF VS for the M-CL with low (+1.25 D, blue), medium (+1.75 D, orange), and high (+2.50 D, grey) adds, respectively. The no lens condition (black) is shown as a reference. The dashed gray line marks the VS 0.12 threshold for functional vision. Data are for 4-mm pupils.

4.3.2. Through-focus optical performance of the SimVis-simulated M-CLs

FIGURE 4.3 shows the TF optical performance of the SimVis-simulated M-CLs (low, medium, and high adds) experimentally using a high-speed focimeter, with and without correction of the dynamic effects of the TL. The dynamic correction (to which the green lines correspond in **FIGURE 4.3**) was implemented for the on-bench and subject measurements. The SimVis-programmed lenses mimic the real lens TF performance (black line) with high accuracy (RMS difference < 0.009), with a lateral displacement of the peak less than 1/8 diopter for the three designs.

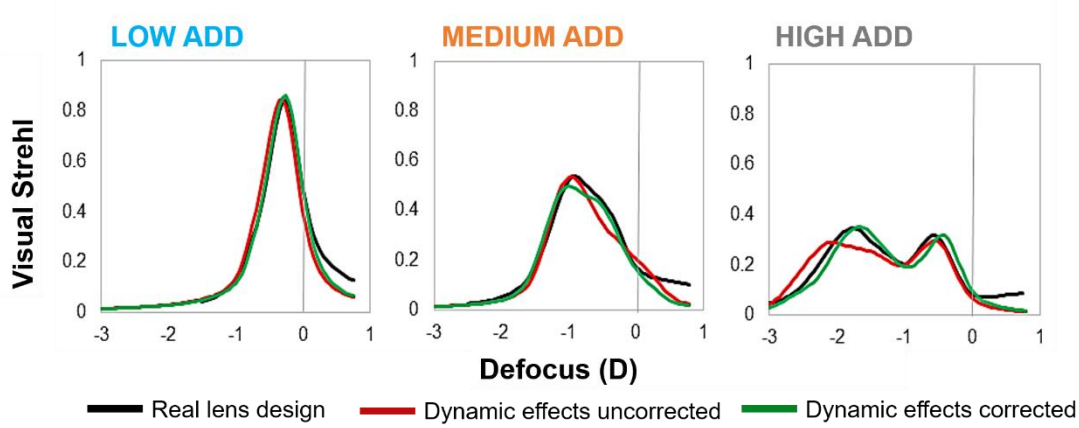

FIGURE 4.3. TF optical performance of the SimVis-simulated M-CLs. TF optical performance of the SimVis-simulated M-CLs compared to the real lens design, in terms of TF VS ratio, for the low- (left), medium- (center), and high-add (right) powers for 4-mm pupil diameter. The black line represents the theoretical real lens; the red line represents the SimVis-simulated M-CLs when the dynamic effects in the TL are not corrected, and the green line represents the SimVis-simulated M-CLs when the dynamic effects in the TL are corrected. Data are for 4-mm pupil diameter.

4.3.3. Experimental through-focus optical performance on-bench

FIGURE 4.4 shows TF raw images (upper panel, A) and TF optical quality (lower panels B and C) of the SimVis-simulated M-CLs on-bench, in the AO system. The top images in each series correspond to DP aerial images. The bottom images in each series correspond to 1P: the E-letter stimulus is captured in a CCD camera at the "retinal" plane of an artificial eye placed at the position of the patient's eye. The results correspond to low-add lenses (top series in A, blue lines in B/C), medium-add lenses (medium series in A, orange lines in B/C), and high-add lenses (bottom series in A, gray lines in B/C).

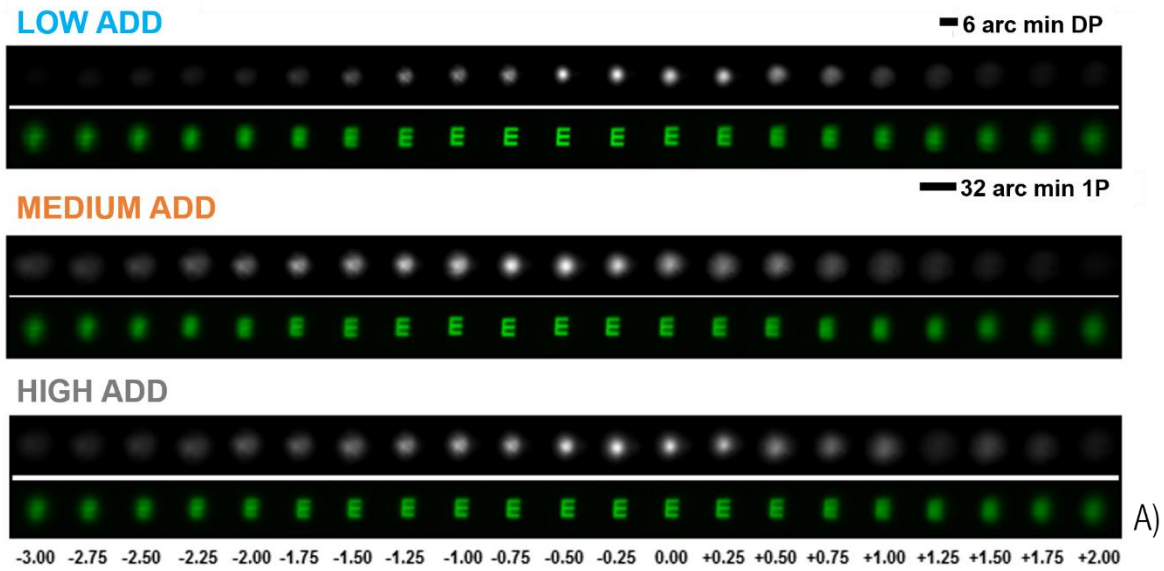

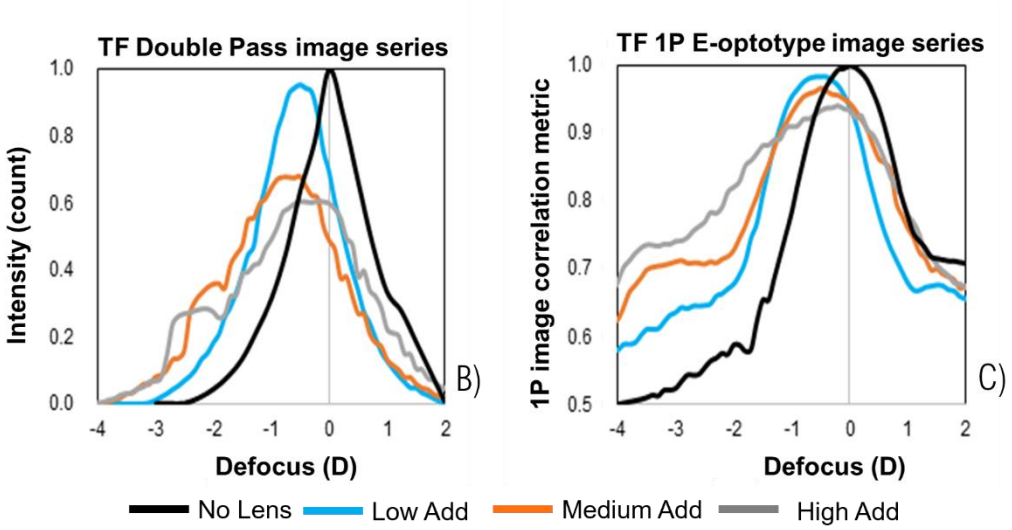

FIGURE 4.4. TF optical quality on bench and TF optical quality metrics. A) On-bench TF DP aerial retinal images (upper images in each series) of a 250 µm point extended source and TF retinal images (1P) of an E-optotype (bottom images in each series) through the simulated M-CLs (series of low-, medium- and high- adds). Scale bars indicate the angular extent of the images (6 arcmin for the DP and 32 arcmin for the 1P images). B) TF DP of image maximum intensity, normalized to the intensity of the best focus no-lens image series; C) TF image correlation metric, each image of the series was correlated to the 0-D image of the monofocal TF range. Blue, Orange and Gray lines correspond to low, medium and high near adds. Black lines correspond to a monofocal lens, as a reference.

The image quality metric in the DP-images is the maximum intensity in the image (normalized to the intensity of the best focus no-lens image series, **FIGURE 4.4** (B)), and in the 1P images an image correlation metric (**FIGURE 4.4** (C)), where the 1P image series were correlated to the 0 D-image of the monofocal TF range (4-mm pupil size). The TF data for the no-lens condition (i.e. monofocal, black lines) are shown as a reference. The experimental TF images capture the expected trends of the simulated M-CLs: ***(1)*** small differences between the low-add lens and no lens condition, as quantified by a shape similarity analysis (DP: lag k=0, rho=0.991; 1P: lag k=0, rho=0.962); ***(2)*** Negative shift of the best-focus peak with the medium- and high-add power lenses; ***(3)*** Broadening of the TF curves for the mid-and high-add lenses.

4.3.4. Experimental through-focus optical and visual quality *in vivo*

FIGURE 4.5 shows TF DP optical quality with the SimVis-simulated M-CLs (red lines) and real M-CLs (green lines) for all subjects (A) and average data across subjects (C), for all three add powers (low, first column; medium, second column; high, third column). The TF DP optical quality measured with no lens (black dotted lines) is shown as a reference in all cases. Data are shown in similar dioptric range for the real and SimVis-simulated M-CLs. TF DP data are expressed in terms of maximum intensity (normalized to the maximum DP aerial image of the no-lens condition). In order to compare the different TF curves, the point of maximum intensity of each curve was set as 0D, shifted in some cases from the subjective focus setting by the subject. DP TF curves can only be compared relatively, as the light intensity was adjusted between measurements with and without the M-CLs. The blue bars show the difference between real and simulated M-CLs curves at each focus position.

The average RMS difference between the real and SimVis-simulated M-CLs TF DP curves was 0.031 ± 0.003, 0.025 ± 0.009 and 0.019 ± 0.009 for the low-, medium-, and high-adds, respectively. Although there are some cases (S#2, S#7, S#8, and S#10) in which the absolute difference was higher than the mean (RMS = 0.005 ± 0.004, 0.097 ± 0.002, 0.062 ± 0.021, and 0.053 ± 0.010, respectively) the relative shape of the TF curves with the real and the SimVis-simulated lens was very similar (**FIGURE 4.5** B)). The shape similarity metrics for the averaged data were lag κ = 0 for all adds, rho = 0.811, rho = 0.792, and rho = 0.861 for the low-, medium-, and high- adds, respectively. Only subjects S#1 and S#7 showed low shape similarity, as shown in **FIGURE 4.5** (B). A point-by point comparison of the curves using paired-samples t-test resulted in significant differences in subjects S#2 ($p = 0.003$), S#7 ($p = 0.004$), S#8 ($p < 0.001$), and S#10 ($p < 0.001$) (normalized intensity DP test).

FIGURE 4.6 shows the TF LogMAR VA with the simulated M-CLs (red lines) and real M-CLs (green lines) for all subjects (A), and the average data across subjects (C) for all three add powers (low-add, first column; medium-add, second column; high-add, third column). Black dots stand for monofocal VA at the best focus of each subject with no lens. The blue bars show the difference between real and simulated M-CL curves at each focus position. The average RMS difference between the real and SimVis-simulated M-CL TF VA curves was 0.025 ± 0.008, 0.015 ± 0.003, and 0.020 ± 0.011 for the low, medium, and high adds, respectively. A paired t-test comparison between TF VA with real and SimVis-simulated M-CLs showed statistically significant differences ($p<0.05$) only in the high-add group, with differences driven by S#7.

The shape similarity metrics between real and SimVis-simulated M-CLs for all subjects are shown in **FIGURE 4.6** (B), which for average data were lag k=0 for all adds, rho=0.895, rho=0.944 and rho=0.915, for the low-, medium- and high-adds, respectively, indicating a large degree of similarity. For S#7, showing the largest RMS difference, the shape of the curves showed high similarity (lag k=0 rho=0.744). Only S#1 shows low shape similarity. RMS difference for TF DP and for TF VA on subjects showed a significant correlation between results obtained with both methods ($r = 0.520$). Excluding S#7, whose TF DP and TF VA results disagree, there is a significant correlation between shape similarity for DP and VA (paired-samples t-test $p= 0.047$).

Also, to understand a potential impact of the patient's eye aberrations on the quality of the SimVis-M-CL simulation we correlated the real lens/SimVis-simulated RMS difference (DP & VA) and the RMS wavefront error, and found that the goodness of the simulation (RMS difference) was uncorrelated with the optical quality of the virgin eye. Finally, we evaluated potential correlations of these parameters with age and refractive error, and did not find significant correlations, although this may be in part associated to the small sample size.

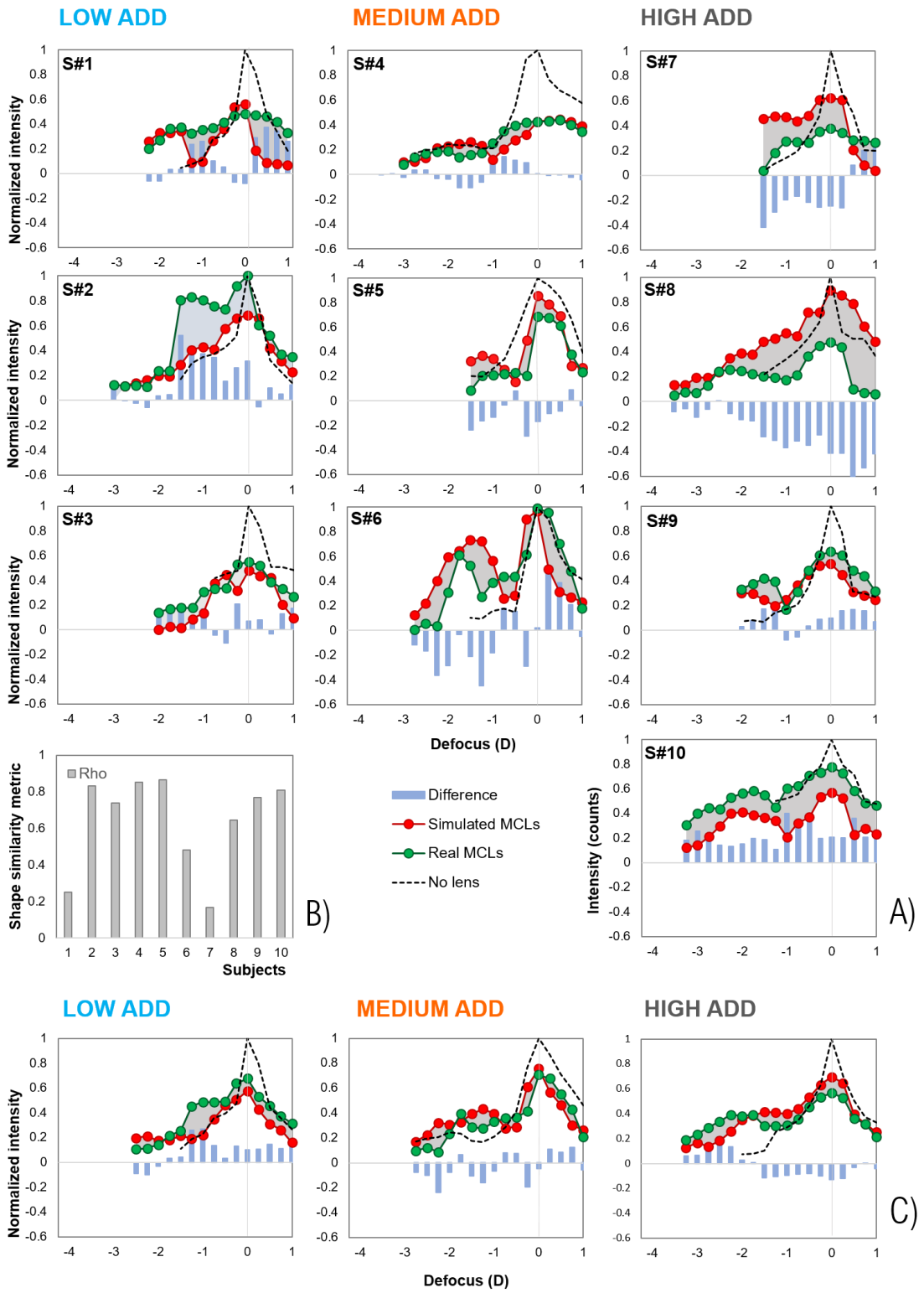

FIGURE 4.5. TF DP optical quality. A) TF DP optical quality (maximum intensity) for all subjects with the simulated M-CLs (red lines), the real M-CLs (green lines), and no lens (black dotted lines) with all three adds (low-add, first column; medium-add, second column; high-add, third column). Blue bars show the difference between real and simulated M-CLs curves. B) Shape similarity metric (crossed correlation, rho) for all subjects. C) Averaged TF DP optical quality with all 3 adds (low-add, first column; medium-add, second column; high-add, third column).

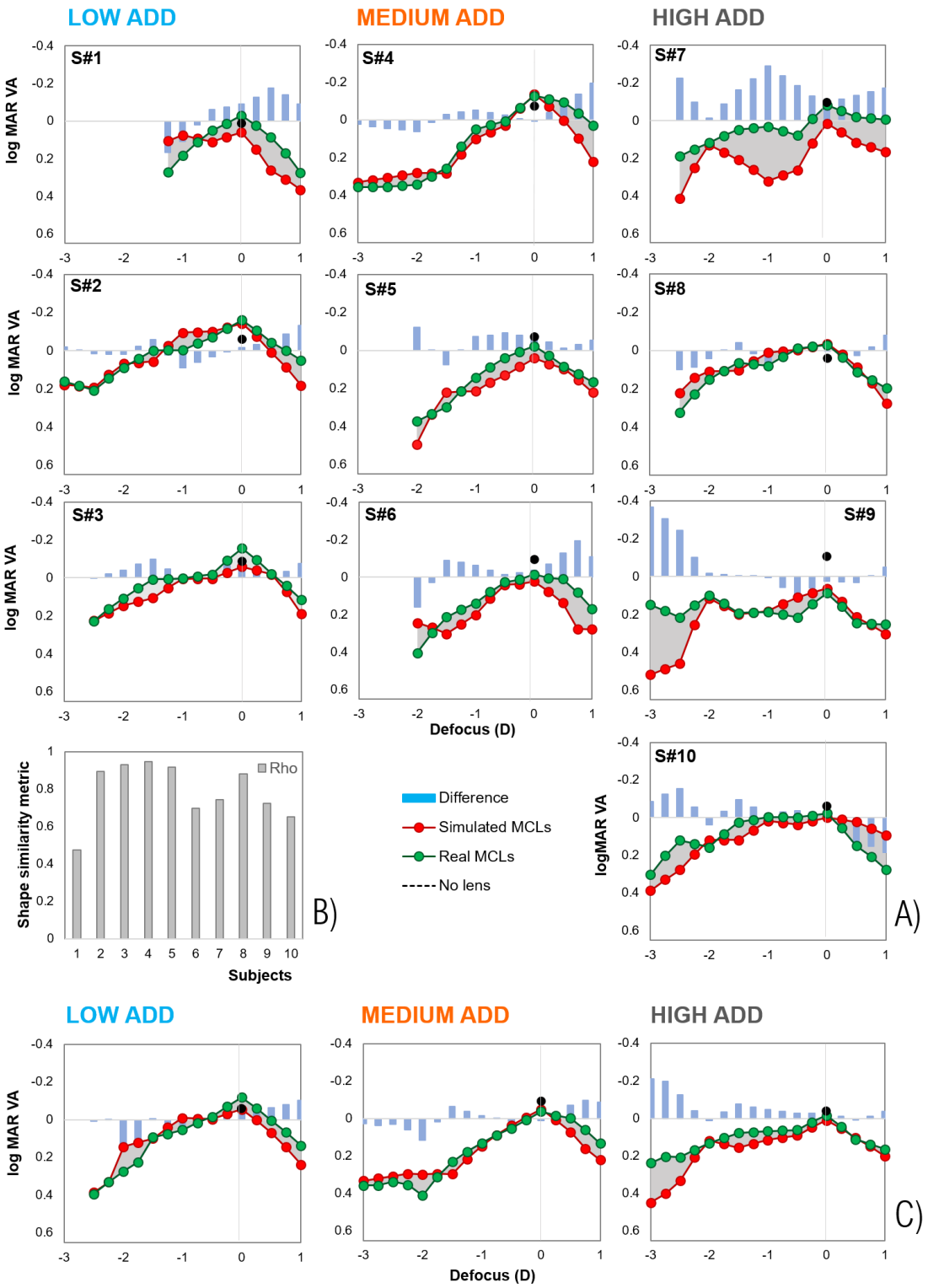

FIGURE 4.6. TF VA. A) TF LogMAR VA for all subjects with the simulated M-CLs (red lines), and the real M-CLs (green lines), with all three adds (low-add, first column; medium-add, second column; high-add, third column). Black dots stand for monofocal VA at the best focus of each subject with no lens. Blue bars show the difference between real and simulated M-CL curves. B) Shape similarity metric (crossed correlation, rho) for all subjects. C) Averaged TF LogMAR VA with all three adds (low-add, first column; medium-add, second column; high-add, third column).

4.4. DISCUSSION

As M-CLs expand as a solution for presbyopia correction, the understanding of their optical and visual performance, as well as their potential simulation prior to fitting becomes important. In this study, we present, to our knowledge, the first combined experimental investigation of the TF optical (through DP measurements) and visual (through VA) performance of multifocal soft contact lenses.

Several authors [342, 343] have reported TF DP retinal image quality using a commercial DP imaging system (the OQAS, or Visual Analyzer) by Visiometrics SL (Barcelona, Spain). In general, DP systems are better suited than Hartmann-Shack wavefront sensors to characterize optical quality with M-CLs, particularly for diffractive designs, and zonal refractive designs with relatively abrupt transitions between near and far. Most of the studies on M-CLs report TF VA and/or contrast sensitivity, and a few report aberrometric data with/without the M-CLs [152, 344]. Only a few studies have used a DP technique to study optical quality with M-CLs. In 2002, Gispets et al. compared the TF optical quality of two concentric bifocal CLs (center-distance design), using the DP technique, and found a better optical quality for distance than for near vision. The authors noted a pupil dependency on the optical performance with those lenses [345]. Also, Pujol et al. evaluated the optical quality at distance, intermediate and near vision in subjects with/without M-CLs and 2 different pupil sizes (3 and 5 mm), and found that optical quality at near was higher with the M-CLs and with 3 mm pupil size and optical quality was lower at distance with the M-CLs [346]. More recently, a DP technique has been used to measure the TF VA and the objective pseudo accommodation with a soft hydrogel CL for presbyopia (1-day Presbyo, Safilens), finding an increase in near visual performance and DOF with the presbyopic CL [347].

We found that although both TF DP and TF VA showed similar trends in the relative performance with the M-CLs of different additions, TF DP curves in subjects generally revealed more structure (i.e. peaks and notches) than the TF VA curves. This is likely due to the fact that the DP image intensities (related to Strehl) has a larger contribution from high frequencies (similarly to VS TF curves for the lens alone, **FIGURE 4.2**) than VA, which may be slightly more insensitive to structured blur, as long as the orientation of the E-letter stimulus is identifiable. These differences can roughly also be observed in the on-bench TF DP and TF 1P (E-letter stimulus), the latter remaining high over a relatively extensive dioptric range. On the other hand, lack of correspondence between optical and visual quality is not uncommon. Ocular aberrations' wavefront provides an excellent description of the eye's optical quality; however, a direct conversion to VA is not directly interpretable from the wavefront alone. Nankivil et al [348], showed that, although MTF alone is sufficient to predict population mean VA (in their study, across all measurements, predicted differed from measured (at 4 m) uncorrected VA by +0.01 and best corrected VA by −0.16), it was not sufficient to predict an individual's VA well. Instead, additional factors such as age and sphero-cylindrical refraction were needed to accurately predict an individual subject's VA, supporting the notion that other factors need to be considered to obtain more accurate estimates of VA.

Several authors have also reported visual performance at various distances with M-CLs, specifically with the designs tested in the current study (1-Day Moist). In a clinical trial on 72 presbyopic eyes, Sha et al. compared high contrast VA at different vision distances (6 m, 2 m, 1 m, 70 cm, 50 am and 40 cm) with three different M-CLs (1-Day Acuvue Moist Multifocal, Johnson & Johnson; BioTrue ONEday for Presbyopia, Bausch & Lomb; and Dailies AquaComfort Plus Multifocal, Alcon) [349]. They found that BioTrue performed better than Acuvue Moist at distance, AquaComfort Plus performed better than BioTrue at near, and Acuvue Moist performed better than BioTrue and AquaComfort Plus at intermediate and near. In the current study, we found that on average high contrast VA decreased with respect to the best corrected VA with no-lens, for 4-mm

pupil diameters. Our values of logMAR VA at far (-0.06), intermediate (0.13, 70 cm) and near (0.31, 40 cm), although nominally similar, are slightly lower than values from Sha et al., -0.05, -0.08 and 0.02 at those distances. Also, our differences in VA across add powers agree with reported values for the same lenses by Moody et al.[350].

We observe a large intersubject variation in the TF performance, even for the same M-CL and addition. For example, S#4 and S#5 are subjects of similar age (48 and 51 yo) and M-CL base power (-3.5 and -2.5) fitted with medium-add M-CLs, however, TF DP (**FIGURE 4.5**) and TF VA (**FIGURE 4.6**) curves are noticeably broader for S#4 than S#5. The underlying natural optical aberrations (in that particular example S#4 has better natural optics than S#5) and residual accommodation likely play a role in the intersubject variability, which occurs only in optical measurements (TF DP). Intersubject differences in perception likely play an additional role in the intersubject variability in TF VA.

The difficulty to predict visual performance and visual perception with M-CLs make the use of visual simulators clinically relevant. To our knowledge, this is the first study that demonstrates the ability of visual simulators to predict the performance of real commercial multifocal contact lenses in subjects. In particular, we have programmed the 1-Day Moist M-CLs in a SimVis system, which operates under the principle of temporal multiplexing. The system had been demonstrated before to simulate refractive and diffractive multifocal IOLs, or theoretical lenses with different energy distributions for near and far [325]. We found a high similarity of the TF optical and visual performance with the M-CL on the eye and with the SimVis-simulated lens. The average TF performance of the real lens and the simulation was nearly identical, indicating that the SimVis captures to a large extent the lens profile and that there is no particular bias for the physical M-CL to outperform the SimVis-simulated, or vice versa. At the individual level, the salient performance with the SimVis-simulation nominally matches the performance with the real M-CL. The differences of the DP retinal intensity metric (real – simulated) are marked only in two subjects. In S#7 and S#1 the DP image intensity values are much higher (indicative of higher quality) with the SimVis-simulated lens than with the real lens, which may be due to tear film disruption with the contact lens, as the DP metric is very sensitive to scattering. On the other hand, the underestimation of the magnitude of the DP metric with SimVis found in S#5 and S#10 does not have a counterpart in the VA measurements. We did not find that the magnitude of the discrepancy (less than 0.096 RMS difference in all cases) was associated with refractive error, the amount of aberrations or age in this group of subjects. Small variations in design of the 1-Day moist M-CLs for different refractive errors [350] (not programmed in this study) do not seem to have a particular relevance in accounting for the small discrepancies in individual subjects. Other differences between the performance of physical contact lenses and the simulations may arise from tear film, contact lens fitting or decentrations (not present in SimVis), and mismatch between pupil size. Also, in previous publications [220, 260] we discussed limitations to the fact that SimVis relies on temporal multiplexing to represent a spatial variation in the multifocal lens. While the evaluation in prior work was done for intraocular lenses, several conclusions can be extrapolated to contact lenses, particularly regarding the effect of ocular aberrations and pupil size in refractive lens designs. Also, we demonstrated that smooth varying lens profiles can be simulated using SimVis, provided that the target TF optical quality is known, and can be described with a limited number of temporal coefficients (150 temporal coefficients, 5.00 D TF range). Novel M-CLs are being designed with surfaces with varying amounts of spherical aberration, also in the transition zones, and their TF optical quality can be obtained from the design, using conventional optical design software. The procedure, and the resultant SimVis simulation, has already been validated in intraocular lenses

with sophisticated surface geometries (zonal refractive or diffractive) [187]. Consequently, novel M-CLs could be visually simulated with SimVis, even before they are manufactured.

4.5. CONCLUSIONS

Our study reveals that the SimVis visual simulator can be used reliably to provide subjects with the experience of multifocal vision, replicating the visual quality at various distances provided by real contact lenses. The study was performed in an experimental setting, with the Sim+Vis™ Technology (TL, operating custom driver and SimVis temporal patterns specifically programmed in this study to replicate those M-CLs) implemented in one of the channels of an AO system. Also, the study was performed for fixed pupil diameters (4 mm) and used high contrast VA targets. It is possible to translate the study to the clinical practice with the same SimVis temporal patterns replicating the M-CLs programmed in a portable SimVis binocular device (the SimVis Gekko™). Future studies will consider natural pupil dynamics (which entails programming the SimVis temporal patterns for a range of pupil diameters), and the use of natural images at far and near to assess visual perception in more realistic conditions.

In the two previous chapters, the optics of the eye have been manipulated using active elements, visual simulators, in the next chapters we will analyze another way of manipulating the optics of the eye and analyze the retinal response through convolution.

5

CHAPTER 5. MATCHING CONVOLVED IMAGES TO OPTICALLY BLURRED IMAGES ON THE RETINA

Convolved images are often used to simulate the effect of ocular aberrations on image quality, where the retinal image is simulated by convolving the stimulus with the Point Spread Function (PSF) derived from the subject's aberrations. However, some studies have shown that convolved images are perceived far more degraded than the same image blurred with optical defocus. We hypothesized that the positive interactions between the monochromatic and chromatic aberrations in the eye are lost in the convolution process. This chapter tried to test this hypothesis evaluated optical and visual quality with natural optics and with convolved images (on-bench, computer simulations, and visual acuity (VA) in subjects) using a polychromatic adaptive optics (AO) system with monochromatic (555nm) and polychromatic light (WL) illumination.

This chapter is based on the paper by **Aissati et al**. 'Matching convolved images to optically blurred images on the retina', published in Journal of Vision (2022). The coauthors are Clara Benedi-Garcia, Maria Vinas, Alberto de Castro, and Susana Marcos.

The work was presented as a poster presentation at ARVO annual meeting 2020 by **Aissati et al**. [351] under the title 'Convolved vs. Optically blurred images – What is the key reason for the observed differences?'.

It was also presented as an oral contribution **Aissati et al**. in an invited talk in the OSA Vision and Color Technical Division Data Blitz Series, under the same title.

The author of this thesis designed the experiment in collaboration with the rest of the authors, implemented the experimental protocol, performed the experimental measurements on subjects, collected and analyzed the data in collaboration with the rest of the authors, and prepared the manuscript in collaboration with Susana Marcos.

5.1. INTRODUCTION

The optics of the eye projects a degraded image on the retina. AO has become a suitable technique to correct or manipulate the ocular HOAs therefore modifying the form and magnitude of retinal blur [235]. AO systems are generally provided with an active element working in a closed-loop operation, such that the combined wave aberration of the AO mirror plus the eye's optics is nearly diffraction-limited. Correction of HOAs has been shown to result in improved VA [237] and contrast sensitivity [239, 352], and to improve certain visual tasks such as familiar face recognition [110].

Resorting to Fourier Optics is a common practice to illustrate the retinal image quality and to investigate the first step in the visual process. In this method, simulations of the images of an external object projected on the retina are obtained by the convolution of the original image ('Object') with the ocular PSF.

The PSF can be either measured experimentally from double-pass retinal images or calculated from the measured wave aberration. Estimations of the PSF of the eye include classical work by Flamant et al [95] where the light distribution curves in the retina were obtained using a slit of light to calculate the Line Spread Function (LSF), and Santamaria et al. [353] and Artal et al. [99] who at the Institute of Optics of the Spanish National Research Council (IO-CSIC) in Madrid reported the first DP PSF from human eyes.

The use of mathematical convolution to represent retinal images or to evaluate the effects of individual aberrations terms on image quality has been extensively used in the literature [102, 354, 355]. In a seminal paper, Artal [102] presented the first calculations of 2-D extended foveal images using experimental DP PSFs. More recently, the PSF used in convolution is calculated from the wave aberration, as the Fourier Transform of the pupil function, where the phase is the wavefront aberration and the modulus is the transmittance of the optical system.

The convolution calculations are often used to illustrate differences in the retinal image quality across patients with different aberration profiles [103], different treatments (for example intraocular lenses on different eyes) [356], or across the peripheral retina in the same subject [105]. Some authors have projected synthetic images (by convolution) on the subject's retina, trying to minimize the impact of the natural optics of the eye. Applegate et al. [107] presented visual acuity charts degraded by the subject's aberrations through a 3-mm artificial pupil size, assuming that this pupil diameter represents a good trade-off between diffraction and aberrations [357]. Lang and Peli [106] tested experimentally the degradation of an IOL in eyes monolaterally implanted with a M-IOL. They filtered the images with the OTF of the eye equipped with a M-IOL (divided by the OTF of the monofocal IOL) and presented them to the contralateral eye with a monofocal IOL for inter-eye comparison. Legras et al. [108] predicted retinal images with various levels of defocus by convolution and compared them with real defocused images with trial lenses, for different pupil diameters and monochromatic and polychromatic light. Various studies used convolved images to simulate different amounts and orientations of blur in psychophysical studies [197, 358].

Previous works use different strategies to minimize further degradation of the convolved stimulus viewed through the subject's optics, either using deconvolution with the observing optics, inverse filters, reducing the size of the observing pupil, or more recently, using AO to correct the eye's aberrations.

Despite the common use of convolved images to represent the retinal image quality, the underlying assumptions of this approach have not been deeply explored. In fact, recent studies report significant differences in VA assessed with simulated stimuli as opposed to optical manipulation of the aberration pattern in natural viewing conditions [113]. In more recent work, Ohlendorf et al. [359] found that VA was worse with simulated spherical error and considerably

worse with simulated astigmatic defocus than with real optical defocus of the same magnitudes. The origin of the discrepancies could not be explained.

Two factors have been argued to potentially impact differently the quality of convolved images projected on the retina through diffraction-limited optics and the quality of images directly degraded by the optics: the OSCE and the chromatic aberration. The SCE is often modeled as an apodized pupil. Some studies anticipate that the attenuation of the impact of the peripheral aberrations produced by pupil apodization may potentially improve the retinal image over constant amplitude in the pupil function [7, 127]. However, except for some experimental studies artificially shifting the peak location of the SCE function by filters which showed a small impact on the MTF and visual performance [93, 360, 361], there is little evidence that the SCE profile produces a significant impact on the retinal image quality [361-363].

The other potential contributor to a discrepancy between the convolved image and the real optical image projected on the retina is chromatic aberration. Convolved images are commonly generated using a monochromatic PSF [364]. However, images, even if projected through diffraction-limited optics, are subject to the chromatic aberration of the eye. Previous work has shown that in fact, the effect of chromatic aberration is more deleterious to vision under perfect optics than under uncorrected aberrations [116, 121]. Under this hypothesis, the convolved images seen through AO-corrected optics would produce the same retinal image as natural images seen through the aberrations of the eye. However, in polychromatic light, with AO, chromatic aberrations are still present and possible favorable interactions between chromatic and monochromatic aberrations would be attenuated.

The purpose of this study is to evaluate to what extent the optical and visual acuity with convolved stimuli is comparable to those obtained with natural optical aberrations, in monochromatic and polychromatic light. Understanding the discrepancy that exists between the images seen through the natural aberrations of the subject and convolved images opens up a breadth of possibilities for simulating different conditions and studying retinal quality through the subject's natural optics. For example, it would be possible to provide the experience of IOLs or CLs designs, refractive surgery patterns, or individual aberrations, without the need of complex optical elements for simulation.

5.2. METHODS

A polychromatic multichannel AO visual simulator system was used to measure and correct the HOAs of seven subjects. Measurements were performed with high-contrast stimuli seen under natural optics, and with convolved stimuli (degraded by the subject's aberrations) seen under AO155 corrected optics. Computational simulations and on-bench measurements were performed to evaluate the effect solely on optical grounds. Measurements of VA and computer simulations were done for monochromatic and polychromatic stimuli to evaluate the effect of chromatic aberration.

5.2.1. Convolved images

Convolved images were generated using standard Fourier Optics [365]. Simulated degraded stimuli of E-letters were used in both on-bench experiments where the stimuli were projected on the CCD camera acting as an artificial "retina" in an artificial eye, and in the VA tests in patients.

The Snellen E-letters stimuli for the VA psychophysical tests ranged between 0.20 to 49.05 arcmin angular subtend (which correspond to -1.3 logMAR to 1.1 logMAR). The Snellen E-letter

used in on-bench experiments subtended 19.62 arcmin (which correspond to 0.7 logMAR). The PSFs were computed from the ocular aberrations (previously measured with the Hartman-Shack) of each participating subject., as well as from the residual aberrations after AO-correction. Calculations were performed using the Fast Fourier Optics function (fft2) in Matlab. The scale of PSFs was calculated to match the pixel/angular scale of the stimulus object, according to the viewing conditions, size of the stimulus, and magnification of the system. The retinal image was simulated as the convolution of the PSF and the object (Eq.(5.1)), using the "conv2" function in Matlab.

$$\text{Image} = \text{PSF}_{555\text{nm}} \otimes \text{Object} \quad \text{Eq. (5.1)}$$

The total energy of the stimulus ('Object') and the energy of the final convolved image must be preserved after the convolution. Thus, the sum of the total energy of the PSF with the aberrations of each subjects was normalized to one.

Computational calculations were performed for 6-mm pupils and a monochromatic wavelength of 555 nm, replicating the experimental conditions, unless otherwise noted. The sets of Zernike terms to calculate the PSF were obtained from measurements with the Hartman-Shack wavefront sensor (wavefront fits up to a 7th order term). Piston and tilts were ignored. Convolved images were simulated for optimal focus, estimated as the defocus term that optimized a VS [259] metric in a TF range (from -4.00D to 4.00D in 0.01D steps). The original images (E-letters) were high contrast images (binary images contain only one bit per pixel to represent two gray values, 0 (black) and 1 (white)). The calculations were performed prior to the on-bench or the VA measurements. The DMD was linearized with the calibrated gamma curve.

5.2.2. On bench testing

The experimental measurement was mimicked with the deformable mirror and an artificial eye. The artificial eye consisted of a 50.8-mm focal length achromatic doublet lens and a CCD camera (DCC1240C - High-Sensitivity USB 2.0 CMOS Camera, 1280 × 1024, Global Shutter, Color Sensor; Thorlabs GmbH, Munich, Germany) acting as an artificial "retina", and was placed in the AO system at the position of the subject's eye. The aberrations of the subjects were mapped in the DM to simulate the condition of optical degradation by the eye's aberrations. In this condition, the Badal optometer was set to the defocus position that maximized the VS for each set of aberrations. Conversely, the deformable mirror was set to correct all the aberrations of the optical system and the artificial eye, and convolved images (simulated using the subject's aberrations) were projected on the retina of the artificial eye through fully corrected optics. The RMS of the residual aberrations was ~0.02 μm on average for a 6-mm pupil diameter. The Michelson contrast [366] of the images captured by the CCD camera in each condition was calculated to compare the contrast degradation produced by real aberrations mapped on the DM or by convolution with the same set of aberrations.

5.2.3. Subjects

Seven young subjects participated in the study, with ages ranging from 28 to 34 years (28.41 ± 1.60). Spherical errors ranged between +0.75 and −3.40 D (1.34 ± 1.90 D), and astigmatism was ≤ −1.25 D in all cases. All participants were acquainted with the nature and possible consequences of the study and provided written informed consent. All protocols met the tenets of the Declaration of Helsinki and had been previously approved by the Spanish National Research Council (CSIC) Ethical Committee.

5.2.4. Experimental protocol

Measurements on subjects took place in two different experimental sessions (seven days apart). In the first session, the HOAs were measured in NIR light. In the second session, VA was measured under different conditions. In all measurements, subjects were stabilized using a dental impression mounted on an x-y-z stage. The eye's pupil was aligned to the optical axis of the instruments using the line of sight as a reference. Pupil centration was verified before each trial and between conditions. Also, all measurements were performed monocularly, in a darkened room, under cycloplegia (Tropicamide 1%, two drops 10-min before the beginning of the experiment, and one drop after one hour) to dilate the subject's pupil and minimize the effects of accommodation during the measurements. All measurements were obtained for 6-mm pupil diameters.

Ocular aberrations measurements

The best subjective focus was initially searched by the subject while viewing a Maltese cross projected on the DMD at the reference wavelength of 555 nm. Then, the subject's aberrations (HOAs) were measured with the Hartmann-Shack wavefront sensor and corrected in a closed loop at 880 nm. The subject was asked again to adjust the Badal system position that provides the best subjective focus for this AO-corrected condition. Each measurement was repeated at least five times per condition.

Visual Acuity measurements

VA was measured following similar protocols to those described in previous studies at best subjective focus for 555nm or WL [113, 237]. Four different conditions for VA were tested: ***(1)*** natural aberrations (with the AO system correcting only the aberrations of the system) with a high contrast stimulus in monochromatic light (555nm), ***(2)*** Same as condition 1, but with the stimulus illuminated in WL, ***(3)*** natural aberrations corrected with DM and a simulated convolved stimulus, degraded by the natural aberrations of the subject, in monochromatic light (555nm), ***(4)*** Same as condition 3, but with the stimulus illuminated in WL. Conditions are represented in **FIGURE 5.1**. VA measurements were performed using an adaptive QUEST algorithm consisting of an eight alternative forced-choice (8AFC) [367] procedure of tumbling E letters programmed in Matlab psychtoolbox [255, 271, 300] to calculate the sequence of the presented stimulus (letter size and orientation) in the test following the subject's response. The QUEST routine for each VA measurement consisted of 40 trials and each one was presented for 0.5 seconds. The measurement was discarded if convergence was not reached and the task was repeated 3 times per condition. VA was expressed in terms of logMAR VA (logMAR = $-\log_{10}$|decimal VA|) [301]. Aberrations were monitored throughout the experiment before every VA measurement to ensure that each trial was performed under the desired state of aberrations correction. The total duration of the experiment was around 1.5 hours.

The luminance of the WL was adjusted perceptually to match that of the SCLS 555-nm light, in a psychophysical equi-luminance test [121, 368, 369]. The value of the neutral density filter was chosen from the average of the settings of 5 subjects.

5.2.5. Simulation of the effects of chromatic aberration

We computed the polychromatic PSF considering a polychromatic source image as a sum of a set of monochromatic PSFs for a representative selection of wavelength [53]. The sampling interval of the spectrum was from 450nm up to 800 nm, in 50 nm steps. In previous studies, the analysis was performed with different sampling intervals (1, 10, and 50 nm), and it was concluded that an interval of 50 nm was suitable for typical eye aberrations [370]. Each PSF was weighted with the luminance L(λ) of the polychromatic source (WL) [94, 364] and the CIE photonic luminosity function V(λ) at the corresponding wavelength [371]. The polychromatic PSF was obtained as the weighted linear sum of the monochromatic PSFs (Eq.(5.2)). The PSFs for all monochromatic wavelengths were computed using the measured HOAs in NIR, given that HOAs do not vary significantly with wavelength [53], and the chromatic difference of focus, obtained from the measured LCA. We assumed the best focus at 555 nm, and the defocus Zernike coefficients for other wavelengths were adjusted according to the psychophysical chromatic difference of focus reported by Vinas et al [281] in the 450-800 nm range.

$$\mathrm{PSF}_{\mathrm{poly}\,(x,y)} = \int \mathrm{PSF}_{(x,y,\lambda_{450\mathrm{nm}\text{-}800\mathrm{nm}})} \cdot \mathrm{L}\,(\lambda) \cdot \mathrm{V}(\lambda)\,\mathrm{d}\lambda \quad \text{Eq. (5.2)}$$

$$\mathrm{Image} = \mathrm{PSF}_{\mathrm{poly}} \otimes \mathrm{Object} \quad \text{Eq. (5.3)}$$

The same conditions of the experimental measurements in subjects were reproduced in the computational simulations, as illustrated in **FIGURE 5.1**: A) High-contrast E-letter targets were simulated to be degraded with natural aberrations with a monochromatic PSF_{555nm} and with a polychromatic PSF_{poly} light (in this condition an optical blur is evaluated, Eq.(5.3)). B) Additionally, convolved E-letter targets were simulated to be degraded by diffraction limit only (AO-simulation), with monochromatic $PSF_{555\ Diff\ Limit}$ and with polychromatic $PSF_{poly\ Diff\ Limit}$. The size of the E-letter used in this stimulus was 45 pixels, which is equivalent to a VA of 0.3 logMAR.

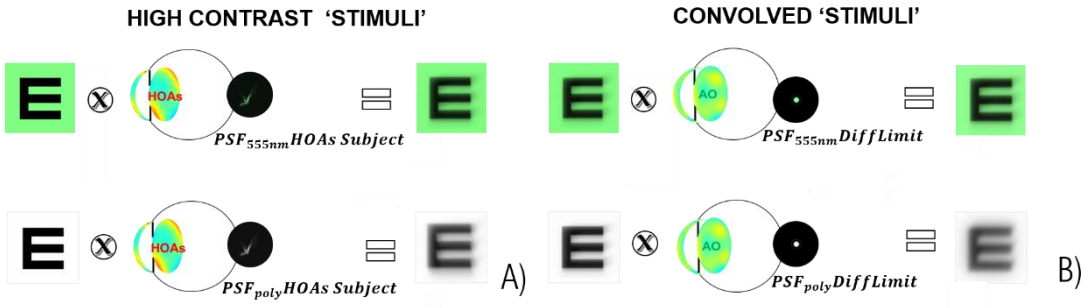

FIGURE 5.1. Illustration of the conditions tested computationally and in patients: A) High-contrast E-letter degraded with a monochromatic (555 nm) or polychromatic (white) PSFs calculated from the subject's aberrations; B) Convolved E-letter degraded with a diffraction-limited PSF both in monochromatic (555 nm) or polychromatic light.

5.2.6. Data analysis

The image quality metric to quantify the optical quality of computer-simulated and experimental images of an E-letter was the correlation coefficient, calculated as the 2D-correlation of the images in each condition with the high contrast E-letter image as the reference [187].

Statistical analysis was performed with SPSS software (IBM SPSS Statistics 27 SPSS, Inc., USA). For measurements in subjects, VA values were compared across conditions (natural

aberrations and convolved stimulus; monochromatic and polychromatic light). For E-letter stimuli, the 2-D correlation metric was compared across conditions (natural aberration and simulated convolution; monochromatic and polychromatic). In all cases, the Shapiro-Wilk test was performed to test for normality.

A non-parametric test (Wilcoxon Signed Ranks Test) was performed to evaluate statistical differences between conditions for VA and simulations. In addition, the different conditions for the 2-D correlation metric and VA were correlated (Pearson or Spearman's rho test) with VS (natural aberrations or convolved stimuli, both for monochromatic and polychromatic).

5.3. RESULTS

5.3.1. Wavefront aberrations (HOAs) and Visual Strehl (VS)

FIGURE 5.2 shows wave aberration maps for natural HOAs and residual HOAs after AO-correction (top panels), and thru-focus VS (bottom panel) for all subjects (6-mm pupil diameter). For illustrative purposes, tilt and defocus Zernike terms were set zero in the wave aberration plots. RMS values for natural HOAs ranged from 0.20 to 0.61μm, and the corresponding VS in green ranged from 0.38 to 0.18. RMS values following AO correction ranged from 0.05 to 0.11μm, and the corresponding VS in green from 0.66 to 0.90 (nearly diffraction-limited in all subjects).

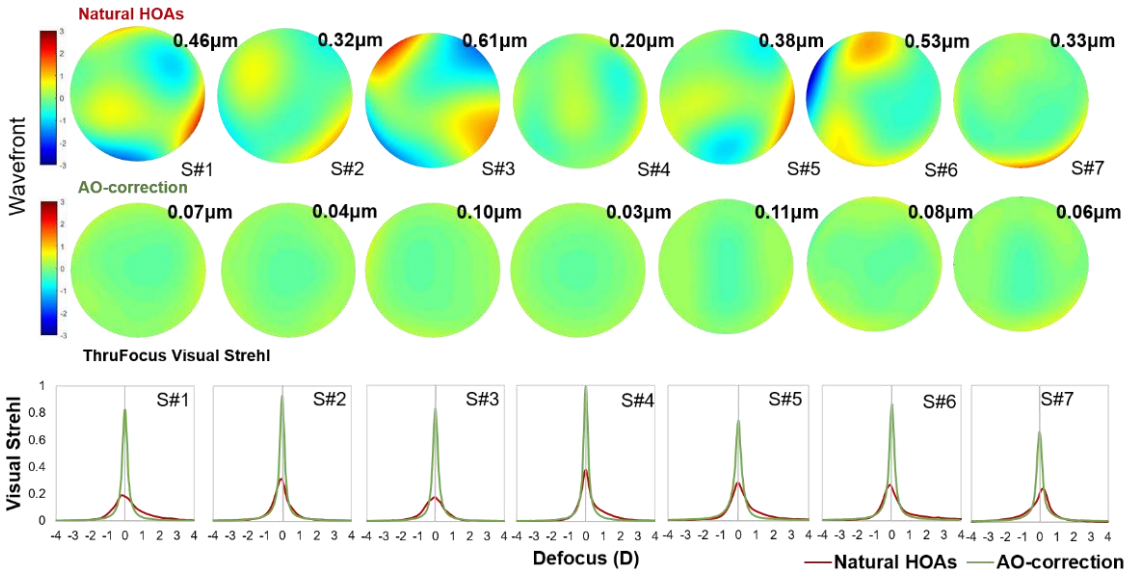

FIGURE 5.2. Subject's optical quality. Top row: wave aberrations (3rd order and higher) under natural conditions, with the corresponding RMS value at the top. Central row: wave aberrations under closed-loop AO-correction. Bottom row: Through-Focus Visual Strehl for natural aberrations (red line) and best AO-correction during Visual Acuity measurements (green line). Data are for 6-mm pupil size.

5.3.2. Experimental convolved images vs optical blur

FIGURE 5.3 A) shows the results for the on-bench study, where stimuli were degraded by the aberrations mapped on the DM (columns 3 and 5) or by convolution (columns 2, 4, and 6) and projected through a diffraction-limited system (row 1), and through natural aberrations (of subjects S#1-S#3). The images were captured on the CCD camera of the artificial eye (zero chromatic aberration) using monochromatic (555nm) and polychromatic (WL) illumination. The reference stimulus (column 1) corresponds to a 100-pixel size E-letter, equivalent to a 0.7 logMAR VA).

FIGURE 5.3 B) shows the values of the Michelson contrast of the retinal image for each tested condition in the on-bench diffraction limit system and through aberrated optics. Estimations were done studying the vertical profiles of the E-letter image. The discrepancy in the contrast between the simulated images degraded by convolution imaged through diffraction-limited optics and high contrast images through the wave aberrations imposed in the (DM) were 3% and 5% for a flat wavefront (diffraction limit) for 555 nm and WL, respectively, and 6% and 12% on average across subjects (S#1-S#3) for 555 nm and WL, respectively. This same procedure was repeated for low-order aberrations (defocus and astigmatism at different angles), as reported by Cheng X et al.[372]. As in the previous report, we found a high similarity between convolved and real images, with average contrast differences within 2% and 3% for 555 nm and WL, respectively.

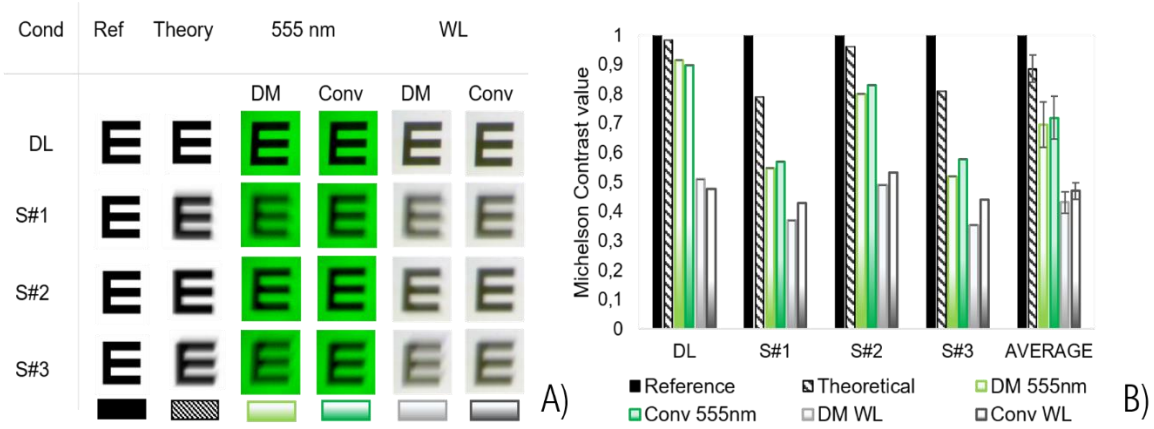

FIGURE 5.3. A) Comparison of images of an E-letter (100 pixels, 0.33 deg angular subtend) stimulus in optical simulations and captured with the CCD camera (at the retinal plane of an artificial eye. Column 1: High-contrast reference image (Ref); Column 2: Computer simulated image, calculated by convolution of the original image with the subject's aberrations and seen through diffraction-limited optics (Theory). Column 3: High-contrast image projected through an artificial eye with natural aberrations induced on a DM, in green light; Column 4: Convolved image projected through diffraction-limited optics (Conv); Column 5: As in 3, with white light; Column 6: As in 4, with WL. B) Michelson contrast value measured according to the maximum and minimum gray-scale values along with a central vertical profile in the image for the conditions shown in A (legend as indicated by the rectangular squares in the bottom of A). The simulations and experimental on-bench measurements A) and contrast analysis B) were performed for a diffraction-limited (DL) artificial eye and aberrations of three subjects enrolled in the study (S#1,2 and 3).

5.3.3. Visual Acuity with real aberrations and convolved images

FIGURE 5.4 shows the logMAR VA in the 7 measured subjects for all conditions. The average VA under natural HOAs was -0.04±0.01 (555 nm, light green squares) and 0.01±0.02 (WL, light gray squares), resulting in a difference of -0.05±0.01 logMAR between monochromatic and polychromatic illuminations. The average VA using convolved stimuli was 0.04±0.02 (555 nm, dark green squares) and 0.14±0.04 (WL, dark gray squares), resulting in a difference of -0.10±0.01 logMAR between monochromatic and polychromatic illuminations. VA was therefore systematically worse for convolved stimuli. The difference in VA with natural HOAs and with the convolved stimulus was larger in polychromatic light (-0.13±0.02 logMAR) than in monochromatic light (-0.06±0.01 logMAR). These differences in logMAR are equivalent to 3 letters in monochromatic illumination (p=0.01) and one complete line + one letter in polychromatic light (p=0.02) in a clinical chart [373]. The error bars in individual data represent the standard deviation of the three repeated measurements per condition and were ≤ 0.02 logMAR (high repeatability) in all cases.

The correlation between VA and visual quality (VS) was evaluated in all conditions. VA and VS were statistically significantly correlated for natural aberrations at 555 nm ($r = 0.73$, $p = 0.02$). However, VA and VS were not significantly correlated for convolved images at 555 nm ($r = 0.52$, $p = 0.18$), nor in WL for neither natural aberrations or convolved images ($r = 0.65$, $p = 0.12$).

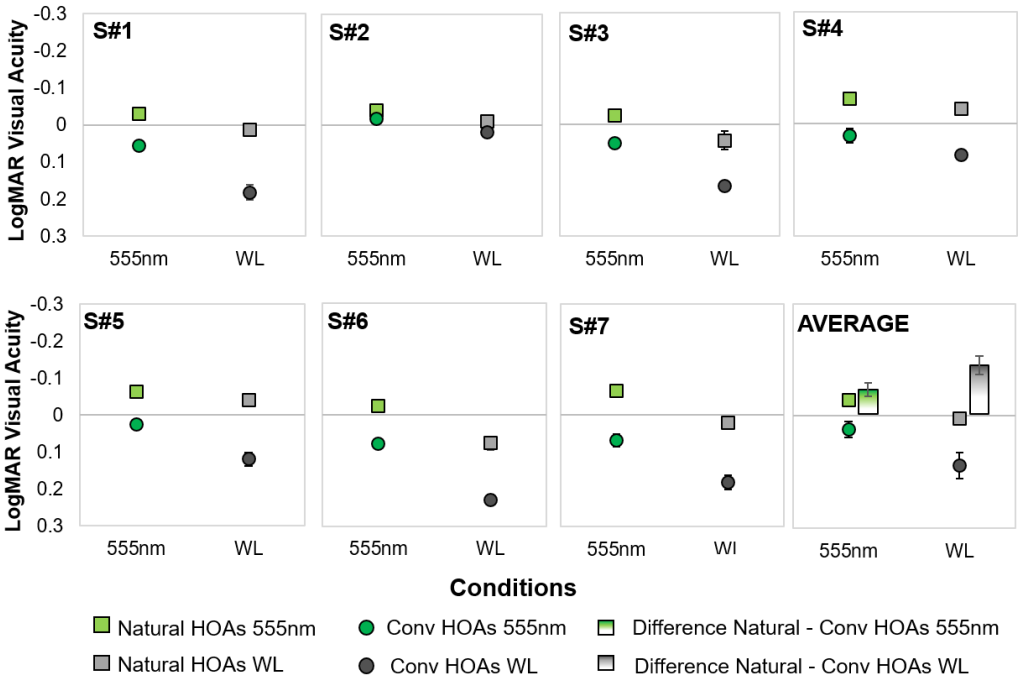

FIGURE 5.4. VA (symbols) for all subjects and average, for the following conditions: High contrast stimulus and natural aberrations in green light (light green squares); Convolved stimulus through natural aberrations, in green light (dark green circles); High-contrast stimulus and natural aberrations in white light (light gray squares); Convolved stimulus through natural aberrations, in WL (dark gray circles). The gradient bars in the average plot represent the VA differences between measurements with natural aberrations and convolved images in monochromatic (green bar) and WL (gray bar), on average. The error bars in the plots for individual subjects stand for the standard deviation of the repeated measurements (in most cases smaller than the symbol). The error bars in the average plot stand for standard deviations across subjects.

5.3.4. Simulations of mono- and polychromatic effects on retinal images

FIGURE 5.5 shows the estimated retinal image quality (2-D correlation metric) for simulated images using the subject's aberrations (bars, left y-axis) and the VA in the same subjects (symbols and dashed lines, right y-axis, for four different conditions: high-contrast green stimuli degraded by a monochromatic PSF_{555nm} (light green bar/squares); high-contrast white stimuli degraded by polychromatic PSF_{poly} (light grey bar/square); green stimuli convolved with PSF_{555nm}, followed by convolution with diffraction-limited optics, $PSF_{555nm\ Diff\ Limit}$ (dark green bar/circle); same convolved stimulus followed by convolution with diffraction-limited optics polychromatic $PSF_{poly\ Diff\ Limit}$ (dark green bar/circle). The 2D-correlation metric difference between real and convolved images was 0.01 in monochromatic green light and 0.04 in white light, this difference being statistically significant (p=0.02). There was a high correlation between 2D-correlation metric values for natural and convolved images in 555nm (p<0.001), but not in WL (p=0.76).

We did not find a correlation between VA with natural aberrations and VA with convolved images at 555nm (p=0.07) or in WL (p=0.54). However, there was a high correspondence between the predictions from optical simulations (2-D correlation metric) and VA in all conditions (r = 0.60, p <0.001, considering all conditions and subjects, with a normalized distribution of the residuals in the regression. The highest correlation between optical quality and VA was found for natural aberrations and monochromatic light (r=0.73, p=0.02), and the lowest with convolved images in WL(r=0.65, p=0.12).

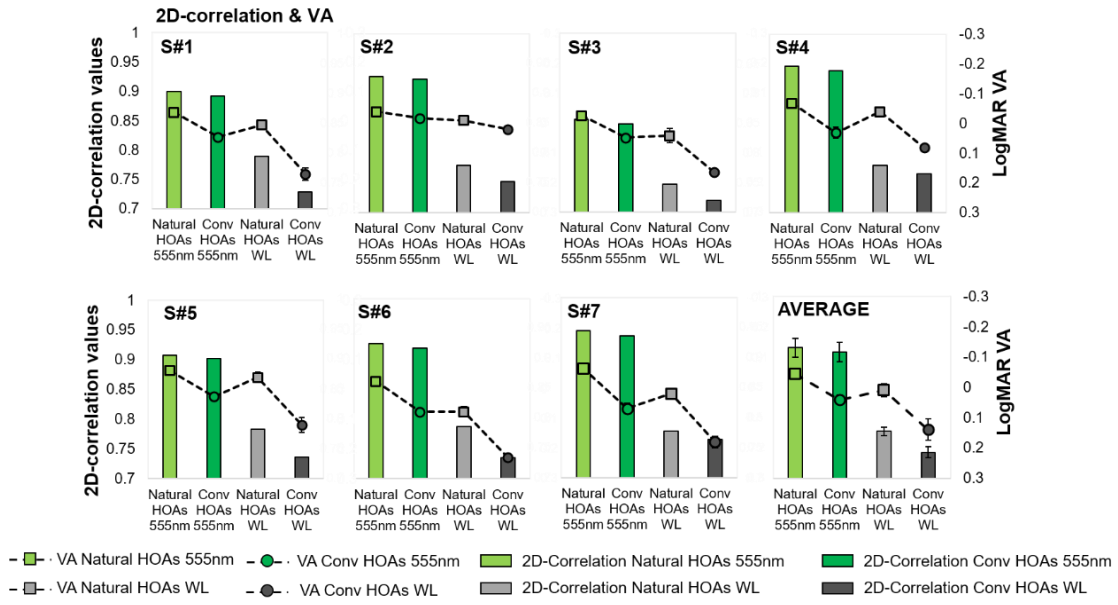

FIGURE 5.5. Optical quality (2-D correlation metric, left axis) and Visual quality (logMAR VA, right-axis) for the following conditions: High contrast stimulus and natural aberrations in green light (light green bar/square); Convolved stimulus through natural aberrations, in green light (dark green bar/circle); High-contrast stimulus and natural aberrations in white light (light gray bar/square); Convolved stimulus through natural aberrations, in WL(dark gray bar/circle); Dashed lines have been included to facilitate comparison of VA across conditions. The error bars in the plots for individual subjects stand for the standard deviation of the repeated measurements (in most cases smaller than the symbol). The error bars in the average plot stand for standard deviations across subjects.

5.4. DISCUSSION

Convolved stimuli to simulate the degradation assessed by HOAs are frequently used in studies aiming at understanding the impact of blur on visual performance. A systematic underestimation of the visual performance with the simulated stimuli, in comparison with real optical degradation, has been reported [113, 359] although the causes for the discrepancies were left unexplained. In the current study, we addressed this comparison in both an artificial eye and seven real subjects, using AO to control and correct the aberrations of the eye and the system, therefore minimizing the impact of double image degradation. Also, having a polychromatic AO system allows evaluating the chromatic effects for both optical blur and convolved stimuli.

We confirmed degradation of VA measured with stimulus degraded by convolution, although this was much lower than in previous reports. For example, a previous study reported a 50% discrepancy in the VA measurement with optical or simulated astigmatic degradation [359], as opposed to 8% for HOAs degradation in the current study at 555nm and 26% in WL.

Approximations in the computational simulation of the convolved image have often been raised as a potential cause for the discrepancy. Differences in the PSF computed using Fourier Optics, the Fraunhofer and Fresnel approximation and the exact solutions have been reported, under certain conditions (i.e. out of focus) [374]. However, our experiments in an artificial eye (without chromatic aberration, achromatic lens doublet) predict minimal differences between contrast degradation with real optics and convolved stimuli (taking into account the double-diffraction): 6% at 555 nm and 12% in WL, for RMS for HOAs ranging from 0 to 0.61µm. These values suggest that relying on assumptions in the computation of retinal images using convolutions is not a significant source of discrepancy, in monochromatic or polychromatic light, particularly in the absence of chromatic aberration.

Although convolved stimuli projected under AO-correction and high-contrast stimuli projected through aberrations induced by DM show some quantitative differences ≤ 12% (**FIGURE 5.3**), the fact that the differences are minimal when the induced aberrations were defocus or astigmatism, suggest that those discrepancies may be associated with a slightly lower compliance of the DM or imaging system when working with higher-order aberrations.

Experiments with both the artificial eye and real eyes were performed using monochromatic/polychromatic stimuli, although only monochromatic aberrations were used in the convolution. The same conditions experienced by the subjects were tested by computer simulation. The chromatic aberration of the instrument and the focusing lens of the artificial eye was expected to be negligible, while the eye is known to suffer from significant amounts of chromatic aberration [64, 266, 375].

However, in computer simulations and real eye measurements, including chromatic aberration resulted in systematic deterioration of the optical/visual quality with convolved images, with respect to the natural condition. This deterioration of VA with convolved images had been found in previous studies in polychromatic illumination [113], but so far, reports were not conclusive whether this decrease also occurred with monochromatic illumination. The current study confirms that the optical degradation of stimuli simulated by convolution and projected on the retina through diffraction-limited optics is significantly higher in polychromatic light than in monochromatic light ($p<0.05$).

This finding supports our hypothesis that chromatic aberrations play an important role in the degradation of the simulated stimulus seen under corrected monochromatic aberrations. Although chromatic and monochromatic aberrations have been shown to interact to improve retinal image or perception under natural conditions, the effect of chromatic aberrations is highly detrimental in diffraction-limited eyes [116, 121], as it occurs in experiments in which convolved stimuli with the

aberrations of the subjects are observed through corrected optical aberrations with AO to avoid double degradation.

Several previous studies have evaluated the impact of chromatic aberrations (both TCA and LCA) in an eye in the presence of monochromatic aberrations or corrected for monochromatic aberrations [53, 67, 236]. In the simulations shown earlier, only the LCA was considered. LCA is fairly constant across subjects, ~2 D between the two ends of the visible spectrum (400-700 nm), in phakic subjects [58, 281, 375, 376]. In contrast, the reported TCA varies largely in the population, both in magnitude and orientation [83, 375, 377]. The TCA in five of the seven subjects participating in the current study was available from previous work (**Chapter 7** of this thesis), and it was on average -0.20±0.10 arcmin in the vertical direction and 1.54±0.10 arcmin in the horizontal direction. We re-calculated the MTFs in all subjects for the four conditions of the study incorporating both the individual measurements of monochromatic aberrations and LCA and TCA, using the method described by Marcos et al. [53]. Unlike other studies [53], and likely due to the small magnitude of the foveal TCA in our subjects, we did not find that incorporating TCA further reduced significantly the MTF, neither under natural aberrations or diffraction-limited optics. Given that the effect seemed to be driven primarily by LCA, we limited the analysis to calculations using LCA only.

The SCE has often been invoked as a potential factor leading to discrepancies in the simulated or real retinal image quality, as the pupil apodization may lead to a smaller effective pupil and therefore improved effective optical quality with natural optics. In a study of this thesis whose results will be presented in **Chapter 7**, we measured the peak positions of the OSCE in a subset of the subjects of the present study (five of the seven subjects). As those measurements were obtained from a reflectometric technique (LRT, measurements in green light) [360], we did not attempt to use the width of the measured OSCE function in the simulations, as there are known differences in the width of the psychophysical and reflectometric OSCE, [378]. We therefore assumed a value of ρ=0.1mm^{-2} for the SCE width. On average, for these subjects, the OSCE peak location lies at 1.20±0.34 mm nasally and -0.34±0.39 mm inferiorly from the geometric center of the pupil. The simulations incorporating the OSCE were analyzed in terms of VS. We found an average increase of only 5% in VS when the SCE was included. We correlated the decentration of the OSCE peak with the discrepancy in the VA measurements from simulations and real aberrations and did not find any statistical trend ($p>0.05$). This analysis suggests that the SCE does not play a significant role on the simulated retinal images, and therefore on differences between VA measured through natural aberrations and convolved stimuli (in green light).

Experiments were conducted under cycloplegia, minimizing the presence of fluctuations of accommodation. However, while in the optically degraded condition, residual accommodation (if still present) may interact favorably with the natural aberrations, those possible favorable interactions are by no means possible with the convolved stimuli displayed on the screen residual aberrations after AO-correction of aberrations. Also, it has been suggested that scattering in the ocular media may combine differently with aberrated or diffraction-limited optics, which could be an additional source of discrepancy [379] between stimuli observed through the natural optics, and convolved images observed through AO-corrected optics (but still subject to diffraction). However, we did not find a significant correlation between the difference in VA with natural aberrations and simulated images (in green light) as a function of residual aberrations in the AO correction ($p> 0.05$).

5.5. CONCLUSIONS

Convolved stimuli are widely used to assess the effects of low and high-order aberrations and optical corrections on visual performance. To our knowledge, this study presents the first direct comparison of visual performance under high-order natural aberrations and that obtained with simulated stimulus by convolution in monochromatic and polychromatic illumination. The use of adaptive optics to minimize the impact of the subjects' natural aberrations has allowed us to perform the comparison in the best comparable conditions, resulting in a better match between natural aberrations and the degradation by simulation of convolved images than previous reports. The systematic decrease in visual performance measured with VA and retinal image quality by simulation with convolved stimulus appears to be primarily associated with the lack of favorable interactions between chromatic and monochromatic aberrations [53, 116, 121, 380].

Optical simulations and VA experiments in real eyes support the hypothesis that a larger degradation with convolved stimuli (observed through corrected optics) in comparison with natural viewing occurs most noticeably in polychromatic light. Besides additional confirmation of the interactive effects of chromatic and monochromatic aberrations, this study has practical implications in studies that use convolved images in psychophysical studies.

In this chapter, we have studied the difference between convolved images and images seen through natural aberrations in monochromatic and polychromatic light. In the next chapter, knowing where the discrepancy comes from, convolution will be used to study everyday tasks such as face gender recognition.

6

CHAPTER 6. GENDER IDENTIFICATION OF FACES UNDER MANIPULATED OCULAR OPTICS

Correcting ocular aberrations of the eye improves certain visual tasks such as visual acuity and familiar face recognition. In addition, the eye appears to be adapted to its native optics. In this chapter, we evaluated how manipulated aberrations influence face gender identification and visual acuity tasks.

This chapter is based on the unpublished manuscript 'Gender Identification of faces under manipulated ocular optics' collaboration with Miguel Eckstein, from Vision and Image Understanding Lab (VIU, Santa Barbara). The co-authors are Clara Benedi-Garcia, **Sara Aissati**, Miguel Eckstein, and Susana Marcos.

This work was presented as a poster presentation at ARVO annual meeting 2020 by Benedi-Garcia et al. [381] under the same title.

The author of this thesis implemented the experimental procedure in collaboration with Clara Benedi-Garcias, performed the experimental measurements on subjects, collected and analyzed the data in collaboration with Clara Benedi-Garcia, and prepared the manuscript in collaboration with Clara Benedi-Garcia and Susana Marcos.

6.1. INTRODUCTION

AO in combination with a psychophysical channel has become a useful tool to test visual performance, manipulating the retinal image quality of the eye.

Most studies are based on analyzing the effects of aberrations on vision using standard visual tests, like visual acuity (VA) and contrast sensitivity (CSF) [239]. However, the importance of using natural images (landscapes, buildings, faces) and evaluating visual performance through tasks closer to the subjects' daily experience is gaining more and more importance. Sawides et al.[243] assess the impact of aberrations on tasks such as a familiar face or facial expression recognition.

Humans recognize one other mostly through their faces. Both basic and applied studies are interested in determining which characteristics make it possible or impossible to recognize a face. Basic research is interested in it since it would explain a fundamental human perceptual process as well as the underlying physiological mechanisms of a difficult visual task. Furthermore, the findings are likely to apply to the perception of other visual stimuli having significant configurational aspects. In the near future, it is of relevance to applied research because it would make it feasible to improve methods for working with eyewitnesses, design video surveillance (CCTV), and with it automatic identification systems, and develop better person/machine interfaces (based on ideal observer).

The research aiming at explaining the face recognition process is divided into three categories: cognitive, psychophysical, and neurophysiological. For our area of knowledge, we will focus on psychophysical.

The psychophysical technique manipulates the image's physical features, usually by filtering specific spatial frequencies (SFs), to see how these influence recognition processes [382].

Any image, whether it's of a human face or another visual object, can be defined in terms of SFs, or the sum of a set of sinusoidal grating with varied frequencies (HiSFs-high spatial frequencies and LoSFs-low spatial frequencies) and orientations. Our perceptual system evaluates visual information on numerous scales or frequencies, according to psychophysical research on contrast detection and adaptation to specific SFs [383]. In early visual processes such as edge, stereopsis, movement, and depth perception, it is now widely accepted that spatial filtering is the basic mechanism for obtaining visual information.

In order to better understand the parameters (neural and optical) that influence the effect of aberration correction on visual performance and whether correcting aberrations represents a real benefit in tasks involving different spatial frequencies or how the manipulation of the aberrations affects the perceptual response of the subjects, we examined the gender identification and visual acuity with convolved images and aberration correction in normal individuals.

In particular, the current chapter addresses the following questions: Do subjects have the impression that natural images look sharper with AO correction and if so, is the correction correlated with the amount of corrected aberrations? Does the effect of the correction have the same impact on tasks with different spatial frequencies? And in the case of optical modifications such as rotation of the aberrations, or external aberrations to the subject? Considering gender recognition as a low spatial frequency task, and visual acuity as a high spatial frequency. Do gender identification and visual acuity have the same behavior for the same study conditions?.

6.2. METHODS

The monochromatic AO system was used to measure gender identification (GI) and VA. For GI we convolved images for different manipulated aberration condiction. The images were presented through AO correction. And VA was measured with conditions mapped in the DM.

6.2.1. Subjects

In this study, nine subjects aged 25 to 47 years (31.6±4.7yrs) participated in the experiments. Spherical errors ranged between -0.25 and -5.75D (-1.39±1.13). The cylinder was ≤ -1.75D in all cases. Subject signed a consent form approved by the Institutional Review Boards after they had been informed of the nature of the study. All protocols met the tenets of the Declaration of Helsinki.

6.2.2. Optical quality

Optical aberrations of each subject were measured in the monochromatic AO system (described in section 2.1.1. of this thesis) and expressed by a Zernike polynomial expansion up to the 6th order, obtained as the average of 3 repeated measurements. VS ratios were estimated as the normalized volume under the MTF, calculated from the measured wave aberrations for 5-mm pupil diameters and green light (550 nm).

6.2.3. Stimuli

The gender face images presented to the subjects were acquired from the collaborator Vision and Image Understanding Laboratory at the University of California (Santa Barbara, USA). When taking the images, the photographed subjects declare their gender, and thus they are clarified in male and female. All the images were grayscale and cropped to remove the background and hair. Gender faces were discarded if any signs of gender were identified, such as beards or mustaches. Conditions are shown for a male and female example in **FIGURE 6.1** (B).

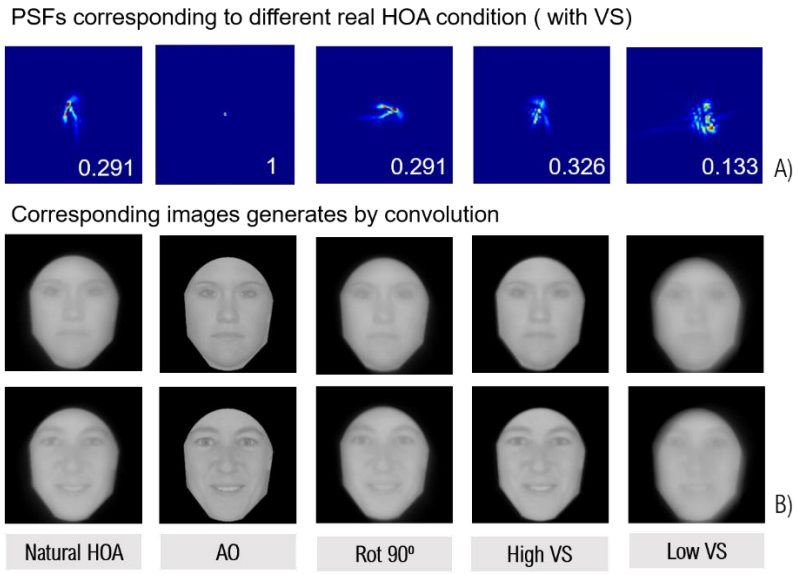

FIGURE 6.1. A) PSFs corresponding to the natural aberration of the subject (low and high order aberration), a rotated version of the PSF 90º, the PSF of a subject with high and low VS (number in the corner). B) Female (up row) and Male (down row) images convolved with the PSF indicated in section A).

An image of a face (female/male) (1.98-deg angular subtend, 480 x 480 pixels) was convolved with the PSF, using standard Fourier Optics technique [91], estimated from each subject's natural aberrations **FIGURE 6.1** A). The sets of Zernike terms to calculate the PSF obtained from measurements with the Hartmann-Shack wavefront sensor (wavefront fits up to a 6th order term). Piston, tilts were set to zero, and the defocus term was the value that optimized a VS metric [259]. All computations were performed for 5mm puìls.

Different sets of images were generated for each subject corresponding to the different conditions tested. Each subject showed convolved images with their own aberrations (Nat), the same aberrations rotated 90° (rot90º), and two sets of external aberrations, one with VS higher (better -NatB) and lower (worst -NatW) than their own VS.

6.2.4. Experimental procedure and Psychophysical measurements.

Measurements on subjects took place in three different experimental sessions. In the first session, the HOAs were measured in NIR light. In the second session, GI and VA were measured under different conditions. All experiments in the second session were performed under full AO corrected aberrations. On the other hand, in the third session, the experiments were performed under natural aberration. In all sessions, measurements were conducted at the best subjective focus, adjusted by the subject with the Badal system (under natural aberration or AO-correction). The subjects were stabilized using a dental impression mounted on an x-y-z stage. The eye's pupil was aligned to the optical axis of the instruments and was verified before each trial and between conditions. Also, all measurements were performed monocularly, in a darkened room, under cycloplegia (Tropicamide 1%, two drops 10-min before the beginning of the experiment, and one drop after one hour) to dilate the subject's pupil and minimize the effects of accommodation during the measurements.

The conditions tested in each of the sessions are described below in **TABLE 6.1**, and the tasks were GI and VA, in both sessions.

TABLE 6.1. Summary of tested conditions.

Session 2	Session 3
Natural aberration (GI_Nat / VA_Nat)	Natural aberration (GI_Nat / VA_Nat)
Aberration correction (GI_AO / VA_AO)	Aberration correction (GI_AO / VA_AO)
Natural aberration rotated 90º (GI_rot90º / VA_rot90º)	Natural aberration 3mm pupil size (GI_p3mm / VA_p3mm)
External aberration Lower VS (GI_NatW / VA_NatW)	Natural aberration + Defocus +0.50D (GI_Def0.50 / VA_Def0.50)
External aberration Higher VS (GI_NatB / VA_NatB)	Natural aberration + Defocus +1.00D (GI_Def1.00 / VA_Def1.00)

The GI conditions were convolved images whereas the VA conditions were mapped in the DM and not convolved.

Gender Identification

The gender identification involved a presentation of 400 faces (200 images of males and 200 females). The task of the subject was to provide a graded response with 3 levels of confidence (very sure, sure, and not sure) by using a numerical keyboard. Each image was presented during 0.5 secs and after, a gray square with a black cross image was indefinitely presented during the subject's response. Images were randomly ordered for each condition. Conditions were split into 4 blocks of 100 trials and blocks were randomized between conditions. Conditions were simulated using convolved images while the DM corrected the subject's aberrations. Aberrations were monitored in each block to ensure that each block had the same visual quality and the RMS was low (less than 0.10 microns).

Visual acuity

VA was measured using an 8AFC procedure with high-contrast tumbling Snellen E-letters. Subjects were asked to identify the orientation of the letter E (pointing right, left, up, down, or oblique) that was displayed on the mini-display. Each run consisted of 35 trials presented for 0.5 seconds. A QUEST algorithm was used to select the size of each stimulus and optimize the estimation of the spatial resolution threshold. Experiments were done at the subject best subjective focus under simulated conditions. Conditions were simulated using the DM.

6.2.5. Data analysis

Optical quality was evaluated in terms of RMS wavefront error (excluding tilt and defocus) and SV. For the analysis of the GI difference in the conditions of natural aberrations (GI_Nat) and natural aberrations rotated 90º (GI_rot90º), the symmetry of the PSF has been studied. And also, the impact of independent aberrations such as the case of astigmatism and its relationship with the best focus of the VS has been analyzed.

Statistical analysis was performed with SPSS software (IBM SPSS Statistics 27, USA). For measurements in subjects, mix linear model is used to analyze the data, with GI as the dependent variable, gender, optical quality group, condition variables as fixed effects, and session as a random effect.

In all cases, the Shapiro-Wilk test was performed to test for normality. A non-parametric test (Wilcoxon Two-Related-Samples) was performed to evaluate statistical differences between conditions (GI and VA) and sessions. The learning effect has also been analyzed using R^2 Nagelkerke test.

6.3. RESULTS

6.3.1. Subject Optical quality

FIGURE 6.2. shows wave aberration maps for natural HOAs and corresponding PSFs for the natural aberration and natural aberration rotate 90º (top panels), and TF VS (bottom panel) for all subjects (5-mm pupil diameter). For illustrative purposes, tilt and defocus Zernike terms were set zero in the wave aberration plots. RMS values for natural HOAs ranged from 0.15 to 1.06μm, and the corresponding VS in red ranged from 0.09 to 0.61. Subjects are ordered according to their VS, defined below, from the worst to the best value, and divided into two groups (Low VS avg 0.2±0.06, High VS avg 0.4±0.2).

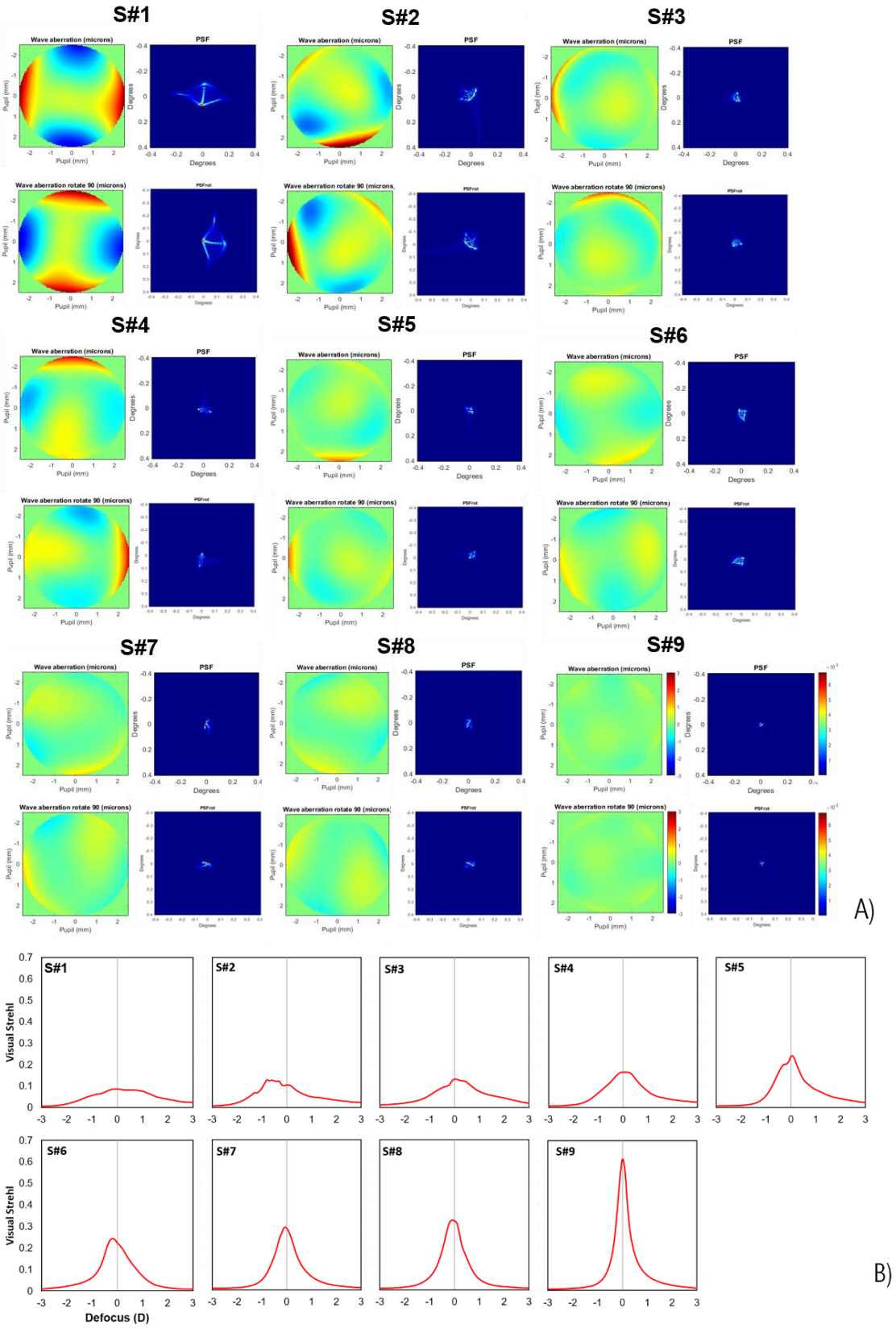

FIGURE 6.2. Subject's optical quality. A) Even row: wave aberrations (3rd order and higher) and compute PSF under natural conditions; Odd row: wave aberration rotate 90º and rotate 90º PSF for each subject; B) TF VS natural aberrations (red line). Data are for 5-mm pupil size.

6.3.2. Gender Identification vs Visual Acuity

FIGURE 6.3. shows the percentage of success in the task of gender identification (% GI, bars) and LogMAR visual acuity (VA, symbols) in the 9 measured subjects for all conditions and sessions. The subjects are divided into LowVS (blue) and HighVS (yellow).

TABLE 6.2. Average (avg) and standard deviation (std) of the conditions tested for the GI and VA tasks in sessions 2 and 3.

Session 2

	%GI (avg±std)		VA (avg±std)	
	VS		**VS**	
	Low	High	Low	High
Nat	66.1±2.0	77.1±2.5	+0.03±0.05	-0.08±0.05
AO	74.8±1.5	79.2±3.0	-0.06±0.04	-0.11±0.06
Rot90º	65.8±4.0	78.5±3.0	0.18±0.15	-0.03±0.05
NatW	50.5±16.5	75.5±4.0	-0.08±0.03	-0.03±0.10
NatB	68.8±2.2	69.4±2.2	-0.02±0.07	-0.03±0.02

Session 3

	%GI (avg±std)		VA (avg±std)	
	VS		**VS**	
	Low	High	Low	High
Nat	67.0±2.0	77.0±2.5	+0.15±0.01	-0.12±0.05
AO	79.3±1.5	77.8±3.0	-0.13±0.02	-0.14±0.03
p3mm	79.3±1.5	75.3±4.0	-0.02±0.03	-0.09±0.04
Def0.50	72.5±16.5	70.3±2.5	+0.06±0.03	-0.03±0.03
Def1.00	64.6±4.0	73.4±4.0	+0.10±0.07	-0.07±0.04

The best condition for both groups of optical quality (all sessions) was the AO condition, however, correcting natural aberrations has a higher impact in the low VS group for both, GI and VA task (difference of 9 vs 1.4 for GI and 0.11 vs 0.02 for VA). The correlation between GI and VA was evaluated in all conditions, and we found a correlation between both variables' tasks ($r = 0.56$). However, only VA was statistically significantly correlated with the mix linear model ($p < 0.05$).

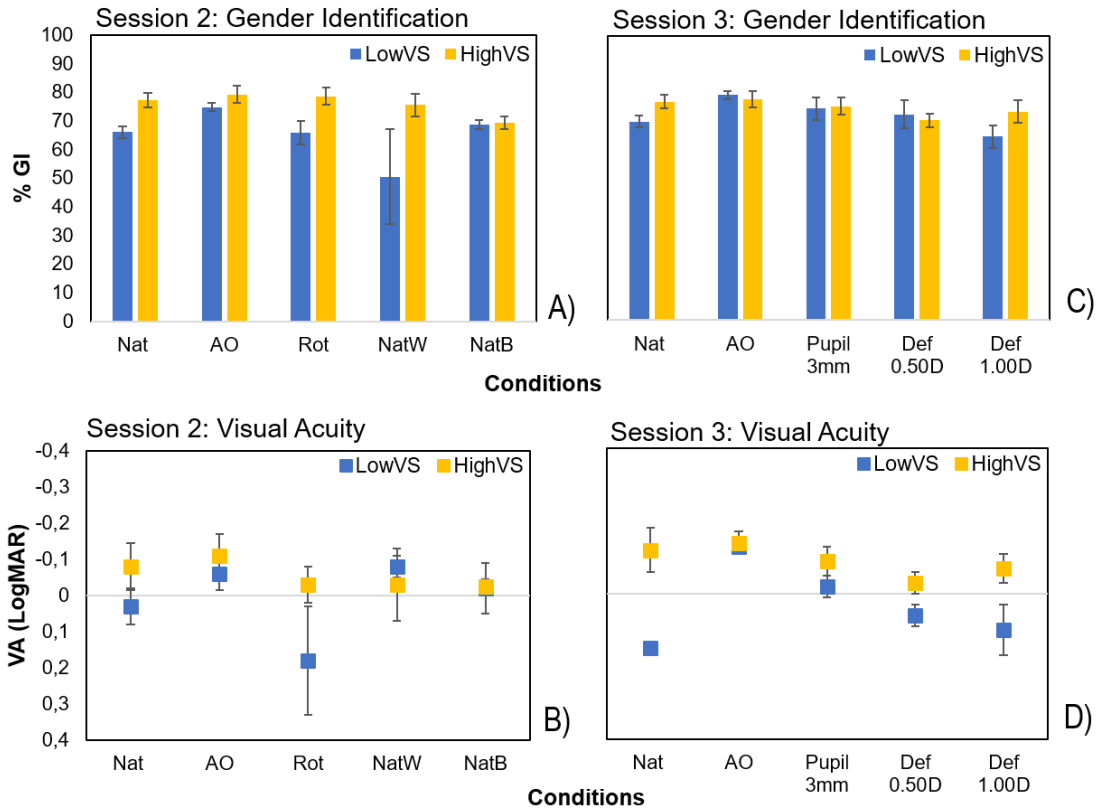

FIGURE 6.3. A) Bar graph - Session 2 - % Gender Identification (% GI) in the different conditions, natural aberration (Nat), AO correction (AO), natural aberration rotate 90º (rot90º), external worst VS (NatW) and external better VS (NatB); B) Scatter plot –Session 2 VA same condition that before. C) Session 3 - % GI in the different conditions, natural aberration (Nat), AO correction (AO); small pupil size (p3mm), induce defocus + 0.50 (Def 0.50) and induce defocus +1.00D (Def 1.00). D) Scatter plot –Session 3 VA same condition that before. In all graphs, the group has Low optical quality (LowVS, blue) and high optical quality (HighVS, yellow). Error bars stand for standard deviations across subjects.

6.3.3. Optical quality and visual performance

FIGURE 6.4 shows the analysis of the computed PSFs from the aberrations of the subjects for studying the symmetry. The PSFs were fitted to an ellipse and their eccentricity were calculated. The PSFs fitted to an ellipse have more eccentricity ('e') the more asymmetric it is. This analysis has been carried out to try to explain why there are subjects who perform the condition of natural aberrations rotated 90º better than the condition of natural aberrations.

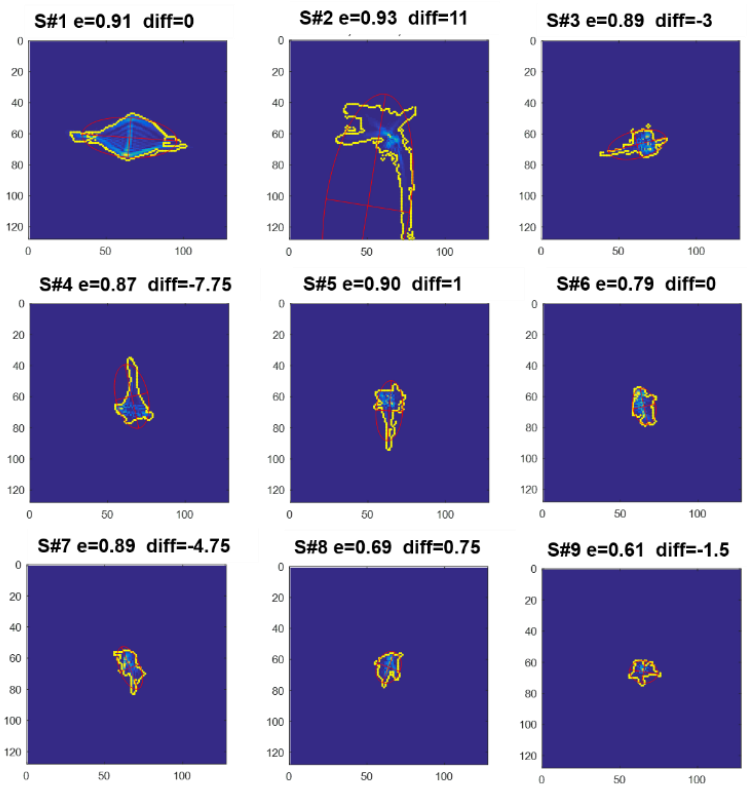

FIGURE 6.4. Analysis of the PSF according to the fitting to an ellipse; where 'e' is the eccentricity, the greater it is, the more asymmetric the PSF is, for each subject; and the value of 'diff' indicates the difference between the natural aberrations and the natural aberrations rotated 90º.

The **FIGURE 6.5** studies the effect of individual aberrations that are affected by orientation, such as astigmatism and coma but also the spherical aberration. In astigmatism, a difference is made between astigmatic with the rule (WTR) and against the rule (ATR). When the value of the difference between the natural aberrations and the aberrations rotated 90º (Dif Nat-Rot) is positive, the subjects perform the task better with their natural aberrations, on the other hand, if this difference is negative, they prefer their rotated 90º natural aberrations.

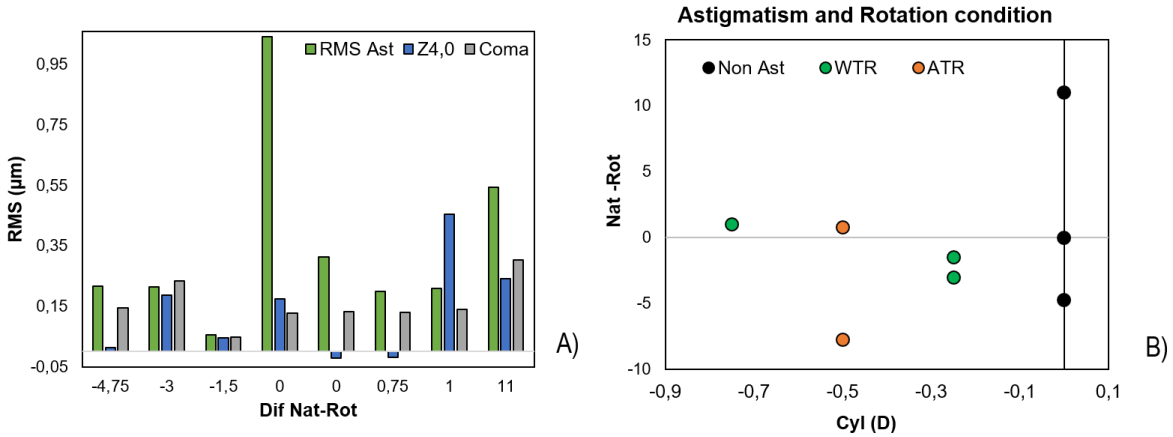

FIGURE 6.5. A) Representations of the RMS value of the individual aberrations of astigmatism (green), spherical (blue), and coma (grey), versus the difference between natural aberrations (Nat) and natural aberrations rotated 90º (rot); B) Classification of refractive astigmatism in with the rule (WTR) or against the rule (ATR) in the Nat-Rot condition.

In **FIGURE 6.6** the effect of astigmatism has been analyzed in function of the VS with which the convolution of the images has been carried out (VS Conv, red), VS taking into account refractive astigmatism (VS Astigmatism, blue) and VS according to the circle of least confusion, (VS Rot, black) midpoint between the two primary focal lines of sphero-cylindrical refraction, for subjects with the highest value in the Nat-Rot condition. This difference between natural and rotated has only been observed in the GI task. For VA, the subjects perform the task better with their natural aberrations than with the rotated one, regardless of their optical quality.

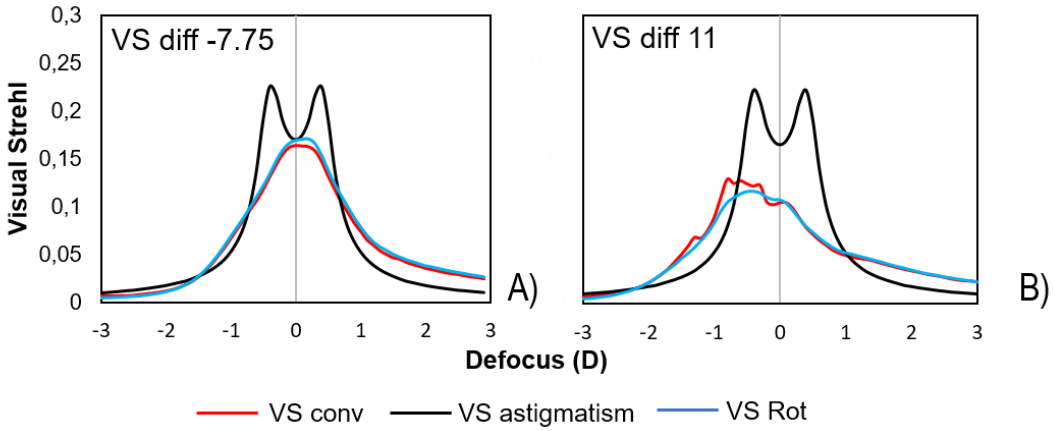

FIGURE 6.6. A) and B) Visual Strehl for different conditions; VS induced in the convolution according to the greater its maximum value (VS conv, red); VS taking into account your refractive astigmatism (VS astigmatism, blue); VS according to the circle of least confusión for each subject (S#4 (A), S#2 (B)).

6.4. DISCUSSION

The GI and VA tasks studied correspond to different spatial frequencies. This leads to perceiving differences when correcting for aberrations and manipulating aberrations in an AO system.

The greatest benefit of correcting aberrations occurred in subjects with poorer optical quality, this finding is in agreement with previous studies [110, 237]. This systematic improvement has been observed both in the GI task and in VA. This finding was found in the study by Sawides et al. [243] where they studied another type of real-life task different from GI but in the same trend, and they were familiar face recognition and facial expression recognition. The increased contrast and spatial frequency content of the image may have made it easier for the subject to recognize the face.

The condition of rotating aberrations involved a decrease in VA, mostly in those subjects with poorer optical quality, but also in those with high visual quality but to a lesser degree. In the case of the gender identification task, the subjects with lower VS also experienced a decrease in the correct response for this condition, although the subjects with higher VS did not. This could be explained because, subjects with lower VS have a more asymmetric PSF, calculated as the eccentricity of the ellipse that fits the PSF of each subject (slope=-0.60, r=0.87). We highlight the subjects (S#2, diff=11; S#4, diff=-7.75, **FIGURE 6.6**) with the higher differences between Nat and Rot90º. Both subjects have a very similar VS when we take into account only astigmatism, however by including all aberrations, the VS shifts towards negative values in the second subject (-0.80D). This shift was included in the convolution in the defocus term, only in S#2 (**FIGURE 6.6** (B)). In previous studies of our group [248, 384], it was found that subjects with astigmatism shift their best

subjective focus towards negative values, which could explain the difference in perception between both subjects.
In addition, the spatial frequencies involved in the task are different [385]. Low spatial frequencies (LoSFs) are relevant for gender face recognition, while high spatial frequencies (HiSFs) are relevant for expression identification [386, 387]. On the other hand, VA is a high-frequency task.

When external aberrations were simulated, all subjects perceived a decrease in performance when the induced aberration pattern has lower optical quality than the native one, in terms of VS. However, only those subjects with lower VS experience an increase in tasks, both GI and AV, when the induced pattern was better than the native one. This could imply a neuronal adaptation to the aberrations of subjects with higher optical quality.

The induction of refractive defocus in the Badal system with values of +0.50 and +1.00 D, produces a reduction in the performance of the subject in both tasks, GI and VA, with no differences between the optical quality groups.

It was also observed that repeated conditions between sessions present similar results and there is no learning effect (R^2 Nagelkerke <<0.3).

A correlation was found between the GI tasks and VA, but only visual acuity was significant ($p<0.05$), which reinforces our hypothesis that VA is more sensitive to optical changes and manipulation of aberrations since it includes high spatial frequencies (HiSFs). To see more significant changes in tasks closer to everyday life, tasks involving high frequencies such as expression recognition (happy, sad, tired) should be chosen [358].

It was not the aim of the study but out of curiosity, the influence on the subject performing the tasks (whether male or female) on face recognition has been studied and as a result, it was found that there wasn't a dependency on the subject's gender. In most cases, there was a higher % of correct answers when the presented image was a man's face (analysis for natural aberrations).

6.5. CONCLUSIONS

Both optical aberrations and neural adaptation to native blur (and its orientation) appear to play a significant role in GI, with a potentially larger role of adaptation to native aberration in subjects with better optics. It is important to take into account the spatial frequency of the tasks to be studied to analyze the discrepancies due to this characteristic.

In these previous chapters, the impact of monochromatic aberrations has been mainly studied, but we live in a polychromatic world so the interaction of monochromatic and polychromatic aberrations is important and it will be studied in the next chapters.

7

CHAPTER 7. TESTING THE EFFECT OF OCULAR ABERRATIONS IN THE PERCEIVED TRANSVERSE CHROMATIC ABERRATION

In polychromatic light, the retinal image is affected by monochromatic and chromatic aberrations, both Longitudinal and Transverse Chromatic Aberration. LCA is typically measured objectively and psychophysically. TCA measurements are scarcer and the impact of all combined factors on vision is seldom investigated. In this chapter, a new channel in an AO visual simulator was implemented to measure TCA under controlled aberrations.

This chapter is based on the paper by **Aissati et al.** [388] 'Testing the effect of ocular aberrations in the perceived transverse chromatic aberration' published in Biomed. Opt. Express (2020). The co-authors are Maria Vinas, Clara Benedi-Garcia, Carlos Dorronsoro and Susana Marcos.

The preliminary results were presented at the PhDay 2018 by **Sara Aissati**, at the Faculty of Optics and Optometry as a task of compulsory activities of the doctorate. The contribution was oral and awarded as the best oral presentation in the oral presentations section.

This work was also presented as an oral presentation at the IONS Barcelona 2019 International OSA Network of Students conference and as a poster contribution at ARVO annual meeting 2019, by **Aissati et al.** under the same title.

The author of this thesis implemented the experimental procedure in collaboration with Maria Vinas, performed the measurements on subjects, collected, analyzed the data, discussed the data with the rest of the authors, and prepared the manuscript in collaboration with Susana Marcos.

7.1. INTRODUCTION

In polychromatic light, the retinal image is affected by both monochromatic and chromatic aberrations of the eye and their interactions [389]. Chromatic aberrations include longitudinal chromatic aberration and transverse chromatic aberration [375].

LCA arises from the dependence of the refractive power of the eye with wavelength and its effect on image contrast is given by defocus [57]. There are numerous literature reports of ocular LCA, measured either with objective (reflectometric) methods [63, 390] or, more extensively, through psychophysical methods [68, 376, 391]. For the adult human eye, it is well accepted that the magnitude of the LCA is ~2 D across the full visible spectrum (400 to 700 nm) [58], ~1.8 D across 450-700 nm and ~1.5 D across 480-700 nm [281].

TCA is the variation of image location and magnification as a function of wavelength since the chief ray passing through the center of the pupil strikes on the retinal surface at different positions depending on wavelength. While the TCA is generally attributed to the lack of centration of the optical components of the eye, including the off-axis position of the fovea, other potential sources contributing to TCA have also been invoked [392]. Besides, significant differences are found in the TCA measured with centered small pupils or with dilated pupils. As DP techniques cancel out the TCA, TCA is generally measured psychophysically [64, 83, 375, 377], except for objective reports using an AO scanning laser ophthalmoscopy [87-89]. The psychophysical measurement of TCA generally relies on alignment techniques, including different forms of a Vernier alignment task [83, 375, 377, 393]. Simonet and Campbell [377], coined the term optical TCA (oTCA) to refer to the TCA that is measured with a small centered pupil and, therefore, not affected by the HOAs of the eye and by the SCE. Conversely, they used the term perceived TCA (pTCA) to refer to the effective TCA with large pupils. It is thought that the HOAs alter the effective centroid of the retinal image, producing shifts in the Vernier alignment, while the SCE further affects the centroiding as a result of differential weights in the effective luminance efficiency across the pupil [394]. Marcos et al. [53] used a spatially resolved refractometer and a point stimulus that the patients viewed through a magenta filter (superimposed to a cross-target viewed with a small centered pupil) as a small entry pupil moved across the dilated natural pupil. The relative lateral separation between the red and blue spots with respect to the reference was taken as the TCA, for different entry pupils. The oTCA was estimated as the lateral separation between the red and blue spots for a centered pupil. The full spot diagrams for blue and red were used to calculate the pTCA (affected by the ocular aberrations, and following a weighting function, the SCE).

Knowledge of TCA is important to estimate polychromatic image quality [53, 392]. TCA has also been reported [377] to play a major role on monocular chromatic diplopia and chromostereopsis [86]. Furthermore, it is well known that monochromatic and chromatic aberrations interact favorably, so that the presence of monochromatic aberrations mitigate the impact of the LCA [389, 395]. Attempts to correct LCA (by means of achromatizing lenses [120], and more recently using Badal systems [396] and SLM [397]) have shown little benefit in improving vision, presumably because of the residual monochromatic aberrations, neural adaptation to chromatic blur and the presence of TCA. Measuring and understanding the TCA is also important in assessing potential benefits of new released intraocular lenses aiming at correcting the LCA, while likely leaving the TCA uncorrected [398, 399].

The role of HOAs in the magnitude and direction of the TCA has been predicted on the basis of the differences of measured TCA with small and large pupils [53, 377]. However, to our knowledge, the impact of the ocular aberrations on pTCA has not been directly measured. Likewise, while the SCE (differences in light efficiency across the pupil arising from cone directionality) has been

invoked as a contributor to shifts in the pTCA with respect to the oTCA, the relative contributions of aberrations and SCE have not been directly evaluated.

AO visual simulators allow manipulating the aberrations of the eye, in particular the correction of its HOAs [235, 236, 400]. In a prior study, we used the VioBio polychromatic multichannel AO visual simulator system [235, 276] to evaluate the impact of the HOAs on the LCA [281]. In this study, we implemented a new psychophysical channel in this polychromatic multichannel AO visual simulator to measure the TCA (both oTCA and pTCA) in normal subjects, under natural and AO-corrected aberrations. In addition, we measured the reflectometric OSCE using an LRT [360] which allowed evaluating the contribution of the OSCE on pTCA.

7.2. METHODS

A polychromatic multichannel AO visual simulator system (described in section 2.1.2) was used to measure TCA (Vernier alignment method) on 11 subjects, with small (2 mm, oTCA) and large (6 mm, pTCA) pupil diameters, and with natural (HOAs) and corrected aberrations (AO-correction). TCA measurements were performed with uncorrected LCA. Measurements of monochromatic aberrations and reflectrometric OSCE on these subjects were performed (using LRT, described in section 2.1.3). Also, LCA was obtained from reflectometric/ psychophysical measurements of best focus at different wavelengths on 5 of the 11 subjects. These measurements were used in computer simulations to evaluate the relative contribution of LCA, HOAs and OSCE on pTCA.

7.2.1. Subjects

Eleven subjects (26.8 ± 3.24 years) participated in the experiment. The TCA was measured in all 11 subjects, LCA was measured in the first 5 subjects (showing values that were confirmatory and consistent with previous literature), and OSCE was measured in 9 of the subjects (who were available for a second session). The measurements were performed monocularly, in the right eye of each subject. Spherical errors ranged between 0 and −6.75 D (-1.91±1.30 D), and astigmatism was ≤ −1.25 D in all cases. All participants were acquainted with the nature and possible consequences of the study and provided written informed consent. All protocols met the tenets of the Declaration of Helsinki and had been previously approved by the Spanish National Research Council (CSIC) Ethical Committee.

7.2.2. Transverse Chromatic Aberration measurement channel

A new channel was developed specifically for this study to measure foveal TCA in the polychromatic multichannel AO visual simulator system. The implemented method is based on two-color two-dimensional Vernier alignment technique developed by Thibos et al [375].

The stimulus consisted of a red square (40 arcmin) surrounded by a blue background (120 arcmin), with black reference lines (2 arcmin) placed at fixed locations on the blue field. A movable black crossed target inside the red square was mapped on the DMD projector (**FIGURE 7.1**) [393]. The DMD was simultaneously illuminated with two wavelengths (490 and 680 nm) coming from the SCLS. To split the two wavelengths and generate a stimulus with two different zone colors, we inserted a filter slide in a conjugate retinal plane. The filter was a photographic slide with two concentric squares in two colors (blue in the background and red in the central square), such that,

considering the magnification of the system, it was superimposed onto the stimulus projected on the DMD.

Extinction tests were carried out to verify that only the corresponding wavelengths passed through each zone, and that there was no spectral leakage. The effective spectral content (combination of the SCLS and filter) was 490 ±10 nm in blue and 680 ±15 nm in red. The measured target luminance was approximately 25 cd/m^2 in blue and red. The luminance of the red field was adjusted by a control group of four subjects to perceptually match the luminance of the blue field, through a computational increase of the gray level of the pixels in the DMD corresponding to the region illuminated in red. The effective reduction in the luminance of the red field was by a factor of 0.02.

The vertical position of the adjustable horizontal line and the horizontal position of the adjustable vertical line in the DMD were controlled by the subject by means of the computer's keyboard. The subject's task was to align the black lines in both the blue and the red regions of the target, both horizontally and vertically. In the initial configuration, the vertical / horizontal black lines of the stimulus were moved with the keyboard in steps of 5 pixels. To refine the alignment, subjects had the possibility to press the central key of the keyboard to change the magnitude of the step to 1 pixel. The precision of the lateral displacements was assessed using an artificial eye (an achromatic lens with a CCD detector at its focal plane) instead of the subject's eye. The offset was found to be 1 pixel (0.1962 arcmin) in both the horizontal and the vertical axes, which was taken as the system's TCA, and subtracted from the values measured in the eye.

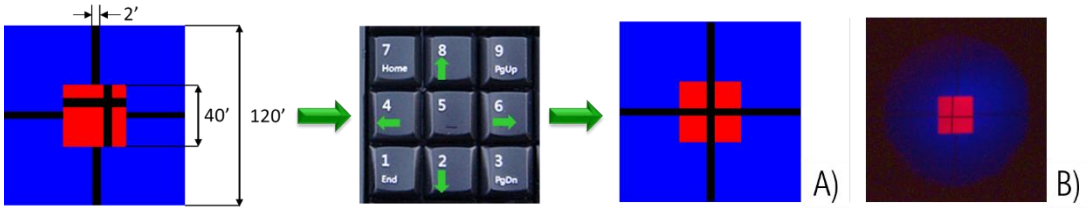

FIGURE 7.1. A) Visual stimuli and Vernier alignment method for the measurement of TCA. The stimulus consists of a small red square in the middle of a larger blue square, with a cross of black bars placed on top of both squares (A, Left) The black bars in the center are purposely misaligned. The subject uses a keyboard (A, Middle) to shift the bars in the central field until they appear to be aligned with the bars in the periphery (A, Right). The TCA is estimated from the shift produced by the subject in the horizontal and vertical lines to achieve the alignment. B) Image of the stimulus captured in the retinal plane of an artificial eye placed in the position of the subject.

7.2.3. Experiments

Measurements were obtained in two experimental sessions: Polychromatic AO system including Hartmann-Shack measurements at various wavelengths, TCA measurements (Session 1, 2 hours duration, performed on 11 subjects), and LRT measurements (Session 2, 20 minutes, performed on 9 subjects).

In all measurements, subjects were stabilized using a dental impression mounted on an x-y-z stage. The eye's pupil was aligned to the optical axis of the instruments using the line of sight as a reference, while the natural pupil is viewed on the monitor. Pupil centration was verified before each trial and between trials. Also, all measurements were performed monocularly (right eye), in a darkened room, under cycloplegia (by instillation of Tropicamide 1%, 2 drops 10 minutes prior to the beginning of the study, and 1 drop every 1 hour), and best correction of subjective defocus using Badal systems.

Monochromatic aberrations.

For all measurements performed with the polychromatic multichannel AO visual simulator system, the best subjective focus was initially searched by the subject while viewing a Maltese cross projected on the DMD at reference wavelength of 555 nm. Ocular HOAs were measured with the Hartmann-Shack wavefront sensor (and corrected in a closed loop) at 880 nm, and at various visible wavelengths (490, 555, 680 nm) for selected subjects. All wave aberrations were obtained for 6-mm pupil diameters. Each measurement was repeated at least 5 times per condition.

LCA measurements.

LCA was obtained from Hartmann-Shack and psychophysical measurements. In objective measurements, the best focus was obtained from the defocus term in the Zernike expansion at each wavelength. In psychophysical measurements, patients selected their best subjective focus using the Badal system while viewing the stimulus illuminated with three different wavelengths in visible light (490, 555, 680 nm). Each setting was repeated 5 times

TCA measurements.

TCA was measured under natural aberrations and under AO-correction, with centered small and large pupils, in the following order: ***(1)*** *Perceived TCA under natural aberrations (pTCA-HOA).* TCA measurements were performed for 6-mm pupil diameters, with the best focus set a 555 nm, and with natural optics*;* ***(2)*** *Perceived TCA AO-correction (pTCA-AO).* TCA measurements were performed for 6-mm pupil diameters, with the best focus set a 555 nm, under AO-correction (closed-loop at 880 nm)*;* ***(3)*** *Optical TCA under natural aberrations (oTCA-HOA).* TCA measurements were performed for 2-mm pupil diameters, with the best focus set a 555 nm, and with natural optics. ***(4)*** *Optical TCA (oTCA-AO).* TCA measurements were performed for 2-mm pupil diameters, with the best focus set a 555 nm, under AO-correction (closed-loop at 880 nm).

Subjects were instructed on the Vernier Alignment task and on the use of the keyboard to shift the horizontal and vertical bars of the cross-target. After an initial trial run, subjects repeated the Vernier alignment 5 times per condition. Aberrations were monitored throughout the experiment every two trials to ensure that each trial was performed under the desired state of aberrations correction.

The small and large pupil diameters (2 and 6 mm) were achieved with an artificial iris (3D printed) placed in a conjugate pupil plane, centered with the help of the pupil monitoring camera.

OSCE measurements.

Five consecutive series of 37 retinal aerial images were captured scanning the subject's pupil, with foveal fixation. Background images (replacing the subject's eye by a black target) were obtained and subtracted from the test images.

7.2.4. Computational Analysis of Perceived Transverse Chromatic Aberration

PSF in blue (490 nm) and red (680 nm) were calculated from the measured HOAs (at the specific measured wavelengths –in the patients in which they were available- or at 880 nm), and the corresponding chromatic difference of focus between 555 nm (for which the best focus was found)

and 490 nm (0.55 D), and between 555 nm and 680 nm (0.90 D) [281]. The same LCA values were used for all subjects. PSFs were calculated for each subject for the measured natural HOAs, or the residual aberrations after AO-correction, both for 2 mm and 6 mm, using Fourier Optics. The modulus of the pupil function was taken either as constant or with a weighted efficiency by the 2D-Gaussian function (normalized Eq.(2.1)) representing the OSCE. For simplicity, a constant ρ of 0.1 mm^{-2} was used in Eq.(2.1) for all subjects [360, 401].

To simulate a Vernier alignment test, Line Spread Functions (LSF) were calculated for horizontal and vertical directions, by integrating the energy in the PSF in both directions. The process is outlined in **FIGURE 7.2.** The shift between the peak of the LSF for blue and red in the horizontal or vertical directions accounts for the shift in the coordinates of the TCA arising from the presence of aberrations only, or aberrations and OSCE [402]. The offset coordinates were vectorially added to the oTCA-AO (2 mm pupil, with corrected aberrations), to generate the computational pTCA-HOA (6 mm, effect of aberrations), and pTCA-HOA-OSCE (6 mm, effect of aberrations and Stiless Crawford), respectively.

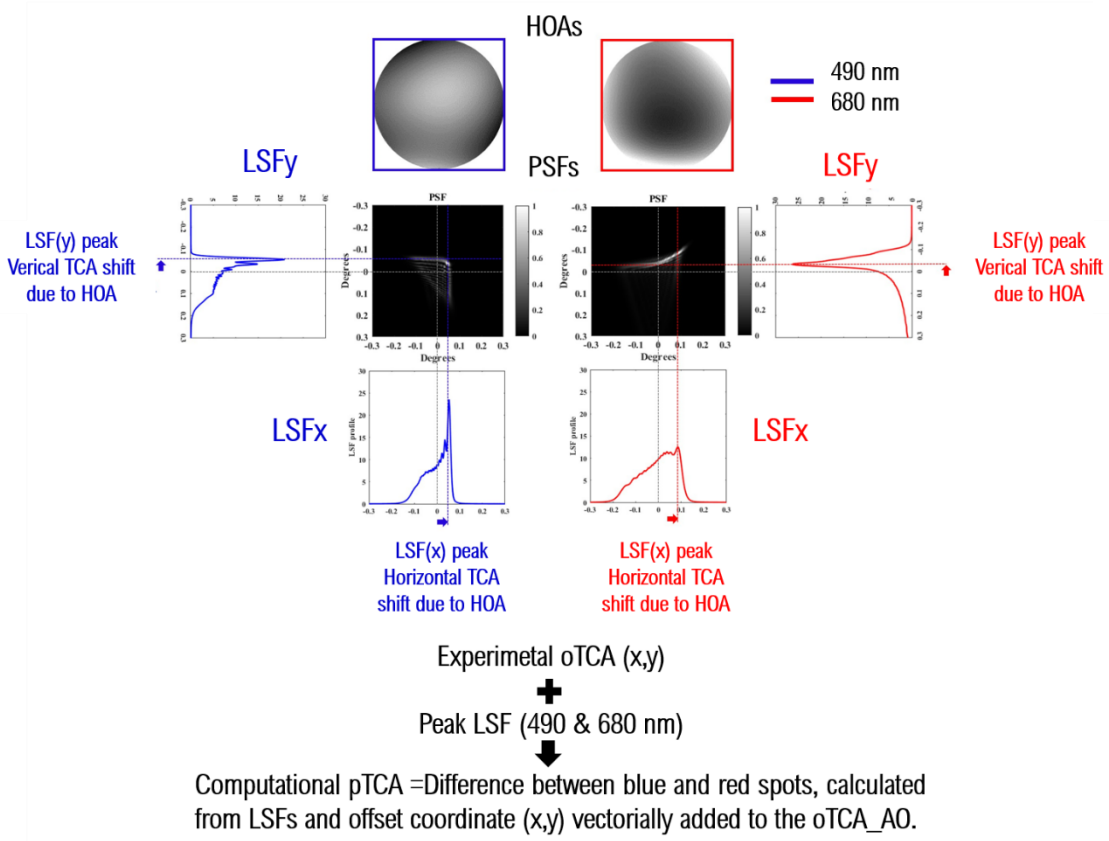

FIGURE 7.2. Illustration of the calculations of the computational pTCA-HOA obtained from estimated Point Spread Functions (PSFs) and Line Spread Functions (LSFx, LSFy) in red and blue for 6-mm pupils, vectorially added to the measured oTCA-AO (2 mm, AO-correction). Calculations of computational pTCA-HOA-OSCE and pTCA-AO-OSCE are performed similarly, including the OSCE (simulated applying a Gaussian pupil mask), with or without aberrations respectively, to calculate the corresponding LSFx, LSFy to add to the oTCA-AO.

A similar approach was followed, to isolate the effect of OSCE, calculating the PSF (and corresponding LSF) for the AO-corrected condition (residual ocular aberrations, 6 mm) and the OSCE Gaussian pupil mask. LSFs and offset coordinates were calculated and vectorially added to the oTCA-AO (2-mm, with corrected aberrations), to generate the computational pTCA-AO-OSCE (6 mm, OSCE).

7.2.5. Data analysis

Statistical analysis was performed with SPSS software Statistics 24.0 . We tested the dependency of HOAs on wavelength (one-way ANOVA) and evaluated the differences between pTCA and oTCA, and AO and HOAs conditions (paired-samples t-test).

7.3. RESULTS

7.3.1. Wave aberration at different wavelengths and AO-correction

Ocular aberrations were measured in three wavelengths in the visible (490, 555, 680 nm) and in the IR (880 nm). We checked that, except for defocus, there was a negligible dependency of the HOAs on wavelength. In particular, we ensured that the AO-correction (which was obtained in a closed-loop in IR), was also efficient at lower wavelengths. **FIGURE 7.3** A) shows an example of wave aberrations for HOA, at all measured wavelengths, for natural aberrations (upper row) and AO-correction (lower row), for one subject (S#3). Wavefront maps are similar, with no systemic change, across wavelengths. **FIGURE 7.3** B) shows the average RMS at each wavelength, for natural aberrations and AO-correction, across all measured subjects. On average, the RMS standard deviation across wavelengths was 0.04 μm for natural aberrations and 0.01 μm for AO-correction. There was no systematic variation of the RMS with wavelength (neither in natural nor in AO-corrected conditions) (one-way ANOVA, p= 0.484 & p = 0.108).

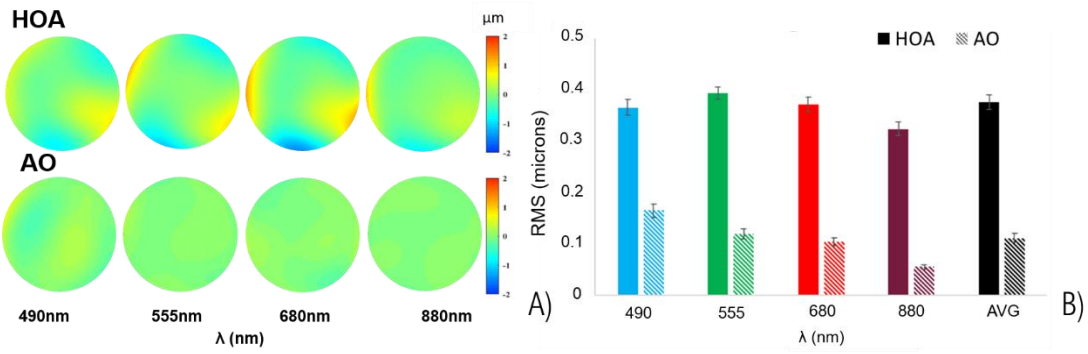

FIGURE 7.3. A) Wave aberrations maps for HOA for different wavelengths in one of the subjects (S#3) for natural aberrations (upper row) and for AO-correction (lower row). B) RMS wavefront error for different wavelengths, with natural aberrations (solid bars) and AO-correction at 880 nm (patterned bars), averaged across subjects and wavelengths (for wavelengths between 490 and 880 nm). Data are for 6-mm pupil diameters.

From the defocus Zernike term (not shown in **FIGURE 7.3**) we could also calculate the chromatic difference of focus between 490 and 680 nm (for objective/reflectometric LCA), which on average was 0.74 ± 0.01 D (with natural aberrations) and 0.74 ± 0.01 D (under AO-correction).

7.3.2. Psychophysical LCA

FIGURE 7.4 shows the psychophysical LCA for all measured subjects, obtained from subjective focus settings between 490 and 680 nm. The LCA was obtained from a linear fitting to the chromatic defocus as a function of wavelength. LCA was 1.41 ± 0.08 D with natural aberrations and 1.39 ± 0.12 D under AO-correction.

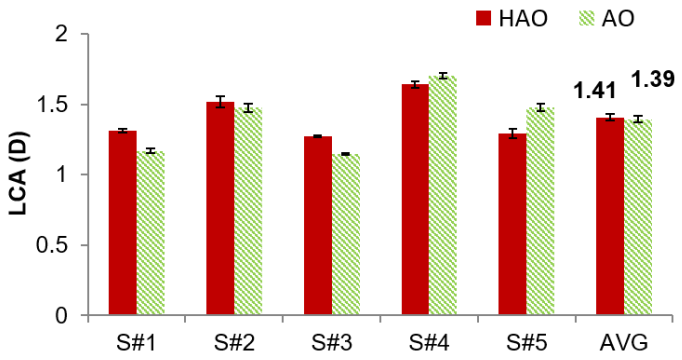

FIGURE 7.4. Psychophysical LCA (490-680 nm) range, in 5 subjects (S#1-S#5) and averaged across subjects. Data are for natural aberrations (solid bars) and AO-correction (patterned bars).

7.3.3. Experimental Optical and Perceived TCA: Impact of AO-correction of HOAs

FIGURE 7.5 shows the horizontal and vertical coordinates of the optical TCA (oTCA, 2 mm, **FIGURE 7.5** A)) and perceived (pTCA, 6 mm, **FIGURE 7.5** B)) measured experimentally in the 11 subjects of the study. Positive horizontal coordinates stand for nasal displacement in the retina and positive vertical coordinates stand for superior displacement in the retina. The average oTCA (2 mm) horizontal coordinates were 1.29.±0.10 arcmin (HOA) and 1.13±0.14 arcmin (AO-correction), and the average oTCA vertical coordinates were -0.11±0.08 arcmin (HOA) and -0.16±0.12 arcmin (AO-correction), coordinates that are represented by small circles in **FIGURE 7.5** C) for measurements obtained under natural HOA (red) and AO-correction (green). The average pTCA horizontal coordinates were 0.11±0.07 arcmin (HOA) and -0.28±0.08 arcmin (AO correction), and the average pTCA vertical coordinates were -0.65±0.11 arcmin (HOA) and -1.01±0.08 arcmin (AO correction), represented by the large circles in **FIGURE 7.5** C). **FIGURE 7.5** D) shows the average absolute shift in TCA when changing the pupil diameter from 2 to 6 mm (pTCA-oTCA), for natural aberrations (0.72±0.11 arcmin, red bar) and AO-correction (1.24±0.08 arcmin, green bar). **FIGURE 7.5** D) also shows the average absolute shift when correcting the HOA aberrations for pTCA (i.e 6 mm pupil, 1.09±0.11 arcmin, solid blue bar) and for oTCA (i.e. 2 mm, 0.23±0.14 arcmin, patterned blue bar). The differences between oTCA_HOA and oTCA_AO (0.23 arc min) are within the order of the resolution of the technique (0.20 arc min), but the differences between pTCA_HOA and pTCA_AO are statistically significant (p-value ranging between=0.001 and 0.03, except for subjects S#1 and S#7). Also, increasing pupil diameter from 2 to 6 mm (oTCA vs pTCA) produces a significant shift in the TCA, both for natural aberrations (p=0.046) and AO-correction (p=0.031).

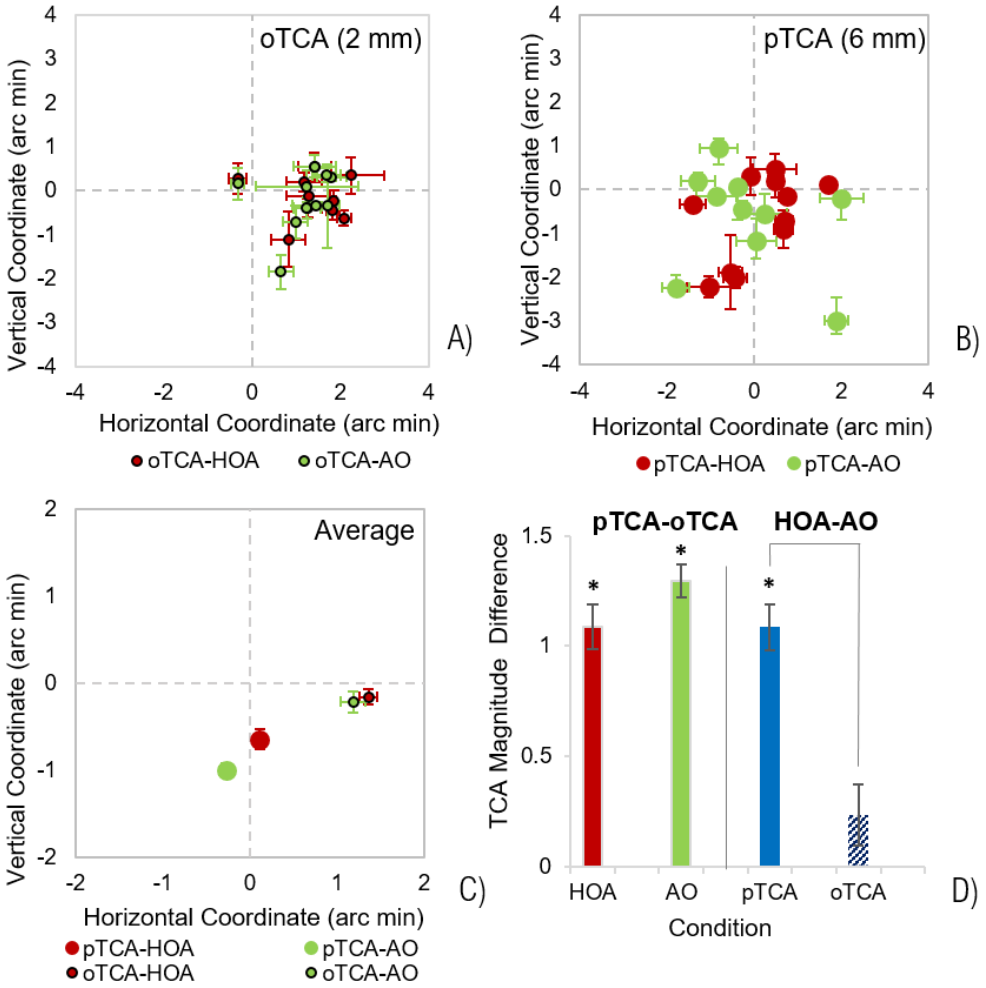

FIGURE 7.5 . A) Optical TCA (oTCA, 2mm), with natural aberrations (oTCA-HOA, small red circles) and AO-correction (oTCA-AO, small green circles), for all subjects. Error bars stand for standard deviation of repeated measurements. B) Perceived TCA (pTCA, 6mm), with natural aberrations (pTCA-HOA, large red circles) and AO-correction (pTCA-AO, large green circles), for all subjects. Error bars stand for standard deviation of repeated measurements. Note: One subject not shown because of falling outside the axis range (-4 to 4 arc min). C) Average (across subjects) coordinates for oTCA (small circles) and pTCA (large circles), for natural aberrations (red symbols) and AO-correction (green symbols). Error bars stand for standard deviations across subjects. D) Absolute TCA magnitude differences, for different conditions: changing the pupil size (pTCA-oTCA) under natural aberration (red solid bar), AO-correction (green solid bar); correcting aberrations, for a given pupil diameter (6 mm, pTCA-HOA – pTCA-AO, blue solid bar and 2 mm, oTCA-HOA – oTCA-AO, blue patterned bar). Error bars stand for standard deviations across subjects.

7.3.4. Reflectometric OSCE

FIGURE 7.6 A) shows the reflectometric OSCE maps (2D-Gaussian fittings) in all measured subjects. The OSCE peak positions are marked with black asterisks. **FIGURE 7.6** (B) shows the coordinates of the OSCE peaks for all subjects. On average, the OSCE peak location lies at 0.89±0.45 mm nasally and -0.20±0.36 mm inferiorly from the geometric center of the pupil.

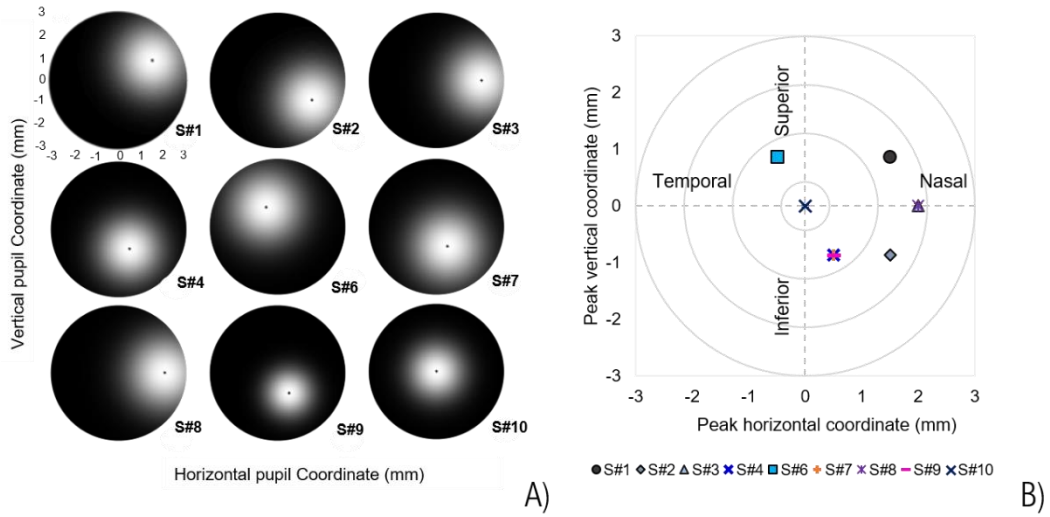

FIGURE 7.6. A) 2D-Gaussian fitting of the LRT aerial image intensities (according to Eq.(2.1)) for all subjects. The asterisk marks the coordinates of the OSCE peak. Positive horizontal coordinates stand for nasal displacements and vertical coordinates stand for superior displacements from the pupil center. The x- and y-axis ranges (pupil coordinates) are shown for S#1, and are similar for all subjects. B) OSCE peak positions in nine eyes of the study. Positive horizontal coordinates stand for nasal displacement and positive vertical coordinates for superior displacement. Each eye is depicted by a different symbol shape. Error bars (standard deviations of estimations from five repeated LRT series) are smaller than the symbols (0.04±0.01 mm).

7.3.5. Computational perceived TCA

FIGURE 7.7 shows an example of the computation of perceived TCA (for various conditions) for one subject (S#3). **FIGURE 7.7** A) shows the estimated shifts of the peak of the blue and red LSFs by the effect of HOAs and OSCE (taking the experimental value of oTCA-AO as a reference). The oTCA-AO is represented by the distance between the small red circle (arbitrarily placed at 0,0) and the small blue circle. The shifts in the peak of the LSFs for red and blue are then added to those reference values for blue and red, considering the effect of HOAs (represented by "x"), considering both HOAs and the OSCE (represented by "**+**"), and considering the effect of OSCE only (represented by "o"). **FIGURE 7.7** B) shows the computational perceived TCA for S#3, estimated from the distances between the estimated blue and red peaks: pTCA-HOA being the distance between the blue and red "x" in **FIGURE 7.7** A), pTCA-HOA-OSCE being the distance between the blue and red "+", and pTCA-OSCE being the distance between the blue and red "o". The graph also shows the experimental TCA measurements (pTCA-HOA, pTCA-AO, oTCA-HOA and oTCA-AO) as solid circles. The computational pTCA-HOA and pTCA-HOA-OSCE are to be compared with the experimental pTCA-HOA. With natural aberrations, it is expected that both HOAs and the OSCE contribute to the difference between pTCA and oTCA. The computational pTCA-AO-OSCE is to be compared with pTCA-AO. Under corrected aberrations, it is expected that residual HOAs and the OSCE contribute to the difference between pTCA-AO and oTCA-AO.

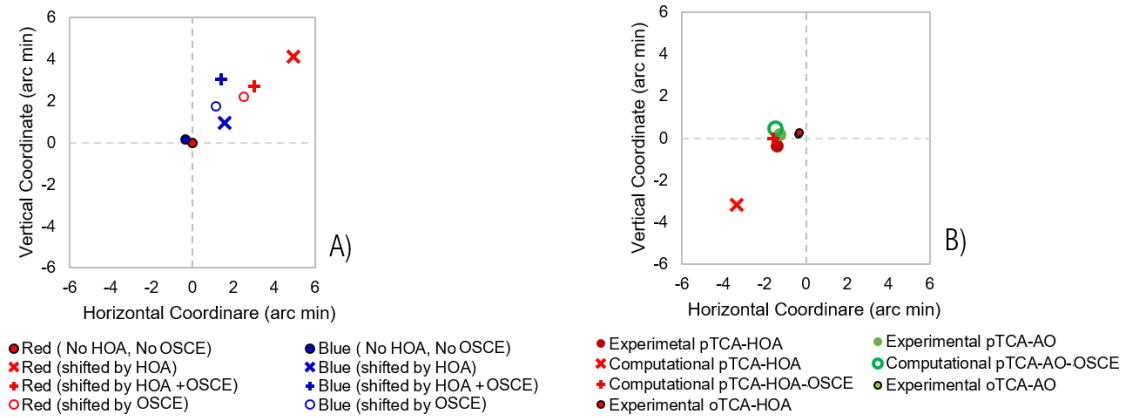

FIGURE 7.7. Illustration for one subject (S#3) of the estimated effects of HOAs and the OSCE on the perceived TCA. A) Estimated shifts in the peak of the LSF in the horizontal and vertical coordinates for blue and red when considering the HOA and OSCE, with respect to the LSF peaks for blue and red in absence of HOAs and OSCE, taken at the (0,0) coordinate for red and shifted by the experimental value of oTCA-AO for blue. The coordinate shift by HOA is represented by the symbol "×", the coordinate shift by HOA+OSCE is represented by "+", and the coordinate shift by OSCE is represented by "o". B) Computational pTCA, calculated from the vectorial difference of the blue and red peak coordinates: pTCA-HOA from the difference of the coordinates represented by "×", pTCA-HOA-OSCE from the difference of the coordinates represented by "+", pTCA-AO-OSCE from the difference of the coordinates represented by "o". The experimental oTCA-HOA, oTCA-AO, pTCA-HOA and pTCA-AO are also shown.

FIGURE 7.8 compares the experimental and computational pTCA in all subjects: the experimental pTCA-HOA and the computational pTCA considering HOAs only (Computational pTCA-HOA), shown in **FIGURE 7.8** A), and the experimental pTCA-HOA and the computational pTCA considering both HOAs and OSCE (Computational pTCA-HOA-OSCE), shown in **FIGURE 7.8** B). The computational pTCA-HOA presents more spread values than the experimental measurement (average difference computational-experimental 2.04 arcmin). However, the computational pTCA-HOA-OSCE captures both the orientation and magnitude of the experimental measurements (average difference computational-experimental 0.37 arcmin, close to the resolution of the technique). **FIGURE 7.8** C) shows the experimental pTCA-AO (i.e. with HOA aberrations corrected) and the computational pTCA-OSCE, with AO-correction but considering the OSCE (average difference computational-experimental 0.58 arcmin). **FIGURE 7.8** D) shows the experimental pTCA-HOA, pTCA-AO and oTCA-AO, and computational pTCA-HOA, pTCA-HOA-OSCE, pTCA-OSCE and oTCA-AO, averaged across subjects.

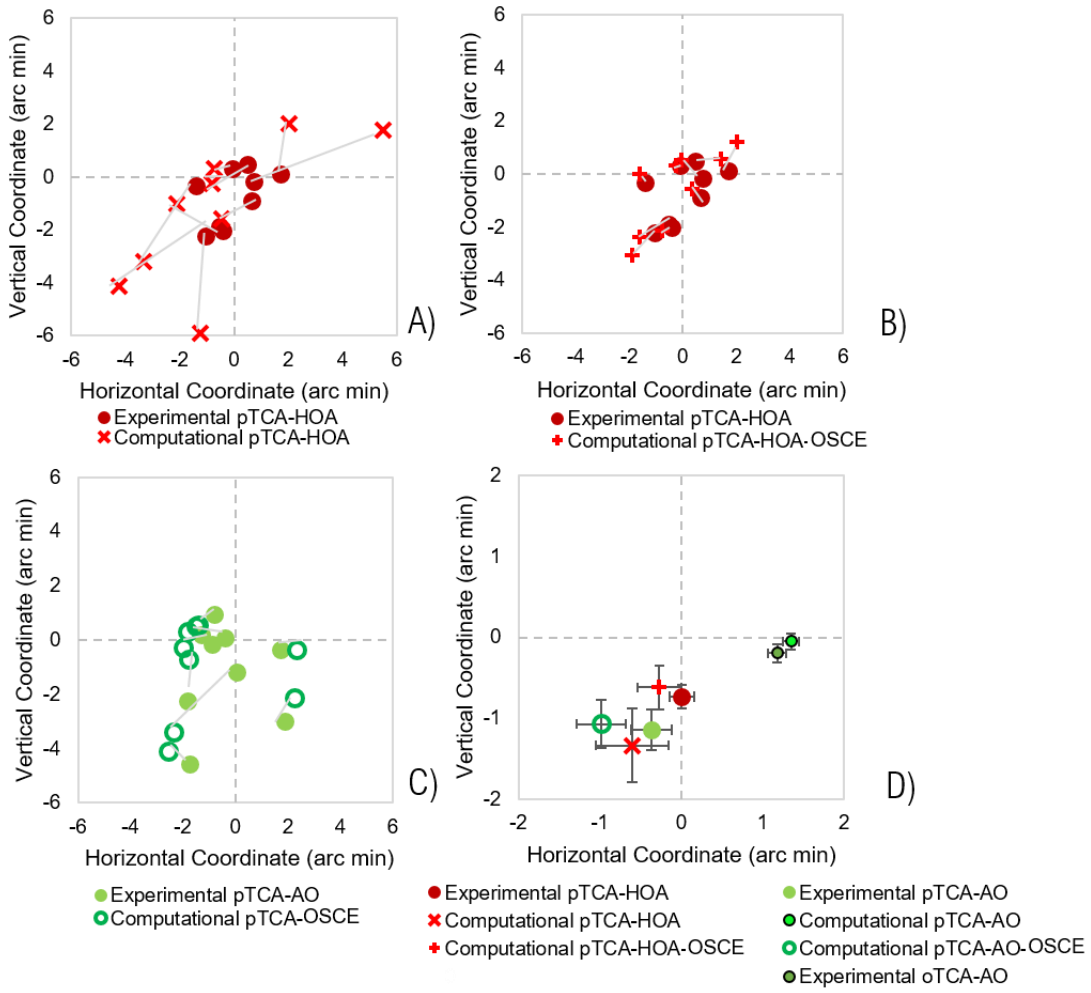

FIGURE 7.8. A) Experimental pTCA-HOA (large red circles) and computational pTCA-HOA (HOAs only, represented by red "×"). B) Experimental pTCA-HOA (large red circles) and computational pTCA-HOA-OSCE (HOAs and the OSCE, represented by red "+"). C) Experimental pTCA-AO (large green circle) and computational pTCA-OSCE (no HOAs, OSCE only, represented by green "○"). The gray lines link the symbols of experimental and computational data for each subject (in A, B, C). D) Experimental pTCA-HOA, pTCA-AO and oTCA-AO and computational pTCA-HOA, pTCA-HOA-OSCE, pTCA-AO and pTCA-AO-OSCE, averaged across subjects. In all the graphs, the red symbols correspond to the HOAs condition, and the green symbols correspond to the AO-correction. Error bars stand for standard Errors across subjects (for horizontal and vertical coordinates).

7.4. DISCUSSION

Using a polychromatic multichannel AO visual simulator, we measured monochromatic aberrations, longitudinal chromatic aberrations and transverse chromatic aberrations in normal human subjects, under natural and corrected monochromatic aberrations. We found that the TCA was systematically shifted nasally for small pupils and that the presence of monochromatic aberrations produced an intersubject spread of the perceived TCA. Correcting HOAs in fact increased the perceived TCA in most subjects. Measurements of the Stiles-Crawford effect in addition to monochromatic aberrations and LCA allowed predictions of the relative impact of OSCE and aberrations on the perceived TCA. We found that incorporating an apodized pupil given by the individual OSCE produced accurate predictions of the experimental perceived TCA.

The polychromatic AO system allows the correction of aberrations while performing psychophysical measurements of LCA and TCA. Even if the closed loop is performed while aberrations are measured and corrected at 880 nm, the level of monochromatic aberration
correction is as high in the visible as in the NIR wavelengths (corrected wave aberration RMS=0.01 μm, for 6-mm). As previously found in the literature, we found that the reflectometric LCA obtained from the defocus term of the Zernike expansion of the Hartmann-Shack measured wave aberrations (+0.74±0.01 D) was consistently lower than the psychophysical LCA (+1.39±0.10 D) in a range of 490-680 nm. In all cases, the magnitude of the measured LCA magnitude is independent of the presence or correction of natural aberrations. These results are in line with reports from Vinas et al. of reflectometric/psychophysical LCA with HOAs and AO-correction [281]and also consistent with known values for LCA [63, 375].

The measured TCA values (490-680 nm spectral range) were of the same order of magnitude as other reported TCA, psychophysically measured through different versions of Vernier alignment tasks. The oTCA (small pupil) measured in this study ranged from -0.3 arcmin temporal to +2.24 arcmin nasal (horizontally) and -1.10 arcmin inferior to +1.33 arcmin superior (vertically) and pTCA (large pupil) ranged from -1.40 arcmin temporal to +1.70 arcmin nasal (horizontally) and -2.20 arcmin inferior to +0.47 arcmin superior (vertically), for natural aberrations (HOAs). As in other studies, TCA was measured while leaving LCA uncorrected. In our study, that also applied to measurements under AO-correction. We have compared the standard deviations values in the Vernier alignment for both conditions (HOA and AO-correction), the value is low for both conditions 0.09±0.01 arc min, so for the subjects, the task was performed with the same challenge, and any observed difference can be attributed to the TCA magnitude alone, and its dependence on the actual measurement condition.

The reported magnitudes of TCA varied across studies, likely due in part to specific measurement conditions. For example, Ogboso and Bedell [83], reported TCA between 0.9 to 3.0 arcmin nasal (435-572 nm) and Rynders et al [393] 0.05 to 2.67 arcmin (497-605 nm) under natural conditions; Simonet and Campbell [377], reported 0.25 arcmin temporal to 1.56 arcmin nasal (486-656 nm) under Maxwellian view [393, 403]. Thibos et al. [375], using a method that involved displacing a pupil, estimated foveal TCAs (433-622 nm) of 0.36 arcmin temporal to 1.67 arcmin nasal for natural pupils . Marcos et al. [53] , using a spatially resolved refractometer in combination with a magenta filter (473-601 nm), reported TCA ranging from -3.77 to +0.20 arcmin (horizontal) and -5.03 to +0.11 arcmin (vertical) for small centered pupils and estimated TCA ranging from -3.29 to 0.22 arcmin (horizontal) and +3.74 to +1.99 arcmin (vertical) for large pupils. Reported objective foveal TCA measurements using AO scanning laser ophthalmoscope (AOSLO) [89] were 2.1 arcmin on average. Despite changes in the spectral range, technique used and pupil diameter, a common conclusion of all the studies is the large intersubject variability of TCA within each sample.

Our study of TCA included 4 different experimental conditions (large and small pupils, HOA and AO-correction , in all subjects) and found that the values were within the range reported in the literature. However, our intersubject variability of oTCA (0.24 arcmin for oTCA-HOA and 0.28 arcmin for oTCA-AO) is much lower in our sample than previously reported. The higher magnitude in the horizontal (+1.36 ± 0.10 arcmin nasal) than in the vertical (-0.16 ± 0.08 arcmin inferior) oTCA coordinates that we found, is consistent with previous findings, and may arise from the mostly horizontal off-axis position of the fovea [404, 405]. We did not attempt to measure angle kappa in these subjects, but we could hypothesize that low intersubject differences in angle kappa may be the cause of the similarity of oTCA across subjects.

Previous studies suggested a potential contribution of HOAs and the SCE to the magnitude, orientation and intersubject variability of the Ptca [84, 86, 406]. These factors have been attributed

to play a major role in the differences in chromosteropsis (depth perception of 2-dimensional blue-red images) across subjects and with pupil size. An earlier publication using a spatially resolved refractometer [53] attempted prediction of the change in TCA magnitude and orientation when the pupil diameter increases. The calculations were performed on two subjects, shifting the lateral positions of blue and red from those corresponding to the centered pupil to the centroid of the respective spot diagrams in red and blue. In a second calculation, the spots were weighted by the pupil luminous efficiency (OSCE peak). Changes in the sign of the TCA were observed both horizontally and vertically.

To our knowledge, the current study represents the first attempt to test directly the impact of aberrations on TCA, performing measurements with natural aberrations and corrected aberrations (with AO) both for small and large pupils. It also presents the first direct comparison of experimental measurements of perceived TCA with computational predictions of perceived TCA, taking into account the HOAs of the patient (measured in the same AO set-up) and their individual SCE (measured through a reflectometric technique, LRT).

The small difference (0.23 ± 0.15 arcmin) between the TCA measured for small pupils between the natural aberrations (oTCA-HOA) and AO-corrected aberrations (oTCA-AO) indicates a small contribution of the HOAs in oTCA measured with 2 mm pupils. This small difference in the RMS values (RMS_HOA= 0.08 ± 0.03 μm and RMS _AO =0.05 ± 0.01 μm) justifies the small difference in the modulus of the oTCA between both conditions (HOA / AO). When the pupil is increased from 2 to 6 mm, there is a slight decrease in the TCA magnitude (particularly for pTCA-HOA) in both meridians, but most remarkably (both for pTCA-HOA and pTCA-AO) there is large change in TCA orientation, shifting from nasal to an arbitrary pattern that changes horizontally (nasal-temporal) and vertically (superior-inferior). A potential shift in the pupil center with pupil dilation, often invoked as a factor playing a role in the differences between oTCA and pTCA [377], can be applied here, because the pupil was concentrically changed using an artificial iris, but the physical center of the pupil may change with dilation. Also, the relatively larger magnitude of pTCA-AO than pTCA-HOA indicates that correcting monochromatic aberrations does not necessarily imply a reduction on pTCA, and in fact it may accentuate its effect. The current findings therefore suggests that we may extend the observation that the presence of monochromatic optical aberrations protects vision against longitudinal chromatic defocus [389] to a protection against the transverse chromatic aberration as well . While a decrease visual benefit of correcting the eye's optics is not surprising given the neural adaptation to the subjects native aberrations [110], the fact that these effects can be predicted by optical simulations suggests that these effects rely, at least in part, on optical grounds.

The realistic computational simulations of pTCA allow understanding the factors contributing to pTCA. A calculation of the pTCA taking into account HOAs predicts a spread of pTCA values and account for 31% of the variance; r^2=0.31 (in the experimental pTCA-HOA vs computational pTCA-HOA correlation). However, when the OSCE was incorporated, the computational pTCA-HOA-OSCE values match highly the experimental values (i.e. HOA and OSCE account for 81% of the variance; r^2=0.81 in the experimental pTCA-HOA vs computational pTCA-HOA-OSCE correlation, and an offset of only 0.37 ± 0.2 arcmin). Our experimental values of the OSCE peaks (0.89±0.45 mm horizontal and -0.20±0.36 mm vertical, on average) are in good agreement with previous reports in the literature, which show that OSCE peaks are in general in the nasal-inferior pupil [7, 123, 129], although intersubject –and even intrasubject- variability occurs [407]. In fact, we found that the average OSCE peak that minimizes the experimental/computational difference (0.94 ± 0.59 mm nasal and -0.59 ± 0.49 mm inferior) is very close to our OSCE peak experimental value. Further adjustments to the impact of the OSCE can be made by modulating the shape factor of the

effect (we assumed ρ=0.1 mm^{-2}, a value generally reported for reflectometric data, but this may differ from psychophysical values and may vary across individuals [401]). It appears that the nasal coordinate of the oTCA is offset by the increase in the luminous efficiency of the pupil towards the nasal side (where the achromatic axis must lie), resulting in a horizontal shift towards the center of the pTCA horizontal coordinate. The vertical inferior shift of the pTCA vertical coordinate may also be associated to the inferior shift of the OSCE peak. The bias by the aberrations may also contribute in this direction, at least in some subjects. The relevance of the OSCE effect on pTCA is further supported by the experimental pTCA-AO results. Despite the minimization of HOAs, pTCA values are spread, and shifted from the oTCA (a condition that given the smaller pupil, also minimizes the contribution of the HOAs). However, when OSCE is uniquely considered (computational pTCA-OSCE), the pTCA-AO is better predicted (40% of the variance; r^2=0.40 in the experimental pTCA-AO vs computational pTCA-OSCE correlation).

7.5. CONCLUSIONS

Experimental measurements of monochromatic aberrations, longitudinal chromatic aberration, and transverse chromatic aberration allow full estimation of the polychromatic image quality. These measurement channels are all available in a polychromatic multichannel AO visual simulator system, which allows correcting the monochromatic aberrations while performing psychophysical measurements, in particular, to assess the impact of chromatic aberrations on vision. Previous studies have shown that correcting HOAs in fact eliminates the protection of the eye against chromatic blur [389, 395]. Here we show that correcting HOAs does not reduce perceived chromatic aberration (with large pupils). Furthermore, simulations incorporating the OSCE indicate that OSCE plays an important role in determining the perceived TCA. It appears that a critical combination of ocular misalignment (likely driving oTCA to a large extent), optical aberrations and pupil luminous efficiency (SCE) optimize the perceived TCA. We may conclude that, while the OSCE may have a secondary effect in the monochromatic Modulation Transfer Function (MTF), it may be critical to predict polychromatic image quality with large pupils, both in calculations that use wavefront, LCA and oTCA, or ray tracing on fully anatomically-based eye models [408, 409]. An open question is an extent to which subjects may be adapted to their own transverse chromatic blur, which may be altered by changes in the optics by disease, treatment, or optical correction. Furthermore, the consideration of TCA becomes relevant with the release of new corrections (i.e. in the form of diffractive IOLs) that aim at modulating LCA, at least at some distances [73, 74, 410].

In this chapter, we have studied the interaction of monochromatic aberrations and chromatic aberration, specifically transverse chromatic aberration in young subjects, in the following chapter we will see how longitudinal chromatic aberration varies in subjects implanted with an intraocular lens.

8

CHAPTER 8. LONGITUDINAL CHROMATIC ABERRATION IN PATIENTS IMPLANTED WITH TRIFOCAL DIFFRACTIVE HYDROPHOBIC IOLs

Understanding the mechanisms behind chromatic aberration and its compensation is essential in pseudophakic eyes since the replacement of the crystalline lens affects the eye's chromatic dispersion properties, which is influenced by the IOL material's refractive index wavelength dependency.
As a result, both the IOL design and the IOL material will influence the optical performance of the pseudophakic in polychromatic light. However, the LCA of pseudophakic eyes has only been assessed in vivo in a few studies. In this chapter, psychophysical approaches are used to quantify the LCA in vivo in patients who have trifocal diffractive IOLs implanted bilaterally.

This chapter is based on the paper by Vinas et al. [411] 'Longitudinal Chromatic Aberration in Patients Implanted With Trifocal Diffractive Hydrophobic IOLs', published in J Refract Surg (2020). The coauthors are Ana Maria Gonzalez-Ramos, **Sara Aissati**, Nuria Garzón, Francisco Poyales, Carlos Dorronsoro, Susana Marcos.

This work was presented as an oral presentation at the XXVI Congress of the European Society of Cataract and Refractive Surgeons (2018) by Susana Marcos with the title 'In vivo measurement of longitudinal chromatic aberration in patients implanted with the FineVision Trifocal IOL'

The author of this thesis implemented the experimental procedure in collaboration with Maria Vinas and Ana Maria Gonzalez, performed the measurements on subjects, collected, discussed the data, and revised the manuscript with the rest of the co-authors.

8.1. INTRODUCTION

In the natural world, the retinal image quality is affected by monochromatic and chromatic aberrations of the ocular optics and by interactions between them. Chromatic defocus results from the fact that the refractive index of the ocular media depends on the wavelength [57, 412, 413]; the difference is known as longitudinal chromatic aberration (LCA) [62, 376].

When an intraocular lens (IOL) replaces the natural crystalline lens of the eye, LCA changes according to the Abbe number of the IOL material. Various studies report the LCA of lenses with different materials, both on bench and once implanted in the eye [56, 71, 72, 191, 193, 414-416]. For example, the psychophysical LCA (480 to 700 nm) in phakic eyes has been reported to be 1.52 D [62], whereas LCA was 1.37± 0.08 D in patients implanted with hydrophobic monofocal IOLs (FineVision hydrophobic raw material) and 1.21 ± 0.08 D in patients implanted with hydrophilic monofocal IOLs (FineVision hydrophilic raw material)[194].

Besides the material, the design of the IOL [153] also influences the chromatic aberrations of IOLs. Therefore, the optical performance of the pseudophakic eye in polychromatic light will be determined by both the IOL material and the IOL design, which is especially relevant in diffractive designs [417-420]. Using diffractive optics, it is possible to alter [181, 296] and even change the sign of the chromatic aberration induced by the lens, at least in several foci [74, 419]. Shifts in the position of the focus peaks of diffractive bifocal lenses with wavelength have also been strategically used to "fill in" intermediate distances and mimic an extended-depth-of-focus in polychromatic light.

Millán et al [70] evaluated, theoretically and on bench, the LCA and TF energy efficiency of four bifocal IOLs of apodized and non-apodized designs with different add powers and materials (Tecnis ZKB00 & ZMA00 by Johnson & Johnson and ReSTOR SN6AD3 and SV25T0 by Alcon Laboratories, Inc, respectively). They found that the chromatic defocus in bifocal IOLs due to the refractive base power is additive to the LCA of the ocular media for far vision and the achromatizing effect of diffractive bifocal IOLs compensates, in part, for the natural eye's LCA in near vision.

Using pseudophakic eye models, Ravikumar et al [417] demonstrated that achromatization by a diffractive IOL may provide significant improvement in polychromatic retinal image quality, whereas the combination of LCA, multifocal design, apodization, and HOAs can significantly affect the near-distance balance provided by a diffractive multifocal IOL.

The trifocal diffractive IOL hydrophilic FineVision POD F lens (PhysIOL, Belgium), which has been available in many markets since 2012, combines two bifocal diffractive patterns (one for far and near vision, and the other for far and intermediate vision) designed to concentrate light into near (+3.50 D), intermediate (+1.75 D), and distant foci [182, 296]. The apodized design of the FineVision trifocal technology benefits the far focus against near/intermediate focus for larger pupils. The energy balance is, as expected, wavelength-dependent, due to variations of diffraction efficiency with wave-length. On-bench studies [419, 421-424] compared the optical performance of diffractive multifocal IOLs with visible and near-infrared light, showing a bias in optical performance of the IOL towards far focus for near-infrared illumination.

Loicq et al [74] published a comprehensive on-bench study comparing the TF modulation of nine different lenses in red, green, and blue wavelengths, and confirmed a compensatory effect between refractive and diffractive contributions for certain foci in diffractive lenses, the actual magnitude depending on material and design.

A new trifocal lens design has been recently introduced by PhysIOL (the FineVisionHP POD F GF), with a similar topographic diffractive profile to the FineVision POD F design, but using a hydrophobic material. This gives us the unique opportunity to test in vivo the impact of the lens material alone on the chromatic performance of a diffractive trifocal IOL, at different foci.

In this study, we present the first in vivo measurements of LCA in patients bilaterally implanted with hydrophobic multifocal diffractive multifocal IOLs (FineVisionHP POD F GF) in the visible range (480 to 700 nm), which will provide insights on the influence of material and multifocal IOL design on the LCA of pseudophakic patients, with a direct impact on the optical and visual performance with these lenses.

8.2. METHODS

LCA was obtained from psychophysical measurements of best focus at different wavelengths and viewing distances in 10 patients bilaterally implanted with a hydrophobic trifocal diffractive IOL (FineVisionHP POD F GF) in each eye. Measurements were performed using a polychromatic multichannel AO visual simulator system (described in section 2.1.2).

8.2.1. Patients

The patients enrolled in this study were bilaterally implanted with a hydrophobic multifocal diffractive IOL (FineVisionHP POD F GF), which is an aspheric diffractive IOL made with a hydrophobic glistening-free material (Abbe number = 41.91). The IOL design has been described previously [182, 297] and in section 1.5.2.2. In brief, it combines two bifocal diffractive structures, one for far and near vision and the other for far and intermediate vision, to provide three useful focal distances: 0.00 D for far vision, +1.75 D addition for intermediate vision, and +3.50 D addition for near vision.

Ten patients (20 eyes) participated in the current study (mean age: 64.56 ± 3.52 years, range: 53 to 71 years) after bilateral implantation of a hydrophobic diffractive multifocal IOL. Patients received a complete ophthalmic evaluation prior to enrollment in the study and surgery at Miranza IOA (Madrid, Spain). All participants were acquainted with the nature and possible consequences of the study and provided written informed consent. All protocols met the tenets of the Declaration of Helsinki and were approved by the Spanish National Research Council Bioethical Committee.

The inclusion criteria were similar to those in our previous study [297], the most relevant being good general health, IOL power between 16.00 and 26.00 D, and postoperative corrected distance visual acuity (CDVA) better than 0.7 decimal (20/30 Snellen or 0.16 logMAR). The same surgeon (FP) performed the surgery in both eyes of all patients, with a time difference of less than 3 days between surgeries, following the same surgical procedure described previously [73].

TABLE 8.1 summarizes the patient profile, multifocal IOL characteristics, and 1-month postoperative data for all 10 patients in the current study.

8.2.2. Psychophysical best focus at different wavelengths and distances

Patients adjusted their best subjective focus using the Badal system while viewing the stimulus illuminated with five different wavelengths in visible light (480, 532, 555, 650, and 700 nm). Best subjective focus was set remotely by the patient moving the motorized stage while viewing a Maltese cross as a fixation target, starting from an initial positive blur. Patients performed a trial before the experiment to become familiar with the test, and afterward repeated each wavelength condition four times. The focus setting for the stimulus illuminated with a 555-nm wavelength was set as zero.

All measurements were performed under mydriasis (tropicamide 1%; two drops 30 minutes before the test start, and one drop every 1 hour) of both eyes. Measurements were performed using a 4 mm diameter pupil (achieved by placing an artificial pupil in a plane conjugate to the natural pupil), with AO–corrected aberrations of the optical system. The eye's pupil was aligned to the optical axis of the instrument, and the patient's head was stabilized using a dental impression on a bite bar. The patient's spherical refractive error was corrected with a Badal system.

The different wavelengths were presented randomly. Measurements were performed at three different viewing distances simulated with the Badal system: 0.00 D for far vision, +1.75 D for intermediate vision, and +3.50 D for near vision. Each measurement session lasted approximately 3 hours.

8.2.3. Data analysis

The best subjective focus at each wavelength was directly obtained from the automatic readings of the Badal optometer. Chromatic differences of focus curves were obtained from the best focus data at each wavelength. The LCA was obtained from the linear fittings to those curves. Statistical analysis was performed with SPSS software (version 24.0; IBM Corporation) to test differences in the estimated LCA across experiments and conditions. A paired-samples t-test was performed to analyze specific differences between conditions (n =10, alpha = 0.05, power = 0.80).

8.3. RESULTS

LCA was obtained from measurements of best focus at different wavelengths from psychophysical experiments and the VA uncorrected and corrected using clinical test (UDVA and CDVA).

8.3.1. Chromatic difference of focus from psychophysical measurements

FIGURE 8.1 shows the LCA from psychophysical measurements for all patients in both eyes and all tested distances (far: green bars; intermediate: red bars; near: blue bars) in the visible range (480 to 700 nm). Results show similar trends for all patients and both eyes, with higher LCA for far than for intermediate and near vision.

TABLE 8.1 summarizes the patient profile, multifocal IOL characteristics, and 1-month postoperative data for all 10 patients in the current study.

Patient/Sex/ Age (y)	Eye	IOL Power (D)	Sphere (D)	Cylinder (D)	Axis (°)	UDVA	CDVA
S1 / M / 53	OD	22.00	0.00	0.00	-	20/10	20/10
	OS	22.00	0.00	0.00	-	20/20	20/20
S2 / F / 70	OD	21.00	-0.50	0.00	-	20/25	20/20
	OS	21.00	-0.50	0.00	-	20/25	20/20
S3 / F / 70	OD	23.50	+0.50	-0.50	95	20/25	20/20
	OS	24.00	+0.50	-0.75	85	20/25	20/20
S4 / F / 53	OD	22.50	0.00	0.00	-	20/20	20/20
	OS	22.50	0.00	0.00	-	20/20	20/20
S5 / F / 69	OD	22.00	0.00	0.00	-	20/10	20/10
	OS	23.00	0.00	0.00	-	20/20	20/20
S6 / F / 67	OD	24.50	-1.00	0.00	-	20/40	20/20
	OS	24.00	+0.25	-0.75	55	20/50	20/20
S7 / F / 71	OD	23.00	+1.25	-1.00	95	20/20	20/20
	OS	22.50	0.00	0.00	-	20/20	20/20
S8 / M / 63	OD	25.50	+0.75	0.00	-	20/30	20/20
	OS	25.00	+0.75	0.00	-	20/25	20/20
S9 / F / 65	OD	24.50	0.00	0.00	-	20/20	20/20
	OS	26.00	+0.75	-0.75	180	20/25	20/20
S10 / F / 71	OD	22.50	-1.00	0.00	-	20/32	20/20
	OS	22.00	-0.50	0.00	-	20/25	20/20

IOL = intraocular lens; D = diopters; UDVA = uncorrected distance visual acuity; CDVA = corrected distance visual acuity; OD = right eye; OS = left eye

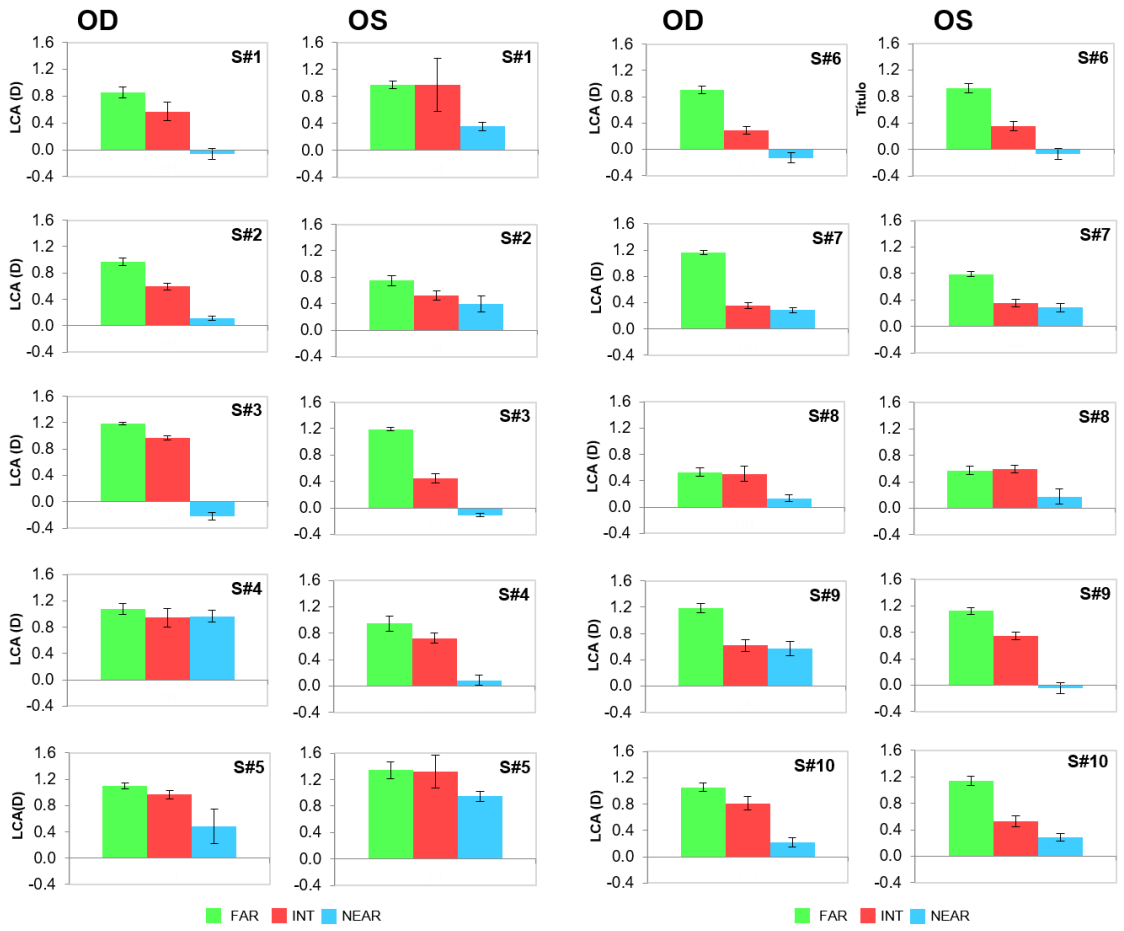

FIGURE 8.1. LCA was obtained from linear fitting of the chromatic difference of focus curves (480 to 700 nm) for all patients, and for each measured distance (far: green bars; intermediate: orange bars; near: purple bars). Error bars indicate inter-patient variability. D = diopters; OD = right eye; OS = left eye.

FIGURE 8.2 shows the average LCA from psychophysical measurements for far (green), intermediate (red), and near (blue) vision in the measured visible range (480 to 700 nm), across patients. The LCA from psychophysical measurements was significantly higher for far vision (0.99 ± 0.06 D) than for intermediate (0.67 ± 0.10 D) and near (0.23 ± 0.08 D) vision (one-way analysis of variance, $p < 0.05$).

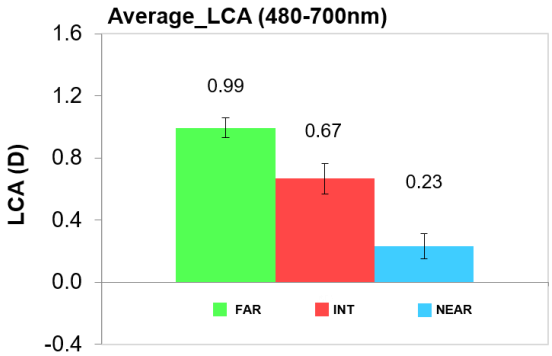

FIGURE 8.2. Average LCA from psychophysical measurements for all measured distances (far: green bars; intermediate: red bars; near: blue bars). Error bars indicate inter-patient variability. D = diopters.

FIGURE 8.3 shows the chromatic difference of focus curves obtained from the focus settings for all patients and distances (far: green; intermediate: red; near: blue) for both eyes (right eye = left column; left eye = right column). Lines represent linear fitting curves to the data. Results show similar trends across patients for the different distances. On average, the regression lines show higher slopes for far (0.005 ± 0.0005 D/nm) than for intermediate (0.003 ± 0.0006 D/nm) and near (0.001 ± 0.0007 D/nm) distances. The standard deviations are higher for near than for intermediate and far distances. We did not find statistical differences in the slopes between right and left eyes: 0.005 ± 0.0005 D/nm (right eye) and 0.004 ± 0.0006 D/nm (left eye) (p= 0.46) for far; 0.003 ± 0.0006 D/nm (right eye) and 0.003 ± 0.0007 D/nm (right eye) (p = 0.33) for intermediate; and 0.001 ± 0.0008 D/nm (right eye) and 0.001 ± 0.0007 D/mm (left eye) (p = 0.05) for near.

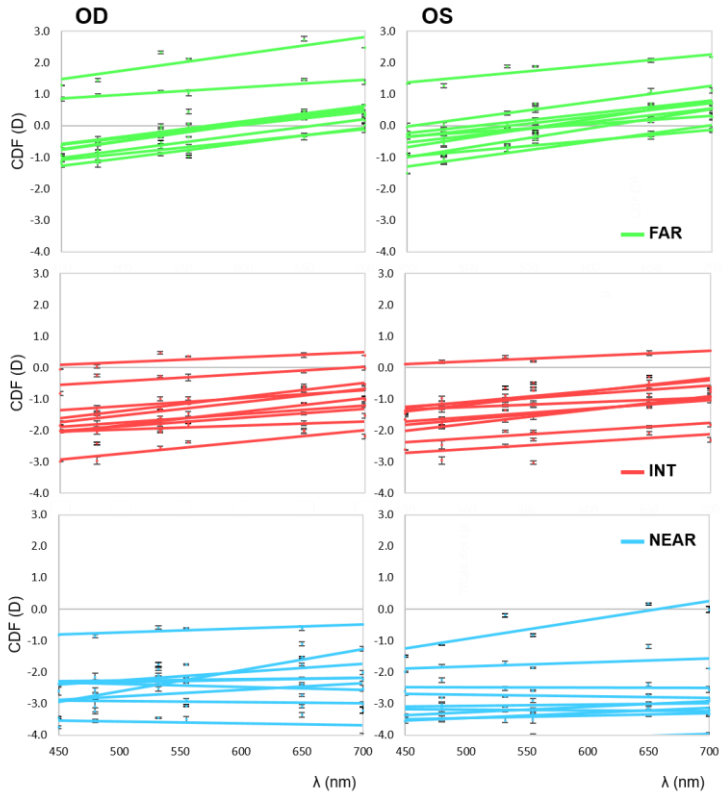

FIGURE 8.3 Chromatic difference of focus (CDF). Psychophysical best focus chosen by each patient for each wavelength (480, 532, 555, 650, and 700 nm), distance (far: green; intermediate: red; near: blue), and eye (right eye, left column; left eye, right column). Error bars indicate standard deviation for each measurement. D = diopters; OD = right eye; OS = left eye.

8.3.2. Refractive and visual outcomes for the IOL implanted

FIGURE 8.4 shows the refractive outcomes (postoperative spherical equivalent refractive and postoperative refractive cylinder) and visual outcomes (UDVA vs CDVA) for the IOL-based procedures in the sample's study.

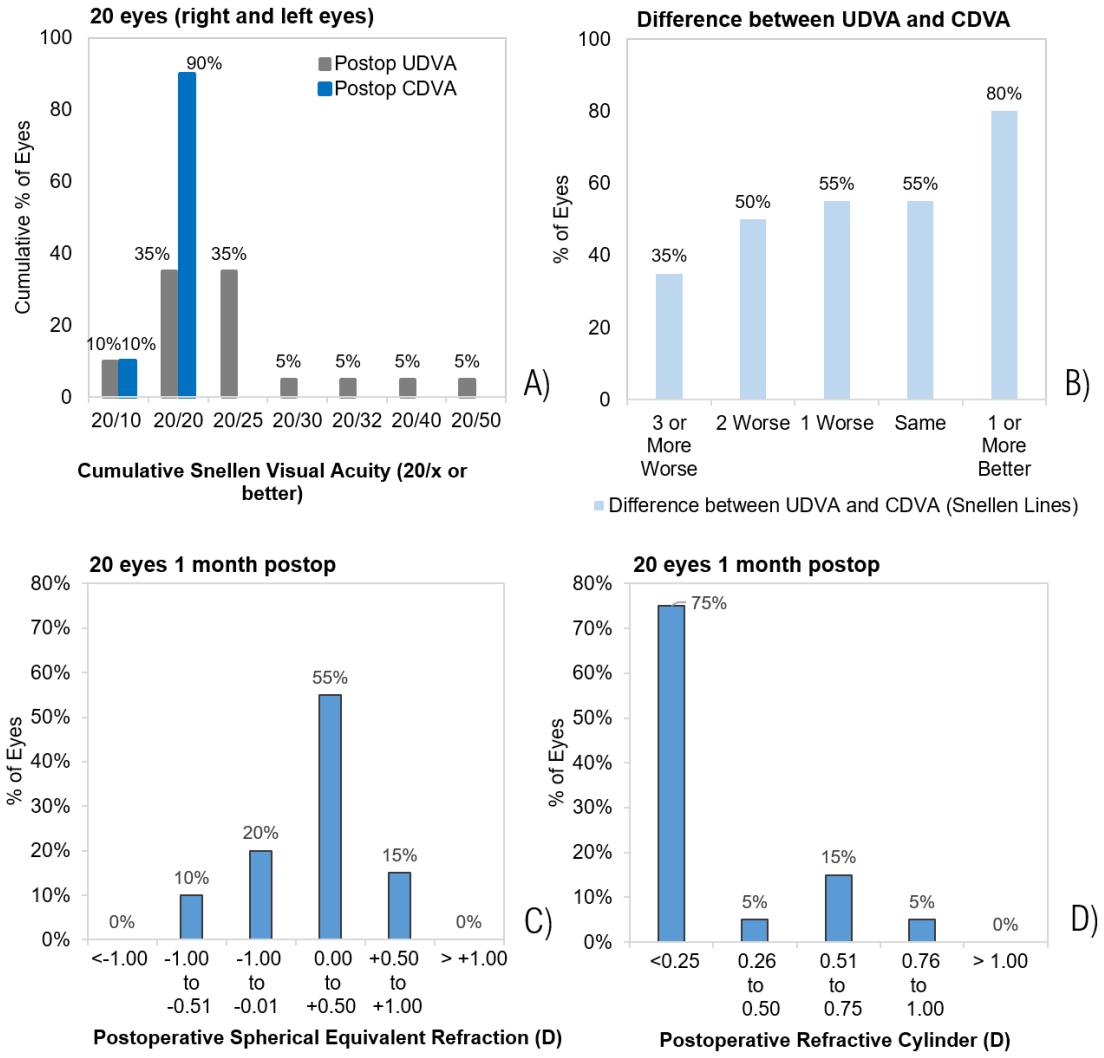

FIGURE 8.4. Refractive outcomes for the intraocular lens-based procedures in the sample's study: A) uncorrected distance visual acuity (UDVA); B) UDVA vs corrected distance visual acuity (CDVA); C) spherical equivalent refraction accuracy, and D) postoperative refractive cylinder. D = diopters.

8.4. DISCUSSION

The optical performance of the pseudophakic eye in polychromatic light is determined by both the material and design of the IOL. This is especially relevant in diffractive designs, such as trifocal diffractive IOLs, aiming at generating an intermediate focal point in the IOL optic to improve the optical range. In a previous study [297], we measured the in vivo subjective LCA of 20 eyes bilaterally implanted with hydrophilic trifocal diffractive IOLs (FineVision POD F) for the different working distances: 0.00 D for far, +1.75 D for intermediate, and +3.50 D for near distances. The LCA from psychophysical measurements was significantly higher for far (0.82 ± 0.05 D) than for intermediate (0.27 ± 0.15 D) and near (0.15 ± 0.15 D) vision. In the current study, LCA of 20 eyes implanted with same design but hydrophobic material (FineVisionHP POD F GF) was obtained from in vivo psychophysical measurements (480 to 700 nm). Similarly, to the hydrophilic design, LCA for far vision was significantly higher than for intermediate and near vision (far: 0.99 ± 0.06 D; intermediate: 0.67 ± 0.10 D; near: 0.23 ± 0.08 D), and, on average, LCA with the hydrophobic IOL was higher than with the hydrophilic IOL for all distances.

Diffractive multifocal IOLs are typically a hybrid refractive–diffractive design, where light energy is split between different foci. In most designs, the far foci receive light that appears to be purely refracted (0 diffraction order), whereas the other foci (inter-mediate and near) are obtained through a combination of diffracted light (first and second order of diffraction). Refractive or diffractive focalization leads to opposite signs of LCA, thus allowing modulation of the chromatic aberration of the eye at different distances. The decrease of the LCA at an intermediate distance in patients implanted with the FineVision trifocal IOL, for both materials, is also supported by recent on-bench work by Loicq et al.[74]. They found that for far vision there is a refractive dominant process, whereas for near the trend is reversed and there is a diffractive dominant process. The LCA (of the IOL alone) was almost fully canceled at an intermediate distance and its sign was reversed at a near distance. This agrees well with our findings of reduction and almost full cancelation at intermediate and near distance in eyes implanted with the IOL.

At every distance, we found a consistently higher LCA value in patients implanted with the hydrophobic IOL than with the hydrophilic IOL. This is consistent with a previous study where patients were bilaterally implanted with monofocal IOLs of the same design, but with hydrophobic material in one eye and hydrophilic material in the contralateral eye [416]. In that study, there was a constant offset of 0.15 D between the LCA measured in vivo in eyes implanted with monofocal IOLs of both materials, which compares with the offset in the LCA found between the hydrophobic and hydrophilic trifocal IOL at far (0.17 D). However, the magnitude of the LCA in patients implanted with monofocal IOL designs was higher (1.37 ± 0.08 D for the hydrophobic and 1.2.1 ± 0.08 D for the hydrophilic) than with the corresponding trifocal designs.

8.5. CONCLUSIONS

LCA for far vision was significantly higher than for intermediate and near vision in hydrophobic trifocal diffractive IOLs, in agreement with a previous study with the same optical design but hydrophilic material IOLs. The LCA for the hydrophobic IOL is slightly higher than for the hydrophilic IOL at far. Different combinations of refractive and diffractive LCA will allow optimizing IOL designs to improve polychromatic image quality. The ability to measure in vivo LCA in monofocal and multifocal IOLs with different materials and designs allows quantifying retinal image quality in polychromatic pseudophakic eyes. Understanding the interactions between monochromatic and chromatic aberrations of the eye and the different multifocal diffractive design improves the resulting polychromatic retinal quality and simultaneous vision quality, therefore opening the path to real custom designs.

CHAPTER 9. CONCLUSIONS

In this thesis we have accomplished the following achievements:

- Ability to predict visual quality values when simulating multifocal intraocular lenses before surgery and after surgery in the same subject. The simulation was performed using two different simulation platforms (1) a custom-developed polychromatic multichannel adaptive optics visual simulator system, with two visual simulator devices: a spatial light modulator and a tunable lens operating under temporal multiplexing (SimVis); and (2) a wearable, binocular, large field of view SimVis2Eyes clinical simulator (SimVis Gekko™ , 2Eyes Vision).

- Ability to reproduce multifocal patterns of contact lenses with different additions (Low, Medium, and High) in a simultaneous vision simulator (SimVis). Obtaining curves that capture the through-focus optical and visual performance of the real multifocal contact lenses in most of the subjects.

- Obtained evidence of the favorable interaction that exists between monochromatic and polychromatic aberrations when using convolved stimuli under adaptive optics correction. Uncovering in this way the mystery of why the convolved images were perceived more degraded than the optically blurred ones, using the same pattern of aberrations.

- Computed the polychromatic point spread function from experimental data, from monochromatic aberrations and chromatic aberrations measure in a real subject (longitudinal chromatic aberration, defocus, and transverse chromatic aberration shift), to simulate more real situations, given the polychromatic world in which we live.

- Implementation of psychophysical paradigm to study visual performance and visual perception under controlled ocular aberration - gender identification, 8 alternative-forced-choice procedures, vernier alignment, and convolved stimuli.

- Implementation of a specific channel in the polychromatic adaptive optics system to measure transverse chromatic aberration (TCA), with aberration control (natural aberrations and adaptive optics correction) and in two different pupil sizes.

- Computationally calculated the perceived TCA (6 mm) from experimental data of the optical TCA (2 mm) and aberrations of the subjects.

- Successfully measurement of the Stiles-Crawford effect peak, to introduce it into the computational calculation of perceived TCA and study its impact, with respect to experimental measurements of perceived TCA.

- Successfully measurements of the longitudinal chromatic aberration in vivo using a psychophysical method in patients bilaterally implanted with a trifocal diffractive intraocular lens design.

- Calibration and alignment of different active elements (spatial light modulator, SimVis, deformable mirror) in the polychromatic multichannel AO visual simulator system to obtain the desired visual performance image.

- Ability to handle three optical systems with different complexity (polychromatic multichannel AO visual simulator system, monochromatic AO system, and the Laser Ray Tracing) and different approaches to developing the project described in this thesis.

The use of a polychromatic multichannel AO visual simulator system, a monochromatic AO system both combined with a psychophysics channel, and a laser ray tracing system has allowed us to obtain the following conclusions:

1. Visual simulations are useful programmable tools to predict visual performance with M-IOLs, both in an AO environment and in a clinical simulator. Pre-operative visual simulations and post-operative data are in good agreement.

2. M-CLs theoretically and effectively expand the depth of focus. A novel simulator, SimVis, captured the through-focus optical and visual performance of the M-CL in most of the subjects.

3. SimVis technology allows subjects to experience multifocal vision non-invasively. We demonstrated equivalence between real multifocal contact lenses and SimVis-simulated lenses. The results suggest that SimVis is a suitable technique to aid the selection of presbyopic corrections in contactology practice.

4. VA with convolved stimuli was lower than VA through natural aberrations, particularly in WL (by 26% in WL). Our results suggest that the systematic decrease in visual performance with VA and retinal image quality by simulation with convolved stimuli appears to be primarily associated with a lack of favorable interaction between chromatic and monochromatic aberrations in the eye.

5. Optical simulations and VA experiments in real eyes support the hypothesis that a larger degradation with convolved stimuli (observed through corrected optics) in comparison with natural viewing occurs most noticeably in polychromatic light.

6. The spatial frequencies involved in a task, influence the effect of aberrations and their manipulation of these to a greater or lesser degree when performing the task.

7. TCA was systematically shifted nasally for small pupils and the presence of monochromatic aberrations produced an intersubject spread of the perceived TCA. Correcting HOAs in fact increased the perceived TCA in most subjects.

8. Measurements of the Stiles-Crawford effect in addition to monochromatic aberrations and LCA allowed predictions of the relative impact of OSCE and aberrations on the perceived TCA. We found that incorporating an apodized pupil given by the individual OSCE produced accurate predictions of the experimental perceived TCA.

9. The results obtained in this thesis indicate that estimates of polychromatic image quality should incorporate patients' specific data of HOAs, LCA, TCA & OSCE.

10. The ability to measure in vivo LCA in multifocal IOLs with different materials and designs allows quantifying retinal image quality in polychromatic pseudophakic eyes. Understanding the interactions between monochromatic and chromatic aberrations of the eye and the different multifocal diffractive designs improves the resulting polychromatic retinal quality and simultaneous vision quality, therefore opening the path to real custom designs.

Scientific activities during this thesis

1. Scientific publications

1. **S. Aissati,** C. Benedi-Garcia, M. Vinas, A. de Castro, and S. Marcos, "Matching convolved images to optically blurred images on the retina," Journal of Vision **22**, 12-12 (2022).

2. C. Benedi-Garcia, M. Vinas, C. M. Lago, **S. Aissati,** A. de Castro, C. Dorronsoro, and S. Marcos, "Optical and visual quality of real intraocular lenses physically projected on the patient's eye," Biomedical Optics Express **12**, 6360-6374 (2021).

3. S. Vedhakrishnan, M. Vinas, **S. Aissati,** and S. Marcos, "Vision with spatial light modulator simulating multifocal contact lenses in an adaptive optics system," Biomedical Optics Express **12**, 2859-2872 (2021).

4. **S. Aissati,** M. Vinas, C. Benedi-Garcia, C. Dorronsoro, and S. Marcos, "Testing the effect of ocular aberrations in the perceived transverse chromatic aberration," Biomedical Optics Express **11**, 4052-4068 (2020).

5. S. Marcos, C. Benedí-García, **S. Aissati,** A. M. Gonzalez-Ramos, C. M. Lago, A. Radhkrishnan, M. Romero, S. Vedhakrishnan, L. Sawides, and M. Vinas, "VioBio lab adaptive optics: technology and applications by women vision scientists," Ophthalmic Physiol Opt **40**, 75-87 (2020).

6. M. Vinas, A. M. Gonzalez-Ramos, **S. Aissati,** N. Garzón, F. Poyales, C. Dorronsoro, and S. Marcos, "Longitudinal Chromatic Aberration in Patients Implanted With Trifocal Diffractive Hydrophobic IOLs," J Refract Surg **36**, 804-810 (2020).

7. M. Vinas, **S. Aissati,** A. M. Gonzalez-Ramos, M. Romero, L. Sawides, V. Akondi, E. Gambra, C. Dorronsoro, T. Karkkainen, D. Nankivil, and S. Marcos, "Optical and Visual Quality With Physical and Visually Simulated Presbyopic Multifocal Contact Lenses," Translational Vision Science & Technology **9**, 20-20 (2020).

8. M. Vinas, **S. Aissati,** M. Romero, C. Benedi-Garcia, N. Garzon, F. Poyales, C. Dorronsoro, and S. Marcos, "Pre-operative simulation of post-operative multifocal vision," Biomedical Optics Express **10**, 5801-5817 (2019).

9. M. Vinas, C. Benedi-Garcia, **S. Aissati**, D. Pascual, V. Akondi, C. Dorronsoro, and S. Marcos, "Visual simulators replicate vision with multifocal lenses," Scientific Reports **9**, 1539 (2019).

2. Scientific publications in proceeding

1. M. Vinas, **S. Aissati,** A. M. Gonzalez-Ramos, M. Romero, L. Sawides, V. Akondi, E. Gambra, C. Dorronsoro, T. Karkkainen, D. Nankivil, and S. Marcos, 'Optical and visual quality with physical and visually simulated presbyopic multifocal contact lenses'. Investigative Ophthalmology & Visual Science 60 (9), 6468-6468.

2. **S. Aissati,** M Vinas, C Benedi-Garcia, C Dorronsoro, S Marcos. 'Testing the effect of ocular aberrations on perceived Transverse Chromatic Aberration'. Investigative Ophthalmology & Visual Science 60 (9), 601-601.

3. S. Vedhakrishnan, M. Vinas, **S. Aissati,** C. Benedi-Garcia, M. Romero, A. Gonzalez-Ramos, C. Dorronsoro, S. Marcos. 'Adaptive-optics vision simulation of multifocal lenses for myopia progression'. Investigative Ophthalmology & Visual Science 60 (9), 605-605.

4. S. Marcos, M. Vinas, A. Gonzalez-Ramos, **S. Aissati**, C. Dorronsoro, N. Garzon, F. Poyales. 'In vivo chromatic aberration in patients implanted with hydrophilic and hydrophobic monofocal and FineVision trifocal IOLs'. ESCRS 2018, Viena (Austria).

5. M. Vinas; M. Romero; **S. Aissati**; JL Mendez-Gonzalez; C. Benedi; E. Gambra; V. Akondi; N. Garzon; F. Poyales; C. Dorronsoro; S. Marcos. 'Comparison of multifocal visual simulations in patients before and after implantation of diffractive trifocal lenses'. Investigative Ophthalmology & Visual Science July 2018, Vol.59, 252.

6. S. Marcos, M. Vinas, C. Dorronsoro, L. Sawides, E. Gambra, C. Benedi, **S. Aissati.** 'AdaptiveOptics based visual simulators: from on-bench to wearable devices' (invited talk). OSA Imaging and Applied Optics Congress. Meeting Adaptive Optics: Methods, Analysis and Applications 2018, Orlando (USA).

7. **S. Aissati,** M. Vinas, M. Romero, C. Benedi, V. Akondi, C. Dorronsoro, S. Marcos.'Visual simulation of multifocal lenses in patients before and after implantation of diffractive trifocal lenses'. AOIM XI 2018, Murcia (Spain).

8. V. Akondi, E. Gambra, M. Vinas, **S. Aissati**, C. Dorronsoro, D. Pascual, S. Marcos. 'Simulating multifocal intraocular lenses with a SLM and a tunable lens'. Investigative Ophthalmology & Visual Science 2017, Vol.58, Issue 8, 1272.

9. S. Marcos, M. Vinas, C. Benedi**, S. Aissati,** V. Akondi, X. Barcala, E. Gambra. 'Visual simulations of real multifocal lenses in a multi-channel Adaptive Optics system'. Investigative Ophthalmology & Visual Science 2017, Vol.58, Issue 8, 1248.

10. V. Akondi, E. Gambra, M. Vinas, D. Pascual, **S. Aissati**, S. Marcos. "Temporal multiplexing and simulation of multifocal intraocular lenses". Frontiers in Optics 2016 OSA Technical Digest (online) (Optical Society of America, 2016), paper FW2A.3

3. Conferences

Personally presented

(authors are indicated by signature order, p=poster, t=talk)

2021-p **S. Aissati,** M. Vinas, C. Benedi-Garcia, AM. Gonzalez-Ramos, S. Vedhakrishnan and S. Marcos, 'Applications of Adaptive Optics Visual Simulators', Reunión Naciona de Óptica, RNO 2021.

2021-t **S. Aissati,** M. Vinas, C. Benedi-Garcia, A. de Castro, S. Marcos. 'Convolved vs. Optically blurred images. What is the key reason for the observed differences?' OSA Vision and Color Summer Data Blast!, Applications of Visual Science Technical Group.

2021-p **S. Aissati,** M. Vinas, C. Benedi-Garcia, A. de Castro, S. Marcos. 'Convolved vs. Optically blurred images. What is the key reason for the observed differences?' ARVO2021 San Francisco (USA).

2019-t **S. Aissati**, M. Vinas, C. Benedi, C. Dorronsoro, S. Marcos. 'Testing the effect of ocular aberrations on perceived Transverse Chromatic Aberration' IONSBCN2019 Barcelona (Spain).

2018-t **S. Aissati,** M. Vinas, C. Benedi, C. Dorronsoro, S. Marcos. 'Testing the effect of ocular aberrations on perceived Transverse Chromatic Aberration' PhDay-FOO 18, PhD in optics, optometry, and vision, School of Optics and Optometry, Complutense University of Madrid.

2018-t **S. Aissati**. 'π Research: New optical technologies for the evaluation and design of multifocal corrections for presbyopia, III National Optics Meeting of Young Researchers in Castellón July 2nd, 2018.

2018-t **S. Aissati**, M. Vinas, M. Romero, C. Benedi, V. Akondi, C. Dorronsoro, S. Marcos. 'Visual simulation of multifocal lenses in patients before and after implantation of diffractive trifocal lenses'. AOIM XI 2018, Murcia (Spain).

2017-t **S. Aissati,** M. Vinas, C. Benedi-Garcia, C. Dorronsoro, V. Akondi, S. Marcos, 'Double-pass technique to compare different visual simulators in an Adaptive Optics environment'. IONS-2017-Paris (Paris, France).

2016-p **S. Aissati**, M. Vinas, C. Dorronsoro, S. Marcos. 'Simulation of multifocal corrections using a tunable lens-based simultaneous vision simulator in an Adaptive Optics system environment'. IONS- Naples2016 (Naples, Italy)

Presented by collaborators

(authors are indicated by signature order, p=poster, t=talk)

2021-p C. Benedi-Garcia, **S. Aissati** , M P. Eckstein , S.Marcos. 'Gender Identification of faces under manipulated ocular optics'. ARVO2021 San Francisco (USA).

2019-p S. Vedhakrishnan, M. Vinas, **S. Aissati**, C. Benedi-Garcia, M. Romero, AM. Gonzalez-Ramos, C.Dorronsoro, S. Marcos. 'Adaptive-optics vision simulation of multifocal lenses for myopia progression'. ARVO2019 Vancouver (Canada).

2019-t M. Vinas, **S. Aissati**, A. Gonzalez-Ramos, M. Romero, L. Sawides, V. Akondi, C. Dorronsoro, E. Martinez-Enriquez, T. Karkkainen, D. Nankivil, S. Marcos. 'Optical and visual quality with physical and visually simulated presbyopic multifocal contact lenses'. ARVO2019 Vancouver (Canadá).

2018-t S. Marcos, M. Vinas, AM. Gonzalez-Ramos, **S. Aissati,** C. Dorronsoro, N. Garzon, F. Poyales. 'In vivo chromatic aberration in patients implanted with hydrophilic and hydrophobic monofocal and FineVision trifocal IOLs'. ESCRS 2018, Viena (Austria).

2018-t M. Vinas, C. Dorronsoro, AM. Gonzalez-Ramos, D. Pascual, **S. Aissati,** N Garzón, F Poyales, S Marcos. In vivo chromatic aberration in phakic and pseudophakic eyes. VPO 2018, Athens (Greece).

2018-t S. Vedhakrishnan, M. Vinas, M. Romero, **S. Aissati**, C. Dorronsoro, S. Marcos. 'Visual Simulations of Bifocal contact lenses in young myopic adults for myopia progression control'. VPO 2018, Athens (Greece).

2018-t M. Romero, M. Vinas, **S. Aissati**, JL. Mendez-Gonzalez, C. Benedi, E. Gambra, V. Akondi, N. Garzon, F. Poyales, C. Dorronsoro, S. Marcos. Comparación de simuladores visuales multifocales antes y después del implante de lentes trifocales difractivas en pacientes reales. RNO2018, Castellón (Spain).

2018-t S. Marcos, M. Vinas, C. Dorronsoro, L. Sawides, E. Gambra, C. Benedi, **S. Aissati.** 'Adaptive-Optics based visual simulators: from on-bench to wearable devices' (invited talk). OSA Imaging and Applied Optics Congress. Meeting Adaptive Optics: Methods, Analysis and Applications 2018, Orlando (USA).

2018-p M. Vinas, C. Dorronsoro, AM. Gonzalez-Ramos, D. Pascual, **S. Aissati,** N. Garzón, F. Poyales, S Marcos. 'In vivo chromatic aberration in phakic and pseudophakic eyes implanted with different materials and designs IOLs'. RNO2018, Castellón (Spain)

2018-p M. Vinas, M. Romero, **S. Aissati,** J.L. Mendez-Gonzalez, C. Benedi, E. Gambra, V. Akondi, N. Garzon, F. Poyales, C. Dorronsoro, S. Marcos. Comparison of multifocal visual simulations in patients before and after implantation of diffractive trifocal lenses. ARVO2018, Hawaii (USA)

2017-t C. Dorronsoro, M. Vinas, C. Benedi, **S. Aissati,** V. Akondi, S. Marcos. Pre-surgical visual simulations of real multifocal lenses with different optical methods. ESCRS, 2017. Lisbon (Portugal).

2017-p V. Akondi , E. Gambra , M. Vinas, **S. Aissati,** C. Dorronsoro, D. Pascual, S. Marcos . 'Evaluation of a spatial light modulator and a tunable lens in simulating multifocal intraocular lenses'. ARVO 2017. Baltimore (Maryland, USA).

2017-p S. Marcos, M. Vinas, C. Benedi, **S. Aissati,** V. Akondi, X. Barcala, E. Gambra, 'Visual simulations of real multifocal lenses in a multi-channel Adaptive Optics system'. ARVO 2017. Baltimore (Maryland, USA).

4. Books & Educational publications

1. "Descubriendo la luz. Experimentos divertidos de Óptica". Co-Author. **S. Aissati**. Editor Catarata-CSIC, Madrid 2018. ISBN: 978-84-00-10397-2

2. "Discovering Light: Fun Experiments with Optics". Co-Author. **S. Aissati.** E-book open Access. Editorial: SPIE, OSA Foundation and CSIC. PDF ISBN: 9781510639362 | Print ISBN: 9781510639355; https://doi.org/10.1117/3.2579764

5. Invited talks

2021 **S. Aissati,** M. Vinas, C. Benedi-Garcia, A. de Castro, S. Marcos. 'Convolved vs. Optically blurred images. What is the key reason for the observed differences?' OSA Vision and Color Summer Data Blast!, Applications of Visual Science Technical Group.

6. Grants during this thesis

2017-2021 FPU-PhD fellowship of the Spanish Government (MECD), to develop this thesis proyect. Advisor: Prof Susana Marcos and Co-Advisor: Dr. Maria Vinas. Visual Optics and Biophotonics Lab, Spanish National Research Council (CSIC).

2021 FPU short research stay Grant 2021

2021 ARVO Foundation Travel Grant 2021

2017 IONS Paris Travel Grant 2017

7. Awards during this thesis

2021	ARVO Global Mentorship Program. A six-month program that supports and sustains the interest of junior researchers with a focus on professional development within the field and engaging in ARVO (the Association for Research in Vision and Ophthalmology).
2018	Second best oral communication in the VII Contest for University Research in the Faculty of Optics and Optometry (Accesit) PhDay-FOO18 (UCM).

8. Visits and stays in research institutions

2021	Sabesan Lab from University of Washington Medicine Opthalmology Vision Science (Seattle). Advisor: Prof. Ramkumar Sabesan; Assistant Research Professor, Ophthalmology, Bioengineering (Adjunct) and Biological Structure (Adjunct) Member, Graduate Program in Neuroscience and UW Institute of Neuroengineering. Short stay funded by the Spanish Government (FPU fellowship).
2022	ARVO 2022 contribution with Sabesan Lab short stay –**S. Aissati**, P. Bharadwaj, E. Slezak, X. Jiang, S. Schleufer, S. Marcos, R. Sabesan, 'Investigating the factors limiting visual acuity at different wavelength'.

9. Teaching experience associated to FPU fellowship

2019	Teaching assistant at the Department of Optics in the Faculty of Optometry of the Complutense University of Madrid (UCM). Program. Graduate in Optics and Optometry. Subject: Physical Optics I (35 hrs), practices, FPU Fellow.
2019-2020	Teaching assistant at the Department of Optics in the Faculty of Optometry of the Complutense University of Madrid (UCM). Program. Graduate in Optics and Optometry. Subject: Physical Optics I (40 hrs), practices, FPU Fellow.
2020	Teaching assistant at the Department of Optics in the Faculty of Optometry of the Complutense University of Madrid (UCM). Program. Graduate in Optics and Optometry. Subject: Physics (20 hrs), practices, FPU Fellow.
2020-2021	Teaching assistant at the Department of Optics in the Faculty of Optometry of the Complutense University of Madrid (UCM). Program. Graduate in Optics and Optometry. Subject: Physical Optics I (35 hrs), practices, FPU Fellow.
2021	Teaching assistant at the Department of Optics in the Faculty of Optometry of the Complutense University of Madrid (UCM). Program. Graduate in Optics and Optometry. Subject: Physics (40 hrs), practices, FPU Fellow.

10. Other scientific activities

2016- today	Member of the IO-CSIC Student Chapter of the Optical Society of America (IOSA, https://sites.google.com/view/iosa-student-chapter-csic/). Secretary from January 2017 to December 2017. Vice-President of the IOSA student chapter from January 2018 to December 2018. President of the IOSA student chapter from January 2019 to December 2019. We organize a cycle of internal scientific seminars of the IOSA student chapter, as well as invited talks and informal coffees with great researchers. We organize activities to promote scientific knowledge among our local community, and in educational centers at all levels. Participation in key events such as the 'Week of Science' or the 'International Day of Women and Girls in Science 11F'. All activities are financed by OPTICA (formerly OSA).
2020	Certified OSA Reviewer
2021	Good Clinical PracticeTraining, CITI Training (Collaborative Institutional Training Initiative), Univerity of Washington.
2021	Laser Worker Safety Training, University of Washington.
2020-2021	Co-founder of the CSIC Doctoral Students NETWORK (RED de Doctorand@s del CSIC), to foster union and interaction between all CSIC doctoral students. Secretary from January 2020 to December 2021.
	Major Committee assignments
2020	Member of the Organizing Committee NETWORK of Ph.D. students of the CSIC. RED de Doctorand@s.
2018	Member of the Organizing Committee I Workshop del Área de Mujer Óptica Fotónica @SEDOPTICA
2018	The organizer of the 4th and 5th editions of the IOSA scientific seminars. Organized by IOSA at the Institute of Optics of the Spanish National Research Council (CSIC) Madrid (Spain).
2018	Member of the Organizing Committee. PhDay-FOO18, Ph.D. in optics, optometry, and vision, School of Optics and Optometry, Complutense University of Madrid.

REFERENCES

1. K. Rogers, *The Eye: The Physiology of Human Perception*, Rosen Education Service (2010).
2. J. Loughman, P. A. Davison, J. M. Nolan, M. C. Akkali, and S. Beatty, "Macular pigment and its contribution to visual performance and experience," Journal of Optometry **3**, 74-90 (2010).
3. C. A. Curcio, K. R. Sloan, R. E. Kalina, and A. E. Hendrickson, "Human photoreceptor topography," J Comp Neurol **292**, 497-523 (1990).
4. C. A. Curcio and K. A. Allen, "Topography of ganglion cells in human retina," J Comp Neurol **300**, 5-25 (1990).
5. H. J. Dartnall, J. K. Bowmaker, and J. D. Mollon, "Human visual pigments: microspectrophotometric results from the eyes of seven persons," Proc R Soc Lond B Biol Sci **220**, 115-130 (1983).
6. D. A. Atchison and G. Smith, *Optics of the Human Eye* (2000).
7. R. A. Applegate and V. Lakshminarayanan, "Parametric representation of Stiles–Crawford functions: normal variation of peak location and directionality," Journal of the Optical Society of America A **10**, 1611-1623 (1993).
8. W. S. Stiles, B. H. Crawford, and J. H. Parsons, "The luminous efficiency of rays entering the eye pupil at different points," Proceedings of the Royal Society of London. Series B, Containing Papers of a Biological Character **112**, 428-450 (1933).
9. W. S. Stiles and J. H. Parsons, "The directional sensitivity of the retina and the spectral sensitivities of the rods and cones," Proceedings of the Royal Society of London. Series B - Biological Sciences **127**, 64-105 (1939).
10. G. Westheimer, "Directional sensitivity of the retina: 75 years of Stiles–Crawford effect," Proceedings of the Royal Society B: Biological Sciences **275**, 2777-2786 (2008).
11. E. R. Kandel, J. H. Schwartz, T. M. Jessell, S. Siegelbaum, A. J. Hudspeth, and S. Mack, *Principles of neural science* (McGraw-hill New York, 2000), Vol. 4.
12. G. Ruskell, "The Human Eye, Structure and Function Clyde W. Oyster " Ophthalmic and Physiological Optics **20**, 349-350 (2000).
13. D. H. Hubel, "THE VISUAL CORTEX OF THE BRAIN," Sci Am **209**, 54-62 (1963).
14. R. R. Bourne, G. A. Stevens, R. A. White, J. L. Smith, S. R. Flaxman, H. Price, J. B. Jonas, J. Keeffe, J. Leasher, K. Naidoo, K. Pesudovs, S. Resnikoff, and H. R. Taylor, "Causes of vision loss worldwide, 1990-2010: a systematic analysis," Lancet Glob Health **1**, e339-349 (2013).
15. M. J. Morgan and R. J. Watt, "Mechanisms of interpolation in human spatial vision," Nature **299**, 553-555 (1982).
16. Z. Malacara, "Angle, Prisms, Curvature, and Focal Length Measurements," in *Optical Shop Testing* (2007), pp. 808-831.
17. M. A. X. Born and E. Wolf, "CHAPTER V - GEOMETRICAL THEORY OF ABERRATIONS," in *Principles of Optics (Sixth Edition)*, M. A. X. Born and E. Wolf, eds. (Pergamon, 1980), pp. 203-232.
18. V. N. Mahajan, "Zernike Polynomial and Wavefront Fitting," in *Optical Shop Testing* (2007), pp. 498-546.
19. W. N. Charman, "Wavefront aberration of the eye: a review," Optometry and vision science : official publication of the American Academy of Optometry **68**, 574-583 (1991).
20. M. Born and E. Wolf, *Principles of Optics,* 6th Edition ed. (Pergamon Press, Oxford, 1993).

21. L. N. Thibos, R. A. Applegate, J. T. Schwiegerling, and R. Webb, "Standards for Reporting the Optical Aberrations of Eyes," in *Vision Science and its Applications*, OSA Technical Digest (Optical Society of America, 2000), SuC1.
22. L. N. Thibos, W. Wheeler, and D. Horner, "Power vectors: an application of Fourier analysis to the description and statistical analysis of refractive error," Optometry and vision science : official publication of the American Academy of Optometry **74**, 367-375 (1997).
23. L. Thibos, X. Hong, A. Bradley, and R. Applegate, "Accuracy and precision of objective refraction from wavefront aberrations," Journal of Vision **4**, 329-351 (2004).
24. T. Young, "II. The Bakerian Lecture. On the mechanism of the eye," Philosophical Transactions of the Royal Society of London **91**, 23-88 (1801).
25. D. A. Atchison and W. N. Charman, "Thomas Young's contribution to visual optics: the Bakerian Lecture "on the mechanism of the eye"," J Vis **10**, 16 (2010).
26. A. Ames and C. A. Proctor, "Dioptrics of the Eye," J Opt Soc Am **5**, 22-84 (1921).
27. D. Ivanoff, "Les aberrations de chromatisme et de sphericite de l'oeil. Leur role en vison nocturne," Rev.Opt.Theor.Instrum. **26**, 145-171. (1947).
28. M. S. Smirnov, "Measurement of the wave aberration of the human eye," Biofizika **6**, 776-795 (1961).
29. B. Howland and H. C. Howland, "Subjective measurement of high-order aberrations of the eye," Science **193**, 580-582 (1976).
30. M. Tscherning, *Physiologic Optics* 2nd Edition ed. (1904).
31. G. Walsh, W. N. Charman, and H. C. Howland, "Objective technique for the determination of monochromatic aberrations of the human eye," Journal of the Optical Society of America A **1**, 987-992 (1984).
32. N. López-Gil and H. C. Howland, "Measurement of the eye's near infrared wave-front aberration using the objective crossed-cylinder aberroscope technique," Vision Res **39**, 2031-2037 (1999).
33. R. H. Webb, C. M. Penney, and K. P. Thompson, "Measurement of ocular local wavefront distortion with a spatially resolved refractometer," Applied Optics **31**, 3678-3686 (1992).
34. R. Navarro and M. A. Losada, "Aberrations and relative efficiency of light pencils in the living human eye," Optometry and vision science : official publication of the American Academy of Optometry **74**, 540-547 (1997).
35. R. Navarro and E. Moreno-Barriuso, "Laser Ray-Tracing Method for Optical Testing," Optics Letters **24**(2000).
36. J. Liang, B. Grimm, S. Goelz, and J. F. Bille, "Objective measurement of wave aberrations of the human eye with the use of a Hartmann–Shack wave-front sensor," Journal of the Optical Society of America A **11**, 1949-1957 (1994).
37. J. Porter, A. Guirao, I. G. Cox, and D. R. Williams, "Monochromatic aberrations of the human eye in a large population," Journal of the Optical Society of America A **18**, 1793-1803 (2001).
38. J. F. Castejón-Mochón, N. López-Gil, A. Benito, and P. Artal, "Ocular wave-front aberration statistics in a normal young population," Vision Res **42**, 1611-1617 (2002).
39. A. Guirao, C. González, M. Redondo, E. Geraghty, S. Norrby, and P. Artal, "Average optical performance of the human eye as a function of age in a normal population," Invest Ophthalmol Vis Sci **40**, 203-213 (1999).
40. J. S. McLellan, S. Marcos, and S. A. Burns, "Age-Related Changes in Monochromatic Wave Aberrations of the Human Eye," Investigative Ophthalmology & Visual Science **42**, 1390-1395 (2001).
41. I. Brunette, J. Bueno, M. Parent, H. Hamam, and P. Simonet, "Monochromatic Aberrations as a Function of Age, from Childhood to Advanced Age," Investigative Ophthalmology & Visual Science **44**, 5438-5446 (2003).

42. H. Howland, "High order wave aberration of eyes," Ophthalmic & physiological optics : the journal of the British College of Ophthalmic Opticians (Optometrists) **22**, 434-439 (2002).
43. L. N. Thibos, X. Hong, A. Bradley, and X. Cheng, "Statistical variation of aberration structure and image quality in a normal population of healthy eyes," J Opt Soc Am A Opt Image Sci Vis **19**, 2329-2348 (2002).
44. X. Cheng, A. Bradley, X. Hong, and L. N. Thibos, "Relationship between refractive error and monochromatic aberrations of the eye," Optometry and vision science : official publication of the American Academy of Optometry **80**, 43-49 (2003).
45. A. Guirao, D. R. Williams, and S. M. MacRae, "Effect of beam size on the expected benefit of customized laser refractive surgery," J Refract Surg **19**, 15-23 (2003).
46. L. Llorente, S. Barbero, D. Cano, C. Dorronsoro, and S. Marcos, "Myopic versus hyperopic eyes: axial length, corneal shape and optical aberrations," J Vis **4**, 288-298 (2004).
47. A. Guirao and P. Artal, "Off-axis monochromatic aberrations estimated from double pass measurements in the human eye," Vision Res **39**, 207-217 (1999).
48. I. Escudero-Sanz and R. Navarro, "Off-axis aberrations of a wide-angle schematic eye model," Journal of the Optical Society of America A **16**, 1881-1891 (1999).
49. R. Navarro, P. Artal, and D. Williams, "Modulation transfer of the human eye as a function of retinal eccentricity," Journal of the Optical Society of America. A, Optics and image science **10**, 201-212 (1993).
50. S. Burns, "The Spatially Resolved Refractometer," J Refract Surg **16**, S566-569 (2000).
51. D. A. Atchison, M. J. Collins, C. F. Wildsoet, J. Christensen, and M. D. Waterworth, "Measurement of monochromatic ocular aberrations of human eyes as a function of accommodation by the Howland aberroscope technique," Vision Res **35**, 313-323 (1995).
52. F. C. Delori and K. P. Pflibsen, "Spectral reflectance of the human ocular fundus," Applied Optics **28**, 1061-1077 (1989).
53. S. Marcos, S. A. Burns, E. Moreno-Barriusop, and R. Navarro, "A new approach to the study of ocular chromatic aberrations," Vision Research **39**, 4309-4323 (1999).
54. L. Llorente, L. Diaz-Santana, D. Lara-Saucedo, and S. Marcos, "Aberrations of the Human Eye in Visible and Near Infrared Illumination," Optometry and vision science : official publication of the American Academy of Optometry **80**, 26-35 (2003).
55. E. Fernandez, A. Unterhuber, B. Považay, B. Hermann, P. Artal, and W. Drexler, "Chromatic aberration correction of the human eye for retinal imaging in the near infrared," Optics Express **14**, 6213-6225 (2006).
56. P. Pérez-Merino, C. Dorronsoro, L. Llorente, S. Durán, I. Jiménez-Alfaro, and S. Marcos, "In Vivo Chromatic Aberration in Eyes Implanted With Intraocular Lenses," Investigative Ophthalmology & Visual Science **54**, 2654-2661 (2013).
57. L. N. Thibos, A. Bradley, and X. X. Zhang, "Effect of ocular chromatic aberration on monocular visual performance," Optometry and vision science : official publication of the American Academy of Optometry **68**, 599-607 (1991).
58. G. Wald and D. R. Griffin, "The Change in Refractive Power of the Human Eye in Dim and Bright Light," J Opt Soc Am **37**, 321-336 (1947).
59. M. C. Rynders, R. F. Navarro, and M. A. Losada, "Objective measurement of the off-axis longitudinal chromatic aberration in the human eye," Vision Research **38**, 513-522 (1998).
60. E. J. Fernández, A. Unterhuber, P. M. Prieto, B. Hermann, W. Drexler, and P. Artal, "Ocular aberrations as a function of wavelength in the near infrared measured with a femtosecond laser," Optics Express **13**, 400-409 (2005).
61. S. Manzanera, C. Canovas, P. M. Prieto, and P. Artal, "A wavelength tunable wavefront sensor for the human eye," Optics Express **16**, 7748-7755 (2008).
62. M. Vinas, C. Dorronsoro, D. Cortes, D. Pascual, and S. Marcos, "Longitudinal chromatic aberration of the human eye in the visible and near infrared from wavefront sensing, double-pass and psychophysics," Biomed Opt Express **6**, 948-962 (2015).

63. W. N. Charman and J. A. Jennings, "Objective measurements of the longitudinal chromatic aberration of the human eye," Vision Res **16**, 999-1005 (1976).
64. L. N. Thibos, M. Ye, X. Zhang, and A. Bradley, "The chromatic eye: a new reduced-eye model of ocular chromatic aberration in humans," Applied Optics **31**, 3594-3600 (1992).
65. J. Wang, T. R. Candy, D. F. W. Teel, and R. J. Jacobs, "Longitudinal chromatic aberration of the human infant eye," Journal of the Optical Society of America A **25**, 2263-2270 (2008).
66. D. A. Atchison and G. Smith, "Chromatic dispersions of the ocular media of human eyes," Journal of the Optical Society of America A **22**, 29-37 (2005).
67. F. W. Campbell and R. W. Gubisch, "The effect of chromatic aberration on visual acuity," The Journal of Physiology **192**, 345-358 (1967).
68. P. A. Howarth, X. X. Zhang, A. Bradley, D. L. Still, and L. N. Thibos, "Does the chromatic aberration of the eye vary with age?," Journal of the Optical Society of America A **5**, 2087-2092 (1988).
69. C. Ware, "Human axial chromatic aberration found not to decline with age," Graefes Arch Clin Exp Ophthalmol **218**, 39-41 (1982).
70. M. S. Millán, F. Vega, and I. Ríos-López, "Polychromatic Image Performance of Diffractive Bifocal Intraocular Lenses: Longitudinal Chromatic Aberration and Energy Efficiency," Investigative Ophthalmology & Visual Science **57 4**, 2021-2028 (2016).
71. T. Nagata, S. Kubota, I. Watanabe, and S. Aoshima, "[Chromatic aberration in pseudophakic eyes]," Nippon Ganka Gakkai Zasshi **103**, 237-242 (1999).
72. D. Siedlecki, A. Jóźwik, M. Zając, A. Hill-Bator, and A. Turno-Kręcicka, "In vivo longitudinal chromatic aberration of pseudophakic eyes," Optometry and vision science : official publication of the American Academy of Optometry **91**, 240-246 (2014).
73. M. Vinas, A. Gonzalez-Ramos, C. Dorronsoro, V. Akondi, N. Garzon, F. Poyales, and S. Marcos, "In Vivo Measurement of Longitudinal Chromatic Aberration in Patients Implanted With Trifocal Diffractive Intraocular Lenses," J Refract Surg **33**, 736-742 (2017).
74. J. Loicq, N. Willet, and D. Gatinel, "Topography and longitudinal chromatic aberration characterizations of refractive-diffractive multifocal intraocular lenses," J Cataract Refract Surg **45**, 1650-1659 (2019).
75. M. S. Millán, F. Vega, F. Poyales, and N. Garzón, "Clinical assessment of chromatic aberration in phakic and pseudophakic eyes using a simple autorefractor," Biomedical Optics Express **10**, 4168-4178 (2019).
76. J. Loicq, N. Willet, and D. Gatinel, *LCA correction in diffractive intraocular lenses: an innovative optical design (Conference Presentation)*, SPIE BiOS (SPIE, 2020), Vol. 11231.
77. P. Simonet and M. C. Campbell, "The optical transverse chromatic aberration on the fovea of the human eye," Vision Res **30**, 187-206 (1990).
78. P. A. Howarth, "The lateral chromatic aberration of the eye," Ophthalmic Physiol Opt **4**, 223-226 (1984).
79. Y. Le Grand, *Optique physiologique. L'espace visuel*, III Éditions de la Revue d'Optique (Paris 1956).
80. G. Walsh, "The effect of mydriasis on the pupillary centration of the human eye," Ophthalmic and Physiological Optics **8**, 178-182 (1988).
81. L. N. Thibos, A. Bradley, D. L. Still, X. Zhang, and P. A. Howarth, "Theory and measurement of ocular chromatic aberration," Vision Research **30**, 33-49 (1990).
82. B. N. Kishto, "The colour stereoscopic effect," Vision Research **5**, 313-IN314 (1965).
83. Y. U. Ogboso and H. E. Bedell, "Magnitude of lateral chromatic aberration across the retina of the human eye," Journal of the Optical Society of America A **4**, 1666-1672 (1987).
84. J. J. Vos, "Some New Aspects of Color Stereoscopy," J Opt Soc Am **50**, 785-790 (1960).
85. M. C. Rynders, "The Stiles-Crawford effect and an experimentaldetermination of its impact on vision," (Indiana University, Bloomington, Ph.D. thesis (unpublished), 1994).

86. M. Ye, A. Bradley, L. N. Thibos, and X. Zhang, "The effect of pupil size on chromostereopsis and chromatic diplopia: interaction between the Stiles-Crawford effect and chromatic aberrations," Vision Res **32**, 2121-2128 (1992).
87. W. M. Harmening, P. Tiruveedhula, A. Roorda, and L. C. Sincich, "Measurement and correction of transverse chromatic offsets for multi-wavelength retinal microscopy in the living eye," Biomedical Optics Express **3**, 2066-2077 (2012).
88. C. M. Privitera, R. Sabesan, S. Winter, P. Tiruveedhula, and A. Roorda, "Eye-tracking technology for real-time monitoring of transverse chromatic aberration," Optics Letters **41**, 1728-1731 (2016).
89. S. Winter, R. Sabesan, P. Tiruveedhula, C. Privitera, P. Unsbo, L. Lundström, and A. Roorda, "Transverse chromatic aberration across the visual field of the human eye," Journal of Vision **16**, 9-9 (2016).
90. A. E. Boehm, C. M. Privitera, B. P. Schmidt, and A. Roorda, "Transverse chromatic offsets with pupil displacements in the human eye: sources of variability and methods for real-time correction," Biomed Opt Express **10**, 1691-1706 (2019).
91. J. Goodman and P. Sutton, "Introduction to Fourier Optics," Quantum and Semiclassical Optics-Journal of the European Optical Society Part B **8**, 1095 (1996).
92. S. Ravikumar, L. N. Thibos, and A. Bradley, "Calculation of retinal image quality for polychromatic light," J Opt Soc Am A Opt Image Sci Vis **25**, 2395-2407 (2008).
93. A. van Meeteren, "Calculations on the Optical Modulation Transfer Function of the Human Eye for White Light," Optica Acta: International Journal of Optics **21**, 395-412 (1974).
94. A. B. Watson, "Computing human optical point spread functions," Journal of Vision **15**, 26-26 (2015).
95. F. Flamant, "Étude de la répartition de lumière dans l'image rétinienne d'une fente. [Study of light distribution in the retinal image of a slit.]," Revue d'Optique Theorique et Instrumentale **34**, 433-459 (1955).
96. G. Westheimer and F. W. Campbell, "Light Distribution in the Image Formed by the Living Human Eye*," J Opt Soc Am **52**, 1040-1045 (1962).
97. F. W. Campbell and R. W. Gubisch, "Optical quality of the human eye," The Journal of Physiology **186**, 558-578 (1966).
98. J. Santamaría, P. Artal, and J. Bescós, "Determination of the point-spread function of human eyes using a hybrid optical–digital method," JOSA A **4**, 1109-1114 (1987).
99. P. Artal, S. Marcos, R. Navarro, and D. R. Williams, "Odd aberrations and double-pass measurements of retinal image quality," Journal of the Optical Society of America A **12**, 195-201 (1995).
100. P. Artal, I. Iglesias, N. López-Gil, and D. G. Green, "Double-pass measurements of the retinal-image quality with unequal entrance and exit pupil sizes and the reversibility of the eye's optical system," Journal of the Optical Society of America A **12**, 2358-2366 (1995).
101. R. Navarro and M. A. Losada, "Phase transfer and point-spread function of the human eye determined by a new asymmetric double-pass method," Journal of the Optical Society of America A **12**, 2385-2392 (1995).
102. P. Artal, "Calculations of two-dimensional foveal retinal images in real eyes," Journal of the Optical Society of America A **7**, 1374-1381 (1990).
103. R. A. Applegate, E. J. Sarver, and V. Khemsara, "Are all aberrations equal?," J Refract Surg **18**, S556-562 (2002).
104. S. Marcos, S. Barbero, and I. Jiménez-Alfaro, "Optical Quality and Depth-of-field of Eyes Implanted With Spherical and Aspheric Intraocular Lenses," Journal of Refractive Surgery **21**, 223-235 (2005).
105. B. Jaeken and P. Artal, "Optical Quality of Emmetropic and Myopic Eyes in the Periphery Measured with High-Angular Resolution," Investigative Ophthalmology & Visual Science **53**, 3405-3413 (2012).

106. E. Peli and A. Lang, "Appearance of images through a multifocal intraocular lens," Journal of the Optical Society of America A **18**, 302-309 (2001).
107. R. A. Applegate, C. Ballentine, H. Gross, E. J. Sarver, and C. A. Sarver, "Visual acuity as a function of Zernike mode and level of root mean square error," Optometry and vision science : official publication of the American Academy of Optometry **80**, 97-105 (2003).
108. R. Legras, N. Chateau, and W. N. Charman, "Assessment of just-noticeable differences for refractive errors and spherical aberration using visual simulation," Optometry and vision science : official publication of the American Academy of Optometry **81**, 718-728 (2004).
109. L. Sawides, P. de Gracia, C. Dorronsoro, M. Webster, and S. Marcos, "Adapting to blur produced by ocular high-order aberrations," Journal of Vision **11**, 21-21 (2011).
110. L. Sawides, P. de Gracia, C. Dorronsoro, M. A. Webster, and S. Marcos, "Vision Is Adapted to the Natural Level of Blur Present in the Retinal Image," PLOS ONE **6**, e27031 (2011).
111. L. Sawides, S. Marcos, S. Ravikumar, L. Thibos, A. Bradley, and M. Webster, "Adaptation to astigmatic blur," J Vis **10**, 22 (2010).
112. M. Vinas, L. Sawides, P. de Gracia, and S. Marcos, "Perceptual Adaptation to the Correction of Natural Astigmatism," PLOS ONE **7**, e46361 (2012).
113. P. de Gracia, C. Dorronsoro, L. Sawides, E. Gambra, and S. Marcos, "Experimental Test of Simulated Retinal Images Using Adaptive Optics," in *Frontiers in Optics 2009/Laser Science XXV/Fall 2009 OSA Optics & Photonics Technical Digest*, OSA Technical Digest (CD) (Optical Society of America, 2009), JWB4.
114. A. Ohlendorf, J. Tabernero, and F. Schaeffel, "Visual Acuity with Simulated and Real Astigmatic Defocus," Optometry and Vision Science **88**, 562-569 (2011).
115. S. K. Shevell, *The science of color* (Elsevier, 2003).
116. J. S. McLellan, S. Marcos, P. M. Prieto, and S. A. Burns, "Imperfect optics may be the eye's defence against chromatic blur," Nature **417**, 174-176 (2002).
117. A. C. S. van Heel, "Correcting the Spherical and Chromatic Aberrations of the Eye," J Opt Soc Am **36**, 237-239 (1946).
118. A. L. Lewis, M. Katz, and C. Oehrlein, "A modified achromatizing lens," Am J Optom Physiol Opt **59**, 909-911 (1982).
119. I. Powell, "Lenses for correcting chromatic aberration of the eye," Applied Optics **20**, 4152-4155 (1981).
120. X. Zhang, A. Bradley, and L. N. Thibos, "Achromatizing the human eye: the problem of chromatic parallax," Journal of the Optical Society of America A **8**, 686-691 (1991).
121. C. Benedi-Garcia, M. Vinas, C. Dorronsoro, S. A. Burns, E. Peli, and S. Marcos, "Vision is protected against blue defocus," Scientific Reports **11**, 352 (2021).
122. F. Autrusseau, L. Thibos, and S. K. Shevell, "Chromatic and wavefront aberrations: L-, M- and S-cone stimulation with typical and extreme retinal image quality," Vision Res **51**, 2282-2294 (2011).
123. S. Marcos and S. A. Burns, "Cone spacing and waveguide properties from cone directionality measurements," Journal of the Optical Society of America A **16**, 995-1004 (1999).
124. B. Lochocki, D. Rativa, and B. Vohnsen, "Spatial and spectral characterisation of the first and second Stiles–Crawford effects using tuneable liquid-crystal filters," Journal of modern optics **58**, 1817-1825 (2011).
125. B. Lochocki and B. Vohnsen, "Defocus-corrected analysis of the foveal Stiles--Crawford effect of the first kind across the visible spectrum," Journal of Optics **15**, 125301 (2013).
126. J. M. Enoch and G. M. Hope, "Directional sensitivity of the foveal and parafoveal retina," Invest Ophthalmol **12**, 497-503 (1973).
127. J. C. He, S. Marcos, and S. A. Burns, "Comparison of cone directionality determined by psychophysical and reflectometric techniques," Journal of the Optical Society of America A **16**, 2363-2369 (1999).

128. A. C. Martins and B. Vohnsen, "Directional light-capture efficiency of the foveal and parafoveal photoreceptors at different luminance levels: an experimental and analytical study," Biomedical Optics Express **10**, 3760-3772 (2019).
129. S. A. Burns, S. Wu, F. Delori, and A. E. Elsner, "Direct measurement of human-cone-photoreceptor alignment," Journal of the Optical Society of America A **12**, 2329-2338 (1995).
130. G. J. van Blokland, "Directionality and alignment of the foveal receptors, assessed with light scattered from the human fundus in vivo," Vision Res **26**, 495-500 (1986).
131. J. Krauskopf, "Some experiments with a photoelectric ophthalmoscope," in *Excerpta Med. Int. Congr. Ser.*, 1965),
132. J.-M. Gorrand and F. Delori, "A reflectometric technique for assessing photorecelptor alignment," Vision Research **35**, 999-1010 (1995).
133. S. Marcos, S. A. Burns, and J. C. He, "Model for cone directionality reflectometric measurements based on scattering," Journal of the Optical Society of America A **15**, 2012-2022 (1998).
134. N. P. A. Zagers, J. van de Kraats, T. T. J. M. Berendschot, and D. van Norren, "Simultaneous measurement of foveal spectral reflectance and cone-photoreceptor directionality," Applied Optics **41**, 4686-4696 (2002).
135. N. P. A. Zagers, T. T. J. M. Berendschot, and D. van Norren, "Wavelength dependence of reflectometric cone photoreceptor directionality," Journal of the Optical Society of America A **20**, 18-23 (2003).
136. S. Marcos and S. A. Burns, "Cone directionality from laser ray tracing in normal and LASIK patients," Journal of modern optics **56**, 2181-2188 (2009).
137. J. S. Werner, D. H. Peterzell, and A. J. Scheetz, "Light, vision, and aging," Optometry and vision science : official publication of the American Academy of Optometry **67**, 214-229 (1990).
138. D. A. Atchison, "Accommodation and presbyopia," Ophthalmic Physiol Opt **15**, 255-272 (1995).
139. W. N. Charman, "The eye in focus: accommodation and presbyopia," Clin Exp Optom **91**, 207-225 (2008).
140. H. v. Helmholtz and J. P. C. Southall, *Helmholtz's treatise on physiological optics* (Optical Society of America, [Rochester, N.Y., 1924).
141. M. C. Puell Marín, "Óptica Fisiológica: el sistema óptico del ojo y la visión binocular," (2006).
142. P. J. Donaldson, A. C. Grey, B. Maceo Heilman, J. C. Lim, and E. Vaghefi, "The physiological optics of the lens," Prog Retin Eye Res **56**, e1-e24 (2017).
143. S. A. Strenk, L. M. Strenk, and J. F. Koretz, "The mechanism of presbyopia," Prog Retin Eye Res **24**, 379-393 (2005).
144. A. Glasser and M. C. Campbell, "Presbyopia and the optical changes in the human crystalline lens with age," Vision Res **38**, 209-229 (1998).
145. A. Glasser, "Can accommodation be surgically restored in human presbyopia?," Optometry and vision science : official publication of the American Academy of Optometry **76**, 607-608 (1999).
146. M. A. Croft, A. Glasser, and P. Kaufman, "Accommodation and Presbyopia," International ophthalmology clinics **41**, 33-46 (2001).
147. A. Duane, "Normal values of the accommodation at all ages," Journal of the American Medical Association **59**, 1010-1013 (1912).
148. T. R. Fricke, N. Tahhan, S. Resnikoff, E. Papas, A. Burnett, S. M. Ho, T. Naduvilath, and K. S. Naidoo, "Global Prevalence of Presbyopia and Vision Impairment from Uncorrected Presbyopia: Systematic Review, Meta-analysis, and Modelling," Ophthalmology **125**, 1492-1499 (2018).

149. B. A. Holden, T. R. Fricke, S. M. Ho, R. Wong, G. Schlenther, S. Cronjé, A. Burnett, E. Papas, K. S. Naidoo, and K. D. Frick, "Global vision impairment due to uncorrected presbyopia," Arch Ophthalmol **126**, 1731-1739 (2008).
150. A. D. Goertz, W. C. Stewart, W. R. Burns, J. A. Stewart, and L. A. Nelson, "Review of the impact of presbyopia on quality of life in the developing and developed world," Acta ophthalmologica **92**, 497-500 (2014).
151. J. C. Bobrow, *2008-2009 Basic and Clinical Science Course (BCSC): Lens and Cataract Section 11*, American Academy of Ophthalmology (2008-2009).
152. W. N. Charman, "Developments in the correction of presbyopia I: spectacle and contact lenses," Ophthalmic Physiol Opt **34**, 8-29 (2014).
153. W. N. Charman, "Developments in the correction of presbyopia II: surgical approaches," Ophthalmic & physiological optics : the journal of the British College of Ophthalmic Opticians (Optometrists) **34**, 397-426 (2014).
154. S. C. Han, A. D. Graham, and M. C. Lin, "Clinical assessment of a customized free-form progressive add lens spectacle," Optometry and vision science : official publication of the American Academy of Optometry **88**, 234-243 (2011).
155. L. Zheleznyak, A. Alarcon, K. C. Dieter, D. Tadin, and G. Yoon, "The role of sensory ocular dominance on through-focus visual performance in monovision presbyopia corrections," J Vis **15**, 17 (2015).
156. B. J. Evans, "Monovision: a review," Ophthalmic Physiol Opt **27**, 417-439 (2007).
157. C. Buznego and W. B. Trattler, "Presbyopia-correcting intraocular lenses," Curr Opin Ophthalmol **20**, 13-18 (2009).
158. T. Ferrer-Blasco and D. Madrid-Costa, "Stereoacuity with simultaneous vision multifocal contact lenses," Optometry and vision science : official publication of the American Academy of Optometry **87**, E663-668 (2010).
159. A. Radhakrishnan, C. Dorronsoro, L. Sawides, and S. Marcos, "Short-term neural adaptation to simultaneous bifocal images," Plos One **9**, e93089 (2014).
160. C. W. Plakitsi A, "Comparison of the depths of focus with the naked eye and with three types of presbyopic contact lens correction," Contact lens Assoc **18**, 119-125 (1995).
161. R. Montés-Micó and J. L. Alió, "Distance and near contrast sensitivity function after multifocal intraocular lens implantation," J Cataract Refract Surg **29**, 703-711 (2003).
162. R. Montés-Micó, E. España, I. Bueno, W. N. Charman, and J. L. Menezo, "Visual performance with multifocal intraocular lenses: mesopic contrast sensitivity under distance and near conditions," Ophthalmology **111**, 85-96 (2004).
163. B. Hutchins and B. Huntjens, "Patients' attitudes and beliefs to presbyopia and its correction," Journal of Optometry **14**(2020).
164. M. Balgos, V. Vargas, and J. L. Alió, "Correction of presbyopia: An integrated update for the practical surgeon," Taiwan J Ophthalmol **8**, 121-140 (2018).
165. W. J. Benjamin, "Simultaneous vision contact lenses: why the dirty window argument doesn't wash," Int Cont Lens Clinic **20**, 239-242 (1993).
166. S. B. Charman WN, "Theoretical and practical factors influencing the optical performance of contact lenses for the presbyope," J Brit Cont Lens Ass. **13**, 67-75 (1990).
167. W. Charman and G. Walsh, "Retinal images with centred aspheric varifocal contact lenses," Int Contact Lens Clin **15**, 87-93 (1988).
168. E. S. Bennett, "Contact lens correction of presbyopia," Clinical and Experimental Optometry **91**, 265-278 (2008).
169. K. Richdale, G. L. Mitchell, and K. Zadnik, "Comparison of multifocal and monovision soft contact lens corrections in patients with low-astigmatic presbyopia," Optometry and vision science : official publication of the American Academy of Optometry **83**, 266-273 (2006).

170. R. C. Bakaraju, K. Ehrmann, A. Ho, and E. Papas, "Inherent ocular spherical aberration and multifocal contact lens optical performance," Optometry and vision science : official publication of the American Academy of Optometry **87**, 1009-1022 (2010).
171. R. Legras, Y. Benard, and H. Rouger, "Through-focus visual performance measurements and predictions with multifocal contact lenses," Vision Res **50**, 1185-1193 (2010).
172. R. Montés-Micó, D. Madrid-Costa, H. Radhakrishnan, W. N. Charman, and T. Ferrer-Blasco, "Accommodative functions with multifocal contact lenses: a pilot study," Optometry and vision science : official publication of the American Academy of Optometry **88**, 998-1004 (2011).
173. A. S. Rajagopalan, E. S. Bennett, and V. Lakshminarayanan, "Visual performance of subjects wearing presbyopic contact lenses," Optometry and vision science : official publication of the American Academy of Optometry **83**, 611-615 (2006).
174. D. J. Apple and J. Sims, "Harold Ridley and the invention of the intraocular lens," Surv Ophthalmol **40**, 279-292 (1996).
175. J. Zvorničanin and E. Zvorničanin, "Premium intraocular lenses: The past, present and future," Journal of current ophthalmology **30**, 287-296 (2018).
176. R. Menapace, O. Findl, K. Kriechbaum, and C. Leydolt-Koeppl, "Accommodating intraocular lenses: a critical review of present and future concepts," Graefes Arch Clin Exp Ophthalmol **245**, 473-489 (2007).
177. K. W. Brydon, A. C. Tokarewicz, and B. D. Nichols, "AMO array multifocal lens versus monofocal correction in cataract surgery," J Cataract Refract Surg **26**, 96-100 (2000).
178. J. L. Alio, A. B. Plaza-Puche, J. Javaloy, M. J. Ayala, L. J. Moreno, and D. P. Piñero, "Comparison of a new refractive multifocal intraocular lens with an inferior segmental near add and a diffractive multifocal intraocular lens," Ophthalmology **119**, 555-563 (2012).
179. Mendoza M.M., Garzón J.N, and Fernández G.A, "Corrección de la presbicia con lentes intraoculares multifocales," Gaceta óptica: Órgano Oficial del Colegio Nacional de Ópticos-Optometristas de España **435**, 36-42 (2009).
180. H. Hashim, A. Al-Hamdani, and H. G.Rahid, "Design and Evaluation of Refractive Multifocal Intraocular Lenses Implanted within the Human Eye Design and Evaluation of Refractive Multifocal Intraocular Lenses Implanted within the Human Eye," IOP Conference Series: Materials Science and Engineering **871**(2020).
181. J. A. Davison and M. J. Simpson, "History and development of the apodized diffractive intraocular lens," J Cataract Refract Surg **32**, 849-858 (2006).
182. D. Gatinel, C. Pagnoulle, Y. Houbrechts, and L. Gobin, "Design and qualification of a diffractive trifocal optical profile for intraocular lenses," J Cataract Refract Surg **37**, 2060-2067 (2011).
183. H. A. Weeber, S. T. Meijer, and P. A. Piers, "Extending the range of vision using diffractive intraocular lens technology," J Cataract Refract Surg **41**, 2746-2754 (2015).
184. M. C. Knorz, "[Presbyopia Correction with Intraocular Lenses]," Klin Monbl Augenheilkd **237**, 213-223 (2020).
185. D. R. Breyer, H. Kaymak, T. Ax, F. T. Kretz, G. U. Auffarth, and P. R. Hagen, "Multifocal intraocular lenses and extended depth of focus intraocular lenses," The Asia-Pacific Journal of Ophthalmology **6**, 339-349 (2017).
186. "FINEVISION (POD F) https://www.bvimedical.com/products/finevision/", retrieved.
187. M. Vinas, C. Benedi-Garcia, S. Aissati, D. Pascual, V. Akondi, C. Dorronsoro, and S. Marcos, "Visual simulators replicate vision with multifocal lenses," Scientific Reports **9**, 1539 (2019).
188. B. Cochener, G. Boutillier, M. Lamard, and C. Auberger-Zagnoli, "A Comparative Evaluation of a New Generation of Diffractive Trifocal and Extended Depth of Focus Intraocular Lenses," J Refract Surg **34**, 507-514 (2018).

189. F. Poyales, N. Garzón, C. Poyales, and B. Poyales, "Clinical Outcomes with a New Model of Extended Depth of Focus Intraocular Lens," Open Journal of Ophthalmology **08**, 161-170 (2018).
190. P. Kanclerz, F. Toto, A. Grzybowski, and J. L. Alio, "Extended Depth-of-Field Intraocular Lenses: An Update," Asia-Pacific journal of ophthalmology (Philadelphia, Pa.) **9**, 194-202 (2020).
191. K. Negishi, K. Ohnuma, N. Hirayama, and T. Noda, "Effect of chromatic aberration on contrast sensitivity in pseudophakic eyes," Arch Ophthalmol **119**, 1154-1158 (2001).
192. George Smith and David A. Atchison, *The Eye and Visual Optical Instruments* (Cambridge University Press, 1997), Vol. https://doi.org/10.1017/CBO9780511609541
193. H. Zhao and M. A. Mainster, "The effect of chromatic dispersion on pseudophakic optical performance," Br J Ophthalmol **91**, 1225-1229 (2007).
194. M. Vinas, C. Dorronsoro, N. Garzón, F. Poyales, and S. Marcos, "In vivo subjective and objective longitudinal chromatic aberration after bilateral implantation of the same design of hydrophobic and hydrophilic intraocular lenses," J Cataract Refract Surg **41**, 2115-2124 (2015).
195. S. S. Choi, N. Doble, J. Lin, J. Christou, and D. R. Williams, "Effect of wavelength on in vivo images of the human cone mosaic," Journal of the Optical Society of America A **22**, 2598-2605 (2005).
196. A. Roorda and D. R. Williams, "Optical fiber properties of individual human cones," J Vis **2**, 404-412 (2002).
197. L. Sawides, P. de Gracia, C. Dorronsoro, M. Webster, and S. Marcos, "Adapting to blur produced by ocular high-order aberrations," J Vis **11**(2011).
198. L. Sawides, "Correction and control of ocular aberrations with adaptive optics. Effects on Human Vision," (Universidad de Valladolid, 2013).
199. H. W. Babcock, "The Possibility of Compensating Astronomical Seeing," Publications of the Astronomical Society of the Pacific **65**, 229 (1953).
200. J. W. Hardy, J. E. Lefebvre, and C. L. Koliopoulos, "Real-time atmospheric compensation," J Opt Soc Am **67**, 360-369 (1977).
201. M. M. Waldrop, "Hubble space telescope takes aim at the stars," Science **247**, 1546-1547 (1990).
202. J. Liang and D. R. Williams, "Aberrations and retinal image quality of the normal human eye," Journal of the Optical Society of America A **14**, 2873-2883 (1997).
203. J. Liang, D. R. Williams, and D. T. Miller, "Supernormal vision and high-resolution retinal imaging through adaptive optics," Journal of the Optical Society of America A **14**, 2884-2892 (1997).
204. D. T. Miller, D. R. Williams, G. M. Morris, and J. Liang, "Images of cone photoreceptors in the living human eye," Vision Res **36**, 1067-1079 (1996).
205. E. J. Fernández, I. Iglesias, and P. Artal, "Closed-loop adaptive optics in the human eye," Optics Letters **26**, 746-748 (2001).
206. H. Hofer, L. Chen, G. Y. Yoon, B. Singer, Y. Yamauchi, and D. R. Williams, "Improvement in retinal image quality with dynamic correction of the eye's aberrations," Optics Express **8**, 631-643 (2001).
207. H. Hofer, P. Artal, B. Singer, J. L. Aragón, and D. R. Williams, "Dynamics of the eye's wave aberration," J Opt Soc Am A Opt Image Sci Vis **18**, 497-506 (2001).
208. L. Diaz-Santana, C. Torti, I. Munro, P. Gasson, and C. Dainty, "Benefit of higher closed-loop bandwidths in ocular adaptive optics," Optics Express **11**, 2597-2605 (2003).
209. Jason Porter, Hope Queener, Julianna Lin, Karen Thorn, and Abdul A. S. Awwal, *Adaptive Optics for Vision Science: Principles, Practices, Design, and Applications*, John Wiley & Sons, Inc (2006).
210. R. K. Tyson, *Principles of adaptive optics* (CRC press, 2015).

211. J. C. He, S. Marcos, R. H. Webb, and S. A. Burns, "Measurement of the wave-front aberration of the eye by a fast psychophysical procedure," Journal of the Optical Society of America A **15**, 2449-2456 (1998).
212. R. Navarro and M. A. Losada, "Aberrations and Relative Efficiency of Light Pencils in the Living Human Eye," Optometry and vision science : official publication of the American Academy of Optometry **74**, 540-547 (1997).
213. R. Navarro, E. Moreno, and C. Dorronsoro, "Monochromatic aberrations and point-spread functions of the human eye across the visual field," Journal of the Optical Society of America A **15**, 2522-2529 (1998).
214. Z. Zhang, Z. You, and D. Chu, "Fundamentals of phase-only liquid crystal on silicon (LCOS) devices," Light: Science & Applications **3**, e213-e213 (2014).
215. F. Vargas-Martín, P. M. Prieto, and P. Artal, "Correction of the aberrations in the human eye with a liquid-crystal spatial light modulator: limits to performance," J Opt Soc Am A Opt Image Sci Vis **15**, 2552-2562 (1998).
216. Rosales-Guzmán, Carmelo Forbes, and Andrew Society, "How to shape light with spatial light modulators" (2017), retrieved https://search.ebscohost.com/login.aspx?direct=true&scope=site&db=nlebk&db=nlabk&AN=1602374.
217. C. Dainty, *Adaptive Optics for Industry and Medicine: Proceedings of the Sixth International Workshop, National University of Ireland, Ireland, 12-15 June 2007* (Imperial College Press, 2008).
218. M. Vinas, C. Dorronsoro, V. Gonzalez, D. Cortes, A. Radhakrishnan, and S. Marcos, "Testing vision with angular and radial multifocal designs using Adaptive Optics," Vision Research **132**, 85-96 (2017).
219. Z. Bouchal, V. Chlup, R. Čelechovský, P. Bouchal, and I. C. Nistor, "Achromatic correction of diffractive dispersion in white light SLM imaging," Optics Express **22**, 12046-12059 (2014).
220. V. Akondi, C. Dorronsoro, E. Gambra, and S. Marcos, "Temporal multiplexing to simulate multifocal intraocular lenses: theoretical considerations," Biomedical Optics Express **8**, 3410-3425 (2017).
221. M. Blum, M. Büeler, C. Grätzel, and M. Aschwanden, "Compact optical design solutions using focus tunable lenses," in *Optical Systems Design*, 2011),
222. https://www.optotune.com/tunable-lenses, "Focus tunable lenses", retrieved.
223. J. Ruiz-Alcocer, D. Madrid-Costa, S. García-Lázaro, C. Albarrán-Diego, and T. Ferrer-Blasco, "Visual simulation through an aspheric aberration-correcting intraocular lens in subjects with different corneal profiles using adaptive optics," Clin Exp Optom **96**, 379-384 (2013).
224. K. M. Rocha, L. Vabre, N. Chateau, and R. R. Krueger, "Enhanced visual acuity and image perception following correction of highly aberrated eyes using an adaptive optics visual simulator," J Refract Surg **26**, 52-56 (2010).
225. L. Hervella, E. A. Villegas, P. M. Prieto, and P. Artal, "Assessment of subjective refraction with a clinical adaptive optics visual simulator," J Cataract Refract Surg **45**, 87-93 (2019).
226. J. Tabernero, C. Otero, and S. Pardhan, "A Comparison Between Refraction From an Adaptive Optics Visual Simulator and Clinical Refractions," Translational Vision Science & Technology **9**, 23-23 (2020).
227. X. Barcala, "Binocular Simultaneous Vision Simulator: validation and implementation of the Sim+Vis technology in the clinic," (Universidad Complutense de Madrid 2021).
228. A. Roorda, F. Romero-Borja, W. J. Donnelly Iii, H. Queener, T. J. Hebert, and M. C. W. Campbell, "Adaptive optics scanning laser ophthalmoscopy," Optics Express **10**, 405-412 (2002).

229. R. H. Webb, G. W. Hughes, and F. C. Delori, "Confocal scanning laser ophthalmoscope," Applied Optics **26**, 1492-1499 (1987).
230. D. T. Miller, J. Qu, R. S. Jonnal, and K. E. Thorn, "Coherence gating and adaptive optics in the eye," in *Coherence Domain Optical Methods and Optical Coherence Tomography in Biomedicine VII*, 2003), 65-72.
231. S. A. Burns, A. E. Elsner, K. A. Sapoznik, R. L. Warner, and T. J. Gast, "Adaptive optics imaging of the human retina," Prog Retin Eye Res **68**, 1-30 (2019).
232. S. Manzanera, P. M. Prieto, D. B. Ayala, J. M. Lindacher, and P. Artal, "Liquid crystal Adaptive Optics Visual Simulator: Application to testing and design of ophthalmic optical elements," Optics Express **15**, 16177-16188 (2007).
233. S. Marcos, J. S. Werner, S. A. Burns, W. H. Merigan, P. Artal, D. A. Atchison, K. M. Hampson, R. Legras, L. Lundstrom, G. Yoon, J. Carroll, S. S. Choi, N. Doble, A. M. Dubis, A. Dubra, A. Elsner, R. Jonnal, D. T. Miller, M. Paques, H. E. Smithson, L. K. Young, Y. Zhang, M. Campbell, J. Hunter, A. Metha, G. Palczewska, J. Schallek, and L. C. Sincich, "Vision science and adaptive optics, the state of the field," Vision Research **132**, 3-33 (2017).
234. A. Roorda, "Adaptive optics for studying visual function: a comprehensive review," J Vis **11**(2011).
235. S. Marcos, J. S. Werner, S. A. Burns, W. H. Merigan, P. Artal, D. A. Atchison, K. M. Hampson, R. Legras, L. Lundstrom, G. Yoon, J. Carroll, S. S. Choi, N. Doble, A. M. Dubis, A. Dubra, A. Elsner, R. Jonnal, D. T. Miller, M. Paques, H. E. Smithson, L. K. Young, Y. Zhang, M. Campbell, J. Hunter, A. Metha, G. Palczewska, J. Schallek, and L. C. Sincich, "Vision science and adaptive optics, the state of the field," Vision Res **132**, 3-33 (2017).
236. G.-Y. Yoon and D. R. Williams, "Visual performance after correcting the monochromatic and chromatic aberrations of the eye," Journal of the Optical Society of America A **19**, 266-275 (2002).
237. S. Marcos, L. Sawides, E. Gambra, and C. Dorronsoro, "Influence of adaptive-optics ocular aberration correction on visual acuity at different luminances and contrast polarities," Journal of Vision **8**, 1-1 (2008).
238. R. Legras and H. Rouger, "Just-Noticeable Levels of Aberration Correction," Journal of Optometry **1**, 71-77 (2008).
239. P. de Gracia, S. Marcos, A. Mathur, and D. A. Atchison, "Contrast sensitivity benefit of adaptive optics correction of ocular aberrations," Journal of Vision **11**, 5-5 (2011).
240. R. A. Applegate, J. D. Marsack, R. Ramos, and E. J. Sarver, "Interaction between aberrations to improve or reduce visual performance," Journal of Cataract & Refractive Surgery **29**, 1487-1495 (2003).
241. P. de Gracia, C. Dorronsoro, E. Gambra, G. Marin, M. Hernández, and S. Marcos, "Combining coma with astigmatism can improve retinal image over astigmatism alone," Vision Research **50**, 2008-2014 (2010).
242. P. Artal, L. Chen, E. J. Fernández, B. Singer, S. Manzanera, and D. R. Williams, "Neural compensation for the eye's optical aberrations," Journal of Vision **4**, 4-4 (2004).
243. L. Sawides, E. Gambra, D. Pascual, C. Dorronsoro, and S. Marcos, "Visual performance with real-life tasks under Adaptive-Optics ocular aberration correction," Journal of Vision **10**, 19-19 (2010).
244. E. Gambra, L. Sawides, C. Dorronsoro, and S. Marcos, "Accommodative lag and fluctuations when optical aberrations are manipulated," Journal of Vision **9**, 4-4 (2009).
245. R. Sabesan, L. Zheleznyak, and G. Yoon, "Binocular visual performance after correcting higher order aberrations," Biomedical Optics Express **3**, 3176-3189 (2012).
246. M. Vinas, "Polychromatic Adaptive Optics to evaluate the impact of manipulated optics on vision," (Universidad Complutense de Madrid 2015).

247. M. Vinas, P. de Gracia, C. Dorronsoro, L. Sawides, G. Marin, M. Hernández, and S. Marcos, "Astigmatism impact on visual performance: meridional and adaptational effects," Optometry and vision science : official publication of the American Academy of Optometry **90**, 1430-1442 (2013).
248. C. Benedi-Garcia, M. Velasco-Ocana, C. Dorronsoro, D. Pascual, M. Hernandez, G. Marin, and S. Marcos, "Perceptual impact of astigmatism induction in presbyopes," Vision Research **165**, 143-151 (2019).
249. M. Vinas, C. Dorronsoro, A. Radhakrishnan, C. Benedi-Garcia, E. A. LaVilla, J. Schwiegerling, and S. Marcos, "Comparison of vision through surface modulated and spatial light modulated multifocal optics," Biomedical Optics Express **8**, 2055-2068 (2017).
250. E. Gambra and "Accommodation: Optical function and crystalline lens imaging," (Universidad de Valladolid, 2015).
251. C. Benedi-Garcia, "Chromatic and monochromatic aberrations and multifocal designs: interaction and impact on vision " (Universidad Complutense de Madrid 2020).
252. S. Marcos, C. Benedí-García, S. Aissati, A. M. Gonzalez-Ramos, C. M. Lago, A. Radhkrishnan, M. Romero, S. Vedhakrishnan, L. Sawides, and M. Vinas, "VioBio lab adaptive optics: technology and applications by women vision scientists," Ophthalmic Physiol Opt **40**, 75-87 (2020).
253. F. C. Delori, R. H. Webb, and D. H. Sliney, "Maximum permissible exposures for ocular safety (ANSI 2000), with emphasis on ophthalmic devices," Journal of the Optical Society of America A **24**, 1250-1265 (2007).
254. C. Benedi-Garcia, M. Vinas, C. M. Lago, S. Aissati, A. de Castro, C. Dorronsoro, and S. Marcos, "Optical and visual quality of real intraocular lenses physically projected on the patient's eye," Biomedical Optics Express **12**, 6360-6374 (2021).
255. D. G. Pelli, "The VideoToolbox software for visual psychophysics: transforming numbers into movies," Spatial Vision **10**, 437-442 (1997).
256. C. Dorronsoro, S. Barbero, L. Llorente, and S. Marcos, "On-eye measurement of optical performance of rigid gas permeable contact lenses based on ocular and corneal aberrometry," Optometry and vision science : official publication of the American Academy of Optometry **80**, 115-125 (2003).
257. P. Pérez Merino, "Anterior segment topography and aberrations for clinical applications ," (Universidad de Valladolid, 2015).
258. "https://www.2eyesvision.com/en/simvis/", retrieved.
259. D. R. Iskander, "Computational aspects of the visual Strehl ratio," Optometry and vision science : official publication of the American Academy of Optometry **83**, 57-59 (2006).
260. V. Akondi, L. Sawides, Y. Marrakchi, E. Gambra, S. Marcos, and C. Dorronsoro, "Experimental validations of a tunable-lens-based visual demonstrator of multifocal corrections," Biomedical Optics Express **9**, 6302-6317 (2018).
261. C. Dorronsoro, X. Barcala, E. Gambra, V. Akondi, L. Sawides, Y. Marrakchi, V. Rodriguez-Lopez, C. Benedi-Garcia, M. Vinas, E. Lage, and S. Marcos, "Tunable lenses: dynamic characterization and fine-tuned control for high-speed applications," Optics Express **27**, 2085-2100 (2019).
262. C. Dorronsoro Díaz and S. Marcos Celestino, "Instrument for the simulation of multifocal ophthalmic corrections," (2009).
263. C. Dorronsoro Díaz, J. R. Alonso Sanz, and S. Marcos Celestino, "Miniaturized simultaneous vision simulator instrument," (2013).
264. C. Dorronsoro Diaz and S. Marcos Celestino, "Miniaturized simultaneous vision simulator instrument by mask generation," (2015).
265. C. Dorronsoro Díaz, E. Gambra Urralburu, X. Barcala Gosende, V. Rodríguez López, and S. Marcos Celestino, "Device for determining the optical power of lenses and measurement method," (2017).

266. M. Rynders, B. Lidkea, W. Chisholm, and L. N. Thibos, "Statistical distribution of foveal transverse chromatic aberration, pupil centration, and angle ψ in a population of young adult eyes," Journal of the Optical Society of America A **12**, 2348-2357 (1995).
267. S. Marcos and S. Burns, "Cone directionality from laser ray tracing in normal and LASIK patients," Journal of modern optics **56**, 2181-2188 (2009).
268. F. Gabbiani and S. J. Cox, "Chapter 1 - Introduction," in *Mathematics for Neuroscientists (Second Edition)*, F. Gabbiani and S. J. Cox, eds. (Academic Press, San Diego, 2017), pp. 1-8.
269. GoodmanJW., "Introduction to Fourier Optics," International Editions **2nd ed.** (1996).
270. D. H. Brainard, "The Psychophysics Toolbox," Spatial Vision **10**, 433-436 (1997).
271. D. B. M Kleiner, Denis Pelli, A Ingling, R Murray and C Broussard, "What's new in psychtoolbox-3," Perception **36**, 1--16 (2007).
272. F. W. Campbell and D. G. Green, "Optical and retinal factors affecting visual resolution," The Journal of Physiology **181**, 576-593 (1965).
273. L. K. Young, G. D. Love, and H. E. Smithson, "Accounting for the phase, spatial frequency and orientation demands of the task improves metrics based on the visual Strehl ratio," Vision Research **90**, 57-67 (2013).
274. J. D. Marsack, L. N. Thibos, and R. A. Applegate, "Metrics of optical quality derived from wave aberrations predict visual performance," Journal of Vision **4**, 8-8 (2004).
275. M. Vinas, S. Aissati, M. Romero, C. Benedi-Garcia, N. Garzon, F. Poyales, C. Dorronsoro, and S. Marcos, "Pre-operative simulation of post-operative multifocal vision," Biomedical Optics Express **10**, 5801-5817 (2019).
276. S. Marcos, C. Benedí-García, S. Aissati, A. M. Gonzalez-Ramos, C. M. Lago, A. Radhkrishnan, M. Romero, S. Vedhakrishnan, L. Sawides, and M. Vinas, "VioBio lab adaptive optics: technology and applications by women vision scientists," Ophthalmic and Physiological Optics **40**, 75-87 (2020).
277. S. Marcos, E. Martinez-Enriquez, M. Vinas, A. de Castro, C. Dorronsoro, S. P. Bang, G. Yoon, and P. Artal, "Simulating Outcomes of Cataract Surgery: Important Advances in Ophthalmology," Annual Review of Biomedical Engineering **23**(2021).
278. M. Vinas, "From Astronomy to the clinic: Adaptive Optics based visual simulators," Europhysics News **51**, 17-19 (2020).
279. S. Aissati, M. Viñas, M. Romero, J. L. M. González, C. Benedí, E. Gambra, V. Akondi, N. Garzón, F. Poyales, C. Dorronsoro, and S. Marcos, "Visual simulation of multifocal lenses in patients before and after implantation of diffractive trifocal lenses. ," in *XI Workshop on Adaptive Optics for Industry and Medicine, Murcia, España (2018). Oral communication.,* (2018).
280. M. Vinas, M. Romero, S. Aissati, J. L. Mendez-Gonzalez, C. Benedi, E. Gambra, V. Akondi, n. Garzon, F. Poyales, C. Dorronsoro, and S. Marcos, "Comparison of multifocal visual simulations in patients before and after implantation of diffractive trifocal lenses," Investigative Ophthalmology & Visual Science **59**, 252-252 (2018).
281. M. Vinas, C. Dorronsoro, D. Cortes, D. Pascual, and S. Marcos, "Longitudinal chromatic aberration of the human eye in the visible and near infrared from wavefront sensing, double-pass and psychophysics," Biomedical Optics Express **6**, 948-962 (2015).
282. A. Radhakrishnan, C. Dorronsoro, and S. Marcos, "Differences in visual quality with orientation of a rotationally asymmetric bifocal intraocular lens design," Journal of Cataract & Refractive Surgery **42**, 1276-1287 (2016).
283. C. Schwarz, P. M. Prieto, E. J. Fernández, and P. Artal, "Binocular adaptive optics vision analyzer with full control over the complex pupil functions," Optics Letters **36**, 4779-4781 (2011).

284. C. Dorronsoro, A. Radhakrishnan, J. R. Alonso-Sanz, D. Pascual, M. Velasco-Ocana, P. Perez-Merino, and S. Marcos, "Portable simultaneous vision device to simulate multifocal corrections," Optica **3**, 918-924 (2016).
285. C. Schwarz, C. Cánovas, S. Manzanera, H. Weeber, P. M. Prieto, P. Piers, and P. Artal, "Binocular visual acuity for the correction of spherical aberration in polychromatic and monochromatic light," Journal of Vision **14**, 8-8 (2014).
286. S. Manzanera and P. Artal, "Minimum change in spherical aberration that can be perceived," Biomedical Optics Express **7**, 3471-3477 (2016).
287. E. A. Villegas, S. Manzanera, C. M. Lago, L. Hervella, L. Sawides, and P. Artal, "Effect of Crystalline Lens Aberrations on Adaptive Optics Simulation of Intraocular Lenses," J Refract Surg **35**, 126-131 (2019).
288. R. Dou and M. K. Giles, "Closed-loop adaptive-optics system with a liquid-crystal television as a phase retarder," Optics Letters **20**, 1583-1585 (1995).
289. G. D. Love, "Wave-front correction and production of Zernike modes with a liquid-crystal spatial light modulator," Applied Optics **36**, 1517-1524 (1997).
290. R. Martínez-Cuenca, V. Durán, J. Arines, J. Ares, Z. Jaroszewicz, S. Bará, L. Martínez-León, and J. Lancis, "Closed-loop adaptive optics with a single element for wavefront sensing and correction," Optics Letters **36**, 3702-3704 (2011).
291. J. Tabernero, C. Schwarz, E. J. Fernández, and P. Artal, "Binocular Visual Simulation of a Corneal Inlay to Increase Depth of Focus," Investigative Ophthalmology & Visual Science **52**, 5273-5277 (2011).
292. L. Zhao, N. Bai, X. Li, L. S. Ong, Z. P. Fang, and A. K. Asundi, "Efficient implementation of a spatial light modulator as a diffractive optical microlens array in a digital Shack-Hartmann wavefront sensor," Applied Optics **45**, 90-94 (2006).
293. S. O. Luque and J. P. Ramo, "Method and system for simulating/emulating vision via intraocular devices or lenses prior to surgery," (2012).
294. W. Brezna, K. Lux, N. Dragostinoff, C. Krutzler, N. Plank, R. Tobisch, A. Boltz, G. Garhöfer, R. Told, K. Witkowska, and L. Schmetterer, "Psychophysical Vision Simulation of Diffractive Bifocal and Trifocal Intraocular Lenses," Translational Vision Science & Technology **5**, 13-13 (2016).
295. J. Pujol, M. Aldaba, A. Giner, J. Arasa, and S. O. Luque, "Visual performance evaluation of a new multifocal intraocular lens design before surgery," Investigative Ophthalmology & Visual Science **55**, 3752-3752 (2014).
296. D. Gatinel and Y. Houbrechts, "Comparison of bifocal and trifocal diffractive and refractive intraocular lenses using an optical bench," J Cataract Refract Surg **39**, 1093-1099 (2013).
297. M. Vinas, A. Gonzalez-Ramos, C. Dorronsoro, V. Akondi, N. Garzon, F. Poyales, and S. Marcos, "In Vivo Measurement of Longitudinal Chromatic Aberration in Patients Implanted With Trifocal Diffractive Intraocular Lenses," Journal of Refractive Surgery **33**, 736-742 (2017).
298. V. Akondi, P. Pérez-Merino, E. Martinez-Enriquez, C. Dorronsoro, N. Alejandre, I. Jiménez-Alfaro, and S. Marcos, "Evaluation of the True Wavefront Aberrations in Eyes Implanted With a Rotationally Asymmetric Multifocal Intraocular Lens," Journal of Refractive Surgery **33**, 257-265 (2017).
299. E. A. Ehrenstein WH, "Modern techniques in neuroscience research," Springer, 1211-1240 (1999).
300. D. H. Brainard, "The Psychophysics Toolbox," Spat Vis **10**, 433-436 (1997).
301. J. T. Holladay, "Proper method for calculating average visual acuity," J Refract Surg **13**, 388-391 (1997).
302. F. Poyales, N. Garzón, J. J. Rozema, C. Romero, and B. O. d. Zárate, "Stability of a Novel Intraocular Lens Design: Comparison of Two Trifocal Lenses," Journal of Refractive Surgery **32**, 394-402 (2016).

303. K. G. Gundersen and R. Potvin, "Trifocal intraocular lenses: a comparison of the visual performance and quality of vision provided by two different lens designs," Clinical ophthalmology (Auckland, N.Z.) **11**, 1081-1087 (2017).
304. D. Madrid-Costa, J. Ruiz-Alcocer, C. Pérez-Vives, T. Ferrer-Blasco, N. López-Gil, and R. Montés-Micó, "Visual simulation through different intraocular lenses using adaptive optics: effect of tilt and decentration," J Cataract Refract Surg **38**, 947-958 (2012).
305. E. J. Fernández, P. M. Prieto, and P. Artal, "Binocular adaptive optics visual simulator," Optics Letters **34**, 2628-2630 (2009).
306. P. de Gracia, C. Dorronsoro, Á. Sánchez-González, L. Sawides, and S. Marcos, "Experimental Simulation of Simultaneous Vision," Investigative Ophthalmology & Visual Science **54**, 415-422 (2013).
307. P. A. Piers, E. J. Fernandez, S. Manzanera, S. Norrby, and P. Artal, "Adaptive Optics Simulation of Intraocular Lenses with Modified Spherical Aberration," Investigative Ophthalmology & Visual Science **45**, 4601-4610 (2004).
308. M. Vinas, S. Aissati, A. M. Gonzalez-Ramos, M. Romero, L. Sawides, V. Akondi, E. Gambra, C. Dorronsoro, T. Karkkainen, D. Nankivil, and S. Marcos, "Optical and Visual Quality With Physical and Visually Simulated Presbyopic Multifocal Contact Lenses," Translational Vision Science & Technology **9**, 20-20 (2020).
309. M. Vinas, S. Aissati, A. Gonzalez-Ramos, M. Romero, L. Sawides, V. Akondi, C. Dorronsoro, E. Martinez-Enriquez, T. Karkkainen, and D. Nankivil, "Optical and visual quality with physical and visually simulated presbyopic multifocal contact lenses," Investigative Ophthalmology & Visual Science **60**, 6468-6468 (2019).
310. R. Perez-Prados, D. P. Pinero, R. J. Perez-Cambrodi, and D. Madrid-Costa, "Soft multifocal simultaneous image contact lenses: a review," Clin Exp Optom **100**, 107-127 (2017).
311. E. S. Bennett, "Contact lens correction of presbyopia," Clin Exp Optom **91**, 265-278 (2008).
312. D. Madrid-Costa, J. Ruiz-Alcocer, S. García-Lázaro, T. Ferrer-Blasco, and R. Montés-Micó, "Optical power distribution of refractive and aspheric multifocal contact lenses: Effect of pupil size," Cont Lens Anterior Eye **38**, 317-321 (2015).
313. P. S. Kollbaum and A. Bradley, "Correction of presbyopia: old problems with old (and new) solutions," Clin Exp Optom **103**, 21-30 (2020).
314. D. Lopes-Ferreira, P. Fernandes, A. Queiros, and J. M. Gonzalez-Meijome, "Combined Effect of Ocular and Multifocal Contact Lens Induced Aberrations on Visual Performance: Center-Distance Versus Center-Near Design," Eye Contact Lens **44 Suppl 1**, S131-S137 (2018).
315. J. Sha, R. C. Bakaraju, D. Tilia, J. Chung, S. Delaney, A. Munro, K. Ehrmann, V. Thomas, and B. A. Holden, "Short-term visual performance of soft multifocal contact lenses for presbyopia," Arq Bras Oftalmol **79**, 73-77 (2016).
316. J. Woods, C. Woods, and D. Fonn, "Visual Performance of a Multifocal Contact Lens versus Monovision in Established Presbyopes," Optom Vis Sci **92**, 175-182 (2015).
317. A. Llorente-Guillemot, S. Garcia-Lazaro, T. Ferrer-Blasco, R. J. Perez-Cambrodi, and A. Cervino, "Visual performance with simultaneous vision multifocal contact lenses," Clin Exp Optom **95**, 54-59 (2012).
318. N. Gupta, S. A. Naroo, and J. S. Wolffsohn, "Visual comparison of multifocal contact lens to monovision," Optometry and vision science : official publication of the American Academy of Optometry **86**, E98-105 (2009).
319. S. Plainis, G. Ntzilepis, D. A. Atchison, and W. N. Charman, "Through-focus performance with multifocal contact lenses: effect of binocularity, pupil diameter and inherent ocular aberrations," Ophthalmic Physiol Opt **33**, 42-50 (2013).

320. R. C. Bakaraju, K. Ehrmann, D. Falk, A. Ho, and E. Papas, "Optical performance of multifocal soft contact lenses via a single-pass method," Optometry and vision science : official publication of the American Academy of Optometry **89**, 1107-1118 (2012).
321. D. Lopes-Ferreira, P. Fernandes, A. Queirós, and J. M. González-Meijome, "Combined Effect of Ocular and Multifocal Contact Lens Induced Aberrations on Visual Performance: Center-Distance Versus Center-Near Design," Eye & Contact Lens **44**, S131-S137 (2018).
322. M. Vinas, C. Dorronsoro, A. Radhakrishnan, C. Benedi-Garcia, E. LaVilla, J. Schwiegerling, and S. Marcos, "Comparison of vision through surface modulated and spatial light modulated multifocal optics," Biomed. Opt. Express **8**, 2055-2068 (2017).
323. M. Vinas, C. Dorronsoro, V. Gonzalez, D. Cortes, A. Radhakrishnan, and S. Marcos, "Testing vision with angular and radial multifocal designs using Adaptive Optics," Vision Res (2016).
324. A. Radhakrishnan, C. Dorronsoro, and S. Marcos, "Differences in visual quality with orientation of a rotationally asymmetric bifocal intraocular lens design," J Cataract Refract Surg **42**, 1276-1287 (2016).
325. M. Vinas, C. Benedi-Garcia, S. Aissati, D. Pascual, V. Akondi, C. Dorronsoro, and S. Marcos, "Visual simulators replicate vision with multifocal lenses," Sci Rep **9**, 1539 (2019).
326. P. de Gracia, C. Dorronsoro, A. Sanchez-Gonzalez, L. Sawides, and S. Marcos, "Experimental simulation of simultaneous vision," Invest Ophthalmol Vis Sci **54**, 415-422 (2013).
327. C. Dorronsoro, A. Radhakrishnan, P. de Gracia, L. Sawides, and S. Marcos, "Perceived image quality with simulated segmented bifocal corrections," Biomedical Optics Express **7**, 4388-4399 (2016).
328. V. Akondi, C. Dorronsoro, E. Gambra, and S. Marcos, "Temporal multiplexing to simulate multifocal intraocular lenses: theoretical considerations," Biomed Opt Express **8**, 3410-3425 (2017).
329. C. Dorronsoro, X. Barcala, E. Gambra, V. Akondi, L. Sawides, Y. Marrakchi, V. Rodriguez-Lopez, C. Benedi-Garcia, M. Vinas, E. Lage, and S. Marcos, "Tunable lenses: dynamic characterization and fine-tuned control for high-speed applications," Opt Express **27**, 2085-2100 (2019).
330. H.-C. S. Moody K, Wooley B et al., "Innovating for multifocal fitting success," Optician **249**, 12-17 (2015).
331. E. Kim, R. C. Bakaraju, and K. Ehrmann, "Power Profiles of Commercial Multifocal Soft Contact Lenses," Optometry and vision science : official publication of the American Academy of Optometry **94**, 183-196 (2017).
332. M. Vinas, S. Aissati, M. Romero, C. Benedi-Garcia, N. Garzon, F. Poyales, C. Dorronsoro, and S. Marcos, "Pre-operative simulation of post-operative multifocal vision," Biomed Opt Express **10**, 5801-5817 (2019).
333. V. Akondi, L. Sawides, Y. Marrakchi, E. Gambra, S. Marcos, and C. Dorronsoro, "Experimental validations of a tunable-lens-based visual demonstrator of multifocal corrections," Biomed Opt Express **9**, 6302-6317 (2018).
334. J. D. Marsack, L. N. Thibos, and R. A. Applegate, "Metrics of optical quality derived from wave aberrations predict visual performance," J Vis **4**, 322-328 (2004).
335. W. H. Ehrenstein and A. Ehrenstein, "Psychophysical methods," in *Modern techniques in neuroscience research*, U. Windhorst and H. Johansson, eds. (Springer, 1999), pp. 1211-1240.
336. D. G. Pelli, "The VideoToolbox software for visual psychophysics: transforming numbers into movies," Spat Vis **10**, 437-442 (1997).
337. M. Kleiner, D. Brainard, D. Pelli, A. Ingling, R. Murray, and C. Broussard, "What's new in psychtoolbox-3," Perception **36**, 1-16 (2007).

338. S. Marcos, E. Moreno, and R. Navarro, "The depth-of-field of the human eye from objective and subjective measurements," Vision Res **39**, 2039-2049 (1999).
339. M. J. Collins, R. Franklin, and B. A. Davis, "Optical considerations in the contact lens correction of infant aphakia," Optometry and vision science : official publication of the American Academy of Optometry **79**, 234-240 (2002).
340. F. Yi, D. R. Iskander, and M. Collins, "Depth of focus and visual acuity with primary and secondary spherical aberration," Vision Res **51**, 1648-1658 (2011).
341. X. Cheng, A. Bradley, and L. N. Thibos, "Predicting subjective judgment of best focus with objective image quality metrics," J Vis **4**, 310-321 (2004).
342. L. Gouvea, G. O. t. Waring, A. Brundrett, M. Crouse, and K. M. Rocha, "Objective assessment of optical quality in dry eye disease using a double-pass imaging system," Clin Ophthalmol **13**, 1991-1996 (2019).
343. V. de Juan, M. Aldaba, R. Martin, M. Vilaseca, J. M. Herreras, and J. Pujol, "Optical quality and intraocular scattering assessed with a double-pass system in eyes with contact lens induced corneal swelling," Cont Lens Anterior Eye **37**, 278-284 (2014).
344. A. Sivardeen, D. Laughton, and J. S. Wolffsohn, "Randomized Crossover Trial of Silicone Hydrogel Presbyopic Contact Lenses," Optometry and vision science : official publication of the American Academy of Optometry **93**, 141-149 (2016).
345. J. Gispets, M. Arjona, and J. Pujol, "Image quality in wearers of a centre distance concentric design bifocal contact lens," Ophthalmic Physiol Opt **22**, 221-233 (2002).
346. J. Pujol, J. Gispets, and M. Arjona, "Optical performance in eyes wearing two multifocal contact lens designs," Ophthalmic Physiol Opt **23**, 347-360 (2003).
347. G. Montani, "Objective and subjective visual performance ofa new daily soft contact lens for presbyopia," Contact Lens & Anterior Eye **41S**(2018).
348. D. Nankivil, T. Raymond, G. Hofmann, and D. Neal, *Estimating visual acuity from a single wavefront measurement*, SPIE BiOS (SPIE, 2020), Vol. 11218.
349. J. Sha, D. Tilia, D. Kho, H. Amrizal, J. Diec, N. Yeotikar, M. Jong, V. Thomas, and R. C. Bakaraju, "Visual Performance of Daily-disposable Multifocal Soft Contact Lenses: A Randomized, Double-blind Clinical Trial," Optometry and vision science : official publication of the American Academy of Optometry **95**, 1096-1104 (2018).
350. K. Moody, T. Karkkainen, R. Clark, J. Xu, and S. Hickson-Curran, "Visual acuity performance across different near ADD powers with a new multifocal daily disposable lens," Contact lens and anterior eye **41, supplement 1**, s24 (2018).
351. S. AISSATI, M. Vinas, C. Benedi-Garcia, and S. Marcos, "Convolved vs.Optically blurred images-What is the key reason for the observed differences?," Invest Ophthalmol Vis Sci **62**, 1800-1800 (2021).
352. E. Dalimier, C. Dainty, and J. Barbur, "Effects of higher-order aberrations on contrast acuity as a function of light level," J Mod Opt **11**, 24-29 (2008).
353. J. Santamaría, P. Artal, and J. Bescós, "Determination of the point-spread function of human eyes using a hybrid optical–digital method," Journal of the Optical Society of America A **4**, 1109-1114 (1987).
354. G. J. Burton and N. D. Haig, "Effects of the Seidel aberrations on visual target discrimination," Journal of the Optical Society of America A **1**, 373-385 (1984).
355. R. A. Applegate, J. D. Marsack, R. Ramos, and E. J. Sarver, "Interaction between aberrations to improve or reduce visual performance," J Cataract Refract Surg **29**, 1487-1495 (2003).
356. S. Marcos, S. Barbero, and I. Jiménez-Alfaro, "Optical quality and depth-of-field of eyes implanted with spherical and aspheric intraocular lenses," J Refract Surg **21**, 223-235 (2005).
357. W. N. Charman, "Wavefront aberration of the eye: a review," Optometry and vision science : official publication of the American Academy of Optometry **68**, 574-583 (1991).

358. L. Sawides, E. Gambra, D. Pascual, C. Dorronsoro, and S. Marcos, "Visual performance with real-life tasks under adaptive-optics ocular aberration correction," J Vis **10**, 19 (2010).
359. A. Ohlendorf, J. Tabernero, and F. Schaeffel, "Visual acuity with simulated and real astigmatic defocus," Optometry and vision science : official publication of the American Academy of Optometry **88**, 562-569 (2011).
360. S. Marcos and S. A. Burns, "Cone directionality from laser ray tracing in normal and LASIK patients," J Mod Opt **56**, 2181-2188 (2009).
361. D. A. Atchison, S. Marcos, and D. H. Scott, "The influence of the Stiles–Crawford peak location on visual performance," Vision Research **43**, 659-668 (2003).
362. D. A. Atchison, A. Joblin, and G. Smith, "Influence of Stiles–Crawford effect apodization on spatial visual performance," Journal of the Optical Society of America A **15**, 2545-2551 (1998).
363. S. A. Burns and S. Marcos, "Evaluating the role of cone directionality in image formation," in *Vision Science and its Applications*, OSA Technical Digest (Optical Society of America, 2000), FA2.
364. S. Ravikumar, L. N. Thibos, and A. Bradley, "Calculation of retinal image quality for polychromatic light," Journal of the Optical Society of America A **25**, 2395-2407 (2008).
365. J. W. Goodman, *Introduction to Fourier Optics*, International Editions (1996), Vol. 2nd ed.
366. A. A. Michelson, *Studies in optics* (The University of Chicago Press, Chicago, Ill., 1927).
367. W. H. Ehrenstein and A. Ehrenstein, "Psychophysical methods," in *Modern techniques in neuroscience research* (Springer, 1999), pp. 1211-1241.
368. S. Anstis and P. Cavanagh, "A minimum motion technique for judging equiluminance," Colour Vision: Psychophysics and Physiology (1983).
369. S. Raphael and D. I. A. MacLeod, "Mesopic luminance assessed with minimum motion photometry," Journal of Vision **11**, 14-14 (2011).
370. C. Font, J. C. Escalera, and M. J. Yzuel, "Polychromatic Point Spread Function: Calculation Accuracy," Journal of modern optics **41**, 1401-1413 (1994).
371. A. Stockman, D. MacLeod, and N. Johnson, "Spectral sensitivities of human cones," J Opt Soc Am A Opt Image Sci Vis **10**, 2491-2521 (1994).
372. X. Cheng, A. Bradley, S. Ravikumar, and L. N. Thibos, "Visual impact of Zernike and Seidel forms of monochromatic aberrations," Optometry and vision science : official publication of the American Academy of Optometry **87**, 300-312 (2010).
373. I. L. Bailey and J. E. Lovie-Kitchin, "Visual acuity testing. From the laboratory to the clinic," Vision Res **90**, 2-9 (2013).
374. S. Barbero and S. Marcos, "Analysis of the optical field on the human retina from wavefront aberration data," Journal of the Optical Society of America A **25**, 2280-2285 (2008).
375. L. N. Thibos, A. Bradley, D. L. Still, X. Zhang, and P. A. Howarth, "Theory and measurement of ocular chromatic aberration," Vision Res **30**, 33-49 (1990).
376. R. E. Bedford and G. Wyszecki, "Axial Chromatic Aberration of the Human Eye," J Opt Soc Am **47**, 564_561-565 (1957).
377. P. Simonet and M. C. W. Campbell, "The optical transverse chromatic aberration on the fovea of the human eye," Vision Research **30**, 187-206 (1990).
378. S. Marcos and S. A. Burns, "Cone spacing and waveguide properties from cone directionality measurements," J Opt Soc Am A Opt Image Sci Vis **16**, 995-1004 (1999).
379. G. M. Pérez, S. Manzanera, and P. Artal, "Impact of scattering and spherical aberration in contrast sensitivity," J Vis **9**, 19.11-10 (2009).
380. S. Ravikumar, A. Bradley, and L. N. Thibos, "Do Monochromatic Aberrations Protect The Eye Against Chromatic Blur?," Invest Ophthalmol Vis Sci **47**, 1505-1505 (2006).
381. C. Benedi-Garcia, S. AISSATI, M. P. Eckstein, and S. Marcos, "Gender Identification of faces under manipulated ocular optics," Investigative Ophthalmology & Visual Science **62**, 504-504 (2021).

382. N. P. Costen, D. M. Parker, and I. Craw, "Effects of high-pass and low-pass spatial filtering on face identification," Perception & Psychophysics **58**, 602-612 (1996).
383. G. Westheimer, "The Fourier Theory of Vision," Perception **30**, 531-541 (2001).
384. S. Marcos, M. Velasco-Ocana, C. Dorronsoro, L. Sawides, M. Hernandez, and G. Marin, "Impact of astigmatism and high-order aberrations on subjective best focus," Journal of Vision **15**, 4-4 (2015).
385. M. Ruiz and F. Beltran, "Face perception: An integrative review of the role of spatial frequencies," Psychological research **70**, 273-292 (2006).
386. L. Aguado, I. Serrano-Pedraza, S. Rodríguez, and F. J. Román, "Effects of Spatial Frequency Content on Classification of Face Gender and Expression," The Spanish journal of psychology **13**, 525-537 (2013).
387. C. Deruelle and J. Fagot, "Categorizing facial identities, emotions, and genders: attention to high- and low-spatial frequencies by children and adults," J Exp Child Psychol **90**, 172-184 (2005).
388. S. Aissati, M. Vinas, C. Benedi-Garcia, C. Dorronsoro, and S. Marcos, "Testing the effect of ocular aberrations in the perceived transverse chromatic aberration," Biomedical Optics Express **11**, 4052-4068 (2020).
389. J. S. McLellan, S. Marcos, P. M. Prieto, and S. A. Burns, "Imperfect optics may be the eye's defence against chromatic blur," Nature **417**, 174 (2002).
390. L. Llorente, L. Diaz-Santana, D. Lara-Saucedo, and S. Marcos, "Aberrations of the human eye in visible and near infrared illumination," Optom Vis Sci **80**, 26-35 (2003).
391. P. A. Howarth and A. Bradley, "The longitudinal chromatic aberration of the human eye, and its correction," Vision Res **26**, 361-366 (1986).
392. S. Marcos, S. A. Burns, P. M. Prieto, R. Navarro, and B. Baraibar, "Investigating sources of variability of monochromatic and transverse chromatic aberrations across eyes," Vision Research **41**, 3861-3871 (2001).
393. M. Rynders, B. Lidkea, W. Chisholm, and L. N. Thibos, "Statistical distribution of foveal transverse chromatic aberration, pupil centration, and angle psi in a population of young adult eyes," J Opt Soc Am A Opt Image Sci Vis **12**, 2348-2357 (1995).
394. B. H. C. W. S. Stiles, and J. H. Parsons "The luminous efficiency of rays entering the eye pupil at different points," Proceedings of the Royal Society of London. Series B, Containing Papers of a Biological Character, 428-450 (1933).
395. C. B. S. Marcos, M. Vinas, C. Dorronsoro, S. A. Burns, and E. Peli, "Visual benefit of correcting high order aberrationsin blue or green light: an optical effect?," ARVO abstract 2018 (2018).
396. X. Jiang, J. A. Kuchenbecker, P. Touch, and R. Sabesan, "Measuring and compensating for ocular longitudinal chromatic aberration," Optica **6**, 981-990 (2019).
397. N. Suchkov, E. J. Fernández, and P. Artal, "Impact of longitudinal chromatic aberration on through-focus visual acuity," Optics Express **27**, 35935-35947 (2019).
398. H. A. Weeber and P. A. Piers, "Theoretical performance of intraocular lenses correcting both spherical and chromatic aberration," J Refract Surg **28**, 48-52 (2012).
399. N. W. J. Loicq, and D. Gatinel "LCA correction in diffractive intraocular lenses: an innovative optical design," in *SPIE BiOS,* (SPIE, 2020).
400. S. Marcos, L. Sawides, E. Gambra, and C. Dorronsoro, "Influence of adaptive-optics ocular aberration correction on visual acuity at different luminances and contrast polarities," J Vis **8**, 1.1-12 (2008).
401. J. C. He, S. Marcos, and S. A. Burns, "Comparison of cone directionality determined by psychophysical and reflectometric techniques," J Opt Soc Am A Opt Image Sci Vis **16**, 2363-2369 (1999).

402. D. A. Atchison, D. H. Scott, A. Joblin, and G. Smith, "Influence of Stiles–Crawford effect apodization on spatial visual performance with decentered pupils," Journal of the Optical Society of America A **18**, 1201-1211 (2001).
403. A. Bradley, L. Thibos, and D. Still, "Visual acuity measured with clinical Maxwellian-view systems: effects of beam entry location," Optom Vis Sci **67**, 811-817 (1990).
404. L. N. Thibos, "Calculation of the influence of lateral chromatic aberration on image quality across the visual field," Journal of the Optical Society of America A **4**, 1673-1680 (1987).
405. M. Tscherning, *Physiological Optics* Keystone (1924).
406. M. C. Rynders, "The Stiles-Crawford effect and an experimental determination of its impact on vision," (Indiana University, Bloomington, Ph.D thesis 1994).
407. S. Marcos and S. A. Burns, "On the symmetry between eyes of wavefront aberration and cone directionality," Vision Research **40**, 2437-2447 (2000).
408. P. Rosales and S. Marcos, "Customized computer models of eyes with intraocular lenses," Optics Express **15**, 2204-2218 (2007).
409. M. Sun, P. Pérez-Merino, E. Martinez-Enriquez, M. Velasco-Ocana, and S. Marcos, "Full 3-D OCT-based pseudophakic custom computer eye model," Biomedical Optics Express **7**, 1074-1088 (2016).
410. M. Nakajima, T. Hiraoka, T. Yamamoto, S. Takagi, Y. Hirohara, T. Oshika, and T. Mihashi, "Differences of Longitudinal Chromatic Aberration (LCA) between Eyes with Intraocular Lenses from Different Manufacturers," **11**, e0156227 (2016).
411. M. Vinas, A. M. Gonzalez-Ramos, S. Aissati, N. Garzón, F. Poyales, C. Dorronsoro, and S. Marcos, "Longitudinal Chromatic Aberration in Patients Implanted With Trifocal Diffractive Hydrophobic IOLs," J Refract Surg **36**, 804-810 (2020).
412. K. Graef and F. Schaeffel, "Control of accommodation by longitudinal chromatic aberration and blue cones," Journal of Vision **12**, 14-14 (2012).
413. W. N. Charman, "Optics of the Human Eye," C. Press, ed. (CRC Press, CRC Press, 1991).
414. M. Nakajima, T. Hiraoka, T. Yamamoto, S. Takagi, Y. Hirohara, T. Oshika, and T. Mihashi, "Differences of Longitudinal Chromatic Aberration (LCA) between Eyes with Intraocular Lenses from Different Manufacturers," PLOS ONE **11**, e0156227 (2016).
415. C. W. Bobier and J. G. Sivak, "Chromoretinoscopy and its instrumentation," Am J Optom Physiol Opt **57**, 106-108 (1980).
416. S. Marcos, M. Romero, C. Benedí-García, A. González-Ramos, M. Vinas, N. Alejandre, and I. Jiménez-Alfaro, "Interaction of Monochromatic and Chromatic Aberrations in Pseudophakic Patients," J Refract Surg **36**, 230-238 (2020).
417. S. Ravikumar, A. Bradley, and L. N. Thibos, "Chromatic aberration and polychromatic image quality with diffractive multifocal intraocular lenses," J Cataract Refract Surg **40**, 1192-1204 (2014).
418. F. Castignoles, M. Flury, and T. Lepine, "Comparison of the efficiency, MTF and chromatic properties of four diffractive bifocal intraocular lens designs," Optics Express **18**, 5245-5256 (2010).
419. F. Vega, M. S. Millán, N. Vila-Terricabras, and F. Alba-Bueno, "Visible Versus Near-Infrared Optical Performance of Diffractive Multifocal Intraocular Lenses," Invest Ophthalmol Vis Sci **56**, 7345-7351 (2015).
420. M. J. Simpson, "Diffractive multifocal intraocular lens image quality," Applied Optics **31**, 3621-3626 (1992).
421. J. S. Pepose, D. Wang, and G. E. Altmann, "Comparison of through-focus image sharpness across five presbyopia-correcting intraocular lenses," Am J Ophthalmol **154**, 20-28.e21 (2012).
422. M. J. Kim, L. Zheleznyak, S. Macrae, H. Tchah, and G. Yoon, "Objective evaluation of through-focus optical performance of presbyopia-correcting intraocular lenses using an optical bench system," J Cataract Refract Surg **37**, 1305-1312 (2011).

423. W. A. Maxwell, S. S. Lane, and F. Zhou, "Performance of presbyopia-correcting intraocular lenses in distance optical bench tests," J Cataract Refract Surg **35**, 166-171 (2009).
424. F. Vega, F. Alba-Bueno, and M. S. Millán, "Energy Distribution between Distance and Near Images in Apodized Diffractive Multifocal Intraocular Lenses," Investigative Ophthalmology & Visual Science **52**, 5695-5701 (2011).